Influence of Process Parameters on Microstructural Characteristics and Mechanical Properties of Ti-6Al-4V Samples Manufactured through Electron Beam Melting Manufacturing

Camille Bernier-Tremblay

A Thesis

in

The Department

of

Mechanical, Industrial, and Aerospace Engineering (MIAE)

Presented in Partial Fulfillment of the Requirements

for the Degree of Master of Applied Science at

Concordia University

Montreal, Quebec, Canada

February 2024

Concordia University

School of Graduate Studies

This is to certify that the thesis prepared

By: Camille Bernier-Tremblay

Entitled: Influence of Process Parameters on Microstructural Characteristics and Mechanical Properties of Ti-6Al-4V Samples Manufactured through Electron Beam Melting Manufacturing

and submitted in partial fulfillment of the requirements for the degree of

Master of Applied Science (Mechanical Engineering)

complies with the regulations of the University and meets the accepted standards with respect to originality and quality.

Signed by the final Examining Committee:

_____ Chair

Dr. Mehdi Hojjati

_____ Internal Examiner

Dr. Mehdi Hojjati

_____ External Examiner

Dr. Paria Karimi

_____ Supervisor

Dr. Catharine Marsden

Approved by:

_____ 2024

Dr. Martin Pugh, Chair of Department

_____

Dr. Mourad Debbabi, Dean of Faculty

Abstract

Influence of Process Parameters on Microstructural Characteristics and Mechanical Properties of Ti-6Al-4V Samples Manufactured through Electron Beam Melting Manufacturing

Camille Bernier-Tremblay

Metal Additive Manufacturing (MAM) is a manufacturing technique that builds solid components layer by layer. In comparison to traditional manufacturing methods, metal additive manufacturing offers advantages by allowing the creation of intricate geometries while reducing the buy-to-fly ratio of components. Understanding how manufacturing parameters affect the mechanical properties of produced components is applicable to the research and development of materials used in aero-engine and biomedical applications.

The study that is the subject of this thesis examines the microstructure of Ti64 samples printed using Electron Beam Melting (EBM) with specific variations in process parameters, such as adjustments in beam current and scan speed intended to achieve varying microstructural properties. The study compares the variations in process parameters with the types of defects and overall sample porosity. Additionally, this research explores the relationship between process parameters, defect production, and the tensile and fatigue properties of the printed samples.

The results of the microstructure examination indicate that individual process parameters significantly influence print porosity for the same Volumetric Energy Density (VED). However, VED alone does not dictate alpha lath thickness or variations in tensile properties. While porosity and defect size do not notably affect tensile properties, they impact the fatigue life of the samples with larger defects leading to a shorter fatigue life. Optical microscopy analysis of print samples provides a local estimation of defect parameters for an initial assessment and prediction of global porosity in larger printed components.

Acknowledgements

I would like to thank the National Research Council of Canada, Cascade Aerospace, Marinvent Corporation, and the Royal Military College of Canada, without whom this research would not have been possible.

Many thanks to my supervisor, Dr. Catharine Marsden, for her endless support, guidance, and encouragements throughout this project. I would like to express my sincere thanks to Dr. Paria Karimi and Dr. Esmaeil Sadeghi for imparting their extensive knowledge and expertise on EBM, providing an amazing learning experience throughout the course of this project.

Thank you to Dr. David Duquesnay for providing his support and expertise on fatigue testing, and to Captain Pantuso for introducing me to this project and providing me the samples printed for his research.

Thank you to the staff from the Concordia Materials Characterization Platform, and the Concordia Mechanical Engineering technicians for their support in materials testing. A big thank you to the staff from the Royal Military College machine shop and the Concordia University machine shop for their support in manufacturing and sample preparation.

Table of Contents

List of Figures

List of Tables

List of Acronyms

AM	Additive Manufacturing
ASTM	American Society for Testing and Materials
BCC	Body Centered Cubic
CNC	computer numerical control
CT	Computed Tomography
EBM	Electron Beam Melting
EBSD	Electron Backscatter Diffraction
EDS	Energy Dispersive X-Ray Spectroscopy
HCP	Hexagonal Close-Packed
HIP	Hot Isostatic Pressing
HRC	Rockwell Hardness, C Scale
HV	Vickers Hardness
IPF	Inverse Pole Figure
LOF	Lack of Fusion
L-PBF	Laser Powder Bed Fusion
MAM	Metal Additive Manufacturing
MIP	Mercury Intrusion porosimetry
PBF	Powder Bed Fusion
rpm	revolutions per minute
SEM	scanning Electron Microscope
S-N	Stress-Cycles to failure
STEM	Scanning Transmission Electron Microscope
UTS	Ultimate Tensile Strength
VED	Volumetric Energy Density
XCT	X-Ray Computed Tomography

Chapter 1 Introduction

Metal Additive Manufacturing (MAM) is a production method that builds solid parts layer by layer [1]. Compared to traditional manufacturing, metal additive manufacturing offers advantages like enabling the production of intricate geometries while reducing the buy-to-fly ratio of components [2]. The method is increasingly utilized in the aerospace and biomedical industries [3][4].

Electron beam melting (EBM) is a powder bed MAM technique specifically used in the aerospace industry. EBM involves selectively melting particles on a powder bed using an electron beam. The process takes place under a vacuum and allows components to be produced with little to no residual stresses [1]. A key player in EBM machine manufacturing is ARCAM from GE Additive. The control software used on ARCAM EBM machines has a graphical user interface which offers a variety of functions depending on the machine type. The software controls the electron beam, the beam path, motors, pumps and build parameters [5], all of which are encompassed in "build themes" tailored to the specific material being printed [2]. The build parameters include part geometry and orientation, powder chemistry, use of supports, and machine settings. The build theme comprises a comprehensive set of process parameters optimized by the machine manufacturer, such as ARCAM [2], and are typically not adjustable by the user.

ARCAM EBM has formed partnerships with academic institutions to grant researchers the ability to adjust process parameters and access full control of scan speed, beam current, hatch spacing, layer height, and focus offset; thus enabling the development of new materials and processes [6]. An example of such a partnership is the Holistic Innovation in Additive Manufacturing (HI-AM) Network in Canada, which has leveraged this opportunity to study an expanded range of feedstock metal materials and to investigate process parameters for increased process repeatability and reliability [7]. Researchers have concentrated on ensuring that the EBM process can be repeatable and reliable to effectively control the final quality and material properties of the finished part [7]. Understanding the connections between process parameters, microstructure development, and resulting mechanical properties is key to this reliability and reproducibility [2][8].

Continued research on process parameters is important, as the absence of information regarding the choice of build parameters hinders quantitative comparisons between different studies. Many studies have been conducted on the effect of process parameters on microstructure and tensile properties [9], [10], [11], [12], [13], but not all variable parameters are presented by all authors, which often prevents the community from gaining insight into the impact of these parameters on material properties [2]. Some authors present print parameters in terms of speed function index (SF), which varies the beam current and scan speed to achieve optimal printing parameters. The SF index is an algorithm which is used to dynamically control the translation of electron beam [14]. This algorithm controls and alters process parameters, allowing the production of parts of differing sizes and geometry, with a uniform melt pool size and surface temperature [15]. Although this algorithm provides optimal prints, the actual process parameters used to produce these prints is unknown.

Understanding the implications of process parameters for the mechanical properties of EBM-manufactured components is applicable to the research and development of lightweight and high-temperature alloys for engine-aero applications such as adapting Nickel alloy 718 to powder bed fusion [16]. The identification of mechanical properties and their variation based on process parameters is equally important in the biomedical field. The EBM process has been used to fabricate porous medical metallic implants with mechanical properties matching those of bone tissue. Bone tissue is characterized by a low Young's modulus, and the printed components must match with bone tissue to facilitate the integration of the implant and achieve better fixation [4]. The occurrence of defects and porosity resulting from non-optimal process parameters also poses a significant concern for the internal surfaces of parts, particularly in the case of fine channels and thin-walled structures [17]. Consequently, there is a need to identify an optimal process window that allows for the melting of a stable and continuous single track while mitigating these challenges [17]. The widespread adoption of Electron Beam Melting (EBM) depends on the ability of the industry to consistently achieve improved mechanical properties in the final product.

The study that is the subject of this thesis compares the microstructure of Ti64 EBM samples produced with specific variations in process parameters including adjustments in beam current and scan speed intended to achieve different energy density levels. The variation in process parameters is then compared to the types of defects and the overall printed sample porosity. The study explores process parameters and their relationship to the production of defects, as well as the tensile and fatigue properties of the prints in relation to the identified defects.

Chapter 2 Literature review

2.1 Post processing techniques for additively manufactured components

Post-processing is often used in metal 3D printed components to improve surface finish quality or mechanical properties. Examples of post-processing techniques include machining, polishing, heat treatment, and annealing [18]. In safety-critical applications, post-processing is necessary to eliminate some common defects associated with EBM such as gas pores or lack of fusion in the powder [19]. Hot isostatic pressing (HIP) is a technique that addresses these issues by applying heat and pressure to the material for a specified duration, effectively closing pores. HIP not only significantly reduces material defects but also facilitates alpha lath grain growth, increasing the ductility of the material [20], [21].

While components printed with ARCAM build themes exhibit minimal defects, post-processing heat treatments enhance ductility at the expense of strength [22], [23], [24], [25], [26]. Although heat treatments developed for castings have been used on EBM components, these post processing methods do not yield optimal properties in the case of EBM-printed components due to their different microstructural and defect characteristics [27]. ARCAM and Quintus technologies have conducted studies on the effects of microstructure and porosity on the final mechanical properties of components after hot isostatic pressing (HIP). By optimizing process parameters for the as-built state, the melt pool geometry can be manipulated. Adjusting the melt pool to reduce the as-built grain size while minimizing aluminum sublimation during the EBM process allows the post-HIP material to achieve greater final strength with the same ductility compared to using the original ARCAM themes [19].

The success of post-processing, therefore, hinges on understanding and optimizing the as-built state, and in the study that is the subject of this thesis, Ti6Al4V samples were built using a range of process parameters. The as-built state was examined to characterize microstructure, defect characteristics, and porosity. Tensile and fatigue samples were produced to examine the static and fatigue characteristics of the material in the as-built condition.

2.2 EBM process parameter studies

Researchers focusing on as-built samples have investigated a spectrum of process parameters including beam voltage, beam current, scan speed, line offset, layer height, focus offset, and energy density. In Electron Beam Melting (EBM), the beam voltage is usually set at 60 kilovolts, and beam power is adjusted by modifying the beam current. Scan speed is the velocity at which the electron beam traverses while melting material along the build surface and is measured in millimeters per second. The line offset represents the distance between two successive beam lines, with a standard value being 0.1 millimeters [28]. The layer height is the thickness of the powder layer distributed through the rake system of the machine [28]. The focus offset regulates the size of the spot generated by the electron beam incident on the powder bed, where a smaller spot results in a deeper melting pool between the layers of powder. The focus offset is specified in milliamps, as magnetic lenses control the focus of the electron beam [29]. Energy input can be measured in different ways during the printing process. Energy is directly correlated to the principal process parameters through equations (1) and (2). The volumetric energy density in equation (1) quantifies the average applied energy per unit volume of material in the process of scanning a single layer. When considering a single track, equation (2) calculates the energy per unit length of the track, known as linear energy input, and quantifies the ratio between beam power and scanning speed [17].

$$Volumetric\ energy\ density\ \left(\frac{J}{mm^3}\right) = \frac{voltage\ (kV)\ \cdot current(mA)}{scanning\ speed\ \left(\frac{mm}{s}\right) \cdot layer\ thickness\ (um) \cdot lineoffset\ (um)} \quad (1)$$

$$Linear\ energy\ input\ \left(\frac{J}{mm}\right) = \frac{voltage\ (kV)\ \cdot current(mA)}{scanning\ speed\ \left(\frac{mm}{s}\right)} \quad (2)$$

According to Karimi et al. [17], the two primary influences on the geometrical features of the melt pool are the scanning speed followed by the beam current, while the focus offset has a quantitatively lesser effect. Controlling the linear energy input affects the interaction among the beam, powder, and solid underlying layers in Electron Beam Melting (EBM). Modifying the track geometry has been identified as an approach to alter the thermal gradient and solidification conditions of the melt pool [17]. A comprehensive understanding of the effects of process parameters on densification and microstructure is an important initial step in manipulating these parameters to tailor specific mechanical properties and microstructures. The attainment of desired mechanical properties is contingent on the characteristics of individual single melted tracks and single layers [17], and the fine-tuning of microstructure through scan speed control provides an avenue to customize material properties [30], [31]. Ding et al.'s study [32] further supports this by revealing a nearly linear increase in the width and depth of the melt pool with line energy. Researchers have established that energy input stands out as the most significant process parameter in Powder Bed Fusion (PBF) processes, particularly with respect to microstructural characteristics [17], [33], [34], [35], [36].

Alternatively, some researchers propose a shift towards considering individual parameters rather than focusing solely on volumetric energy density and line energy in the optimization of EBM processes. Moritz et al. [37] highlight that varying these contributing parameters could result in distinct part properties. They emphasize the significance of beam current as the primary factor influencing swelling and aluminum evaporation, noting that high beam currents consistently lead to surface bulges and pronounced fluctuations. While line energy and volumetric energy density serve as valuable tools for streamlining process parameter optimization for new materials, they fall short in addressing the intricate interactions within the process zone inherent in powder bed-based additive manufacturing. Consequently, the authors suggest that it is advisable to adjust individual parameters, such as beam power or scanning velocity, particularly for materials prone to evaporation of aluminum or microstructural variations [37].

Some studies vary single parameters to comprehend their impact on the resultant microstructure of components in the as-built state [17], [38], while others study the influence of a combination of parameters by varying energy density [32], [39], [30]. The primary objective of these investigations is to establish a process window for EBM, where the density of lack of fusion (LOF) and keyhole defects define an effective process window. According to Mostafaei et al., a print achieved within an effective process window has a density of 99%, meaning that defects count for 1% or less of the total volume of the print [40].

Silvestri et al. [39] conducted a study using cubes to provide an overview of the impact of process parameters on microstructure, hardness, and surface roughness. The research investigates variations in beam current, scan speed, and line offset while maintaining a constant volumetric energy density throughout the process. The authors show that the interplay between the electron beam and the material is affected by both beam current and scan speed, and the amount of energy absorbed by the material fluctuates based on the selected process parameters, even when the energy density remains constant. In their study, samples produced under identical energy density but with different combinations of scan speed, beam current, and line offset exhibited distinct properties with respect to top surface roughness and microstructure.

Gong et al. [41] explored the impact of current, focus offset, line offset, and speed function on defects in their study of Ti-6Al-4V. The variables were systematically varied at three different levels to analyze the influence of each parameter on part quality. Their results show that input energy characteristics play an important role in defect generation within powder bed fusion processes. Parameters with excessively high or low energy input levels exhibit distinct defect generation mechanisms. Defects arise from melt pool discontinuities and a lack of overlap in melt pools, and the entrapment of powder particles also contributes to the formation of defects. For example, low energy density causes lack of fusion defects, while high energy density causes keyhole type defects.

Kirchner et al. [30] varied beam current and scan speed to assess the porosity and density of prints. Achieving full densification of Ti-6Al-4V requires a minimum energy input. EBM specimens with lower line energies exhibit over 1% porosity, leading to reduced tensile strength and significantly decreased ductility. Energy inputs beyond a specific threshold cause noticeable aluminum loss, and further increases result in pronounced swelling of the specimen's top surface. The authors conclude that high-quality specimens can be produced by utilizing line energies ranging between 100 and 200 J/m.

Sharowsky et al. [9] systematically varied energy density and scan speed to achieve Ti64 prints with a density exceeding 99.5%. The resulting porosity is notably influenced by both the energy density input during the printing process and the chosen scan speed.

Pobel et al. [31] investigated the influence of beam power and scan speed on the quality of the print in terms of porosity and the swelling of the top surface, indicating an important loss of aluminum during printing. The authors show that increasing the scan speed from 2.5 to 6.0 m/s improved the quality of the molten layers from significantly uneven to completely plane surfaces. When further increasing speeds from 7.0 to 10.0 m/s however, they observed porosity because of the decreasing energy input.

2.3 As-built EBM microstructure

The adjustment of process parameters in Electron Beam Melting (EBM) produces a range of mechanical property variations in as-built specimens. These changes in mechanical properties are attributed to alterations in the grain structure [9]. The as-built microstructure of Ti-6Al-4V printed through EBM exhibits both alpha and beta phases. Ti–6Al–4V is a typical α (hcp: hexagonal close-packed) + β (bcc: body-centered cubic) dual-phase alloy. The columnar grain boundaries are from the beta phase which nucleated above the beta transus temperature (Tβ of 995°C) when the electron beam initially melts the powder. The β grains undergo a phase transformation from the high-temperature body-centered cubic structure to the hexagonal α phase when the temperature falling below 995°C [9], [42]. The grain boundaries are considered to originate from the ‘‘prior beta grains’’, as the alpha phase precipitates on the β grain boundary to form basket-weave or colony structures, as depicted in Figure 2.1 and Figure 2.2 [43].

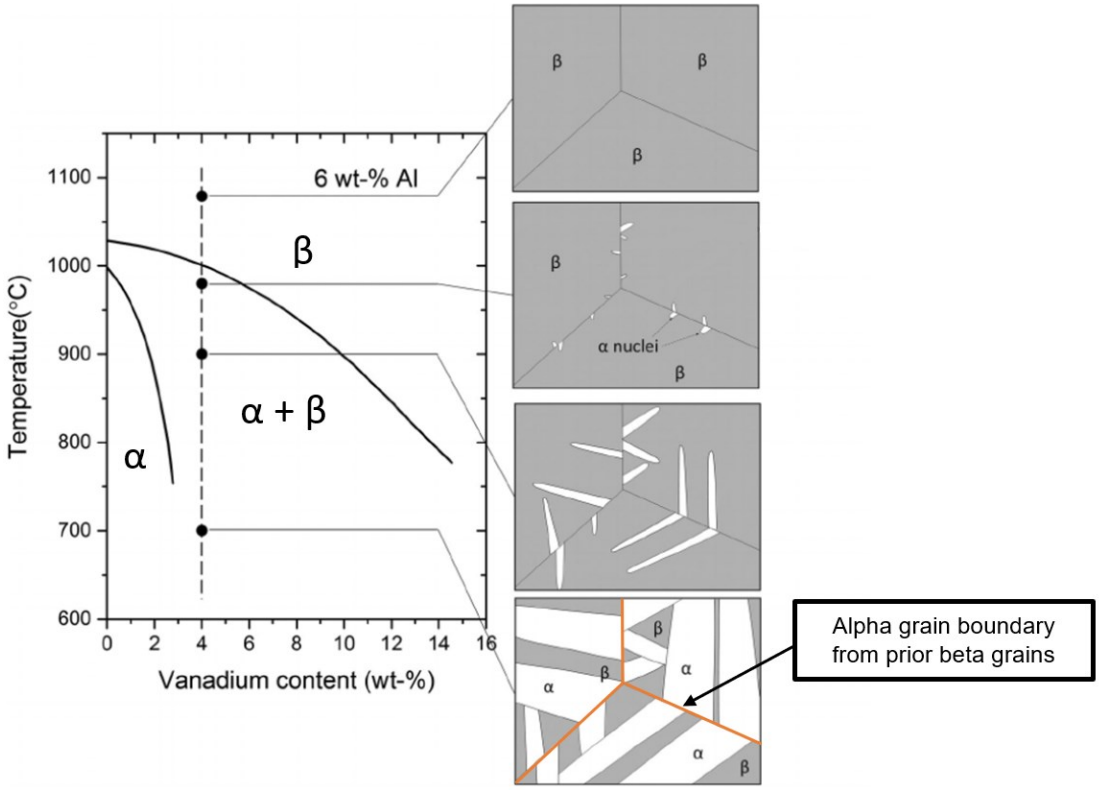

Figure 2.1 : Phase transformations during cooling of Ti–6Al–4V from above β-transus [44].

The alpha laths are illustrated in the enlarged circles of Figure 2.2 and Figure 2.3. Alpha laths are characterized by their thickness. The thickness of alpha laths varies along the build direction of the print, which can be attributed to the thermal history of each printed layer. Tan et al. [43] reported a region containing near-equiaxed prior β grains with a height of ~250μm at the bottom of the print in Figure 2.2. An equiaxed-to-columnar transition for the prior β grains occurs due to the thermal gradient in the melt pool. In practice, the bottom equiaxed-to-columnar transition region will be removed once a build is completed, as it is directly on the build plate [43]. The prior β grains grow in alignment with the build direction, as the build direction dictates the thermal gradient [43].

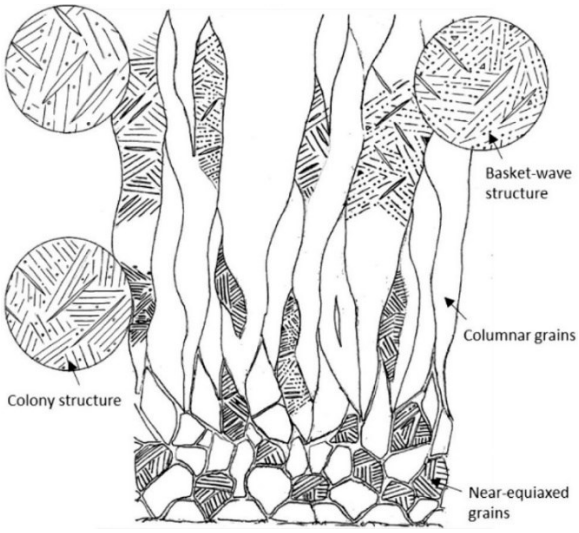

Figure 2.2 : Schematic microstructure of EBM-built Ti–6Al–4V on X–Z plane [43].

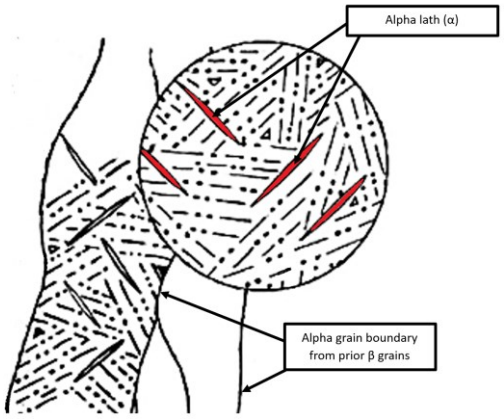

Figure 2.3 : Alpha lath and grain boundary in basket-weave structure [43].

Adjusting the energy input in the part has a direct impact on the thickness of the alpha laths within the prior beta grains. Additionally, the energy input plays a role in determining the percentage of the alpha and beta phases in the printed material [22]. This variation in the percentage of each phase and the thickness of the alpha laths significantly affects mechanical properties including yield strength, tensile strength, and hardness, as highlighted in studies by Sharowsky et al. [9], Kirchner et al. [30], Silvestri et al. [39], and Pobel et al. [31].

Prisco et al. [45] investigated the impact of EBM process parameters on the resulting microstructure of printed materials. Their findings reveal that a coarser microstructure is generated with high heat input and low line offset. Increasing the heat input or, conversely, decreasing the line offset resulted in higher lath thickness, leading to lower hardness values [45]. The study varied focus offset, line offset, and line energy density, printing 36 different combinations of process parameters with three different levels for each parameter. Line energies ranged between 0.71 J/mm and 3.77 J/mm; the columnar β size increased from around 60μm to approximately 100μm when the heat input rate rose from 0.71 J/mm to 3.77 J/mm at 0.07 mm of line offset. The α lath thickness also increased from 1.5μm to 2μm with the same variation in heat input. The finest microstructures, observed at 0.71 J/mm and 0.21 mm of line offset, resulted in the highest microhardness of 400 HV.

Sharowsky et al. [9] explored the impact of scanning strategy on both the microstructure and mechanical properties of Ti64. Their experiment involved varying the scan speed from 0.2 m/s to 10 m/s, resulting in different volumetric energy densities for each sample. The researchers observed a nearly linear increase in α platelet thickness with volumetric energy. Higher scan speeds led to lower volumetric energy, resulting in a finer microstructure. The specimen produced at a scan speed of 4.0 m/s and a volumetric energy density of 30 J/mm^3 displayed a microstructure featuring the minimum α platelet thickness of 0.37μm. This microstructural change manifested as an augmented thickness of the α platelets with increasing scan speed and volumetric energy. The rise in these parameters suggests elevated heat input and reduced heat loss, indicating a larger melt pool size and a lower cooling rate, which, in turn, determines the size of the α platelets.

Hrabe and Quinn [8] conducted a study exploring the impact of processing variables on the microstructure and mechanical properties of Ti-6Al-4V. They varied the speed factor (SF) and considered the orientation and placement of parts on the build plate to examine the influence of these factors on the resulting microstructure. As the speed factor increased and energy input/melt pool size decreased, there was a reduction in lath thickness. Additionally, the prior-β grain size showed a decreasing trend with increasing speed factor. Notably, the y-oriented part exhibited a smaller α lath thickness. The authors focused on the energy input over a range of speed factors (30–40) while ensuring complete melting of parts. They observed that higher energy input and larger melt pool sizes were associated with an increase in α lath thickness and prior-β grain size.

Puebla et al. [10] also investigated the impact of melt scan rate on both microstructure and macrostructure. The study incorporated scan rates of 100, 400, 500, 600, 700, and 1000mm/s. Throughout the fabrication of cylindrical specimens, the beam focus and scan spacing were consistently maintained. Elevating the melt scan rate from 100 to 1000mm/s during the Electron Beam Melting (EBM) process for oriented Ti-6Al-4V cylinders led to an escalation in the cooling rate, resulting in a reduction in α-phase grain thickness. Specifically, scan speeds of 100mm/s for horizontally printed specimens on the build plate yielded an α lath thickness of 8μm, while scan speeds of 1000mm/s for specimens printed in the same orientation resulted in an α lath thickness of 3μm.

Ran et al. [12] conducted a study on the microstructure of Ti-6Al-4V samples produced using EBM. They fabricated fifteen cubic specimens while varying focus offset, speed factor, and line offset at five different levels for each parameter. The chosen focus offsets ranged between 39mA and 51mA, the speed factors between 29 and 41, and the line offsets between 0.16mm and 0.28mm. The morphology of Ti-6Al-4V samples with line offsets of 0.16 mm and 0.28 mm was examined. Image-J image was used to measure the average α lath thickness of the samples. The results revealed that the average α lath thickness for samples with a line offset of 0.16 mm was 1.24μm, whereas a thickness of 0.53μm was measured for those with a line offset of 0.28 mm. Notably, samples with a higher energy input exhibited a coarser microstructure.

Al-Bermani et al. [13] investigated the origin of microstructural diversity, texture, and mechanical properties in Ti-6Al-4V produced using EBM. They carried out four separate identical builds at chamber temperatures of 625°C, 650°C, 675°C, and 700°C, each consisting of ten cylinders measuring 80mm in length and 10mm in outer diameter. To determine cooling rates and melt pool geometry, individual melt tracks were printed on a heated (650°C) base plate. In the cylindrical prints, the columnar nature of prior β grains resulted directly from the thermal gradient in the z-direction. The base plate and deposited material acted as a heat sink during deposition, while the electron beam served as the heat source from above. In the as-built condition, processing at a higher temperature of 700°C led to an increase in α lath width and a colony scale factor. Variances in build temperature between 626°C and 700°C significantly affected both microstructure and mechanical properties. Temperatures above 678°C resulted in decreased mechanical properties due to microstructural coarsening in the as-built condition. The authors also observed that for individually printed tracks, a beam current of 6mA produced a slightly deeper melt pool. Beam currents of 8, 10, and 12mA resulted in melt tracks of nearly identical depth but with an increase in length. Solidification along the z-axis was most relevant in this study, as deeper melt pools have slower cooling rates and promote microstructural growth.

Gong et al. [38] conducted a study on the effects of beam speed on Ti–6Al–4V microstructures in EBM manufacturing. Four different samples with varying speed factors (SFs) of 20, 36, 50, and 65 were examined to investigate the impact of beam speed on microstructure of the EBM parts. The SF 20 sample, characterized by the lowest beam speed, exhibited the largest prior β grain size of 85.2μm. In contrast, specimens from SF 36, SF 50, and SF 65 demonstrated similar β grain sizes, all measuring less than 50μm. The alpha (α) lath thickness ranged from 1.0μm (standard deviation 0.3) to 1.5μm (standard deviation 0.3) for SF 65 and SF 20, respectively. The experimental findings from this study indicated that the α-lath size did not decrease further with an increased cooling rate for beam speeds from SF36 to SF65. The authors suggest that the size of α-laths could also be influenced by the size of prior β grains. Notably, the size of prior β grains remained similar between SF36 and SF65, suggesting that their size could be a factor influencing α-lath size, which was found to be 1.1 (0.3 standard deviation) and 1.0 (0.3 standard deviation) for SF36 and SF65 respectively.

2.4 As-built EBM mechanical properties

While the previous authors investigated microstructure analysis in their studies, not all studies offer detailed information on mechanical properties and process parameters. This section discusses the influence of process parameters on tensile properties.

Sharowsky et al. [9] investigated the influence of scanning strategy on both the microstructure and mechanical properties of Ti64. The maximum yield strength and ultimate tensile strength were found to be 1048 and 1102 MPa, respectively, at a low volume energy of 30 J/mm^3. With an increase in volume energy up to 60 J/mm^3, there was an observed decrease of approximately 8% in yield strength and 7% in ultimate tensile strength. For samples with a low scan speed of 0.2 m/s, the yield and tensile strengths were 1045 and 1011.1 MPa, respectively, with a fracture elongation of 15%. Under a constant scan speed of 4.0 m/s, the fracture elongation increased by up to 16% for a volume energy of 50 J/mm^3. However, further increases in volume energy led to a reduction in fracture elongation. The sample printed with a scan speed at 4.0 m/s and VED of 30 J/mm^3 exhibited a microstructure with the smallest a platelet thickness of 0.37 µm, resulting in the best mechanical properties with a tensile strength of 1100 MPa. Conversely, an increase in a platelet thickness to 1.31µm at a scan speed of 4.0 m/s and a VED of 60 J/mm^3 resulted in a 5% reduction in tensile strength compared to the highest achieved strength.

Hrabe and Quinn [8] also examined the impacts of processing on the microstructure and mechanical properties of Ti-6Al-4V. The authors varied the speed factor (SF) and explored the effects of the orientation and location of parts on the build plate, aiming to understand the influence of these parameters on resulting mechanical properties. Ten specimens with a speed factor of 30 and another ten with a speed factor of 40 were tested. As the speed factor increased and energy input/melt pool size decreased, the ultimate tensile strength (UTS) exhibited a 2% increase, rising from 1007 ± 8.4 MPa to 1029 ± 7.0 MPa. The yield strength (YS) also increased by 3%, climbing from 952.2 ± 9.9 MPa to 982.9 ± 5.7 MPa. Microhardness rose from 364.8 ± 8.7 HV to 372.0 ± 7.2 HV. However, there was no statistically significant difference observed in the percentage of elongation (% EL). Vertically oriented parts demonstrated a substantially lower % EL (30% change) compared to horizontally oriented parts; a finding attributed to variations in the orientation of the tensile axis with the direction of elongated prior-β grains. No difference in UTS or YS was noted. Orientation within the x–y plane and location each had less than a 3% effect on ultimate strength and yield strength. Exterior parts printed on the build plate exhibited a 1% change in UTS, a 2% change in YS, and lower microhardness compared to interior parts.

Puebla et al. [10] investigated the impact of melt scan rate on the microstructure and mechanical properties of Ti64. The study considered scan rates ranging from 100 to 1000 mm/s, with the beam focus and scan spacing consistently maintained during the fabrication of cylindrical specimens. The highest ultimate tensile strength (UTS) and yield strength were observed at a scan speed of 500 mm/s, measuring 1080 MPa and 990 MPa, respectively. The corresponding hardness for this print was recorded at 38 HRC. The lowest UTS and yield strength were noted at a scan speed of 1000 mm/s, registering values of 640 MPa and 560 MPa, respectively, with a hardness of 23 HRC. The authors also provide information on the porosity of the prints; a scan speed of 100 mm/s resulted in a porosity of 4.7%, while a scan speed of 1000 mm/s yielded a higher porosity of 12.5%. The study revealed that increasing the melt scan rate led to an increase in porosity due to the creation of un-melted powder volumes within the layers. This rise in porosity correlated with a decrease in hardness (HRC).

Ran et al. [12] conducted a investigation into the impact of speed factor, focus offset, and line offset on the microstructure and mechanical properties of EBM Ti-6Al-4V. The study involved varying focus offset values between 39 and 51 mA; speed factor values between 29 to 41; and line offset values from 0.16 to 0.28 mm. Fifteen different combinations of these parameters were printed at five factor levels, with each combination having three identical cylindrical tensile samples. Throughout the experiment, when one factor was altered, the other two were held constant. The authors observed that changes in line offset, speed factor, and focus offset had a minimal effect on tensile strength, with the alteration being less than 30 MPa. Among these factors, line offset exerted the most significant influence on yield strength. As the line offset increased from 0.16 to 0.28 mm, the yield strength of the sample increased from 666.4 MPa to 871.2 MPa. The tensile strength of EBM Ti-6Al-4V samples ranged from 966 to 1000 MPa, reaching a maximum at a focus offset of 48 mA, a speed factor of 35, and a line offset of 0.28 mm. The authors noted that the maximum Vickers hardness, recorded at 335 HV, was achieved at a focus offset of 51 mA, a speed factor of 41, and a line offset of 0.28 mm. Within the studied range of process parameters, the authors concluded that the change in line offset had the most substantial impact on the yield strength of EBM Ti64 samples.

Al-Bermani et al. [13] studied the microstructural diversity, texture, and mechanical properties in electron beam melted Ti-6Al-4V samples. The authors printed four separate but identical builds at chamber temperatures of 625 °C, 650 °C, 675 °C, and 700 °C, where each build contained ten cylinders of 80mm length and 10 mm outer diameter. The part printed at the highest temperature of 700°C showed a yield strength of 883.7MPa (10.6 MPa standard deviation), a UTS of 993.9MPa (5.6 MPa standard deviation), and an elongation of 13.6% (0.9% standard deviation). The part printed at the lowest temperature of 626°C showed a yield strength of 938.5MPa (10.9 MPa standard deviation), a UTS of 1029.1MPa (14.9 MPa standard deviation), and an elongation of 13.2% (0.4% standard deviation). The authors concluded that increasing the temperature above 951 K (678 °C) resulted in a decrease in mechanical properties associated with microstructural coarsening in the as-built condition.

Pasang et al. [46] studied the mechanical properties exhibited by specimens based on their orientation on the build plate. Specimens were produced in vertical, horizontal, and 45-degree orientations on the build plate, with three specimens printed for each configuration. The samples were built with a layer thickness of 50μm, a speed function of 64, a line offset of 0.2 mm, and a current of 30 mA, resulting in an energy density of approximately 94 J/mm³. The horizontally printed samples displayed an average hardness of 360 HV. The vertically printed samples exhibited an average hardness of 319 HV, while those printed at a 45-degree angle had an average hardness of 340 HV. The horizontally printed samples had a yield strength of 770 MPa, an ultimate tensile strength of 811 MPa, and an elongation of 13% at fracture. Vertically printed samples showed a yield strength of 760 MPa, an ultimate tensile strength of 800 MPa, and an elongation of 15% at fracture. Samples printed at a 45-degree angle exhibited a yield strength of 811 MPa, an ultimate tensile strength of 847 MPa, and an elongation of 12% at fracture. The authors observed that for EBM materials, the 45-degree orientation demonstrated higher strengths compared to the 0-degree and 90-degree orientations. The variation in tensile properties was attributed to the reported porosity of the samples, ranging between 3-4%. The authors noted minimal necking during the tensile testing of EBM samples and concluded that the differences in mechanical properties among the printed samples were primarily due to defects introduced during the printing process, and not the orientation of the prints.

2.5 Defect characterization

As indicated by Karimi et al. [3], the presence of defects resulting from non-optimal process parameters is a significant concern, especially in the context of fine channels and thin-walled structures. The primary defects observed in EBM include lack of fusion defects (LOF), gas pores, and keyhole defects [39]. Lack of fusion defects arises when the energy input from the electron beam is insufficient to melt the powder on the bed [40], [41]. The occurrence of LOF is assessed based on the extent of overlap between melt pools to ensure that all points are melted at least once [40]. Two types of LOF defects can manifest; interlayer LOF and intertrack LOF are illustrated in Figure 2.4 [47]. LOF defects can also be a combination of interlayer and intertrack LOF defects overlapping between layers. Alternatively, keyhole defects occur when the energy input into the material is excessively high; as the temperature rises and reaches the boiling point, the generation of metallic vapor creates a recoil pressure. This recoil pressure forces the molten metal downward, leading to the creation of a prolonged, slim gas cavity referred to as the keyhole [40]. Spherical gas pores stem from the trapped gas within the gas-atomized powder particles [40], [48]. A typical keyhole defect is shown in Figure 2.5 and gas pores defects are depicted in Figure 2.6.

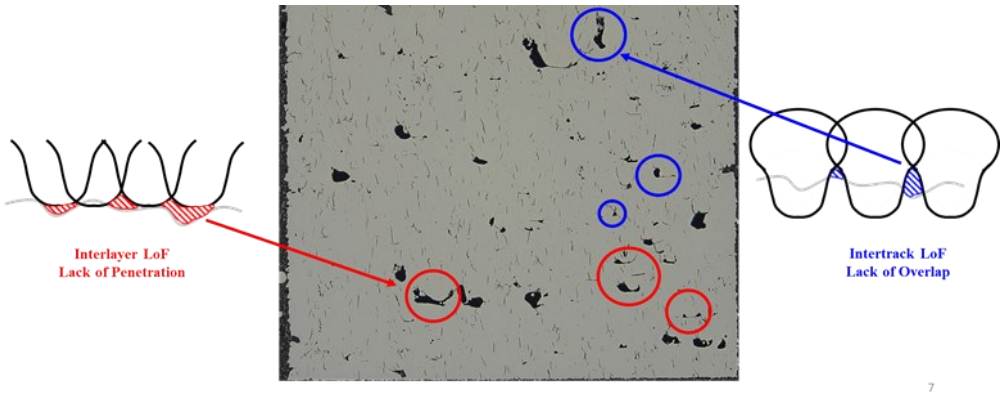

Figure 2.4 : Intertrack and interlayer lack of fusion defects [47]

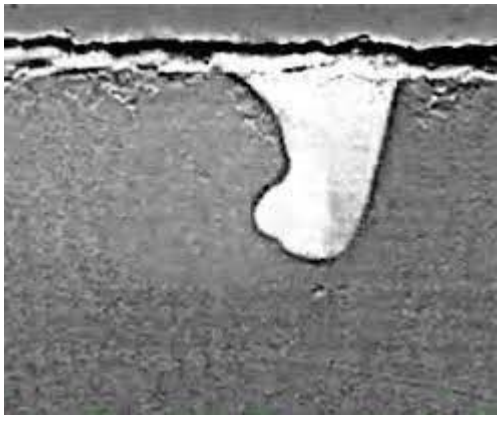

Figure 2.5 : Keyhole defect [49]

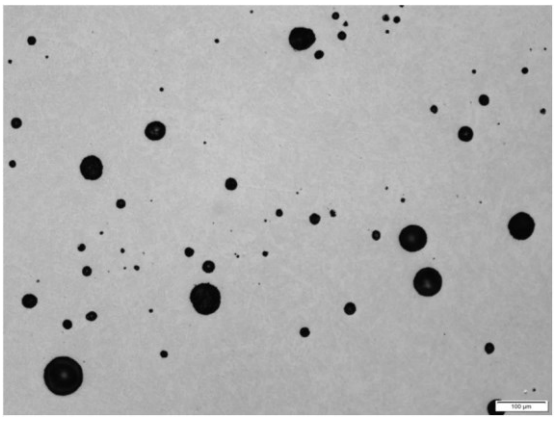

Figure 2.6 : Gas porosity in Ti64 [50]

Defects resulting from the EBM process can be identified using various methods. Typically, defect measurement employs bulk methods such as Archimedean density, ultrasonic inspection, or 2D cross-sectioning to compare pore area to the captured area [12]. The Archimedes method enables the calculation of the density of an object immersed in a fluid, accounting for the buoyancy of the object. Examples of fluids used in this method include deionized water, or acetone [51]. Other density and pore size measurement methods encompass helium pycnometry, water intrusion, and mercury intrusion (MIP) techniques [19]. Figure 2.7 shows the MIP process and setup, where a given pressure is applied on a porous sample immersed in mercury. The size of the pores can be determined from the pressure and the displaced volume of mercury in the penetrometer stem [52]. The Archimedes method, while useful for determining bulk porosity, has limitations in providing detailed information about the size, distribution, and morphology of pores, as noted by Wilson-Heid et al. [53]. The method offers insight into the overall void volume but does not distinguish between intentional internal pore spaces and trapped powder left after fabrication. The inclusion of trapped powder introduces uncertainty in the measurement and prevents an accurate assessment of the true volume of intentional internal pore space. As a result, the Archimedes method may not be suitable for a comprehensive understanding of the specific characteristics and impact of different types of pores on material properties [53].

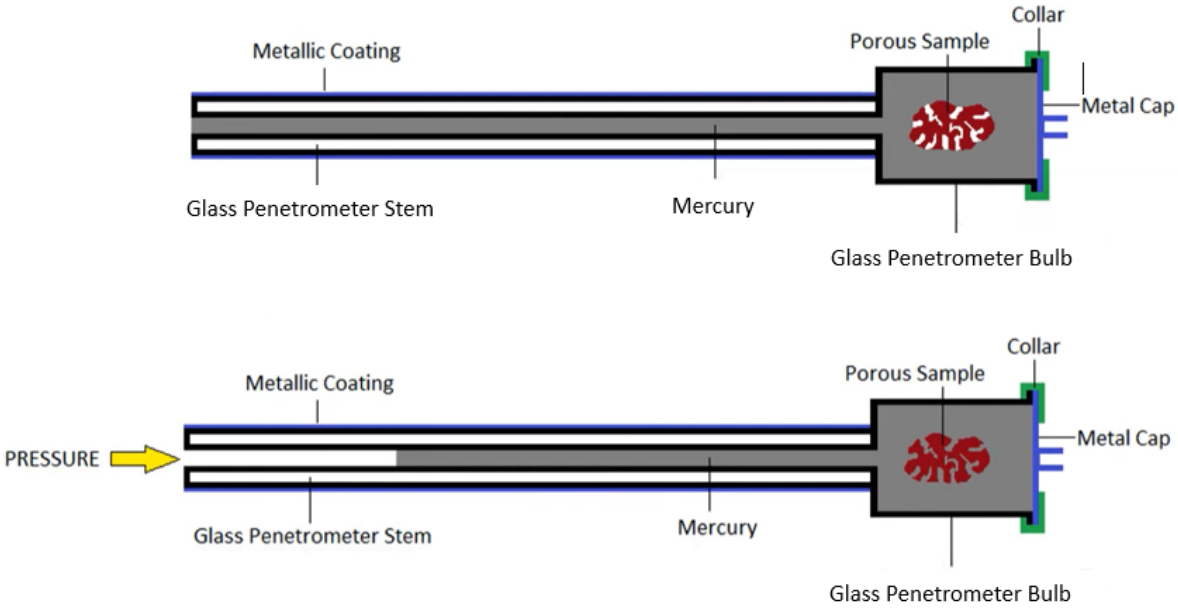

Figure 2.7 : Pores in porous sample filling with mercury under an applied pressure in the glass penetrometer [52].

Optical microscopy is a widely accessible characterization technique employed to observe powder feedstock, microstructure, surface profiles, and defects in AM samples. Low-resolution optical microscopy is commonly utilized to assess the particle size distributions of the powder feedstock before the printing process. When characterizing AM parts, the surfaces of the samples are typically polished using a series of fine grit sandpapers and other grinding solutions such as diamond slurry. A sample can be vertically cut into sections to prepare cross sections of layers lying parallel or vertical to the scan plane of the AM process. Depending on the illumination of the samples, an appropriate preparation of grayscale micrographs is essential. Remaining scratches from the polishing treatment can be eliminated by adjusting the contrast, and selecting the correct threshold values enables a clear identification of the defects. Figure 2.8 illustrates pores visualized using optical microscopy. Figure 2.8a shows pores at the lowest magnification level, while Figure 2.8e shows the same area at a higher magnification [51]. Pores, micro-voids, and cracks can be detected using optical imaging [40], [54].

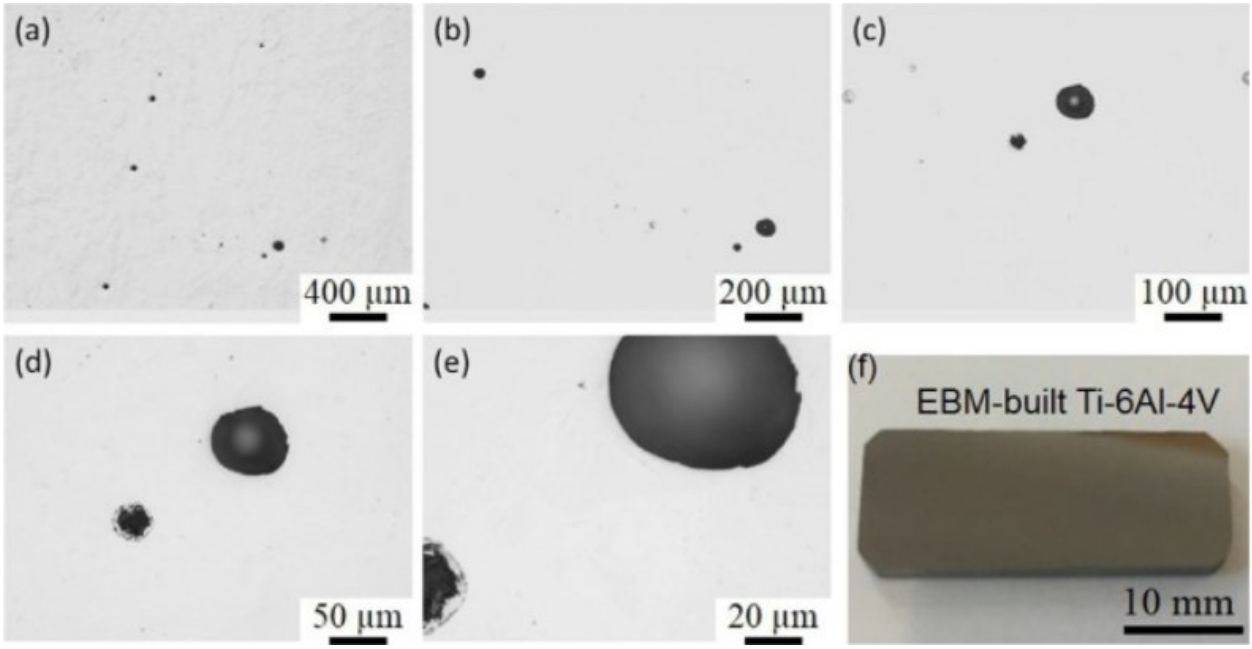

Figure 2.8 : Porosity visible through optical microscopy in Ti64 EBM at different magnifications [55].

While the methods described can be rapid and cost-effective, they only provide a preliminary approximation of the defect structures observed in metal AM and cannot generate information such as the three-dimensional (3D) spatial distribution and morphology of defects [40]. More time-intensive techniques such as X-ray computed tomography (XCT) have proven to be valuable in analyzing defect structures in metal AM [40]. Air (pores) and bulk material have specific gray values in the XCT grayscale, representing their respective intensity values. Air, with little attenuation, is displayed as low density (dark), whereas the fully melted print, exhibiting high attenuation, is displayed as high density (bright) [51], [56]. The difference in attenuation allows defects to be identified in a spatial distribution for a given print. An example of XCT scanning used for pore detection is shown in Figure 2.9.

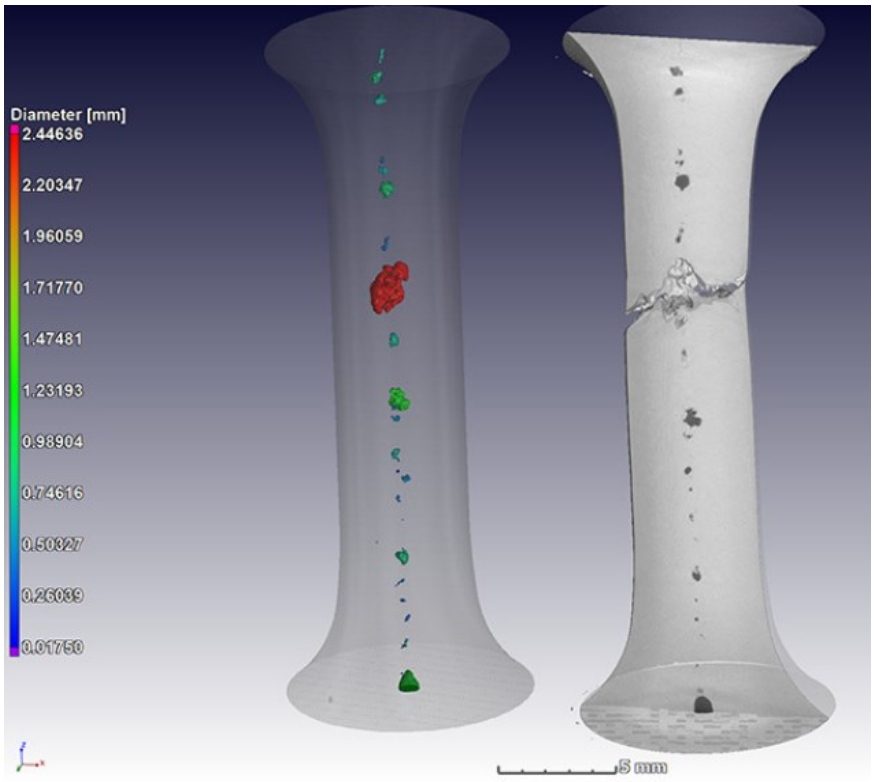

Figure 2.9 : Pores in L-PBF EBM Ti64 detected through x-ray tomography [57].

Murakami [58] explored the potential configurations of defects using the effective defect size $\sqrt{area_{eff}}$, which differs from the actual defect size. Utilizing the effective area method considers the proximity of the defect to the surface. Initial fatigue crack growth for irregularly shaped cracks and defects initiates from the deepest concave corner point due to the high stress intensity factor at that location. Consequently, lack of fusion defects and keyhole defects in as-built parts can have a significant impact on the fatigue properties of the part. The effective area of various defect configurations is illustrated in Figure 2.10 [58].

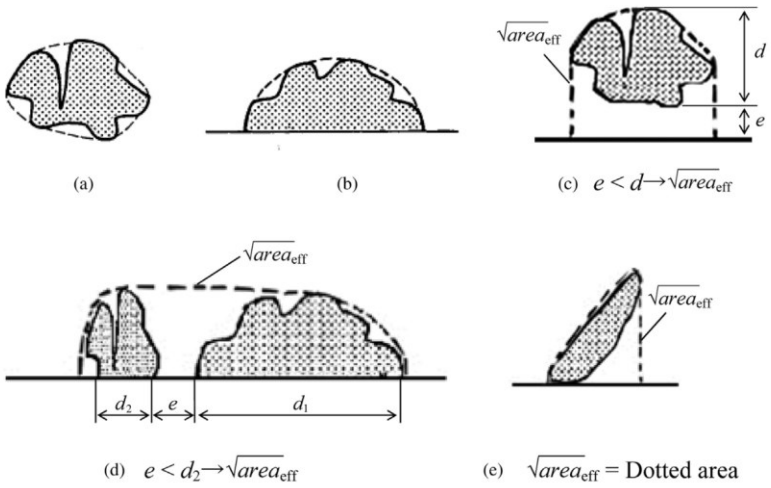

Figure 2.10 : Estimation method for the effective size (dotted line) of irregularly shaped defects and defects near surface. (a) Irregularly shaped internal defect. (b) Irregularly shaped surface defect. (c) Irregularly shaped internal defect in interaction with surface. (d) Interacting adjacent two defects. (e) Inclined defect in contact with surface [58].

Another method used to estimate the sizes of defects is the Feret diameter method, illustrated in Figure 2.11 below. The Feret diameter method considers the largest distance between two parallel tangential lines in any in-plane direction of a defect [59].

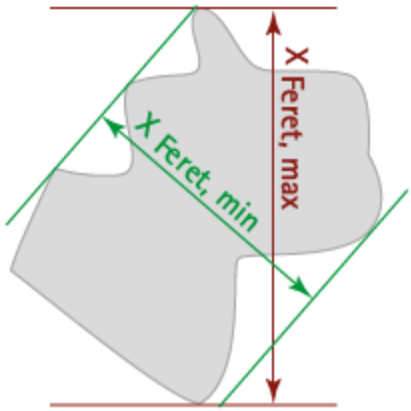

Figure 2.11 : Feret diameter parameter [59]

2.6 Influence of defects on mechanical properties

As additive manufacturing and Powder Bed Fusion (PBF) technologies continue to advance, it becomes evident that the formation of pores and their distributions is complex [57]. Inappropriate process parameters, as emphasized by Ran et al [12], can result in incomplete melting or non-melting of powder, leading to the formation of defects such as gas pores, lack of fusion, and keyhole defects. These defects, in turn, contribute to a reduction in the mechanical properties of specimens. The effects of these pores on mechanical properties are diverse and not yet fully understood. For instance, irregular lack of fusion pores may be expected to act as stress concentrators more than small, near-spherical metallurgical or gas pores. However, explicit testing of this hypothesis has been limited until recently due to the emergence of x-ray tomography in studies focusing on the "effect of defects"[57]. It is important to understand the geometry, location, and distribution of defects to comprehend their influence on mechanical properties.

2.6.1 Tensile properties

Du Plessis et al. [57] studied the effect of defects on mechanical properties in metal additive manufacturing. The authors manufactured a series of Ti-6Al-4V investment cast rods, machined to tensile dog bone geometry, with pores all located in the middle of the tensile axis. The authors artificially induced porosity in the range of 0.7–1.2% by varying process parameters. They found that the ductility is strongly influenced by the porosity level but not the ultimate tensile strength. In a series of tests using X-ray tomography and mechanical testing, it was found by static tensile tests that the failure almost always occurs at the largest pore (despite different microstructures in different batches of samples) and that pore size was inversely correlated with yield strength and ductility. However, even for pores up to 4 mm in diameter in a 6 mm gauge diameter, the yield strength was still close to that of the wrought standard.

In a study conducted by Gong et al [60] on the impact of defects on the mechanical properties of Ti–6Al–4V components, the authors observed that porosity levels of up to 1% had minimal effects on tensile strength or elongation to failure when defects were caused by excessive energy input, specifically in the form of keyhole mode pores, which are rounded. However, when samples were manufactured under non-optimal process parameters with insufficient energy input resulting in lack of fusion defects that were typically larger and irregularly shaped, even 1% porosity had a detrimental effect on mechanical properties [57]. As porosity increased, both strength and ductility were reduced, with failures more likely to initiate at the largest pores. Lack of fusion pores, characterized by their irregular shape, were shown to have a more pronounced impact on mechanical properties compared to other forms of porosity [57].

In an experimental investigation into Laser Powder Bed Fusion (L-PBF) of 316L stainless steel, Wilson-Heid et al. [53] deliberately introduced a single artificial flat, circular pore with varying diameters in 11 different circular EBM samples, emulating lack of fusion. The artificial pores are illustrated in Figure 2.12. The tensile testing performed followed the ASTM E8 testing method, with a strain rate of 0.015 in/in/min. The primary objective of the study was to isolate the role of internal pores on the tensile properties of austenitic stainless-steel samples produced using L-PBF and gain a direct understanding of the impact of initial void size on the material's tensile properties. Utilizing the Archimedes density technique, the researchers determined that the average bulk porosity of the dense samples was $0.60 \pm 0.2\%$. The bulk porosity remained relatively constant up to the maximum designed 4800μm pore samples, which exhibited an average bulk porosity of $0.88 \pm 0.2\%$. Notably, the 4200μm pore samples had the highest measured bulk porosity at $0.95 \pm 0.1\%$. During uniaxial tension testing of both dense samples and those with internal pores, distinct trends in mechanical properties emerged related to pore diameter within the 6 mm diameter sample. The presence of the pre-existing pore did not significantly affect the material's strength or ductility until the pore diameter reached or exceeded 600μm. The artificial defects present in this study were measured using ImageJ. At a pore diameter of 600μm, constituting 10% of the cross-sectional diameter, the inclusion of the pore resulted in a substantial spread in data compared to samples with smaller pores or no pores. At 1200μm (20% of the cross-sectional diameter), seven out of nine samples failed at the pore. For a pore diameter of 1800μm (30% of the cross-sectional diameter), there was a repeatable reduction in the elongation to failure of the samples. Elongation to failure decreased significantly for pore diameters exceeding 1800μm, with the largest pore (4800μm in diameter) resulting in tensile elongations to failure of under 1.5%. Material strength deterioration occurred for pores greater than or equal to 2400μm in diameter within the 6mm diameter gauge region. The Ultimate Tensile Strength (UTS) dropped from 619 ± 3 MPa in the dense samples to 580 ± 5 MPa for samples with an internal pore measuring 2400μm in diameter. The strength of the material continued to decrease with increasing pore diameter, reaching a UTS of 297 ± 5 MPa in the sample with the maximum pore diameter of 4800μm.

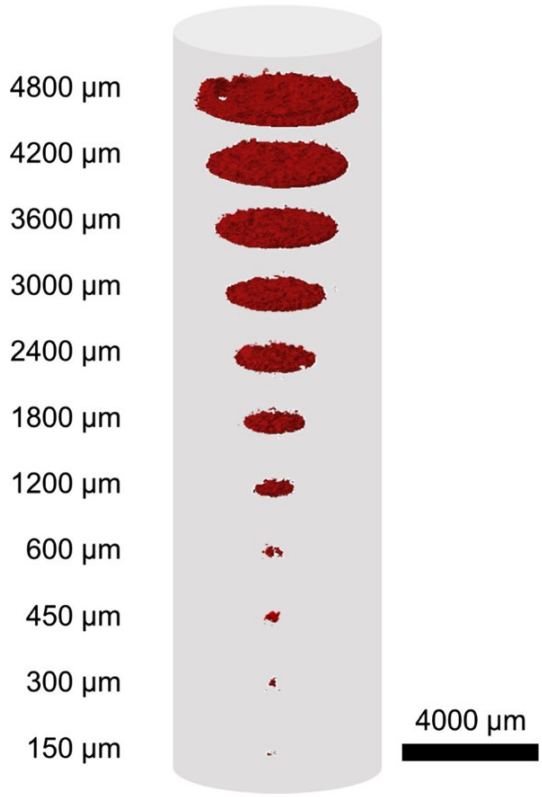

Figure 2.12 : Eleven artificial pores characterised with XCT in different sample with 6mm gauge diameter [53].

In a study by Ran et al [12] involving fifteen Ti-6Al-4V samples, samples 1 through 5, had line offset and speed factors which were kept constant while varying focus offset at levels of 39mA, 42mA, 45mA, 48mA, and 51mA. The purpose of the study was to determine the effect of process parameters on defect production and their influence on microstructure and tensile properties. The author reported no microstructural variation with the change in focus offset. The relative densities of these samples were reported as 98.49%, 98.55%, 98.63%, 98.19%, and 97.24%, respectively. The sample with the most defects (97.24% density) exhibited an ultimate tensile strength (UTS) and yield strength of 994.7MPa and 825.8MPa, respectively, with a Vickers hardness of 306.5HV. Conversely, the sample with the highest relative density showed a UTS and yield strength of 982.6MPa and 782.6MPa, respectively, with a Vickers hardness of 326.2HV. These findings suggest that the percentage of defects in a part may not be directly correlated with UTS and yield strength. In Ran et al.'s study, Vickers hardness increased with an increase in density.

In a study by Radolf et al. [61] on the impact of defects on the mechanical properties of Ti-6Al-4V prints, it was observed that an increasing defect area resulted in decreased elongation at fracture. However, the study revealed that the defect area itself is not solely responsible for the elongation at fracture. For instance, tensile samples built in the vertical direction exhibited approximately 8% elongation with a defect area of approximately 0.20-0.25mm², which corresponds to 0.4-0.5% of the fracture surface. In contrast, horizontal build prints with the same defect area exhibited 3% elongation. This discrepancy indicates that the size of the defect alone cannot fully account for the induced elongation. Other factors such as the shape, location, orientation of defects with respect to the load direction, and possibly their interaction with the printing orientation should also be considered in understanding the influence of defects on mechanical properties.

2.6.2 Fatigue properties

Murakami [58] explored techniques for estimating the fatigue life based on the effective root area parameter presented in Section 2.5. The correlation between fatigue limit and Vickers hardness is presented in equation (3). Individual specimens were found to have different fatigue limits due to the presence of unique defects. Thirteen PBF specimens in the as-built condition were polished and tested at a stress ratio of R= -1. The specimens which had a runout for N= $1x10^7$ were tested again at a higher stress and the size of defects at fracture origins was identified. This second testing was used to estimate the fatigue limit for individual specimens according to their actual defects, and then compare this estimate to the actual fatigue limit where the runout occurred. Accordingly, the author derived equation (4) to estimate the actual fatigue limit for the samples as a function of the effective root area parameter.

$$\sigma_{w,ideal} = 1.6H_v \pm 0.1H_v \tag{3}$$

$$\sigma_w = \frac{C_1(H_v + 120)}{\sqrt[\frac{1}{6}]{area_{eff}}} \tag{4}$$

In equation (4), σ_w is the fatigue limit of the sample in MPa, Hv is the Vickers Hardness, C_1 is the location parameter, and $\sqrt{area_{eff}}$ is Murakami's effective area parameter, in μm, introduced in Section 2.5.

The fatigue limit is influenced by the location parameter C_1 in equation (4). This parameter was derived experimentally by Murakami and estimated to be 1.43 for surface defects, 1.41 for defects touching the surface and 1.56 for internal defects [62]. However, the author suggests an in-depth exploration of the configuration of defects and the potential heterogeneous microstructure surrounding defects caused by a lack of fusion. Given that the fatigue limit of AM specimens is impacted by the size of defects within each specimen, establishing a conclusive fatigue limit for a material based solely on S-N data is challenging without also considering defects. Furthermore, the author notes that lack of fusion defects proved to be more detrimental to fatigue life compared to other potential sources of failure.

Radolf et al. [61] examined the monotonic and fatigue behavior of Ti-6Al-4V EBM solid samples using experimental, analytical, and numerical investigations. The authors printed 10 vertically and 10 horizontally oriented circular fatigue coupons for cyclic testing. Strain-controlled testing at R= -1 was performed on an Instron hydraulic machine. After fracturing the samples and obtaining a strain amplitude-reversals to failure curve, a fractography analysis was performed under an optical microscope. The fractography analysis revealed that the failure was initiated either by lack of fusion defects or by porosity defects, occurring in both vertical and horizontal prints. Further, the fractography analyses revealed that LOF defects are the primary crack initiation factor in all investigated EBM Ti-6Al-4V samples. Figure 2.13a) and b) show an example of the fracture surface of a sample with a surface LOF defect. Figure 2.13c) and d) show an example of the fracture surface of a sample with an internal LOF defect, and Figure 2.13e) through f) show examples of a fracture surface containing both LOF and gas porosity defects.

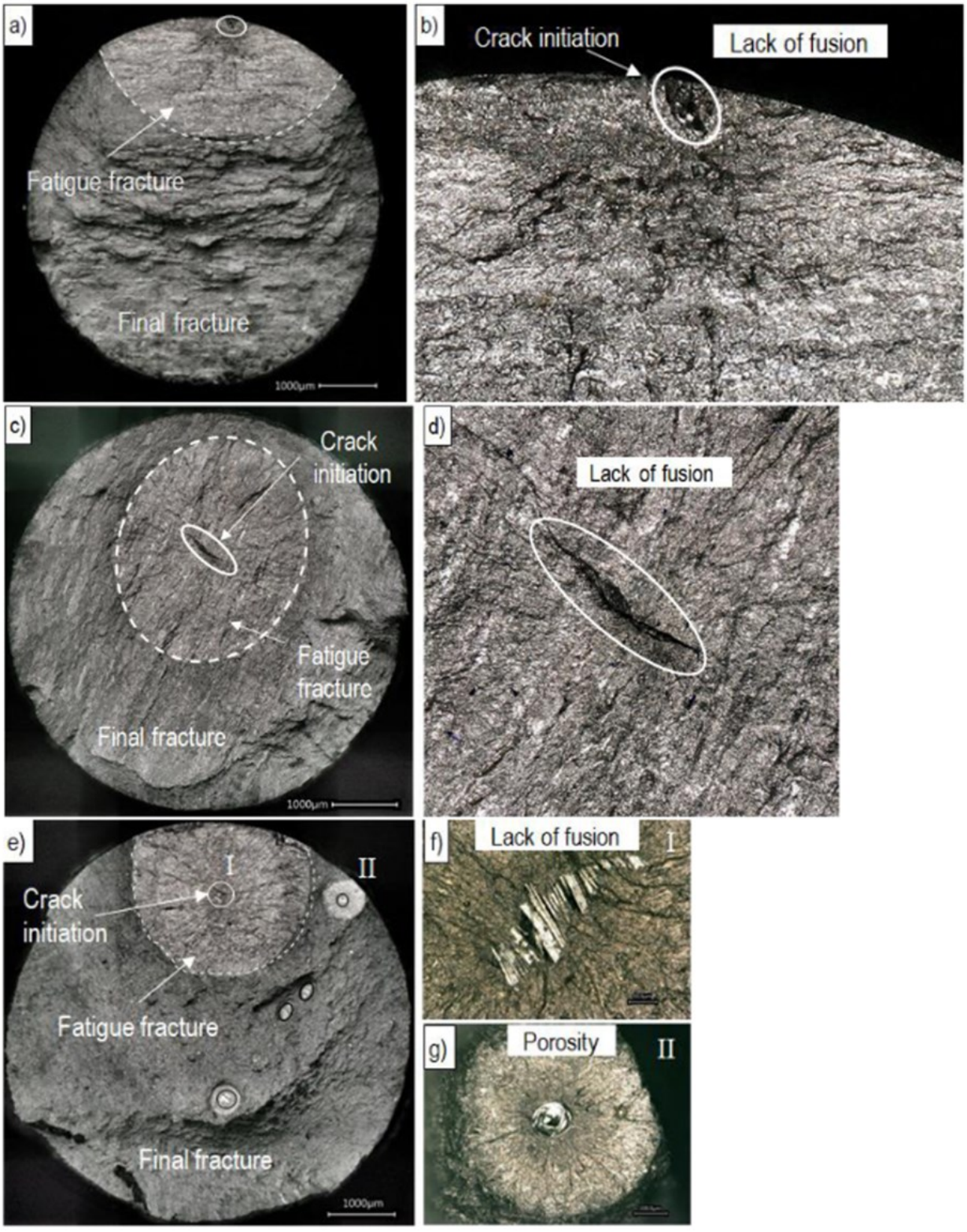

Figure 2.13 : Comparison of fatigue fracture surfaces of EBM manufactured Ti-6Al-4V samples [61].

Radolf et al. [61] analyzed these defects to predict the fatigue limit of the samples using the Root Area method, following Murakami's approach. The defect sizes fall within the range of approximately 120–300µm for vertically built specimens and 75–200µm for horizontally built specimens. A strain-life curve was calculated, revealing that the initially observed disparities in the stress-life curve between the vertical and horizontal directions were not the primary driving factor for the shorter fatigue life. Instead, the authors conclude that the size and location of defects play a more important role in determining the fatigue life of Ti64 EBM samples [61].

Sandell [63] conducted a study using X-ray micro tomography (XCT) of internal defects in electron beam melted Ti6Al4V and their impact on fatigue behavior. The researcher machined 12 samples, which were then subjected to testing following the ASTM E606 standard (Strain-controlled fatigue testing, R= -1) at a 1% strain level. In the 12 tested samples, the initiating defect size was measured to be 213µm, placing it in the 100th percentile of the total pores identified. This specimen failed after 12 334 cycles. The smallest initiator measured was 68.9µm, falling in the 93.6th percentile, and this specimen failed after 18 712 cycles. In both cases, the pores were located within their diameter's distance from the surface. Figure 2.14 illustrates an example of pore sizes and their distribution.

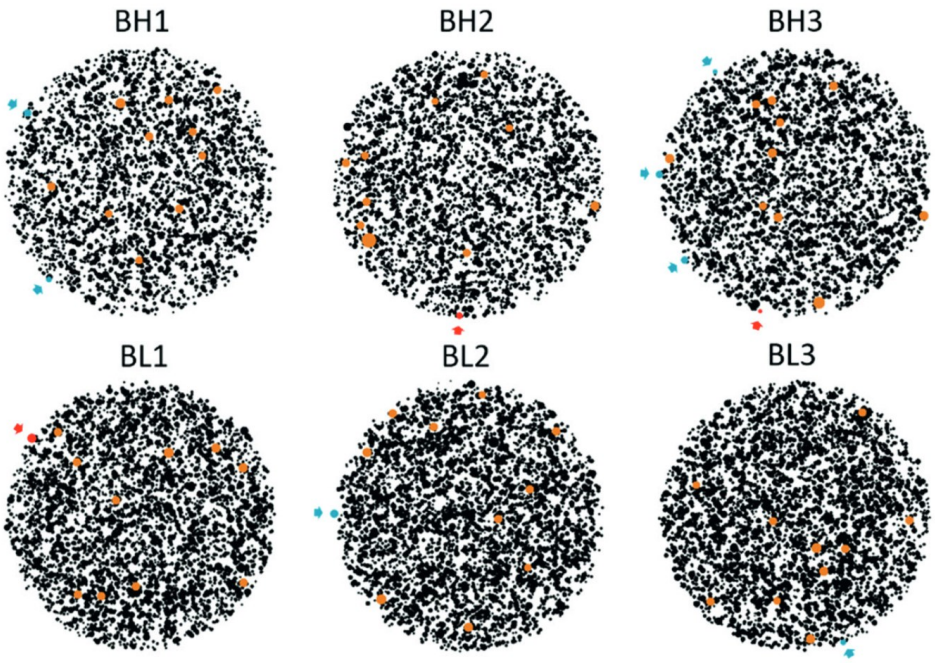

Figure 2.14 : Defect distributions in the gauge length projected along the load axis of the specimens. Black: all pores segmented from the XCT data. Orange: the ten largest segmented pores in each scan. Red: fracture initiating pores segmented in the XCT data. Blue: fracture initiating pores not segmented in the XCT data. Green: fracture initiating LOF defect. Arrows highlight defect positions [63].

Eleven out of the twelve samples experienced fractures at pores, while one sample fractured at a LOF defect. Except for two fracture-initiating pores located outside the XCT scanned volume, all other defects could be identified in the XCT data. Notably, all samples had fractures initiating at surface defects, and every initiation occurred at pre-existing defects. None of the samples had fractures initiated by any of the ten largest pores segmented in the sample gauge length. This observation suggests that, at the relatively high strain/stress level selected for the study, the proximity of the pore to the surface had a greater influence than the overall size of the pore in determining fracture initiation. Among all initiations identified in the fractography, only one pore was not at or within one pore diameter from the surface. The authors emphasize that closeness to the surface is a more indicative factor than size in predicting the location of failure at the stress levels investigated. Pores of all detectable sizes exhibited a seemingly random distribution in the plane perpendicular to the building direction. Moreover, at the tested loads, samples with larger pores generally had a shorter average life than samples with smaller pores. Notably, all fracture-critical defects were found to be in the 90th to 100th percentile range of defect size, suggesting that using this portion of the collected data for statistical analysis and modeling is an effective tool to predict fatigue life. However, this method may be unreliable, as fatigue critical LOF defects were unable to be identified in the study [63].

Tammas-Williams et al. [64] investigated the impact of porosity on fatigue crack initiation in additively manufactured titanium components, using fractography and CT scanning techniques. Following the ASTM E466 standard (load-controlled fatigue testing at R= 0), the authors subjected 13 samples to testing and examined the fracture surfaces to characterize critical defects. The stress-cycle to failure curve with the characterization of defects is illustrated in Figure 2.15. Upon fractography analysis of all the samples tested, the researchers observed that critical fatigue cracks had originated from facets in 2 samples and from pores in 11 samples. Notably, in 10 out of the 11 samples with pore-initiated cracks, the pores were situated very close to the surface. Both samples with facets at the critical crack initiation location were found to have secondary cracks originating from a surface pore.

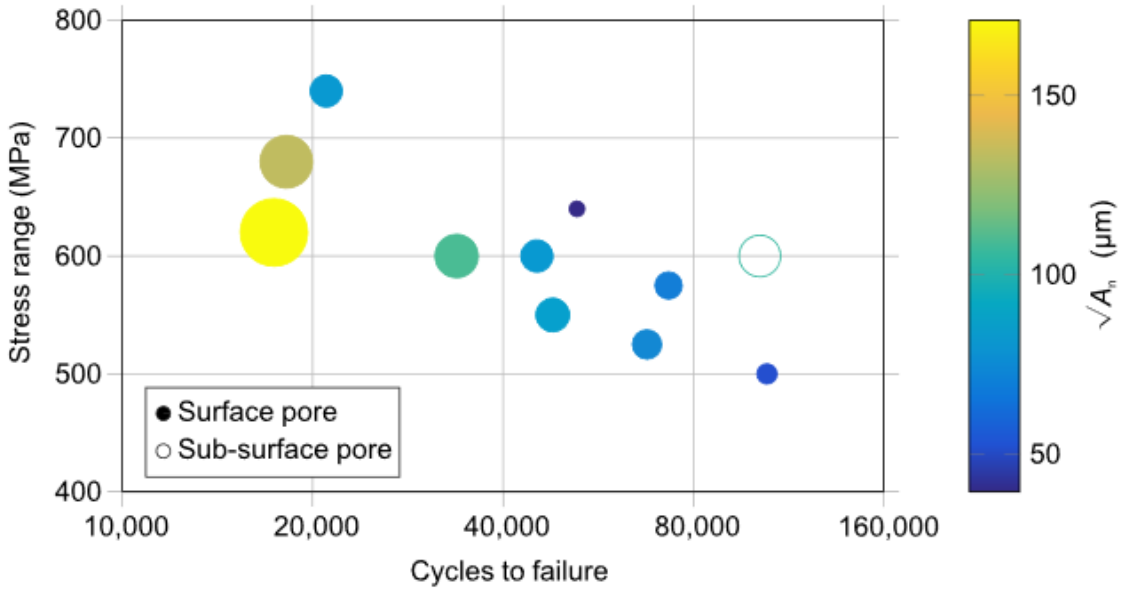

Figure 2.15 : Effect of pore size on fatigue life – S-N curve showing only those samples that failed from porosity. The size and colour of the markers indicate the size of the pore (A_n) measured from SEM images of the fracture surface [64].

Tammas-Williams et al. [64] also investigated the identification of pores most likely to initiate fatigue cracks by employing ranking strategies that considered pore size, aspect ratio, and proximity to the surface and to other pores. In this exploration, four fatigue samples were tested using the same standard, and interrupted fatigue testing with periodic CT inspections was conducted. During the testing, the authors identified both the specific pore from which cracks initiated and the number of cycles required for crack initiation in each of the four samples tested at 600 MPa. The fatigue testing maintained identical sample geometry and adhered to the same standard as in the previous tests, with periodic CT inspections carried out every 10,000 cycles. Cracks were detected by CT after 70,000, 100,000, and 120,000 cycles. Analysis revealed that in three out of the four samples, surface-initiating defects with root area parameters of 60µm, 50µm, and 50µm were observed. The sample with a bulk-initiating defect had a defect size of 170µm. Post-mortem fractography indicated that fatigue life was significantly influenced by the size of the initiating defect. However, CT scans demonstrated that the initiating defect was not necessarily the largest defect in all cases. The authors confirmed that the fatigue lives of samples manufactured by EBM AM are notably impacted by the presence of retained porosity. It was observed that in many cases, a surface defect, traditionally considered more benign from a conventional fracture mechanics perspective, could initiate a crack much earlier than suggested by the Murakami analysis. This highlights the importance of understanding and improving the fatigue life of AM components, where careful control of manufacturing process conditions can help avoid surface defects and enhance overall performance [64].

Chapter 3 Research questions

In the study that is the subject of this thesis, both the microstructure and mechanical properties of Ti-6Al-4V EBM samples produced with varying volumetric energy density were examined. Fifteen-millimetre cubes were first printed to examine the microstructural characteristics of the material. Ten tensile and twenty-four fatigue specimens were then printed to correlate the microstructural characteristics to mechanical properties.

The influence of volumetric energy density on print density and the types of defects produced was studied, as well as the microstructural characteristics stemming from the selection of process parameters. The tensile properties and hardness of the specimens were obtained, as well as stress-cycle to failure curves for printed specimens with respect to volumetric energy density. The experiments carried out aim to address the following research questions.

- How does varying EBM process parameters such as energy density, scanning speed, and beam current influence the microstructure of Ti64 components?
- What is the impact of EBM process parameters on the mechanical properties, such as tensile strength and hardness, of Ti64?
- How do defects produced through the EBM process affect the fatigue properties of Ti64, and what are the critical factors that influence fatigue behaviour under load-controlled fatigue testing?
- To what extent do variations in EBM process parameters contribute to the development of defects such as porosity and lack of fusion in Ti64 components, and how do these defects influence both mechanical properties and fatigue behaviour?

Chapter 4 Methodology

4.1 Process window development

Researchers employ a variety of approaches to establishing process windows for (EBM). Processing parameters including power, scan speed, layer thickness, hatch spacing, and scan strategy play an important role in determining the occurrence of defects and in defining the process window or printing a specific material. Typically, process windows are presented based on beam current or energy density plotted against scan speed. The boundaries on these plots delineate the process window and correspond to the prevention of defects such as lack of fusion, keyhole formation, and top surface swelling. The ultimate objective is to set these boundaries to achieve fully dense printed parts. Full density is often quantified as samples with a volumetric density exceeding 99%, although even within the established processing window, the occurrence of large defects remains a possibility [40].

Kirchner et al. [30] varied beam current and scan speed to evaluate the porosity and density of prints using the process window shown in Figure 4.1. Sharowsky et al. [9] varied energy density and scan speed to achieve dense Ti64 prints with a density surpassing 99.5% using the process window illustrated in Figure 4.3. Pobel et al. [31] examined the impact of beam power and scan speed on print quality, specifically focusing on porosity and the swelling of the top surface with the process window shown in Figure 4.2. The cited authors use different strategies to develop their process windows and do so by varying different process parameters.

The process window used for the study that is the subject of this thesis is shown in Figure 4.5, and was developed in a previous work conducted by Pantuso [65]. The current study evaluates the print quality in terms of beam power and scan speed as shown in in Figure 4.5, where the units of the process windows developed by Pantuso have been converted to beam power to ensure all process windows are compared using the same process parameters.

The motivation behind incorporating insights from three distinct studies into the development of a process window for the study conducted by Pantuso [65] was to assess the repeatability of prints based on print parameters, and to identify any consistent trends across the studies described above. All three process windows share common parameters, including a layer height of 0.05mm and a line offset of 0.1mm, which have been adapted in Figure 4.4. However, the focus offset, provided only by Kirchner et al. at 3mA, introduces a potential source of variation among the prints from the three studies.

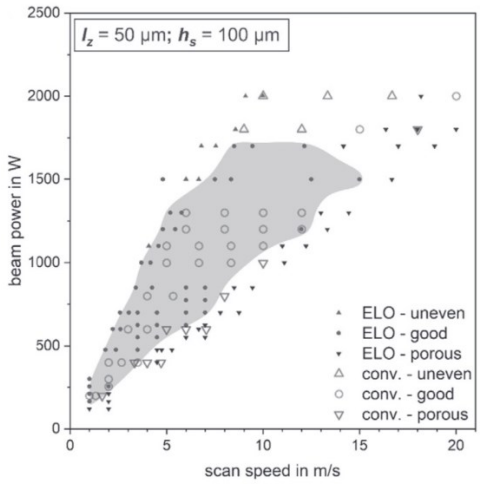

Figure 4.1 : Ti64 process window for EBM with varying beam power and scan speed [31].

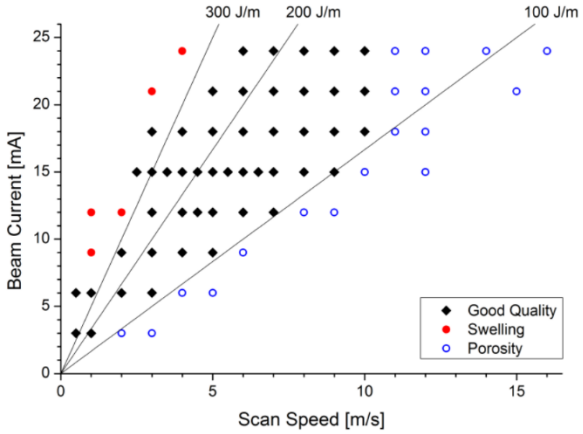

Figure 4.2 : Process window for EBM of Ti64 with varying beam current and scan speed. Blue circles mark samples with more than 1% porosity, while red circles mark pronounced swelling on top surface [30].

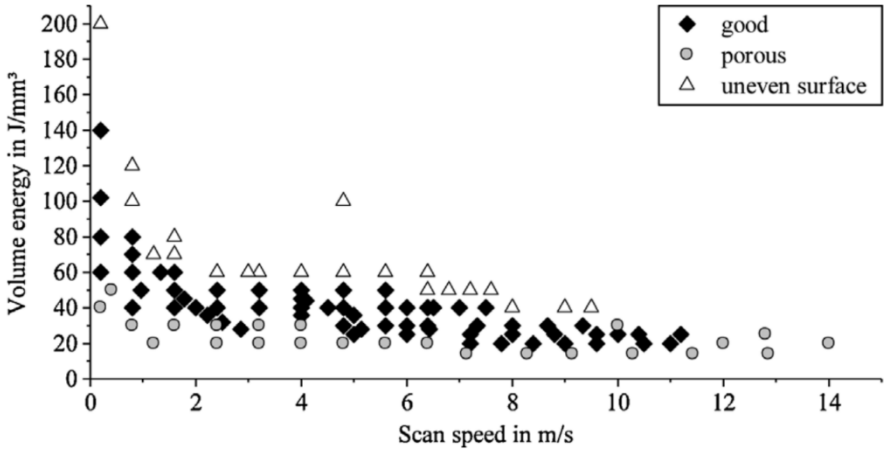

Figure 4.3 : Process window of Ti64 for EBM as a function of volume energy and scan speed [9].

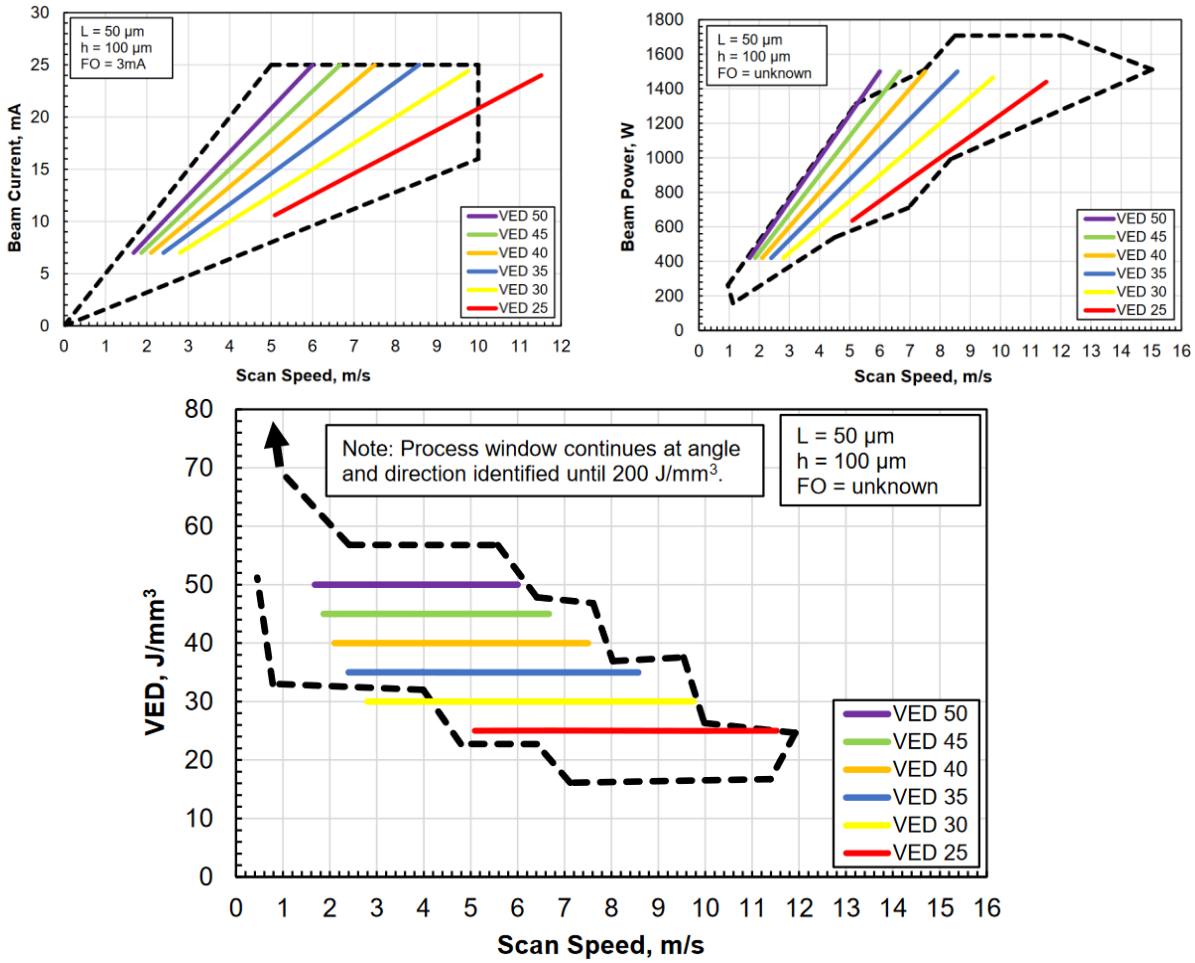

Figure 4.4 : Process window developed by Pantuso according to beam current, beam power, VED, and scan speed [65].

The relationship between beam power and beam current is given by Ohm's law, where the beam power is given by the beam current multiplied by the beam voltage. All the samples from the studies used to define the process window have been printed on EBM equipment with a beam voltage of 60kV. The study by Sharowsky et al. [9] varies VED with respect to scan speed, and provides a layer height and hatch spacing of 50 µm and 100 µm respectively. Using equation (1), VED can be converted to beam power using the layer height and hatch spacing.

Converting all three studies to the same units allows their visualization on a single graph to define a process window incorporating a greater number of samples. The red markers in the process of window of Figure 4.5 indicate porous prints; the yellow markers indicate swelling of the top print surface; and the green markers indicate prints having a density exceeding 99%.

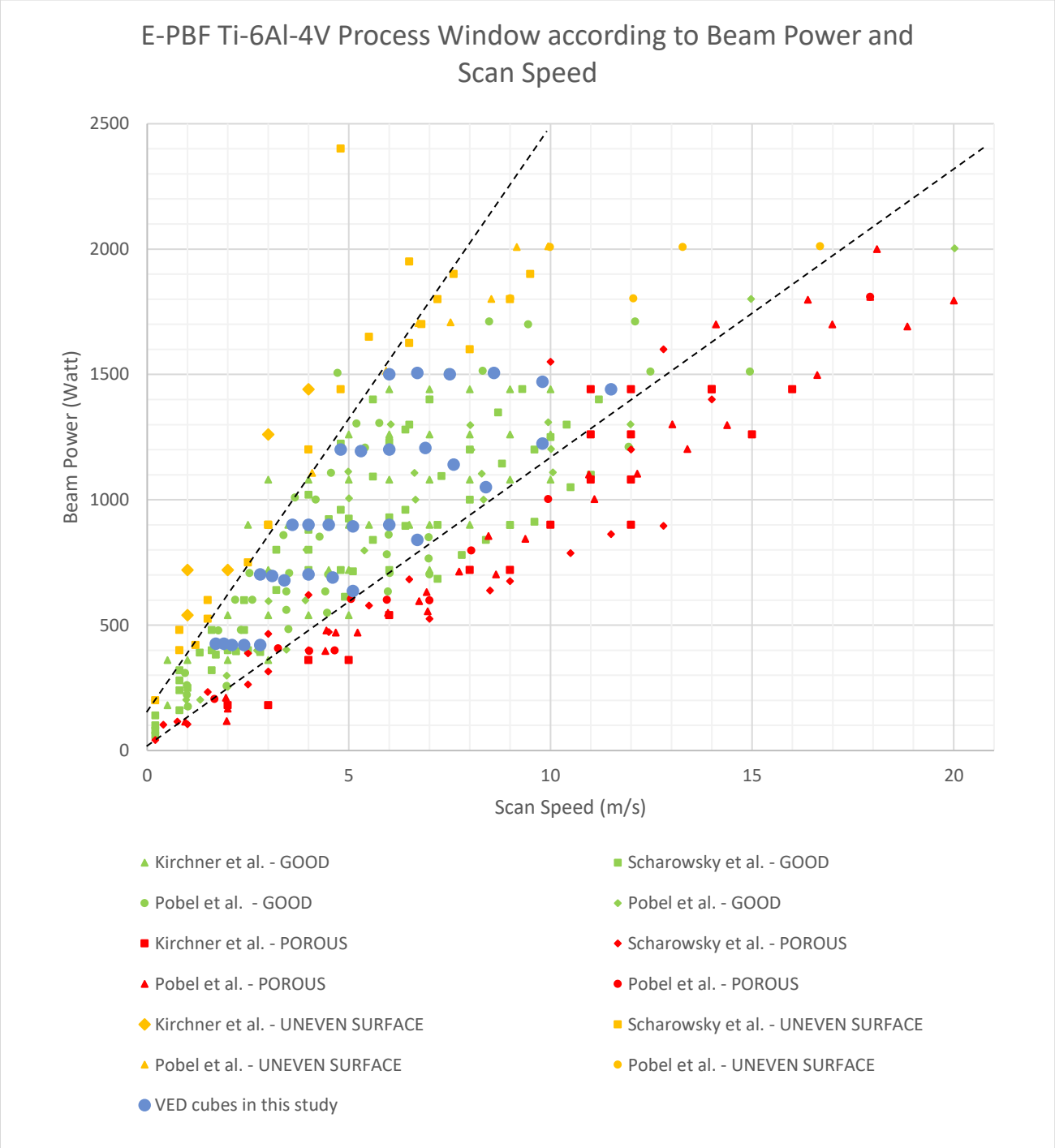

Figure 4.5 : Process window for beam power versus scan speed used in this study. Adapted from [9], [30], [31], [65].

The studies used in the process window in Figure 4.5 have different nomenclatures with respect to print quality. These nomenclatures are GOOD, POROUS, or UNEVEN SURFACE. GOOD is used to describe parts with a density over 99%. POROUS is used to describe parts with a density less than 99%. UNEVEN SURFACE is used to describe parts with noticeable aluminum loss, causing swelling on the top print surface. In Figure 4.5, two discernible boundaries are visible: the interface between yellow and green markers indicates the boundary for the top surface swelling defect, while the red-green interface indicates the boundary for the lack of fusion defect. The beam power and scan speed parameters selected for this study have been tailored to fall within these identified boundaries.

The larger blue markers in Figure 4.5 represent the process parameters selected by Pantuso [65] for the specimens used in the current study. Converting beam power to VED using equation (1), these parameters correspond to volumetric energy inputs ranging from 25J/mm^3 to 50 J/mm^3. For each blue marker in Figure 4.5, two cubes were printed, each with a different focus offset value.

4.2 VED cubes

4.2.1 Manufacturing

Two sets of VED cubes were printed during the previous work [65]. The first set is shown in Figure 4.6 and Figure 4.7, and was printed with a focus offset of 25mA. This did not allow for a proper focus of the electron beam on the print bed, creating multiple lack of fusion defects. This porosity was visible on the top surface of the samples. The unevenness of the top printed surface can be used as an indicator for the quality of the print; bumpy surfaces indicate the presence of defects, while swelled surfaces indicate a loss of aluminum by sublimation. This set was not used as part of the current study. All prints for this study used Ti6Al4V powder supplied by ARCAM, with a 45µm to 106µm standard deviation in powder particle size [66].

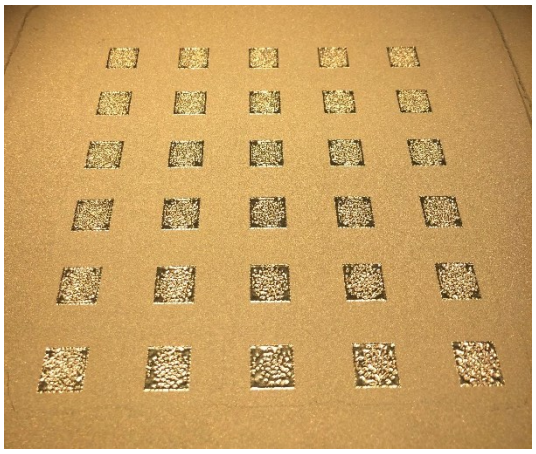

Figure 4.6 : VED cubes layout on powder bed

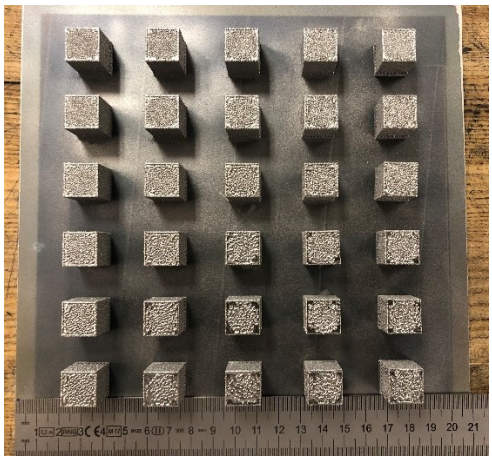

Figure 4.7 : VED cubes layout off build plate

The second set printed by Pantuso [65] had an adjusted focus offset of 6mA to allow a better focus of the beam on the build plate. The resulting samples, shown in Figure 4.8, were used as part of the current study. The process parameters used for the VED cubes are listed in Table 4.1. Calculated line energy, volume energy, and beam power parameters are also provided.

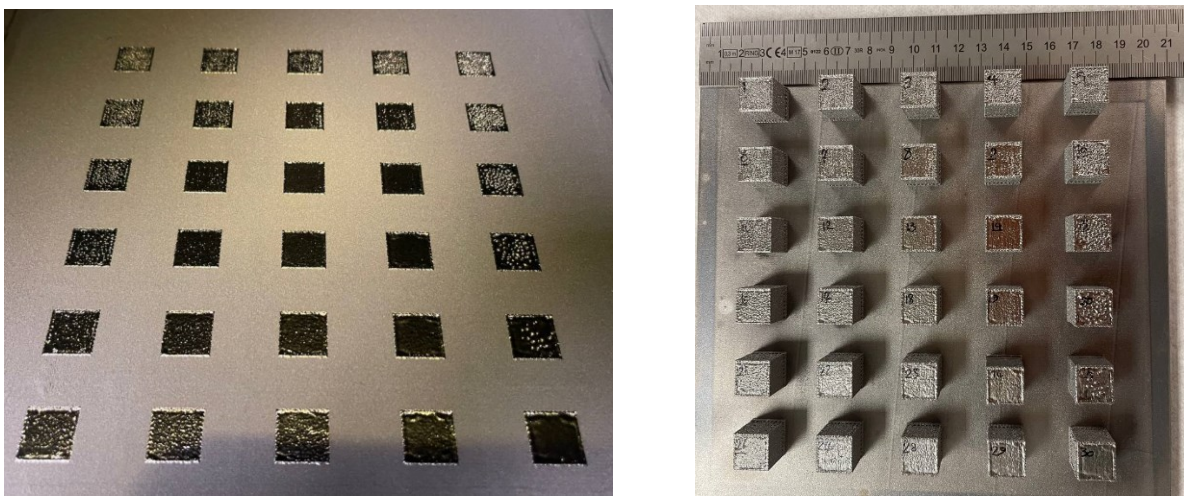

Figure 4.8 : Set of 30 VED cubes printed with a beam voltage of 60 kV, hatch spacing of 0.1mm, layer thickness of 0.05mm, and focus offset of 6mA.

Two stages of the manufacturing process are shown in Figure 4.9 and Figure 4.10. Figure 4.9 shows the preheating of the powder, while Figure 4.10 shows the melting of the powder with the electron beam.

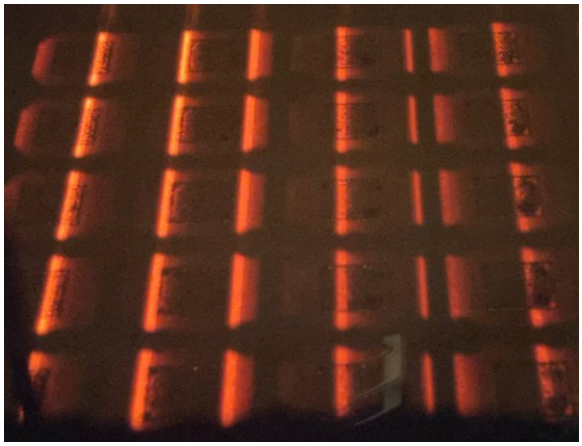

Figure 4.9 : Powder preheating stage

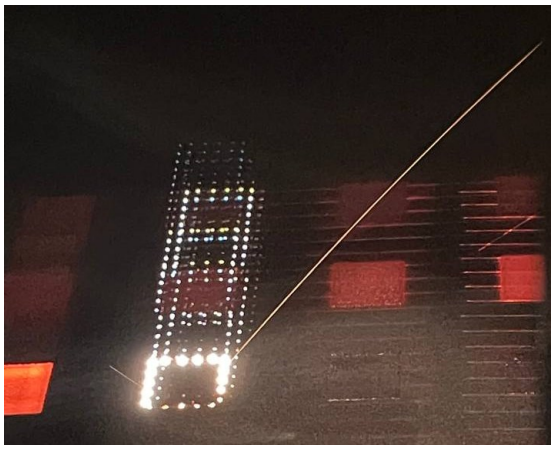

Figure 4.10 : Powder melting stage

Table 4.1 : VED Cubes Process Parameters

Test No.	Sample side length [mm]	Melt strategy	Focus Offset [mA]	Speed [mm/s]	Speed [m/s]	Beam Current [mA]	Line offset (mm)	Lateral speed (mm/s)	Line Energy [J/mm]	Volumetric Energy [J/mm^3]	Beam Power (Watt)
Cube 1	15	Snake	6	5100	5.1	10.6	0.1	34.0	0.12	24.9	636
Cube 2	15	Snake	6	6700	6.7	14.0	0.1	44.7	0.13	25.1	840
Cube 3	15	Snake	6	8400	8.4	17.5	0.1	56.0	0.13	25.0	1050
Cube 4	15	Snake	6	9800	9.8	20.4	0.1	65.3	0.12	25.0	1224
Cube 5	15	Snake	6	11500	11.5	24.0	0.1	76.7	0.13	25.0	1440
Cube 6	15	Snake	6	2800	2.8	7.0	0.1	18.7	0.15	30.0	420
Cube 7	15	Snake	6	4600	4.6	11.5	0.1	30.7	0.15	30.0	690
Cube 8	15	Snake	6	6000	6.0	15.0	0.1	40.0	0.15	30.0	900
Cube 9	15	Snake	6	7600	7.6	19.0	0.1	50.7	0.15	30.0	1140
Cube 10	15	Snake	6	9800	9.8	24.5	0.1	65.3	0.15	30.0	1470
Cube 11	15	Snake	6	2400	2.4	7.0	0.1	16.0	0.18	35.0	420
Cube 12	15	Snake	6	4000	4.0	11.7	0.1	26.7	0.18	35.1	702
Cube 13	15	Snake	6	5100	5.1	14.9	0.1	34.0	0.18	35.1	894
Cube 14	15	Snake	6	6900	6.9	20.1	0.1	46.0	0.17	35.0	1206
Cube 15	15	Snake	6	8600	8.6	25.1	0.1	57.3	0.18	35.0	1506
Cube 16	15	Snake	6	2100	2.1	7.0	0.1	14.0	0.20	40.0	420
Cube 17	15	Snake	6	3400	3.4	11.3	0.1	22.7	0.20	39.9	678
Cube 18	15	Snake	6	4500	4.5	15.0	0.1	30.0	0.20	40.0	900
Cube 19	15	Snake	6	6000	6.0	20.0	0.1	40.0	0.20	40.0	1200
Cube 20	15	Snake	6	7500	7.5	25.0	0.1	50.0	0.20	40.0	1500
Cube 21	15	Snake	6	1900	1.9	7.1	0.1	12.7	0.22	44.8	426
Cube 22	15	Snake	6	3100	3.1	11.6	0.1	20.7	0.22	44.9	696
Cube 23	15	Snake	6	4000	4.0	15.0	0.1	26.7	0.23	45.0	900
Cube 24	15	Snake	6	5300	5.3	19.9	0.1	35.3	0.23	45.1	1194
Cube 25	15	Snake	6	6700	6.7	25.1	0.1	44.7	0.22	45.0	1506
Cube 26	15	Snake	6	1700	1.7	7.1	0.1	11.3	0.25	50.1	426
Cube 27	15	Snake	6	2800	2.8	11.7	0.1	18.7	0.25	50.1	702
Cube 28	15	Snake	6	3600	3.6	15.0	0.1	24.0	0.25	50.0	900
Cube 29	15	Snake	6	4800	4.8	20.0	0.1	32.0	0.25	50.0	1200
Cube 30	15	Snake	6	6000	6.0	25.0	0.1	40.0	0.25	50.0	1500

4.2.1.1 Initial visual examination

The set of cubes printed with a focus offset of 6mA contained five smaples with a VED of 25J/mm^3, five at 30J/mm^3, five at 35J/mm^3, five cubes at 45J/mm^3, and five cubes with a VED of 50J/mm^3 for a total of thirty cubes. The samples were numbered from 1 to 30, with the first 25J/mm^3 cube starting at number 1. The top surface of the samples were examined to assess the print quality and select process parameters and final settings for the manufacture of tensile and fatigue specimens.

From the 50 VED samples, Cube #29 had the most even surface. From the 30 VED samples, Cube #8 had the most even surface. Figure 4.11 depicts the difference in the top surface smoothness from different specimens printed in the second run at a focus offset of 6mA. The surface of Cube #20 at 40VED is uneaven and bumpy compared to the surface of Cube #29, for example. Accordingly, the porosity of Cube #20 is expected to be higher than the porosity of Cube #29.

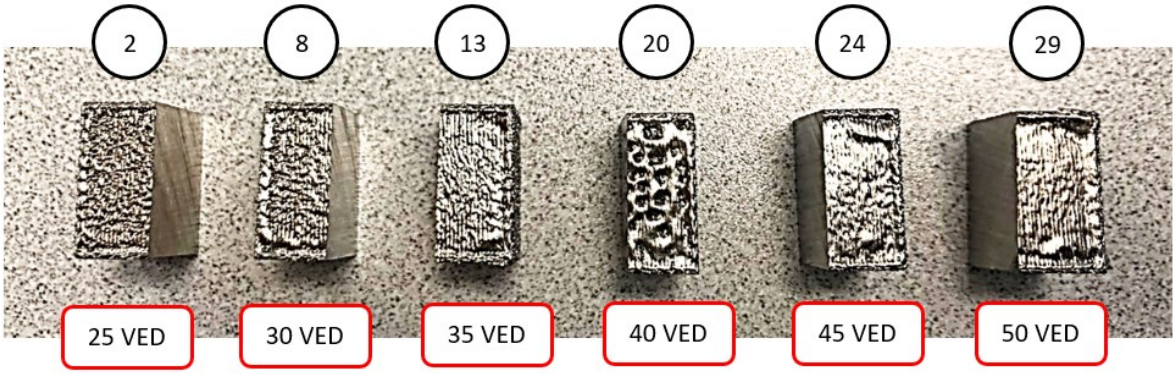

Figure 4.11 : Difference in top surface of VED cubes related to pint quality.

Cubes 8 (30 VED) and 29 (50VED) were selected to be used as the 30VED and 50VED parameters for the printing of the tensile and fatigue samples. The parameters were chosen based on criteria determined during the previous study by Pantuso [65].

All cubes printed in the second set of VED cubes were used as part of the current study regardless of their porosity level. The samples were prepared for microstructural evaluation to correlate process parameters to microstructure.

4.2.2 Preparation of VED cubes

The VED cubes were cut parallel to the build direction to view the different layers on the print. The cut was performed using a Struers SETOCOM-15 automatic precision cutting machine. A diamond-coated cut-off wheel of 200 mm outer diameter rotating at 1000rpm was used, advancing at a constant rate of 0.1mm/s. The cutting plane on the samples and the equipment are shown in Figure 4.12 and Figure 4.13.

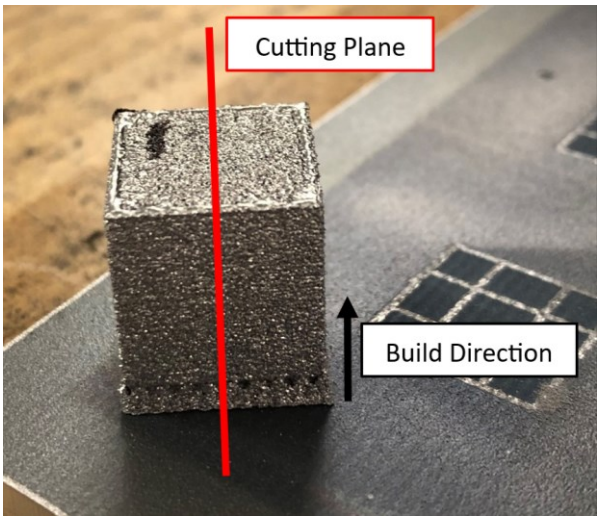

Figure 4.12 : VED cubes cutting plane parallel to build direction

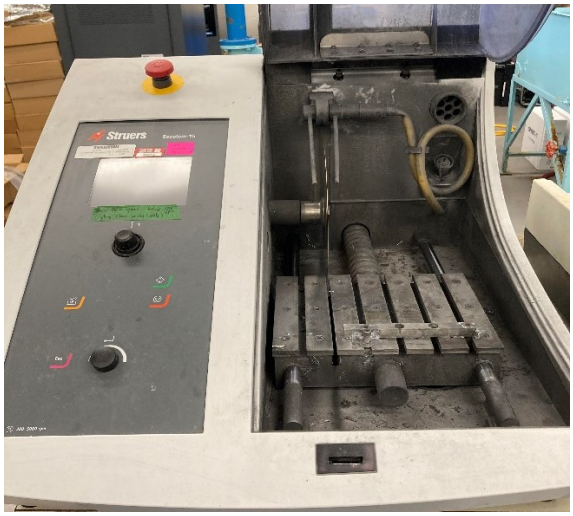

Figure 4.13 : Struers SECOTOM-15 automatic cutting machine

The half cubes were mounted with Buehler PhenoCure™ black pre-molds with a 1.25in outer diameter and set in a Struers Prestopress-3™. The samples were heated for 8 minutes with a 26kN force, then cooled with water for 4 minutes. The Struers mounting equipment and mounted samples are shown in Figure 4.14 and Figure 4.15, respectively.

Figure 4.14 : Struers Prestopress-3

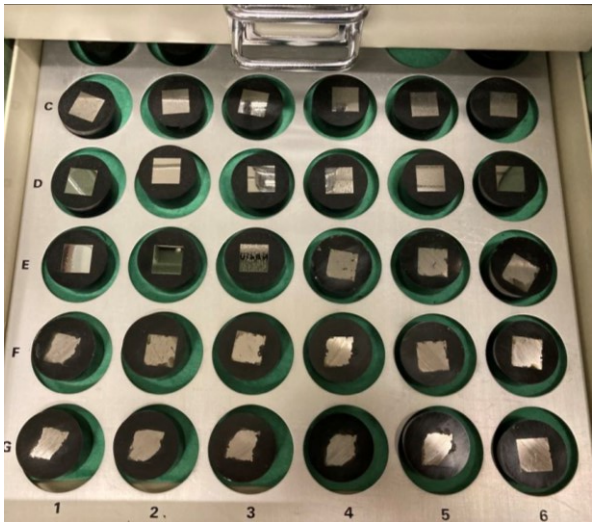

Figure 4.15 : Mounted VED cubes

The mounted samples were polished using a three-step process performed following the guideline in the Buehler polishing guide [67]. The first step is grinding with a 320-grit sandpaper at 240rpm in the clockwise direction using water as a lubricant. Once no more saw marks were present on the specimens' surface, the specimens were washed with soap and water to remove sanding/polishing material and dried using 70% or greater isopropyl alcohol.

The second polishing step was performed on a nylon napless polishing cloth. The polishing compound is a 9µm MetaDi™ diamond paste. This step was performed at 120rpm in the counterclockwise direction on an automatic polisher using 10lbs of force on 5 samples using MetalDi™ fluid as lubricant. The criterion for successful coarse polishing is that no marks can be observed under the optical microscope at 50× magnification. After coarse polishing, the samples were washed with soap and water to remove sanding/polishing material, and dried using 70% or greater isopropyl alcohol. This process is depicted in Figure 4.16.

The last polishing step involves a Microcloth™ napped polishing cloth with MasterMet™ colloidal silica at 120rpm in the counterclockwise direction. This step was performed for 15 minutes. The criterion for successful fine polishing is that no marks from fine grinding can be observed under the optical microscope at 50× magnification. After fine polishing, the samples were washed with soap and water to remove polishing material and dried using 70% or greater isopropyl alcohol.

Figure 4.16 : Polishing process on nylon polishing pad with 9µm diamond paste.

Because the samples were porous, the surface of each specimen was cleaned with compressed air after washing. If particles were observed coming out of the pores under the optical microscope at 50× magnification after being cleaned with compressed air, the washing process was repeated until no particles are observed. This process avoids large scratches occurring at the next polishing steps because of cross-contamination.

The last step of the sample's preparation was to etch the samples with Kroll's reagent. Kroll's reagent is composed of 92.82% water, 6.11% nitric acid, and 1.07% hydrofluoric acid. The VED cubes were etched with this solution for 15 seconds, then rinsed with distilled water. The samples were then placed in an ultrasonic cleaner with distilled water for 30 minutes to remove all remaining hydrofluoric acid.

4.3 Tensile samples

4.3.1 Manufacturing

The tensile sample blanks were printed as part of the previous work by Pantuso [65]. Ten tensile specimens were printed on a single stack on the build plate. Five of these samples were printed with 30VED, denoted by the odd numbers in Figure 4.17. Five of the samples were printed with 50VED denoted by the even numbers.

The drawing of the initial geometry of the tensile samples is presented in Appendix A.

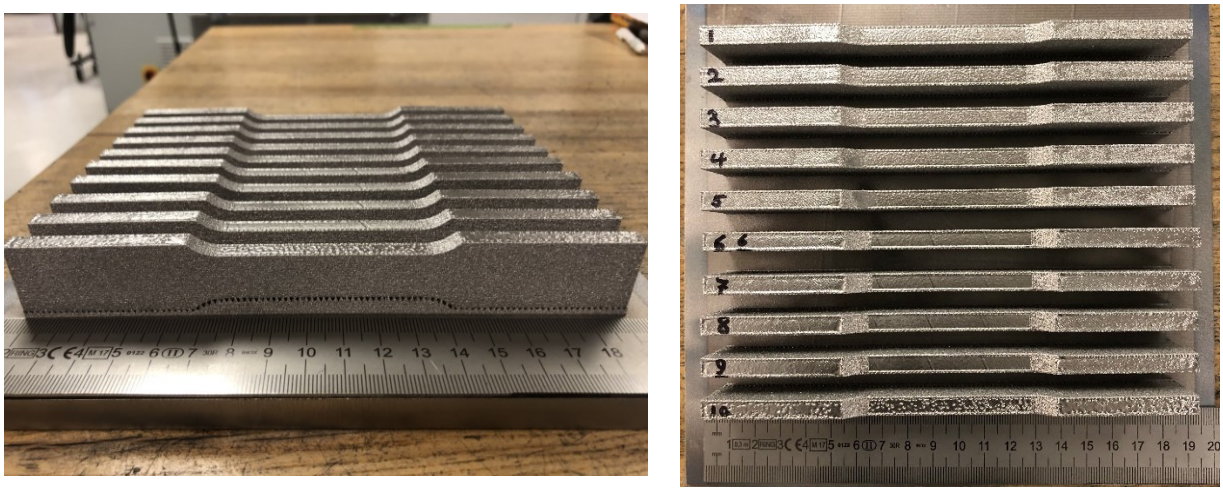

Figure 4.17 : Set of 10 tensile samples printed with a beam voltage of 60 kV, hatch spacing of 0.1mm, layer thickness of 0.05mm, and focus offset of 6mA. 30VED samples have a scan speed of 6.0 m/s and a beam current of 15.0 mA. 50VED samples have a scan speed of 4.8 m/s and a beam current of 20.0 mA.

4.3.2 Preparation of tensile samples

Prior to machining the tensile samples, the support material was removed with a hammer and chisel. The tensile sample blank was manufactured with a nominal thickness of 7mm.

Guo et al. [68] observed that the surface roughness can be improved with a material removal of 100um, or 0.1mm. The final thickness of the sample has a nominal thickness of 6mm, allowing 0.5mm to be removed from the top and bottom surfaces of the sample. In the case of this study, 0.5mm corresponds to one build layer being removed from the top and bottom surfaces of the samples, allowing the gauge surface of the dogbone to be fully machined and smooth on all sides.

After the support material is removed and the dogbone machined to the desired thickness, the samples were machined to their final shape by placing the specimen in a jig with three dowel pins to locate the specimen on the X and Y axes. The jig is shown in Figure 4.18 and Figure 4.19.

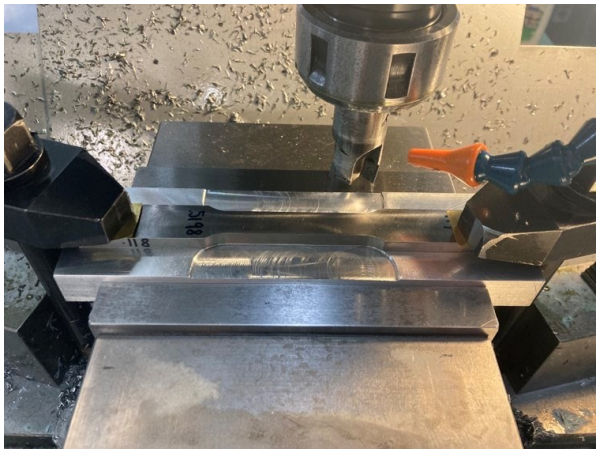

Figure 4.18 : Machining jig on milling machine

Figure 4.19 : Dowel pin positioning on machining jig

The drawing for the final geometry of the tensile samples is presented in Appendix C. An inspection report for the tensile specimens is presented in Appendix F.

4.4 Fatigue samples

4.4.1 Manufacturing

The fatigue sample blanks were manufactured as part of the previous work conducted by Pantuso [65]. Twenty-four fatigue specimen blanks were printed, stacked in three layers on the build plate as shown in Figure 4.20 [69]. The drawing of the initial geometry of the fatigue samples is presented in Appendix B. Twelve of these samples were printed with 30VED, denoted by the odd numbers in Figure 4.17. The other twelve of the samples were printed with the 50VED and are denoted by the even numbers in Figure 4.20.

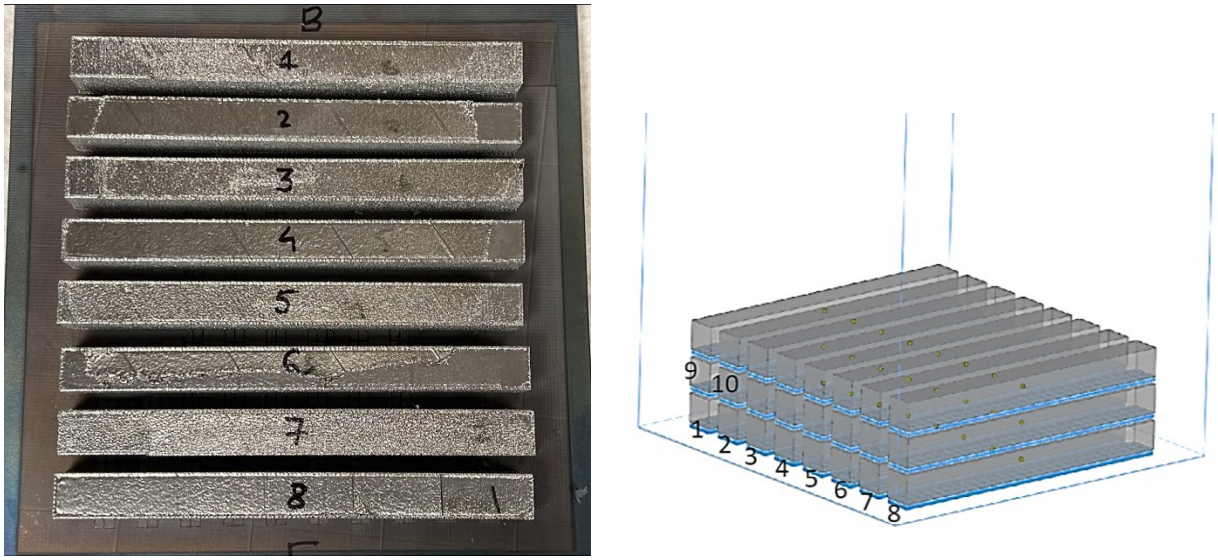

Figure 4.20 : Set of 24 fatigue samples printed with a beam voltage of 60 kV, hatch spacing of 0.1mm, layer thickness of 0.05mm, and focus offset of 6mA. 30VED samples have a scan speed of 6.0 m/s and a beam current of 15.0 mA. 50VED samples have a scan speed of 4.8 m/s and a beam current of 20.0 mA.

4.4.2 Preparation of fatigue samples

Prior to the machining of the fatigue samples, the support material was first removed with a hammer and chisel as shown in Figure 4.21. The samples were then centered on a four-jaw chuck to turn a diameter for gripping on the CNC lathe used to cut the profile as shown in Figure 4.22. The sample was then supported between centers on the CNC lathe to ensure a uniform gauge diameter is obtained throughout the gauge length of the specimen as shown in Figure 4.23.

Figure 4.21 : Removal of support material from fatigue samples.

Figure 4.22 : Turning of fatigue sample gripping diameter on four-jaw chuck.

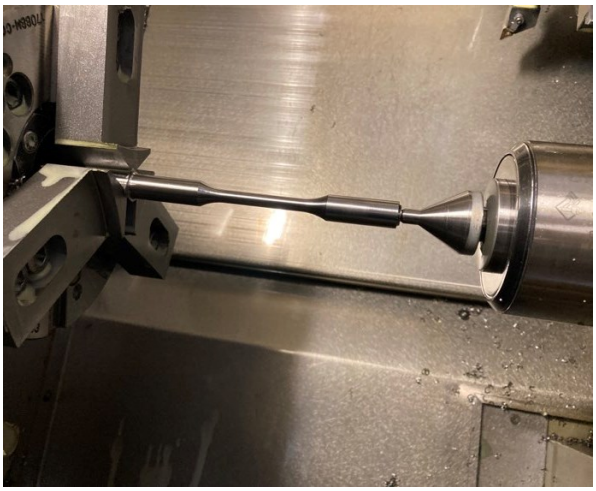

Figure 4.23 : Turning fatigue profile between centers on CNC lathe.

The part drawing for the final geometry of the fatigue samples in presented in Appendix D. An inspection report for the fatigue samples is presented in Appendix G.

4.5 Microstructure analysis

4.5.1 Optical microscopy

Microstructure

An optical microscope was used to examine the VED cubes for microstructure and porosity defects. The samples were examined at 200X magnification, and an example is shown in Figure 4.24. An additional examination was done at 500X magnification, and an example is provided in Figure 4.25, where the alpha lath structure is visible.

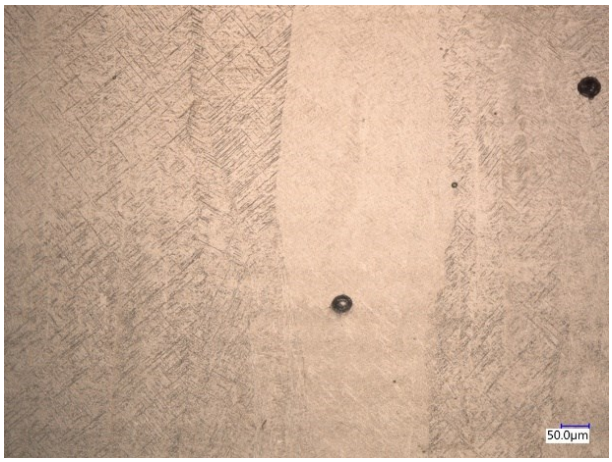

Figure 4.24 : VED cube 1 etched surface at 200X magnification.

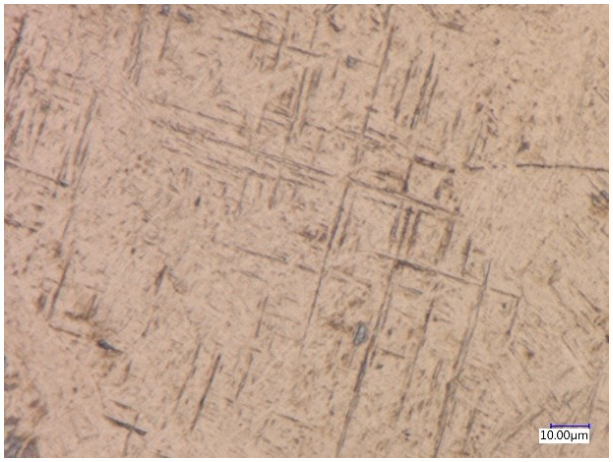

Figure 4.25 : VED cube 30 etched surface at 500X magnification.

Tensile samples and fatigue samples were observed under the optical microscope to determine the type of porosity defects present in the samples as a function of VED. The samples taken from the fatigue specimens were extracted at the extremity of the specimen from the material which had previously been used to hold the sample in the lathe as depicted in Figure 4.26. The porosity evaluation and fatigue testing could therefore be performed on the same specimen. The tensile sample coupons were extracted from the gauge length of the samples after they were tested as shown in Figure 4.27. The build orientation was noted for the rectangular tensile samples, but not for the round fatigue samples.

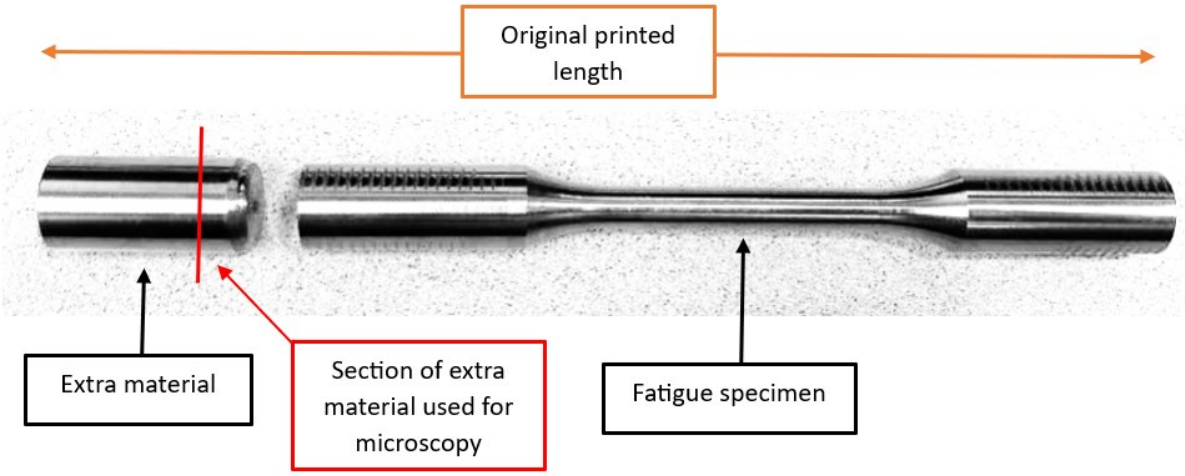

Figure 4.26 : Coupon extraction location from fatigue samples.

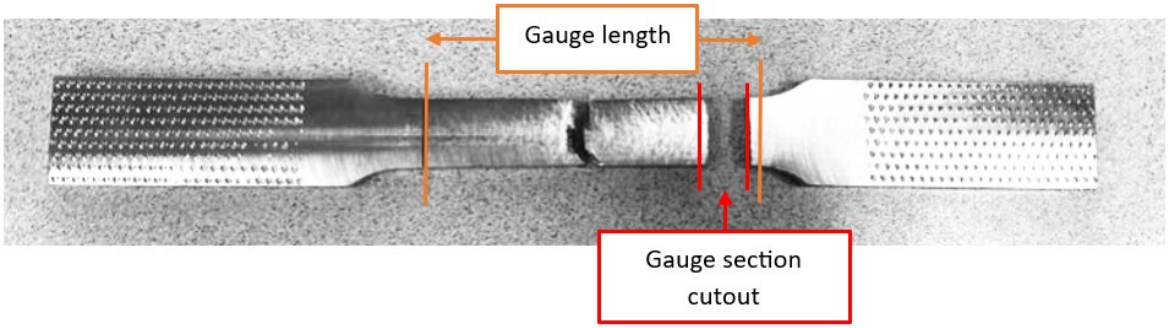

Figure 4.27 : Coupon extraction location from tensile samples.

The tensile samples were analysed using optical microscopy to determine the configuration of defects with respect to print orientation. This observation and qualification of defect orientation is used to determine the type of lack of fusion produced. The defect configuration in the 30VED and 50VED tensile samples is shown in Figure 4.28 and Figure 4.29. The photographs are taken on an optical microscope at 200X magnification.

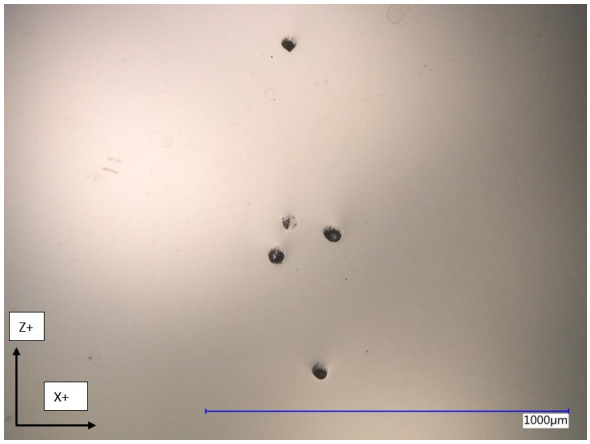

Figure 4.28 : Defects in tensile sample #6 (50VED) at 200X magnification.

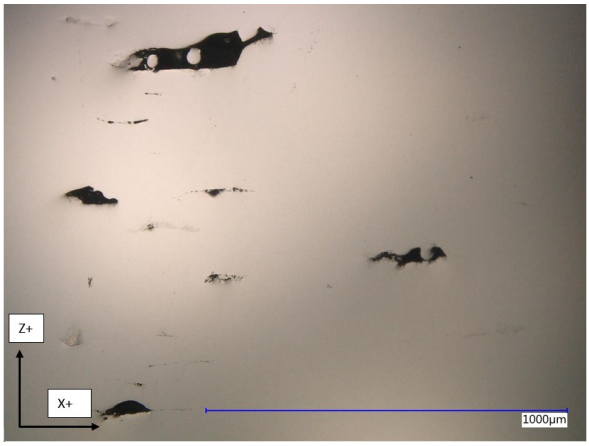

Figure 4.29 : Defects in tensile sample #1 (30VED) at 200X magnification.

The porosity of the fatigue samples was examined using optical microscopy to associate porosity to fatigue behavior. Five samples of the 30VED fatigue samples and five of the 50VED fatigue samples were used to obtain porosity measurements.

Optical microscopy is used to determine the porosity of the section of the sample by determining the area of pores at a given cross-section in the sample. This method allows the size of defects to be captured in 2D but does not allow the 3D geometry of the defect to be captured. Lack of fusion defects with trapped powder are also difficult to capture using this method, as this defect is not entirely void and may not have the required color brightness contrast to be captured. In addition, this method is area-specific, meaning each cross section will yield a different porosity value. An example of the method is provided in Figure 4.30 and Figure 4.31.

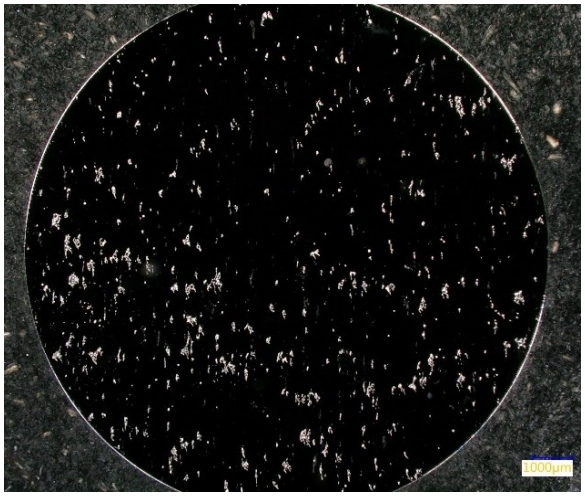

Figure 4.30 : Original photograph of 30 VED sample with pixel contrast between defects and metal.

Figure 4.31 : Original photograph of 50 VED sample with pixel contrast between gas pores and metal.

MIPAR was used to detect pores in cross sections of the fatigue samples. The brightness contrast of the pores with respect to the bulk material is captured by the software, which highlights the pores in red as shown in Figure 4.32.

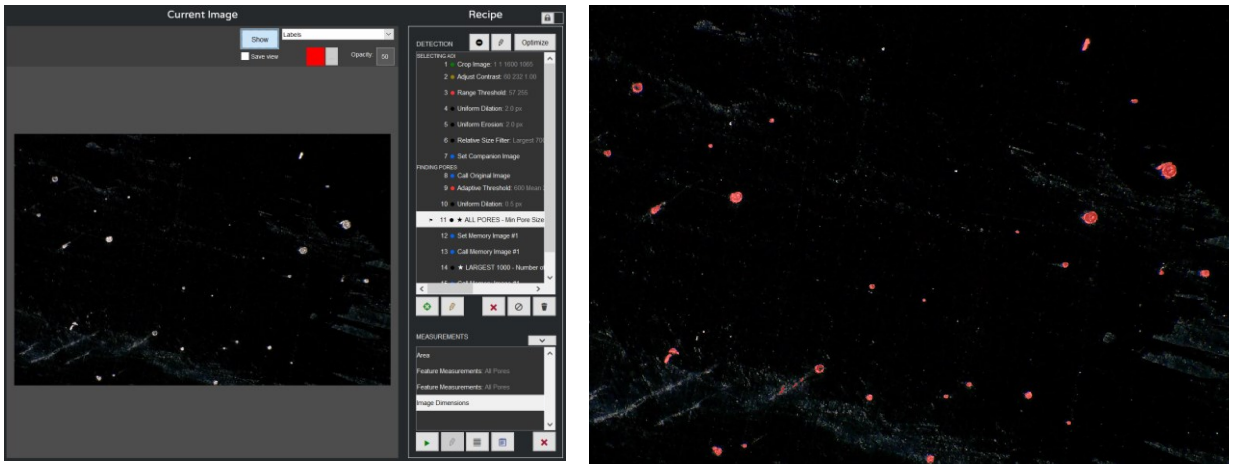

Figure 4.32 : Pore recognition from optical microscopy photograph.

After the optical microscopy images were obtained, an approximation of the porosity level of the samples was obtained, however, the alpha laths could not be seen clearly, even at high magnification. The alpha lath width on the photographs did not contain enough pixels to be measured accurately and repeatedly.

4.5.2 Scanning electron microscopy

The VED cubes were viewed under a scanning electron microscope to allow the alpha lath thickness to be measured. Photographs of the specimen were taken at 1000X, 2000X, and 4000X magnification. The electron microscope and a photograph of the VED sample 24 can be seen in Figure 4.33 and Figure 4.34. All images were taken with an accelerating voltage of 15kV.

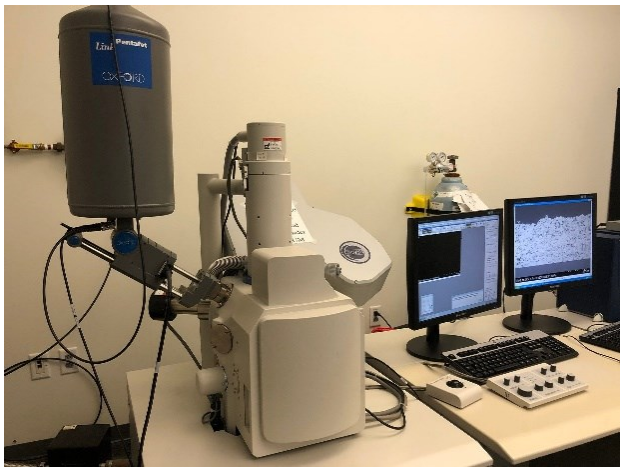

Figure 4.33 : Scanning electron microscope

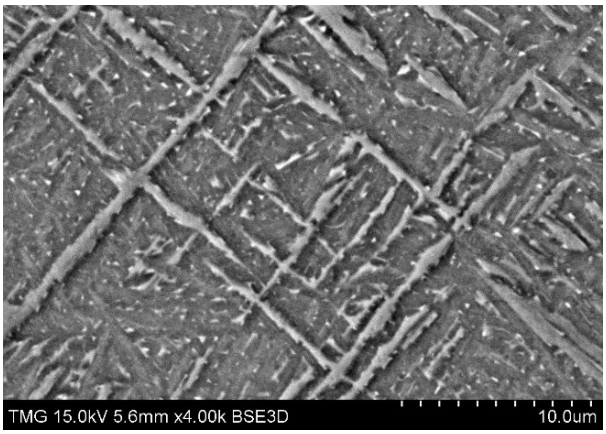

Figure 4.34 : Sample 24 microstructure at 4000X magnification

After the VED cubes were photographed on the SEM, the images were analysed using the image processing software MIPAR. The contrast between the alpha laths and the background was captured to measure the thickness of the laths. The advanced thickness algorithm of MIPAR was used, a method that quantifies the local thickness along features by measuring the diameter of the largest circle that can fit inside a feature with the center of the circle at each point along the feature's skeleton [70]. Twenty laths were measured for each specimen, and measurements of the laths which were visible and identifiable were compiled. The highlighting of the alpha lath and the resulting thickness measurement is shown in Figure 4.35.

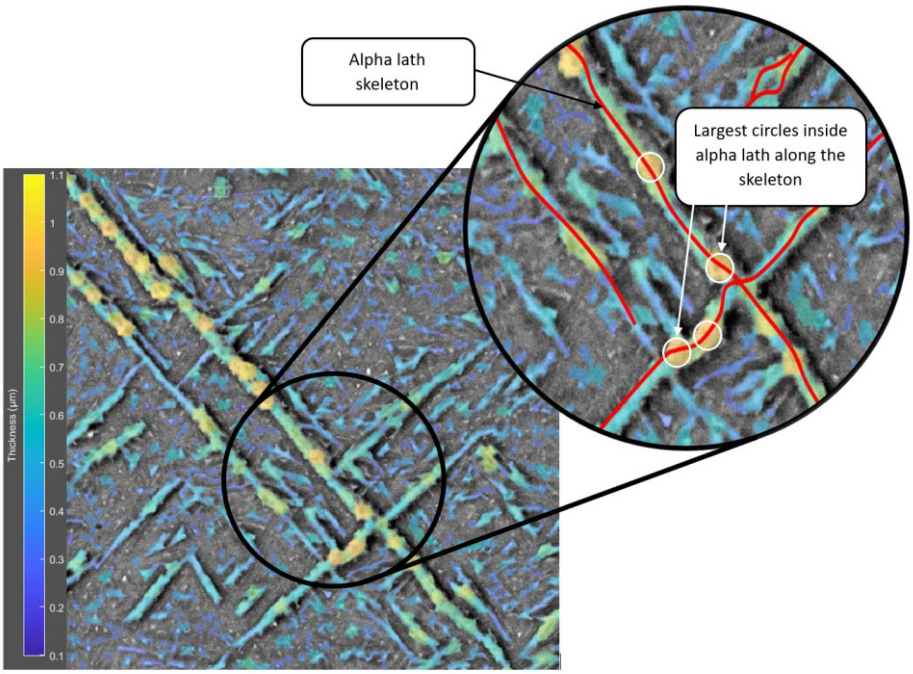

Figure 4.35 : Alpha lath thickness measuring algorithm.

4.5.3 Mercury intrusion porosimetry

Mercury Intrusion Porosimetry (MIP) is a technique used for characterizing the pore size distribution, pore volume, and porosity of solid and powder materials. Samples are placed in a cell surrounded by liquid mercury, and pressure is exerted to drive the mercury into any voids or pores within the sample bed. Larger voids and pores are filled first at lower pressure, and as the pressure is elevated, progressively smaller pores begin to fill. The volume of mercury intruded into the sample is recorded at each pressure point. This method enables the determination of the volume of mercury intruded into the sample at each specific pore diameter, providing valuable information about the material's pore structure [71].

The porosity obtained through this process uses equation (5) and requires the bulk volume of the sample and the skeletal volume of the sample as inputs. The bulk volume is calculated using equation (6), and includes the volume occupied by the pores. The skeletal volume is calculated using equation (7) and does not include the pores in the material connecting to the surface. Figure 4.36 illustrates a penetrometer diagram used in MIP, with the different variables used to calculate porosity [72].

.

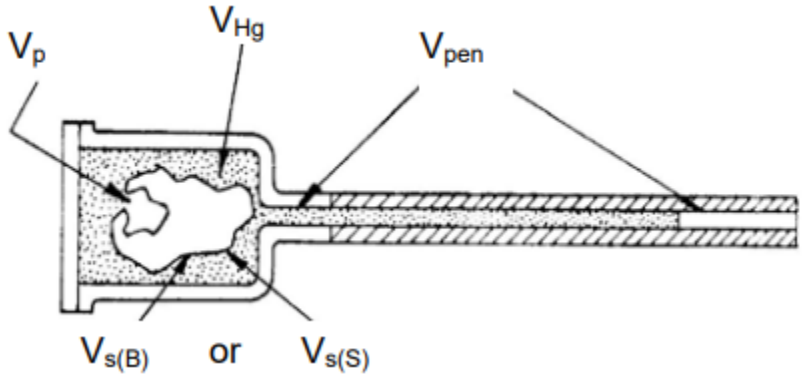

Figure 4.36 : Penetrometer diagram in MIP [72]

In equations (5) through (7), $V_{s(B)}$ is the bulk volume of the sample, $V_{s(S)}$ is the skeletal volume of the sample, V_{pen} is the penetrometer volume, V_{Hg} is the volume of mercury occupying the remaining space, and V_p is the total volume of pores filled by mercury. W_{PSHg} is the total assembly weight, W_{pen} is the penetrometer volume, W_s is the sample weight, and ρ_{Hg} is the density of mercury. All the weights are obtained prior to placing the penetrometer in the equipment for analysis. The variable V_p is obtained experimentally from the mercury entering the pores of the sample [72].

$$Porosity(\%) = \frac{V_{s(B)} - V_{s(S)}}{V_{s(B)}} \cdot 100 \tag{5}$$

$$V_{s(B)} = V_{pen} - \left[\frac{W_{PSHg} - W_{pen} - W_s}{\rho_{Hg}}\right] \tag{6}$$

$$V_{s(S)} = V_{s(B)} - V_p \tag{7}$$

The pore diameter is obtained using the Washburn equation, assuming all pores are spherical [73]. The Washburn Equation (8) is applied to establish a relationship between the applied pressure and the corresponding pore diameter.

$$r_p = \frac{2\gamma cos\theta}{p} \tag{8}$$

Where r_p is the radius of the pore, the contact angle θ for mercury is 130 degrees, p is the applied pressure, and mercury surface tension γ is 485 dyne per cm.

Mercury intrusion porosimetry (MIP) was used in this study to quantify the porosity of the fatigue samples. This method offers the advantage of capturing the porosity throughout the surface of the sample and not only through a 2D section.

The Micrometrics AutoPore 9500 V1.09 shown in Figure 4.38 was used to perform the MIP analysis. This equipment has a low-pressure port to measure larger diameter pores, and a high-pressure port for measuring smaller diameter pores. Sections of the fatigue samples were cut in four pieces, as shown in Figure 4.37, and the weight of the samples was between 1.0 and 1.5 grams. The mercury cell used has a volume of 5mL. For porosity measurements, two of the four pieces provided for each specimen were selected so that the penetrometer volume used is between 1% and 3%.

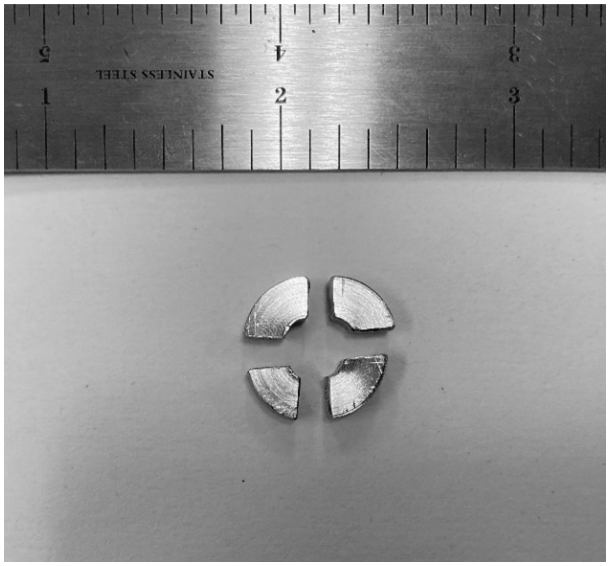

Figure 4.37 : Porosimetry samples in four pieces of 1.0g to 1.5g

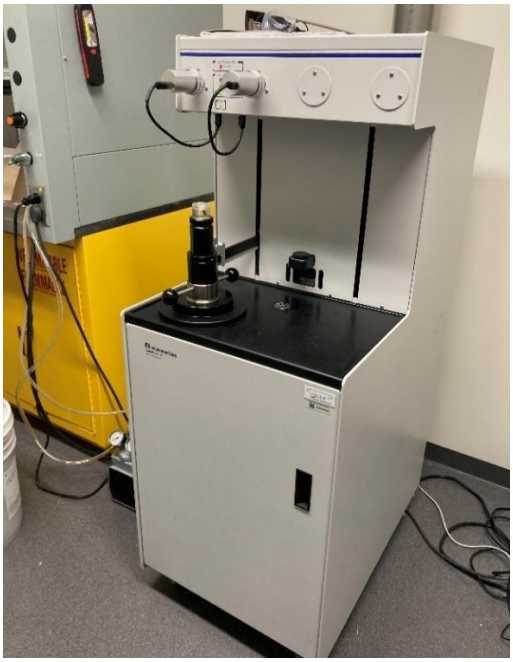

Figure 4.38 : Micrometrics AutoPore IV 9500 mercury porosimeter

The specifications for the low-pressure and high-pressure settings are presented in Table 4.2. These different settings allow for different pore sizes to be detected by the equipment.

Table 4.2 : Micrometrics AutoPore IV 9500 low-pressure and high-pressure specifications [74]

Parameters	**Low-Pressure**	**High-Pressure**
Pressure	0- 50 psia	Atmospheric pressure- 3000 psia
Resolution	0.01 psi	0.1 psi
Pore Diameter	3.6 - 360 µm	0.005 – 6 µm

Similar to optical microscopy, MIP is unsensitive to trapped powder inside defects. This implies that regions identified as LOF defects are not completely filled with mercury, and therefore, the MIP method might not accurately capture the extent of porosity in these areas. The reason for the discrepancy is that the volume of LOF defects is partly occupied by un-melted powder, resulting in an underestimation of the porosity obtained using the MIP method. MIP may not fully account for the presence of partially melted powder within LOF defects, leading to a lower estimation of porosity than methods involving a precise capture of defects like XCT scanning.

4.5.4 Electron backscatter diffraction analysis

Electron Backscatter Diffraction (EBSD) is a technique for materials characterization using a scanning electron microscope (SEM). In EBSD, the electron beam traverses the surface of a tilted (70 degrees) crystalline sample, producing diffracted electrons at each point. These electron patterns are detected and analyzed to provide information about the phase and crystallographic orientation. The technique enables a comprehensive characterization of the microstructural properties inherent to the sample [75].

EBSD was used for this study to obtain more accurate measurements of the alpha lath thickness. If the surface analysed is under etched, the value obtained for the alpha lath thickness will be smaller than its actual value. EBSD was used to obtain information about the alpha and beta phase percentage in the samples, as well as information on the prior beta grain width and their orientation.

4.5.4.1 Sample preparation

The tensile and fatigue samples were prepared for EBSD by trimming the phenolic mounts to a width of 15mm. The specimens were tilted to 70 degrees during the EBSD process, therefore the width of the specimens needed to be reduced to avoid collisions with the lens during the viewing process. The geometry of an EBSD sample and the EBSD setup are shown in Figure 4.39 and Figure 4.40, respectively.

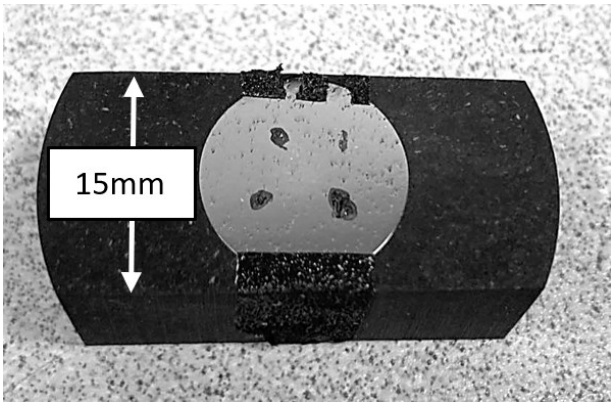

Figure 4.39: EBSD sample geometry

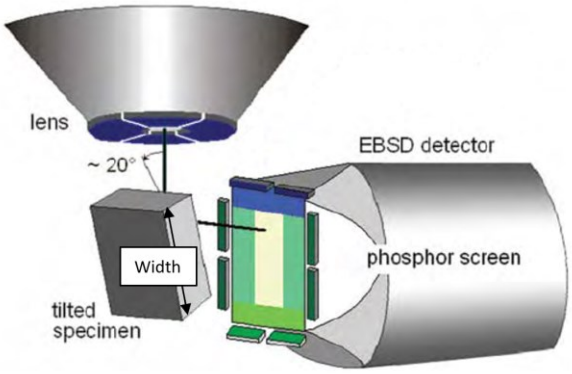

Figure 4.40: EBSD testing setup [76]

4.5.4.2 Ion milling

Ion milling is referred to as mechanical etching. This material processing technique used to remove material from a sample surface by bombarding it with a beam of charged nuclei. Energized ions forcefully displace atoms and molecules from the sample surface through momentum transfer. Ion milling is used to eliminate thin layers of material and is an important tool for sample preparation, unveiling internal structures and facilitating the examination of compositions under electron microscopes [77].

For this experiment, ion milling was performed on the Hitachi ion milling system shown in Figure 4.41. The specimen was tilted at an angle of 80 degrees with a gas flow of 0.1cm^3/min and a discharge current of 400uA. The specimens were ion milled for 20 minutes. The ion milling process is shown in Figure 4.42, and the result of ion milling highlighting the prior beta grain structure of the Ti64 EBM sample is shown in Figure 4.43.

Figure 4.41 : Hitachi ion milling system

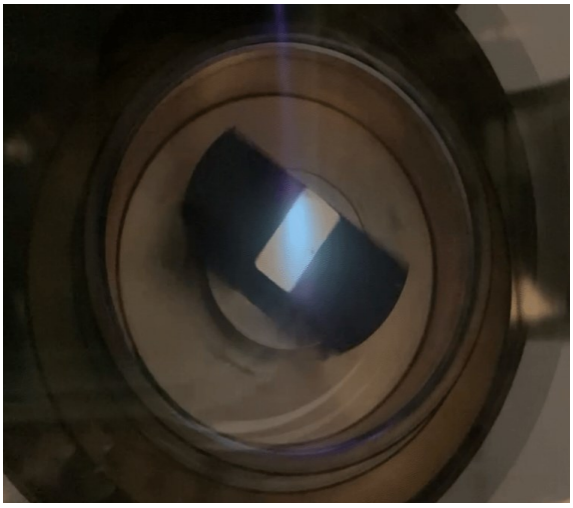

Figure 4.42 : Ion milling process in Hitachi ion milling system

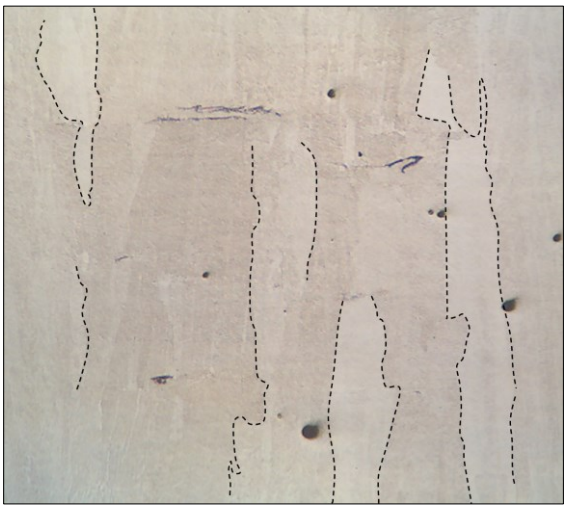

Figure 4.43 : Prior beta grains highlighted with ion milling

4.5.4.3 Specimen mounting

After ion milling, the specimens were mounted and secured on the microscope mounting plate with carbon tape and PELCO© Colloidal Graphite Isopropanol Based as shown in Figure 4.44 and Figure 4.45. Colloidal graphite is specified throughout the SEM industry as a conductive path from sample to SEM mount. The colloidal graphite was applied using a soft brush to mark the area of interest where ion milling was performed. The prepared sample is then place in the Hitachi ultra-high resolution scanning transmission electron microscope (STEM) shown in Figure 4.46.

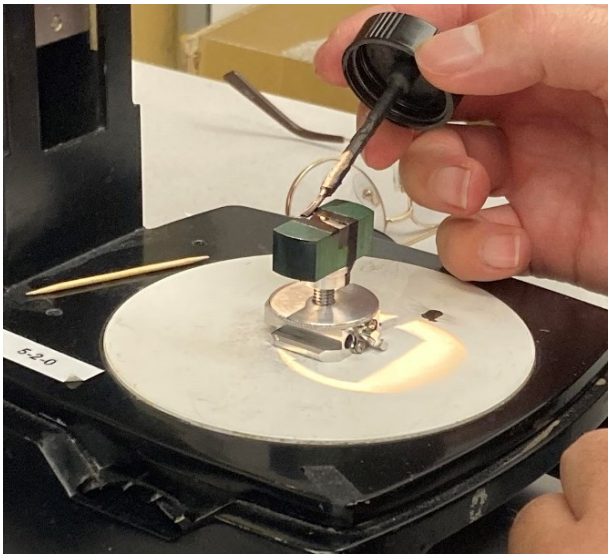

Figure 4.44 : PELCO© colloidal graphite application on ion-milled sample

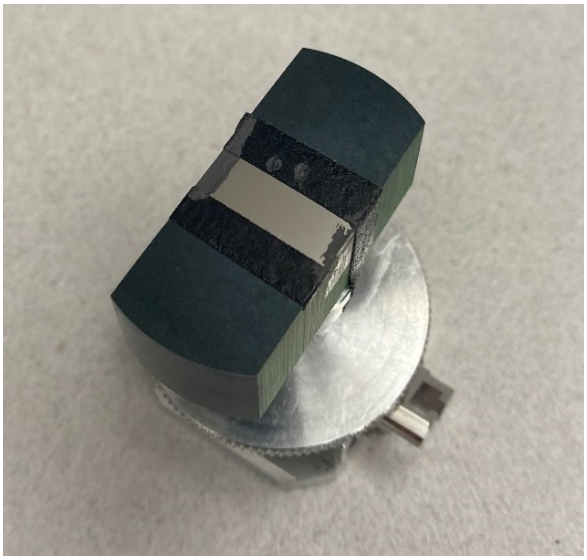

Figure 4.45 : Sample prepared for EBSD with colloidal graphite and carbon tape

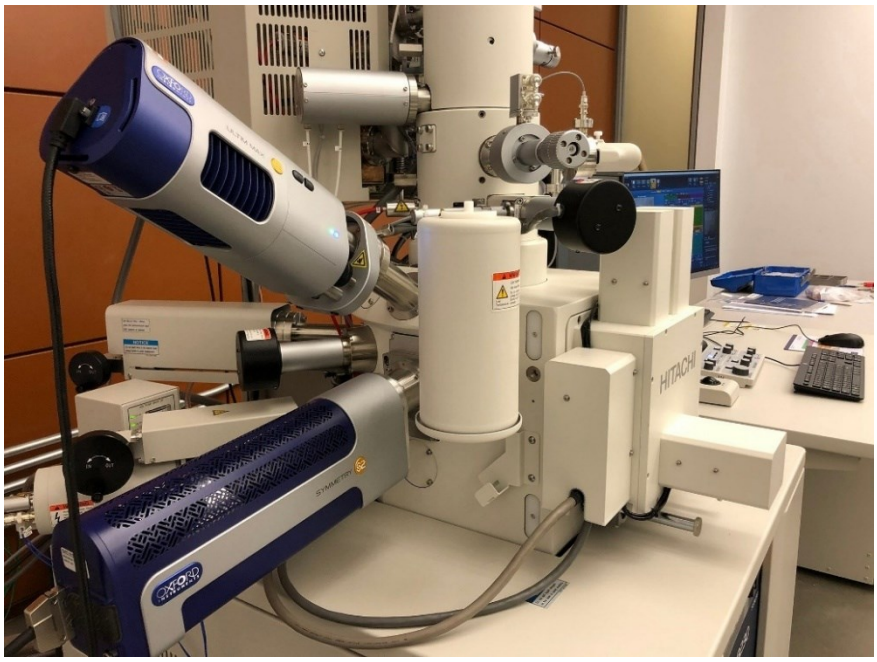

Figure 4.46 : Hitachi ultra-high resolution scanning transmission electron microscope (STEM)

4.5.4.4 Image analysis

The alpha lath thickness for the tensile and fatigue samples obtained from the Electron Backscatter Diffraction Analysis (EBDS) was obtained from the grain boundary map in Figure 4.47. MIPAR was used to perform the selection of alpha laths based on the contrast of the white grains and their darker grain boundary, and colors the grains in red, as shown in Figure 4.48. Figure 4.49 provides a visual representation of the alpha lath thickness map obtained through this method. The thickness of each grain was calculated using the MIPAR advanced thickness algorithm, mentioned in section 4.5.2.

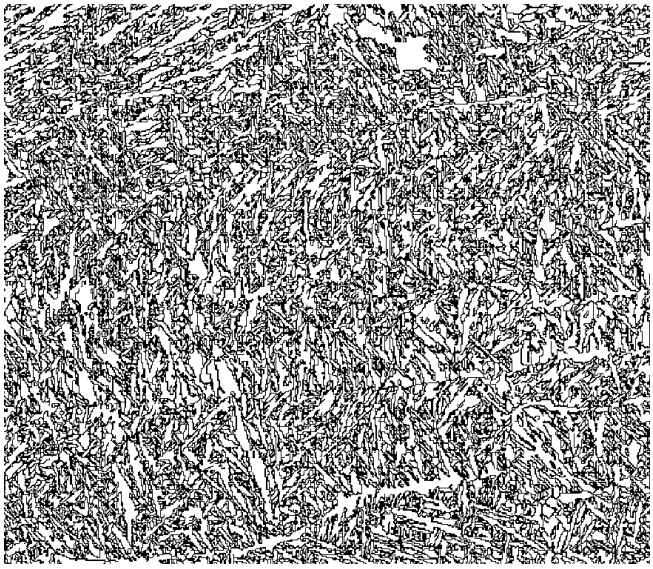

Figure 4.47 : EBSD grain boundary map.

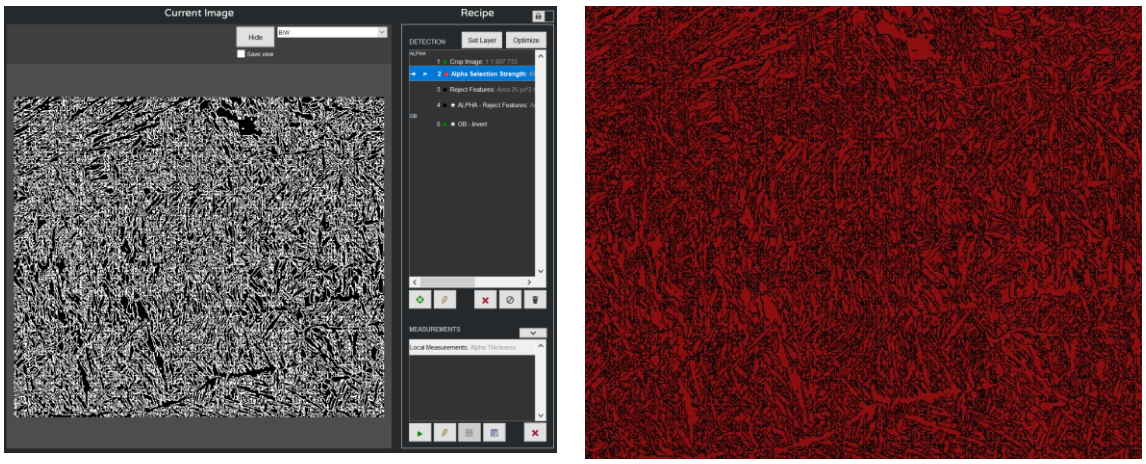

Figure 4.48 : Alpha lath recognition from grain boundary map

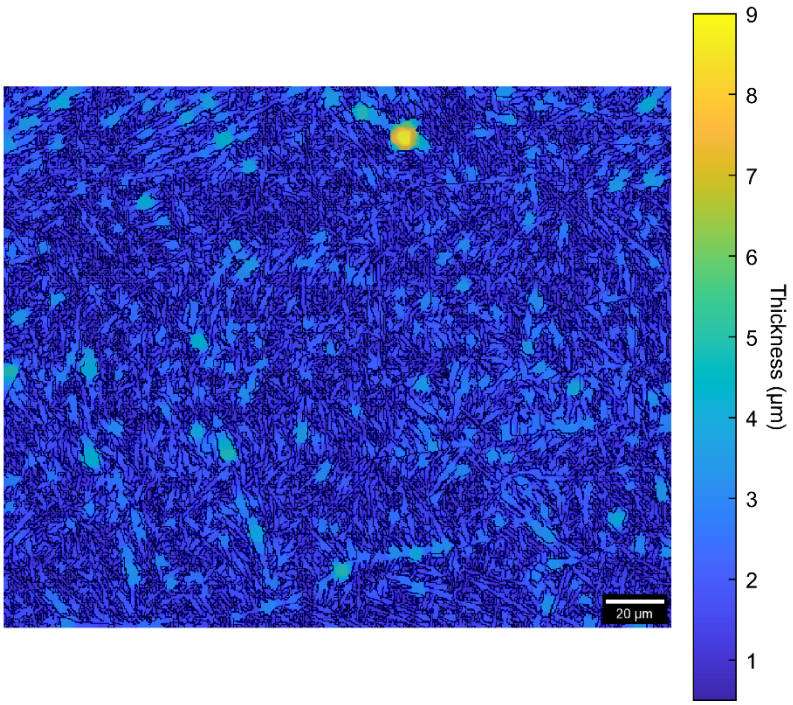

Figure 4.49 : Alpha lath thickness map obtained through MIPAR.

4.6 Mechanical properties

4.6.1 Tensile testing

Ten tensile specimens were tested according to the ASTM standard E8 [78]. The initial strain rate was set at 0.015 in/in/min. The testing machine operated in closed-loop control using the extensometer signal to determine the yield properties. The strain rate in in/min is obtained by multiplying the measured rate by the gauge length of the specimen. Once the yield properties were obtained, the strain rate was increased to 0.050 in/in/min. The extensometer is shown in Figure 4.50, and the setup of the test is shown in Figure 4.51. The Instron tensile testing system with the EBM tensile samples setup is shown in Figure 4.52.

The gips used for this experiment are Instron's manual wedge action grips. Flat serrated grips were used, capable of holding specimens up to 0.250in in thickness. This type of grip can apply holding forces up to 50kN.

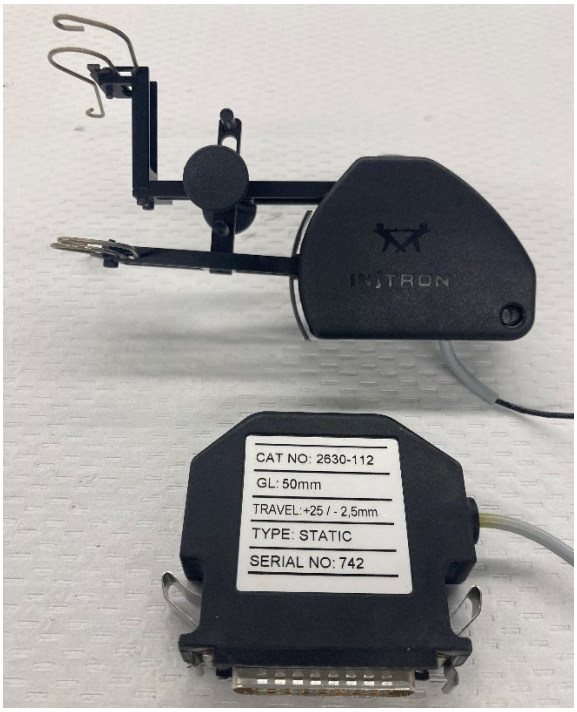

Figure 4.50: Extensometer used for tensile samples tensile testing

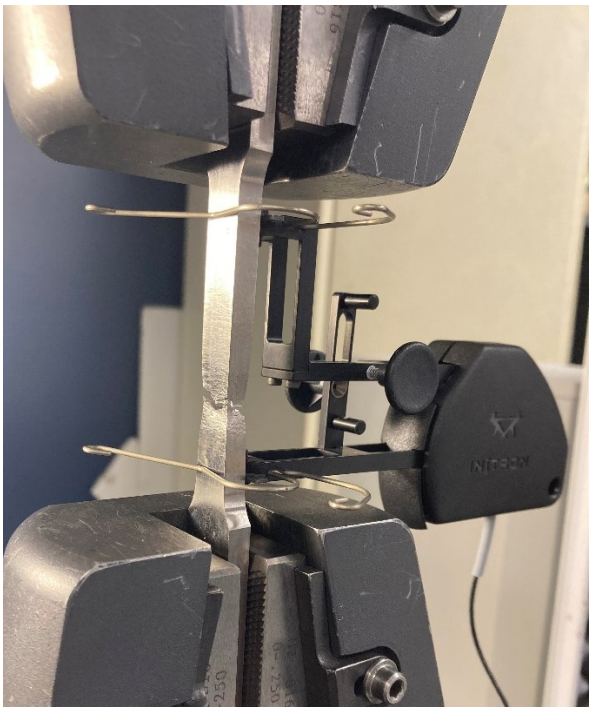

Figure 4.51: Test setup for tensile testing of tensile samples

Figure 4.52 : Tensile testing of specimens on Instron tensile testing system.

4.6.2 Hardness testing

The hardness of all 10 tensile and 24 fatigue samples was obtained using a NewAge Industries Rockwell hardness testing system as shown in Figure 4.53 and 4.54.

Figure 4.53 : Rockwell hardness testing of tensile samples

Figure 4.54 : Rockwell hardness testing of fatigue samples

The C scale was used for the Rockwell hardness testing. A load of 150kg load was applied to the specimen with a diamond tip. For each sample, 5 different readings were taken on each specimen. The readings were taken on the grips of the specimen, where the grips were not deformed by the clamping of the tensile testing.

The round fatigue specimens had the measured Rockwell hardness values corrected by adding 2 to the obtained value on the C scale. This correction is applied for specimens with a ½" outer diameter reading values between 35 and 40 HRC.

4.6.3 Initial tensile testing on fatigue samples

Before subjecting the specimens to fatigue cycling, an initial tensile test was carried out to experimentally obtain the yield strength and Young's Modulus for each of the 24 fatigue samples. The application of less than 10 pre-strain cycles at 1% strain has been demonstrated to decrease both fatigue life and data scatter in steel and aluminum [79], [80]. The samples in this study were all subjected to a small plastic pre-strain with the objective of reducing data scatter. In addition, the data obtained from the pre-strain was used to estimate the yield strength of the fatigue samples and compare them to the results obtained from the tensile samples.

The specimens were tested according to the ASTM standard E8 [78]. The strain rate was set to 0.015 in/in/min. The testing machine operated in closed-loop control using the extensometer signal for determining the yield properties. The specimens were held with Instron's mechanical wedge action tensile grips with a V-serrated pitch. The grips can hold specimens from 0.500in to 0.625in. The extensometer used has a gauge length of 25mm with a travel of 12.5mm. The extensometer and specimen setup with the grips and extensometer on the testing equipment are shown in Figure 4.55 and Figure 4.56.

The fatigue specimens were subjected to a plastic pre-strain, where the strain increased linearly at a rate of 0.015 in/in/min. The specimen was tested until a final strain rate of approximately 1.2% was obtained.

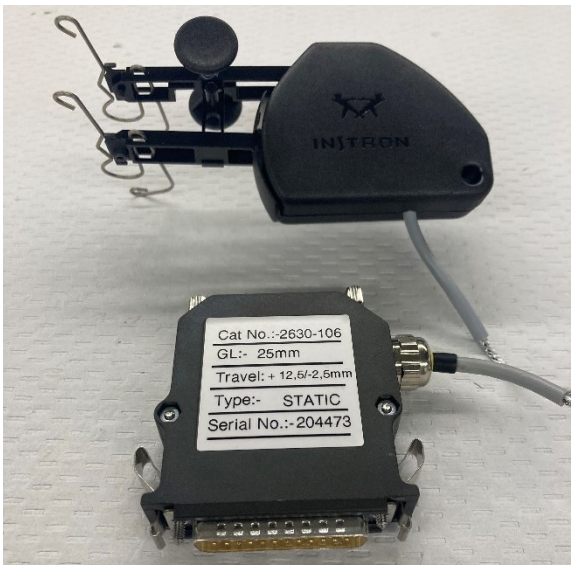

Figure 4.55 : Extensometer used for yield properties of fatigue samples

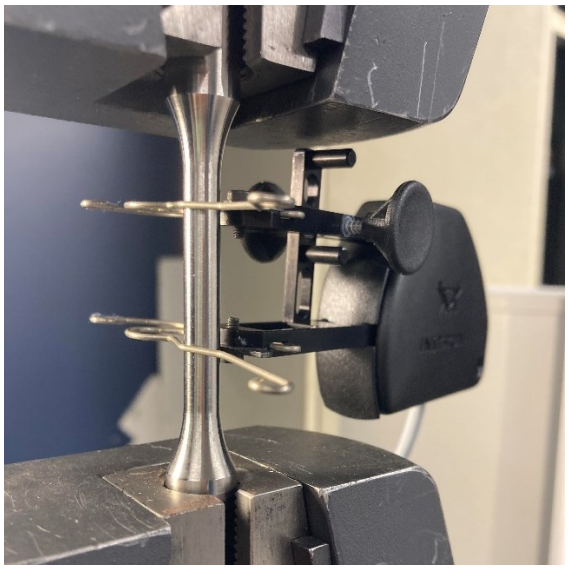

Figure 4.56 : Fatigue samples tensile testing test setup

4.6.4 Fatigue testing

A baseline curve was determined with 14 solution heat treated and aged Ti64 samples prior to testing the EBM samples. The samples used for this baseline were tested following the ASTM E466 load controlled fatigue testing guidelines, which was the same standard used for the fatigue samples [81]. A runout fatigue sample from the baseline curve testing is shown in Figure 4.57. The drawing for the baseline curve samples is provided in Appendix E. The tests were performed at frequencies between 2 and 5Hz, and the error in the stress applied was +/1 2.5MPa.

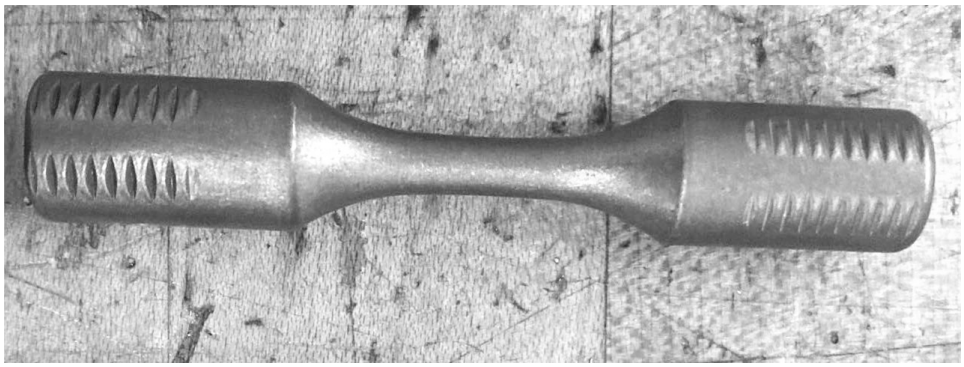

Figure 4.57 : Baseline Ti64 STA fatigue sample.

Following the baseline tests, the EBM fatigue samples were tested according to the standard ASTM E466 [81]. The baseline curve was used to get a starting point for the stress levels of the EBM fatigue samples. As the baseline curve had a maximum testing stress of 1025MPa, the starting stress for testing was 900MPa. The stress was then converted to an applied load according to the diameter of the samples. The fatigue testing hydraulic grips are shown in Figure 4.58, and the overall testing setup is shown in Figure 4.59.

Figure 4.58 : MTS hydraulic wedge grips

Figure 4.59: Fatigue testing setup on MTS hydraulic testing system

The runout criterion for the samples was set at 2 million cycles. After specimens failed under fatigue testing, their number of cycles to failure was recorded next to their respective testing stress. The broken specimens were wrapped with masking tape to have their fracture surface examined under the optical and electron microscope.

4.6.5 Fracture surface analysis

The fracture surface of each broken fatigue sample was examined using a Keyence VHX-5000 digital optical microscope shown in Figure 4.60. The contrast in color between the fatigue crack growth region and the rapid fracture region can be identified by the crack growth regions being brighter than the fracture regions. Examples of fatigue surfaces from the 30 VED and 50 VED samples are presented in Figure 4.61 and Figure 4.62. The images were captured at 30X magnification.

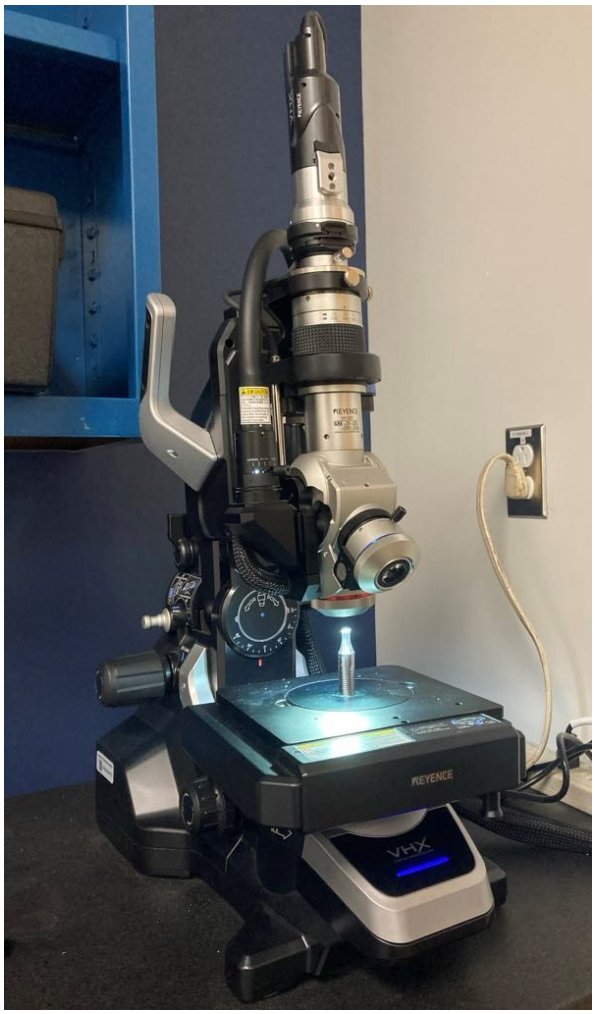

Figure 4.60: Keyence VHX-5000 digital optical microscope.

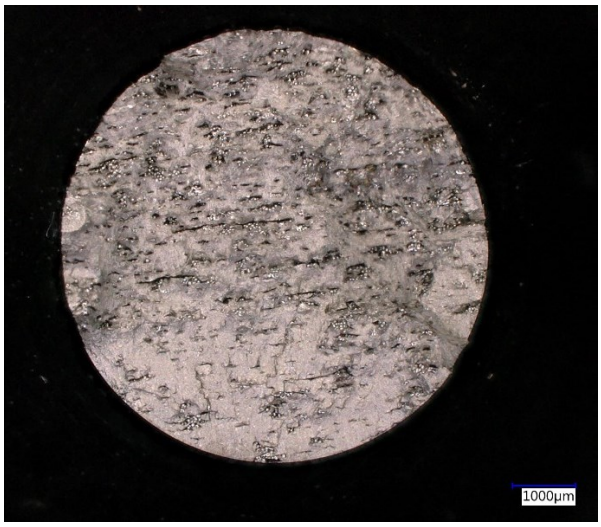

Figure 4.61 : Sample 18 fracture surface at 30X magnification.

Figure 4.62 : Sample 19 fracture surface at 30X magnification.

After the initial defects were located, the pictures were taken again at a higher magnification to isolate the critical defects causing failure. The size of the critical defect was then characterized using two different methods: Murakami's root area method and the Feret diameter method, both presented in section 2.5.

Murakami's root area method considers the size of the defect, as well as the proximity of the defect to the surface. The closer the defect is to the surface, the larger its root area is.

The Feret diameter method considers the largest distance between two parallel tangential lines in any in-plane direction of a defect [82]. As opposed to the root area method, the Feret diameter method does not take the proximity of the defect to the surface into account. The image processing software Image J was used to determine both the Feret diameter and the root area of the defects.

4.6.6 Energy-dispersive x-ray spectroscopy

Energy Dispersive X-ray Spectrometry (EDS) is a method used to analyze the elemental composition of materials in a Scanning Electron Microscope (SEM). When a sample is exposed to an electron beam in a vacuum, the interaction generates electrons, X-rays, and light. These signals can be utilized to examine microstructure, composition, and crystal structure [83]. The microscope voltage was set to 15kV, which is the minimum recommended voltage for EDS. The accelerating voltage influences the interaction volume of the sample, as depicted in Figure 4.63.

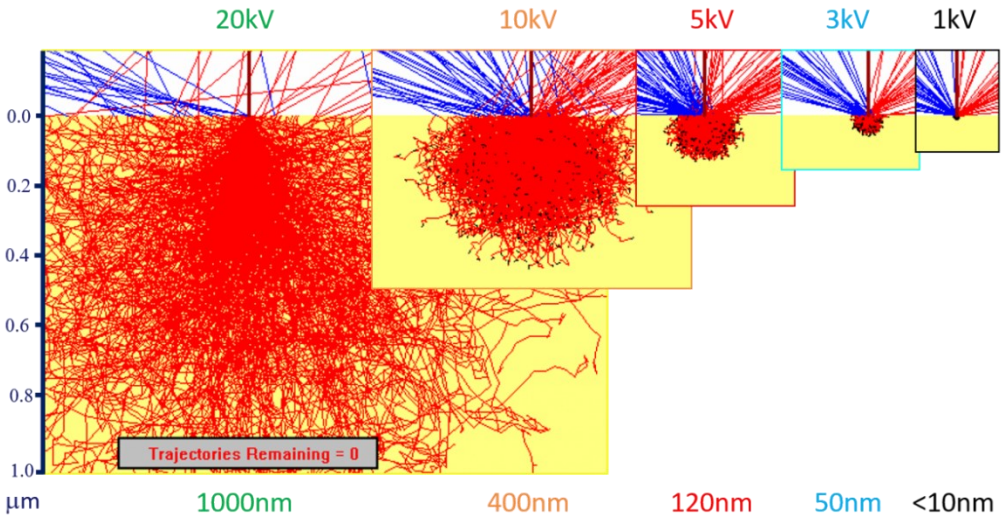

Figure 4.63 : Energy dispersive x-ray spectroscopy interaction volume according to accelerating voltage [84].

Prior to EDS, the samples were placed in an ultrasonic bath with alcohol to remove any residue from the fracture surface. The fracture surfaces of the fatigue samples were then placed in a scanning electron microscope for EDS analysis. The intent was to check the sample fracture surface for oxide contamination. An example of fatigue sample #5 undergoing EDS analysis is shown in Figure 4.64. The spectrum points shown indicate the points of analysis for elemental composition at various locations on and around the defect which had caused the fatigue failure.

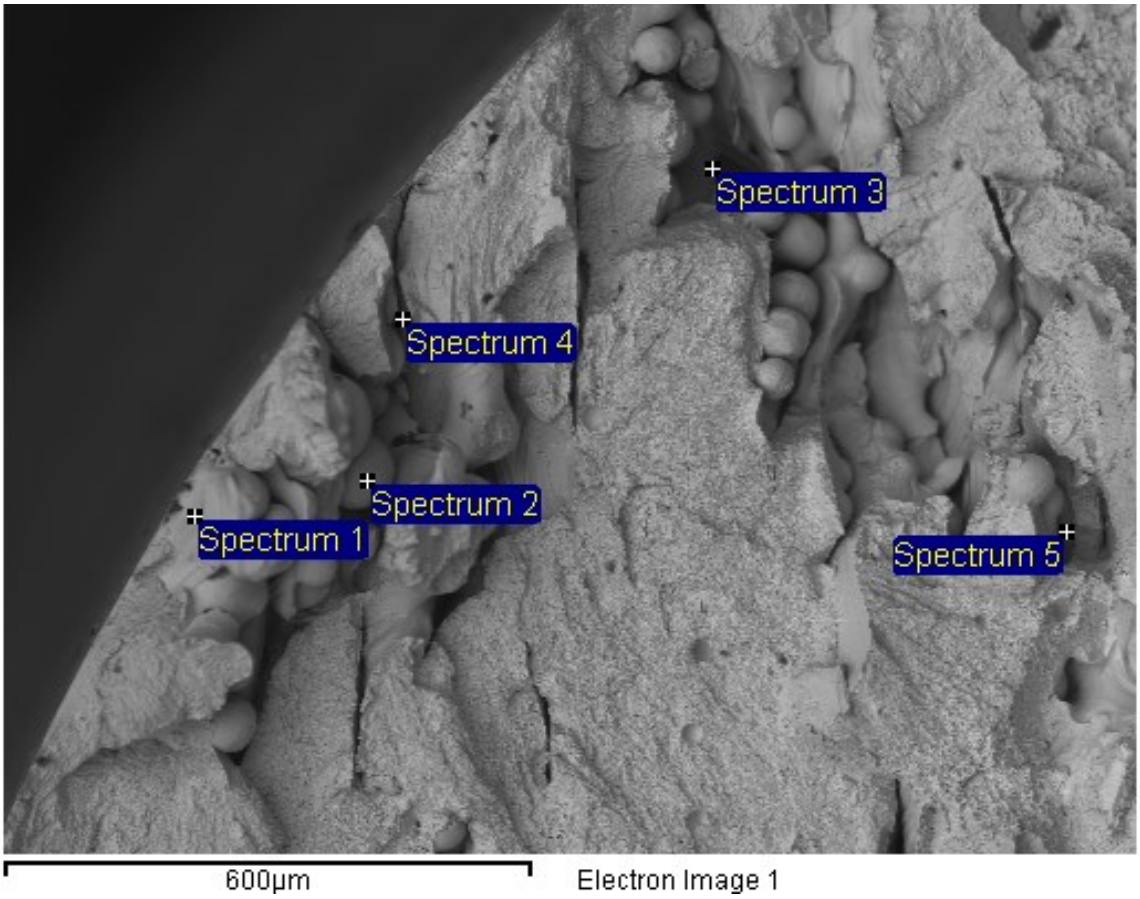

Figure 4.64 : Fatigue sample 5 EDS using points of analysis.

Chapter 5 Results and discussion

The following chapter presents the results obtained for the VED cubes, the tensile specimens, and the fatigue specimens, as well as a discussion on how the results compare to literature.

5.1 Microstructure analysis

5.1.1 Volumetric energy density cubes microstructure

5.1.1.1 Top print surface visual inspection for porosity

Results

Upon examining the upper surfaces of the VED cubes, preliminary observations regarding sample porosity can be discerned. Figure 5.1 provides a visual representation, revealing that cubes 10, 15, 20, and 25 exhibit rough top surfaces, indicative of high porosity. In contrast, samples 26-30 present notably smoother surfaces, suggesting lower porosity. The rough surfaces are highlighted by red circles in Figure 5.1, while the smoother surfaces are identified by green circles.

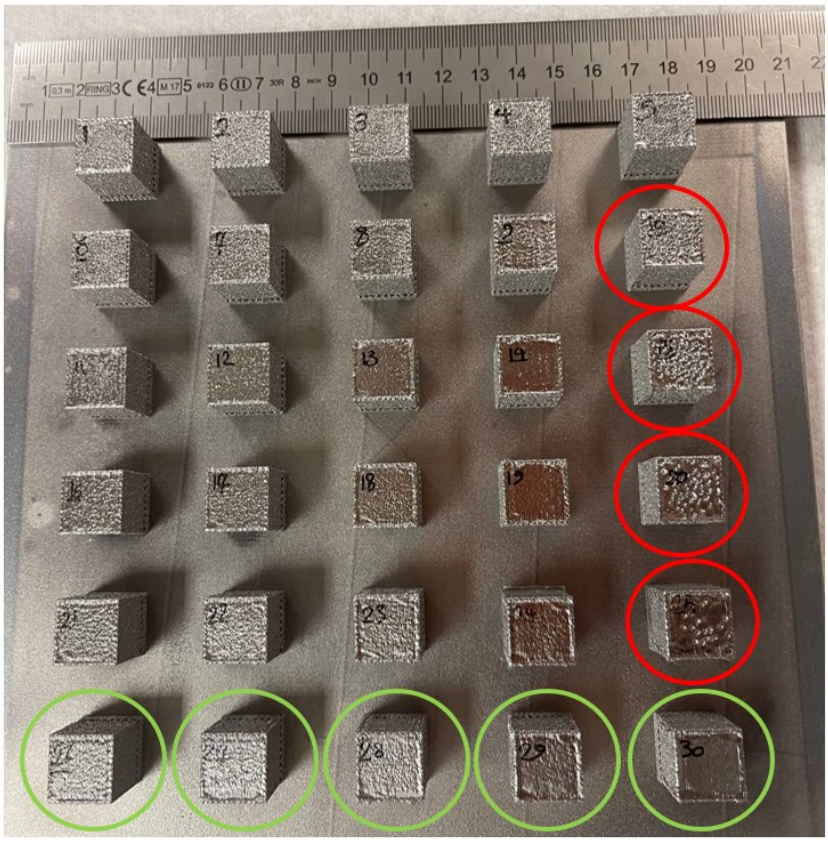

Figure 5.1 : VED cubes top surface inspection.

Discussion

Ranking cubes with moderate porosity on their print surfaces (not denoted by red or green circles in Figure 5.1) relative to each other posed challenges. A viable approach to rate the porosity of the top surfaces would involve recording surface roughness through microscopy or employing a contact point surface roughness tester. This type of testing was not within the scope of the current study, however, could be considered for future investigations. Such an investigation would be useful for providing a more detailed analysis of surface characteristics and aiding in the accurate ranking of cubes in terms of porosity without the need to prepare the samples for metallography with mounting and polishing.

5.1.1.2 Optical Microscopy

5.1.1.2.1 Types of defects

Results

The identification of defects in the VED cubes followed the method outlined in Section 4.5.1. Two types of LOF defects were identified: intertrack and interlayer lack of fusion defects. Figure 5.2 depicts both types of defects: the interlayer LOF are circled in red, and the intertrack LOF are circled in blue for VED Cube 10 in the ZX plane at 50X magnification, with positive Z being the build direction. This VED cube was built using a scan speed of 9800mm/s and a beam current of 25.5 mA.

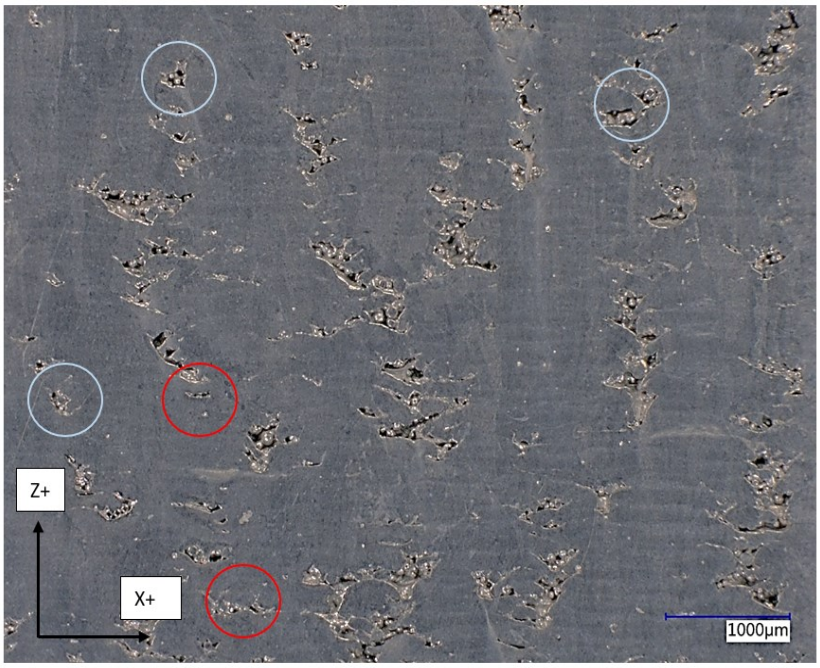

Figure 5.2 : VED cube 10 interlayer and intertrack lack of fusion.

Figure 5.3 shows the surface of VED Cube 8 in the ZX plane at 50X magnification, with positive Z being the build direction. This cube was manufactured using a scan speed of 6000 mm/s and a beam current of 15 mA. In comparison to VED Cube 10, this parameter combination yields only interlayer type LOF defects.

Figure 5.3 : VED cube 8 interlayer lack of fusion.

Figure 5.4 presents the surface of VED cube 27 in the Z-X plane at 50X magnification, with positive Z being the build direction. This cube was manufactured using a scan speed of 2800 mm/s, and the beam current was set to 11.7 mA. This parameter combination yields gas porosity defects from trapped gas within the initial powder particles.

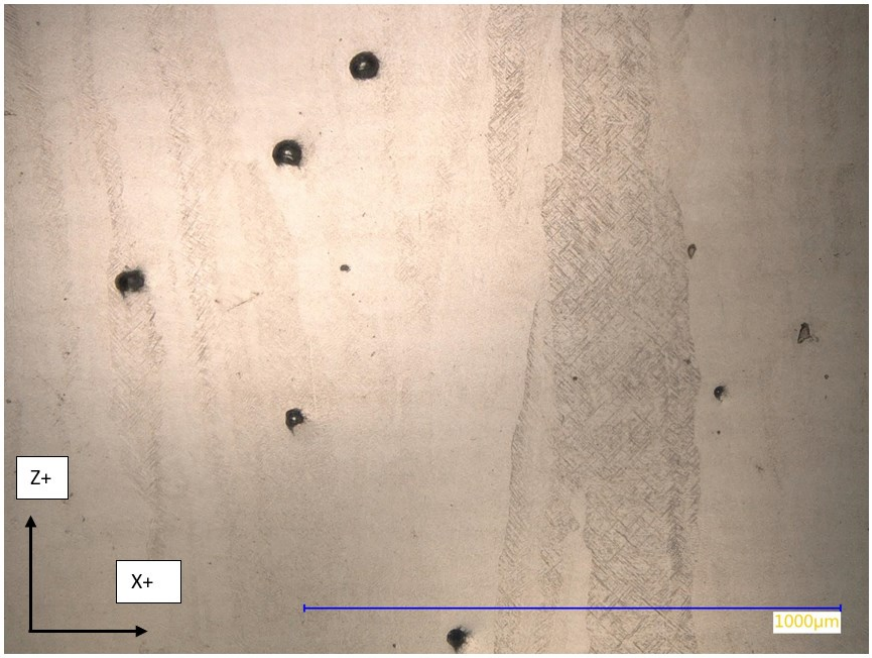

Figure 5.4 : VED cube 27 gas porosity.

Discussion

Gas pores exclusively characterize the surface defects observed on Cube 27, chosen as a representative example for 50VED. Similarly, Cubes 26 and 28-30 also exhibit only gas porosity defects. The creation of these defects is inherent to the Electron Beam Melting (EBM) process, originating from trapped gas within gas-atomized powder particles. This implies that the selection of process parameters for the 50 J/mm³ VED cubes was performed to ensure uniform melting of all particles, thereby avoiding Lack of Fusion (LOF) defects.

In contrast, Cubes 8 and 10, both printed with a Volumetric Energy Density (VED) of 30 J/mm³, manifest different types of defects. This highlights the impact of individual print parameters on the overall print quality. For VED cube 10, adjusting the line offset (originally 0.1mm) and layer thickness (originally 0.05mm) could allow an increased overlap in the melt pool between melt tracks and layers. Alternatively, as only interlayer defects are present in VED cube 8 with this parameter combination, reducing the initially selected layer thickness of 0.05mm might increase the overlap between melt pools within layers and allow for a better print quality. All 30 J/mm^3 VED cubes have some form of LOF defect, meaning one or more parameters need adjustment to increase the overlaps between the melt pool.

5.1.1.2.2 Porosity quantification

Results

Figure 5.5 shows the highlighted gas pores from VED Cube 27. The methodology used to identify the pores and defects on the VED cubes is presented in Section 4.5.1. The calculated area for the pores is compared to the total area of the picture to obtain a value for porosity in the form of percentage.

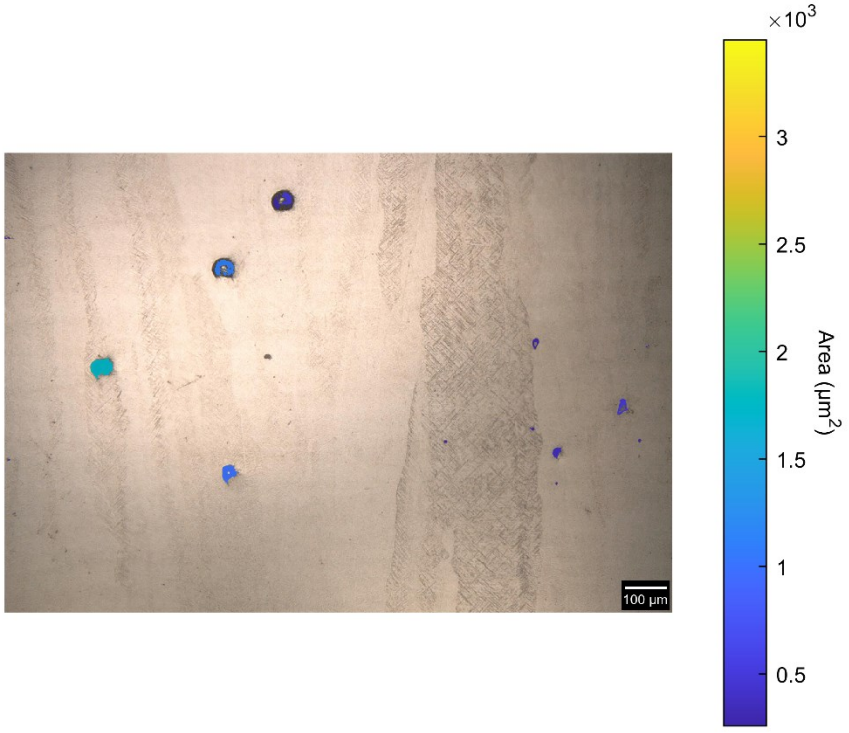

Figure 5.5 : Calculation of gas pore area with MIPAR.

Table 5.1 summarizes the porosity levels of the VED cubes determined using optical microscopy. The method to determine this porosity is based on one photograph of the sample. This approach provides a capture of the porosity at one specific area in the sample but does not provide a value for overall porosity. All the micrographs and porosity distributions for the VED cubes are presented in Appendix H. Figure 5.6 to Figure 5.11 present an example of the pore area distribution obtained using MIPAR for the 25VED to 50VED samples. The width of the columns for the 25VED, 30VED, 35VED, 40VED, 45VED, and 50VED samples are 2500µm^2, 2500µm^2, 2000µm^2, 2000µm^2, 1000µm^2, and 1250µm^2, respectively.

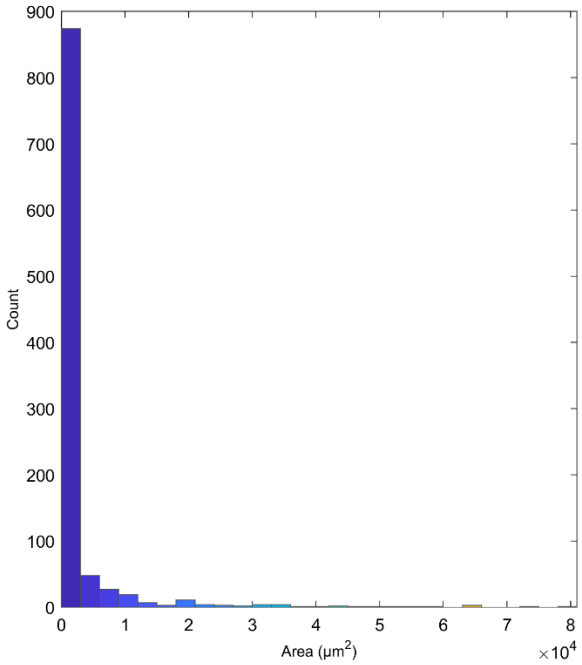

Figure 5.6 : VED cube sample 1 porosity area distribution for 25 VED.

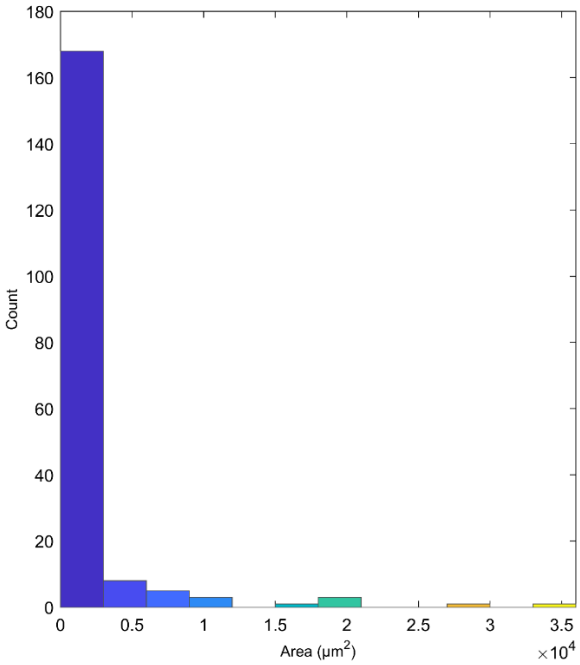

Figure 5.7 : VED cube sample 8 porosity area distribution for 30 VED.

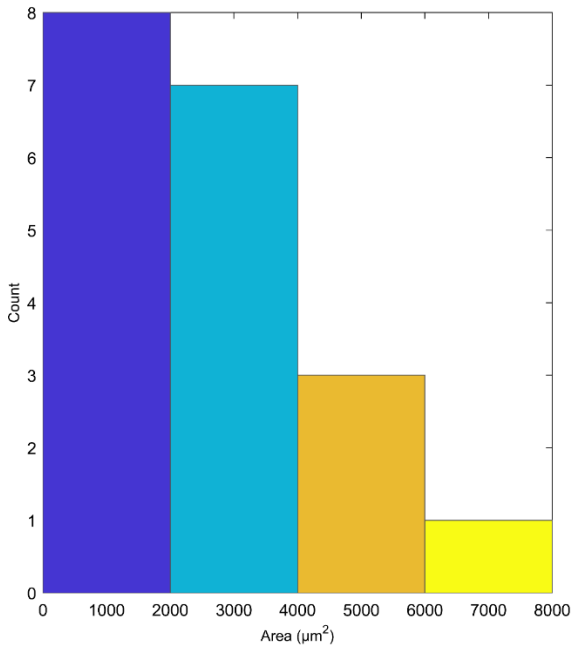

Figure 5.8 : VED cube sample 13 porosity area distribution for 35 VED.

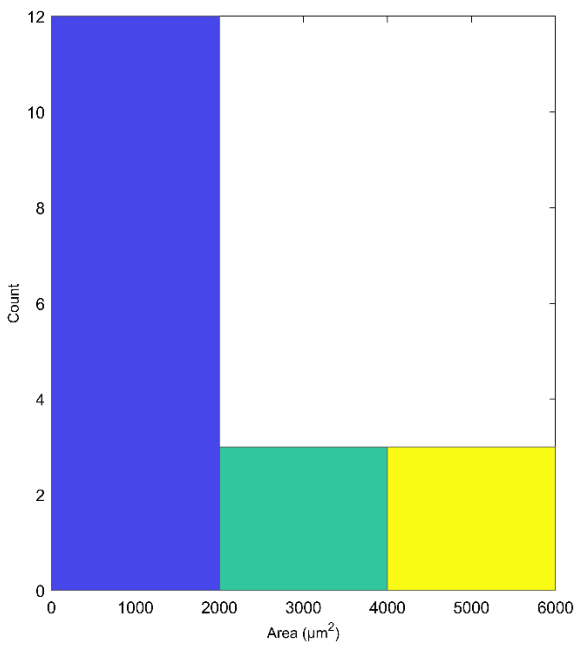

Figure 5.9 : VED cube sample 17 porosity area distribution for 40 VED.

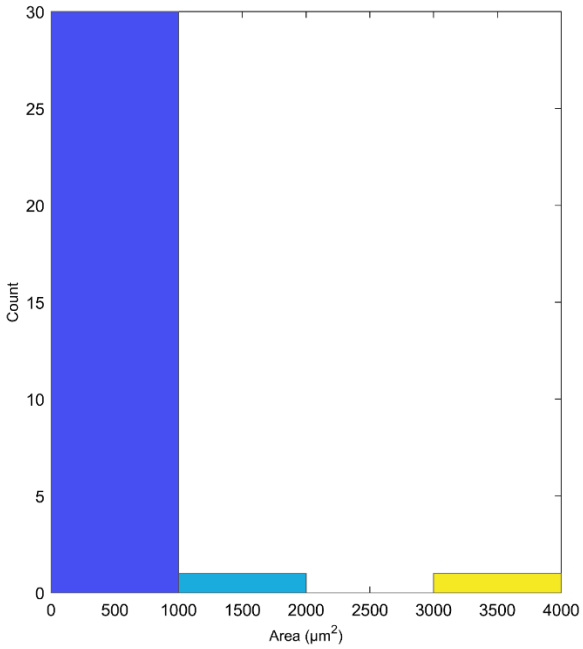

Figure 5.10 : VED cube sample 22 porosity area distribution for 45 VED.

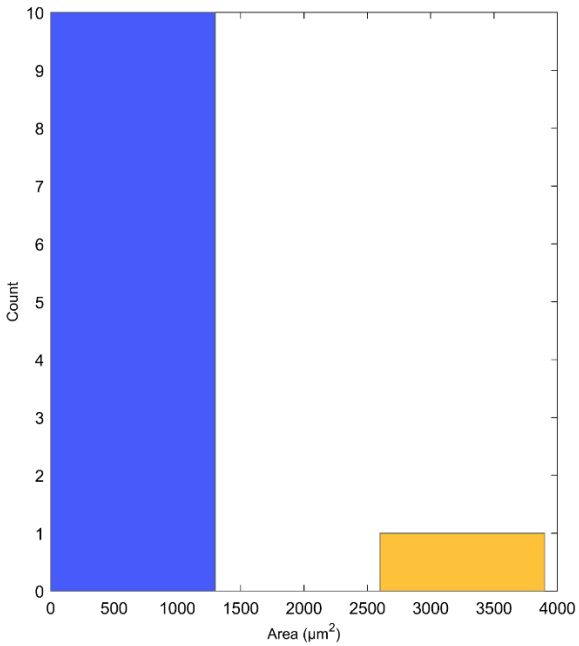

Figure 5.11 : VED cube sample 29 porosity area distribution for 50 VED.

Table 5.1 : VED Cubes Optical Microscopy Porosity

Test No.	Focus Offset [mA]	Speed [mm/s]	Speed [m/s]	Beam Current [mA]	Line offset (mm)	Lateral speed (mm/s)	Line Energy [J/mm]	Volumetric Energy [J/mm^3]	Beam Power (Watt)	Image area (um^2)	Pores Area (um^2)	Porosity (%)
Cube 1	6	5100	5.1	10.6	0.1	34.0	0.12	24.9	636	2.88E+07	2.86E+06	9.91%
Cube 2	6	6700	6.7	14.0	0.1	44.7	0.13	25.1	840	2.88E+07	2.14E+06	7.42%
Cube 3	6	8400	8.4	17.5	0.1	56.0	0.13	25.0	1050	2.88E+07	3.40E+06	11.78%
Cube 4	6	9800	9.8	20.4	0.1	65.3	0.12	25.0	1224	2.88E+07	2.09E+06	7.25%
Cube 5	6	11500	11.5	24.0	0.1	76.7	0.13	25.0	1440	2.88E+07	3.84E+06	13.32%
Cube 6	6	2800	2.8	7.0	0.1	18.7	0.15	30.0	420	2.88E+07	2.61E+06	9.04%
Cube 7	6	4600	4.6	11.5	0.1	30.7	0.15	30.0	690	2.88E+07	1.10E+06	3.81%
Cube 8	6	6000	6.0	15.0	0.1	40.0	0.15	30.0	900	2.71E+07	3.63E+05	1.34%
Cube 9	6	7600	7.6	19.0	0.1	50.7	0.15	30.0	1140	2.88E+07	4.85E+05	1.68%
Cube 10	6	9800	9.8	24.5	0.1	65.3	0.15	30.0	1470	2.88E+07	5.15E+06	17.84%
Cube 11	6	2400	2.4	7.0	0.1	16.0	0.18	35.0	420	2.88E+07	1.49E+06	5.18%
Cube 12	6	4000	4.0	11.7	0.1	26.7	0.18	35.1	702	2.88E+07	3.66E+05	1.27%
Cube 13	6	5100	5.1	14.9	0.1	34.0	0.18	35.1	894	1.75E+06	5.19E+04	2.97%
Cube 14	6	6900	6.9	20.1	0.1	46.0	0.17	35.0	1206	1.75E+06	6.86E+04	3.93%
Cube 15	6	8600	8.6	25.1	0.1	57.3	0.18	35.0	1506	2.88E+07	3.08E+06	10.67%
Cube 16	6	2100	2.1	7.0	0.1	14.0	0.20	40.0	420	2.88E+07	7.81E+05	2.71%
Cube 17	6	3400	3.4	11.3	0.1	22.7	0.20	39.9	678	1.75E+06	3.46E+04	1.98%
Cube 18	6	4500	4.5	15.0	0.1	30.0	0.20	40.0	900	1.75E+06	3.38E+04	1.94%
Cube 19	6	6000	6.0	20.0	0.1	40.0	0.20	40.0	1200	1.75E+06	3.32E+03	0.19%
Cube 20	6	7500	7.5	25.0	0.1	50.0	0.20	40.0	1500	2.88E+07	2.16E+06	7.49%
Cube 21	6	1900	1.9	7.1	0.1	12.7	0.22	44.8	426	1.75E+06	6.52E+03	0.37%
Cube 22	6	3100	3.1	11.6	0.1	20.7	0.22	44.9	696	1.75E+06	8.11E+03	0.46%
Cube 23	6	4000	4.0	15.0	0.1	26.7	0.23	45.0	900	1.75E+06	2.84E+03	0.16%
Cube 24	6	5300	5.3	19.9	0.1	35.3	0.23	45.1	1194	1.75E+06	1.29E+03	0.07%
Cube 25	6	6700	6.7	25.1	0.1	44.7	0.22	45.0	1506	2.88E+07	1.81E+06	6.29%
Cube 26	6	1700	1.7	7.1	0.1	11.3	0.25	50.1	426	1.75E+06	9.37E+02	0.05%
Cube 27	6	2800	2.8	11.7	0.1	18.7	0.25	50.1	702	1.75E+06	5.89E+03	0.34%
Cube 28	6	3600	3.6	15.0	0.1	24.0	0.25	50.0	900	1.75E+06	4.68E+03	0.27%
Cube 29	6	4800	4.8	20.0	0.1	32.0	0.25	50.0	1200	1.75E+06	5.86E+03	0.34%
Cube 30	6	6000	6.0	25.0	0.1	40.0	0.25	50.0	1500	1.75E+06	3.55E+03	0.20%

Discussion

Cubes 19, 21-24, and 26 through 30 all have porosities lower than 1% when measured using the optical microscopy method. These cubes have a very uniform top print surface, as shown on Figure 5.1. Cubes 10, 15, 20 and 25, however, all have very rough top surfaces after printing. This results in a high porosity level obtained using the optical microscopy method with porosities of 17.84%, 10.67%, 7.49% and 6.29%, respectively. Cubes 10, 15, 20 and 25 with high porosities are located at the extremity of the build plate. It is possible that the angle of the beam reaching these areas contributed to the uneven print.

The range of the distributions for the 25VED and 30 VED cubes is greater than the ranges for the 35 VED to 50VED cubes. This could be attributed to the LOF defects present in the lower VED samples, which contain larger outlying defects, and a majority of smaller LOF defects. Moreover, the frequency of the porosity is lower in the 35VED to 50VED samples. The LOF defects are smaller is size and have less occurrences in the 40VED samples. Cubes with a 45VED and 50VED setting contain gas porosity defects, which are very regular in size. This could explain the narrower range of porosity defects areas obtain through the MIPAR image analysis. The frequency of these types of defects is also smaller than for LOF defects present in cubes with a lower VED.

5.1.1.3 Scanning electron microscopy

Results

The alpha lath thickness values for selected VED cubes are presented in Table 5.2. The alpha lath thickness for these specimens was measured using a scanning electron microscope, following the methodology outlined in Section 4.5.2. Cubes 8 and 29, highlighted in gray in Table 5.2, had process parameters which were used for the fabrication of the tensile and fatigue specimens, with Cube 8 representing 30 VED and Cube 29 representing 50 VED. All the SEM micrographs for the alpha lath thickness measurements are presented in Appendix I.

Table 5.2 : Alpha Lath Thickness for VED Cubes through Scanning Electron Microscopy

Test No.	Focus Offset [mA]	Speed [mm/s]	Speed [m/s]	Beam Current [mA]	Line offset (mm)	Lateral speed (mm/s)	Line Energy [J/mm]	Volumetric Energy [J/mm^3]	Beam Power (Watt)	Average α lath thickness (µm)	Standard Deviation α lath thickness (µm)
Cube 1	6	5100	5.1	10.6	0.1	34.0	0.12	24.9	636	NA	NA
Cube 2	6	6700	6.7	14.0	0.1	44.7	0.13	25.1	840	NA	NA
Cube 3	6	8400	8.4	17.5	0.1	56.0	0.13	25.0	1050	NA	NA
Cube 4	6	9800	9.8	20.4	0.1	65.3	0.12	25.0	1224	NA	NA
Cube 5	6	11500	11.5	24.0	0.1	76.7	0.13	25.0	1440	NA	NA
Cube 6	6	2800	2.8	7.0	0.1	18.7	0.15	30.0	420	NA	NA
Cube 7	6	4600	4.6	11.5	0.1	30.7	0.15	30.0	690	0.65	0.18
Cube 8	6	6000	6.0	15.0	0.1	40.0	0.15	30.0	900	0.73	0.15
Cube 9	6	7600	7.6	19.0	0.1	50.7	0.15	30.0	1140	0.71	0.17
Cube 10	6	9800	9.8	24.5	0.1	65.3	0.15	30.0	1470	NA	NA
Cube 11	6	2400	2.4	7.0	0.1	16.0	0.18	35.0	420	NA	NA
Cube 12	6	4000	4.0	11.7	0.1	26.7	0.18	35.1	702	NA	NA
Cube 13	6	5100	5.1	14.9	0.1	34.0	0.18	35.1	894	0.73	0.16
Cube 14	6	6900	6.9	20.1	0.1	46.0	0.17	35.0	1206	NA	NA
Cube 15	6	8600	8.6	25.1	0.1	57.3	0.18	35.0	1506	NA	NA
Cube 16	6	2100	2.1	7.0	0.1	14.0	0.20	40.0	420	NA	NA
Cube 17	6	3400	3.4	11.3	0.1	22.7	0.20	39.9	678	0.64	0.15
Cube 18	6	4500	4.5	15.0	0.1	30.0	0.20	40.0	900	NA	NA
Cube 19	6	6000	6.0	20.0	0.1	40.0	0.20	40.0	1200	NA	NA
Cube 20	6	7500	7.5	25.0	0.1	50.0	0.20	40.0	1500	NA	NA
Cube 21	6	1900	1.9	7.1	0.1	12.7	0.22	44.8	426	0.80	0.19
Cube 22	6	3100	3.1	11.6	0.1	20.7	0.22	44.9	696	0.66	0.18
Cube 23	6	4000	4.0	15.0	0.1	26.7	0.23	45.0	900	0.75	0.17
Cube 24	6	5300	5.3	19.9	0.1	35.3	0.23	45.1	1194	0.78	0.19
Cube 25	6	6700	6.7	25.1	0.1	44.7	0.22	45.0	1506	NA	NA
Cube 26	6	1700	1.7	7.1	0.1	11.3	0.25	50.1	426	0.66	0.11
Cube 27	6	2800	2.8	11.7	0.1	18.7	0.25	50.1	702	0.74	0.21
Cube 28	6	3600	3.6	15.0	0.1	24.0	0.25	50.0	900	0.72	0.17
Cube 29	6	4800	4.8	20.0	0.1	32.0	0.25	50.0	1200	0.76	0.17
Cube 30	6	6000	6.0	25.0	0.1	40.0	0.25	50.0	1500	0.65	0.15

Discussion

Certain cubes exhibiting extensive porosity lacked accurate readings for their alpha lath thickness due to challenges in achieving proper polishing. The polishing process was hindered by the entrapment of polishing compound in large pores, leading to significant scratches on the sample surfaces. Samples labeled as "NA" in Table 5.2 indicate instances where porosity rendered them unsuitable for analysis with the available resources.

For the 30 VED cubes, the average alpha lath thickness among three cubes was 0.70μm, with a standard deviation of 0.03μm. Similarly, the 50 VED cubes yielded an average alpha lath thickness among five cubes of 0.71μm, with a standard deviation of 0.04μm. There is no statistically significant difference in lath thickness between the 30 VED and 50 VED samples. This observation diverges from expectations based on the existing literature, which suggests that higher VED should result in increased energy input, leading to thicker laths. However, Moritz et al. [37] emphasize the unique influence of individual parameters on the resulting microstructure of printed materials. To induce a statistically significant change in alpha lath, careful consideration and individual variation of each parameter's sensitivity may be required to discern their impact on microstructural variation, as highlighted in this experiment.

5.1.2 Tensile samples microstructure

5.1.2.1 Optical microscopy

Results

Figure 5.12 and Figure 5.13 illustrate the types of defects present in the tensile samples under optical microscopy at 200X magnification. Figure 5.12 is a tensile sample with 30 VED (sample 1), while Figure 5.13 is a tensile sample with 50 VED (sample 6). The build direction for these samples is along the Z+ direction of the figure.

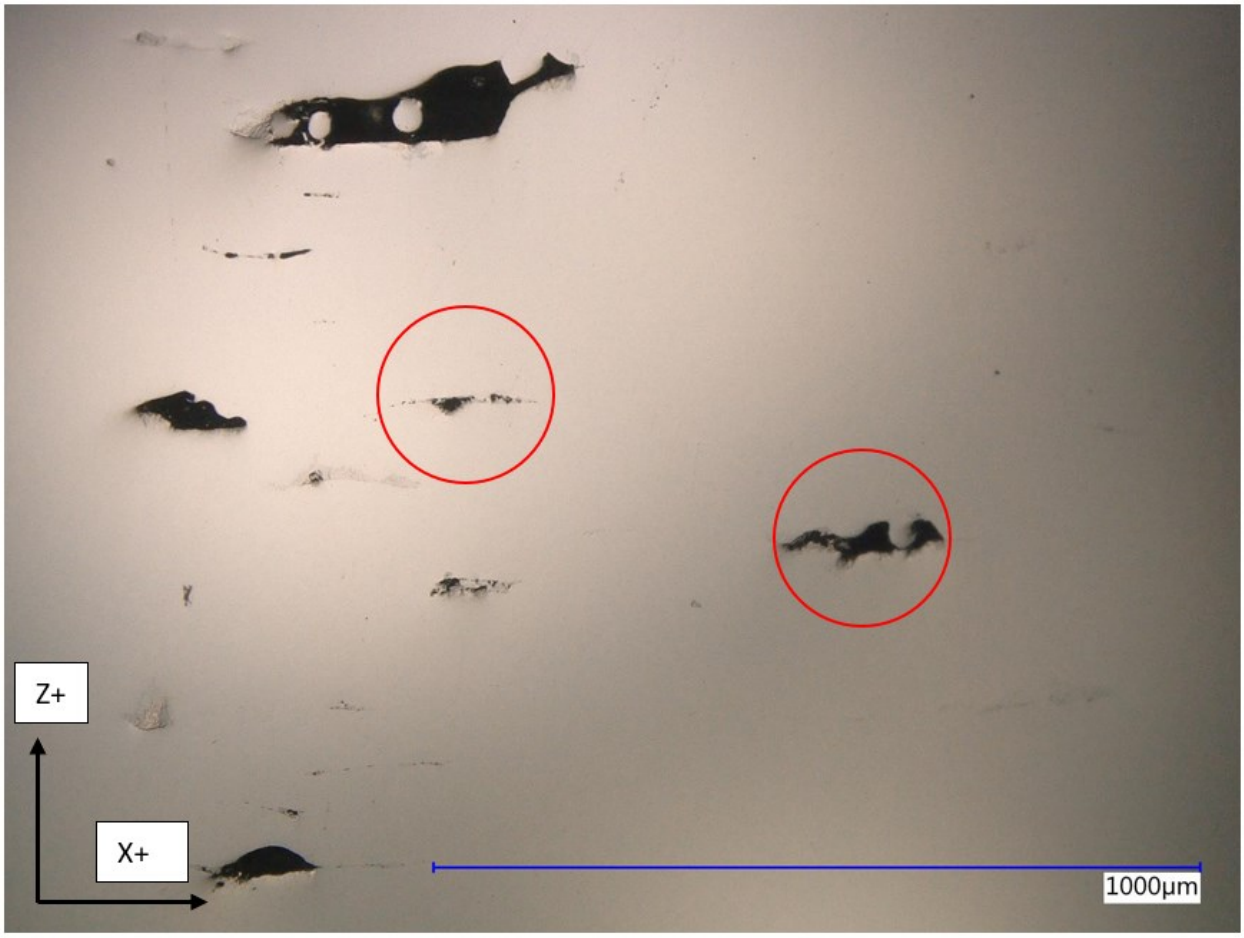

Figure 5.12 : Tensile sample 1 interlayer LOF, printed at a VED of 30J/mm^3, at 200X magnification.

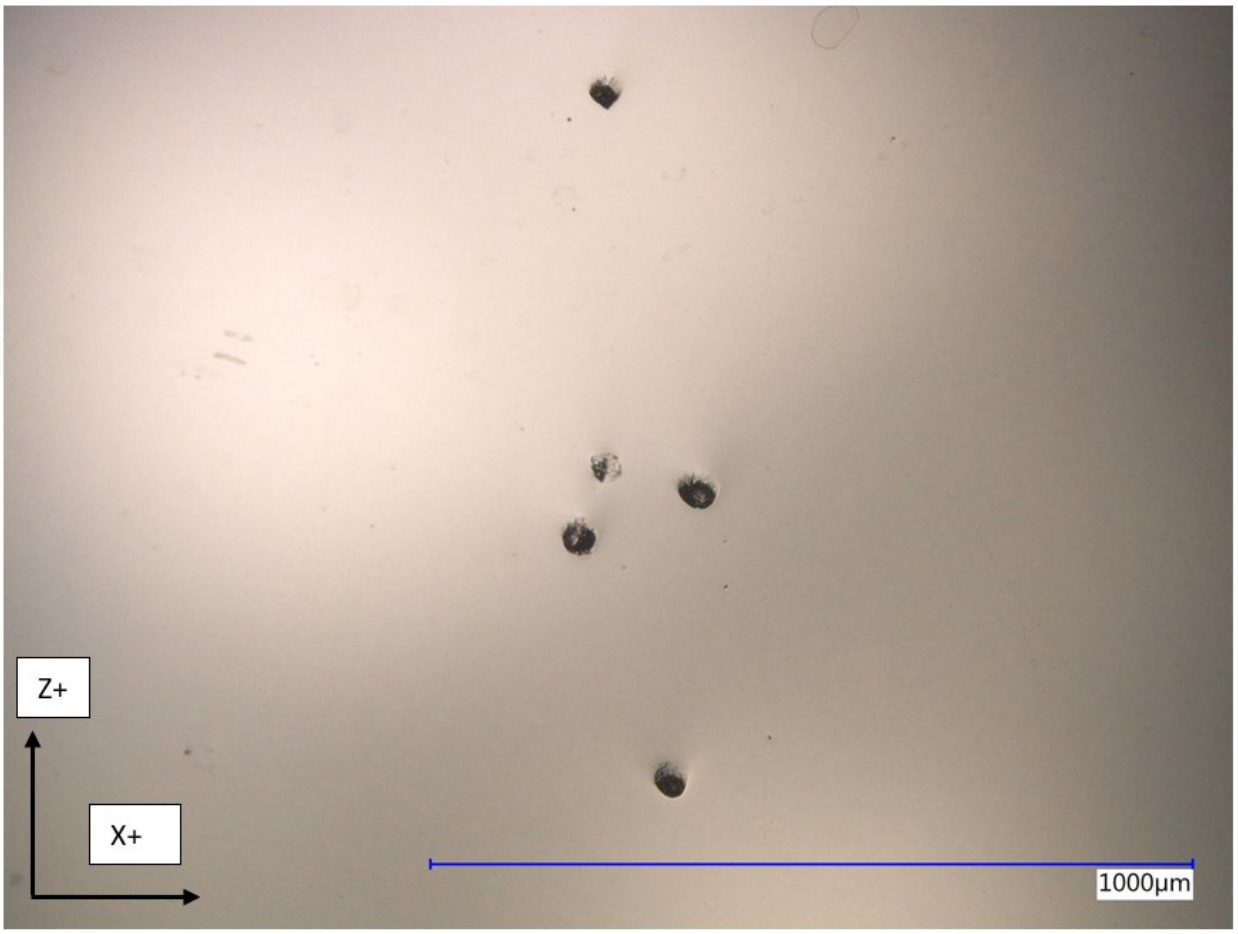

Figure 5.13 : Tensile sample 6, printed at a VED of 50J/mm^3, gas porosity defects at 200X magnification.

Discussion

The 30 VED tensile samples have some interlayer LOF defects present on the prepared surface as illustrated in Figure 5.12. No intertrack LOF defects were observed in any of the 30 or 50 VED samples. The presence of interlayer LOF defects in the 30VED tensile prints are expected, because Cube 8, which was used as a template for the 30VED tensile and fatigue samples, also has interlayer LOF present on the surface. Cubes with a VED of 50 only have gas pores observed on the surface, which corresponds to the defect types observed in the 50 VED tensile specimens such as the one illustrated in Figure 5.13. The porosity and types of defects is also affected by the geometry of the sample, as the melt pool cools differently with a different scanning path length. The types of defects and microstructure in the tensile samples and VED are therefore expected to have some variation with respect to each other.

5.1.2.2 Scanning electron microscopy

Results

The tensile specimens were analysed using the electron backscatter diffraction (EBDS) technique. This technique allows for a more accurate reading of the alpha lath thickness, which is obtained using a crystal orientation map. Prior to obtaining a crystal orientation map, it is necessary to obtain a phase map with a detection rate over 70%. This percentage is necessary to obtain an accurate map. The process of obtaining the phase map and crystal orientation map is outlined in Section 4.5.4. Figure 5.14, Figure 5.15, and Figure 5.16 present the phase maps for tensile samples 1, 5, and 6 respectively.

The phase maps presented show the different phases present in the material. Ti64 exists in the alpha phase and the beta phase. The alpha phase is present in the form of a hexagonal close-packed, or HCP structure. The beta phase is present in the form of a body centered cubic, or BCC structure. The probe used in the EBSD technique captures these phases and presents them using different colors. The blue color represents the alpha phase, while the red color, shown in a close-up view, represents the beta phase. The zero-solution pixels, which are defects, are represented in white. The BCC phase has more slip planes than the HCP phase, meaning that a Ti64 alloy containing a greater percentage of beta is more ductile than an alloy containing a smaller percentage of beta. All images show the samples on the plane parallel to the build direction, in the Y axis of the figures. The phases for acquisition are shown in Table 5.3, where the lattice parameters are given in angstroms.

Table 5.3 : EBSD Phases for Acquisition for Tensile Samples

Phase	a	b	c	Alpha	Beta	Gamma	Space Group	Database
Ti-Hex (HCP)	2.95 Å	2.95 Å	4.73 Å	90.00 °	90.00 °	120.00 °	0	HKL
Ti (BCC)	3.31 Å	3.31 Å	3.31 Å	90.00 °	90.00 °	90.00 °	229	ICSD

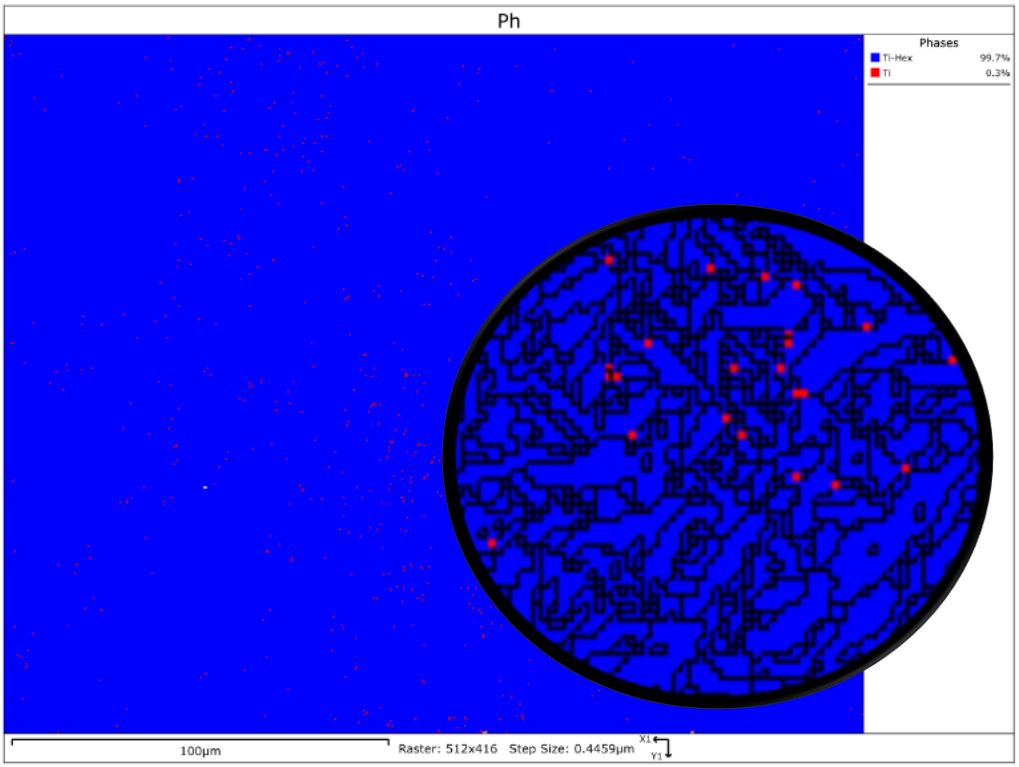

Figure 5.14 : Tensile sample 1 phase map.

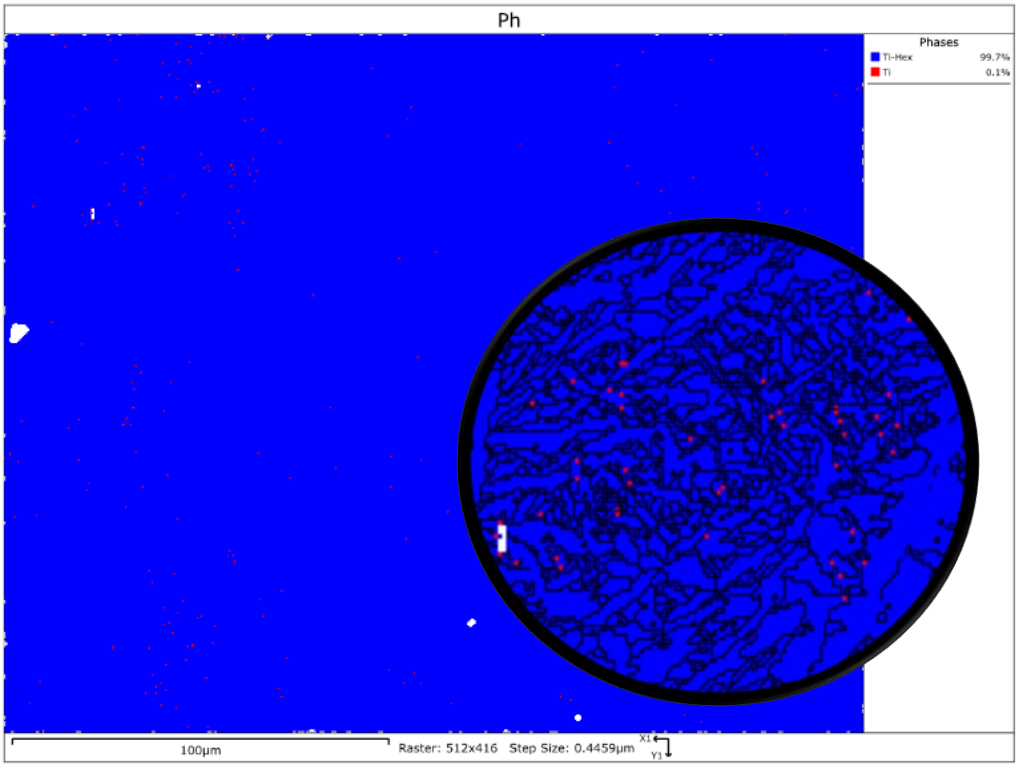

Figure 5.15 : Tensile sample 5 phase map.

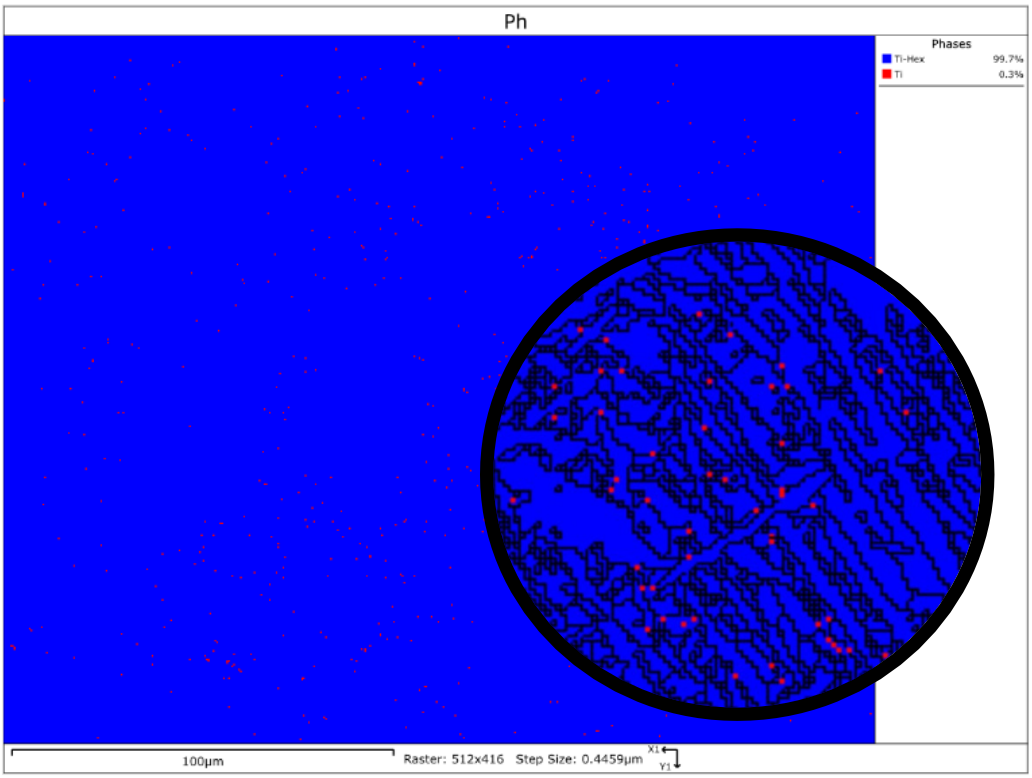

Figure 5.16 : Tensile sample 6 phase map.

The term ‘hit rate’ is used to define the resolvable pixels of EBSD images, where the alpha and beta phases with their orientation can be determined. The hit rates for tensile samples 1,5, and 6, were 85.78%, 81.08%, and 91.69% respectively. After the phase maps for all tensile samples were obtained, the crystal orientation maps were developed. The grain boundaries in black in Figure 5.14, Figure 5.15, and Figure 5.16 separate the individual grains and are set to have a misorientation angle of over 10 degrees. This angle represents the difference in crystal orientation according to a defined axis in a polycrystalline material. Accordingly, as each grain has a different crystal orientation, this difference in orientation is captured, yielding grain boundaries to obtain grain size.

To visualize the prior beta grain structure and the individual alpha lath orientation, the inverse pole figure (IPF) coloring is used. For the crystal orientation maps for tensile samples 1 and 5 shown in Figure 5.17 and Figure 5.18, the IPF coloring in the Y direction was used, and the IPF coloring in the Z direction for tensile sample 6 map shown in Figure 5.19. These orientations are taken according to the sample main coordinate system. The Y axis is the build direction, while the Z axis is out of plane on all the crystal orientation plots. These directions for the IPF coloring have been selected according to which direction showed the most visible contrast between the prior beta grains.

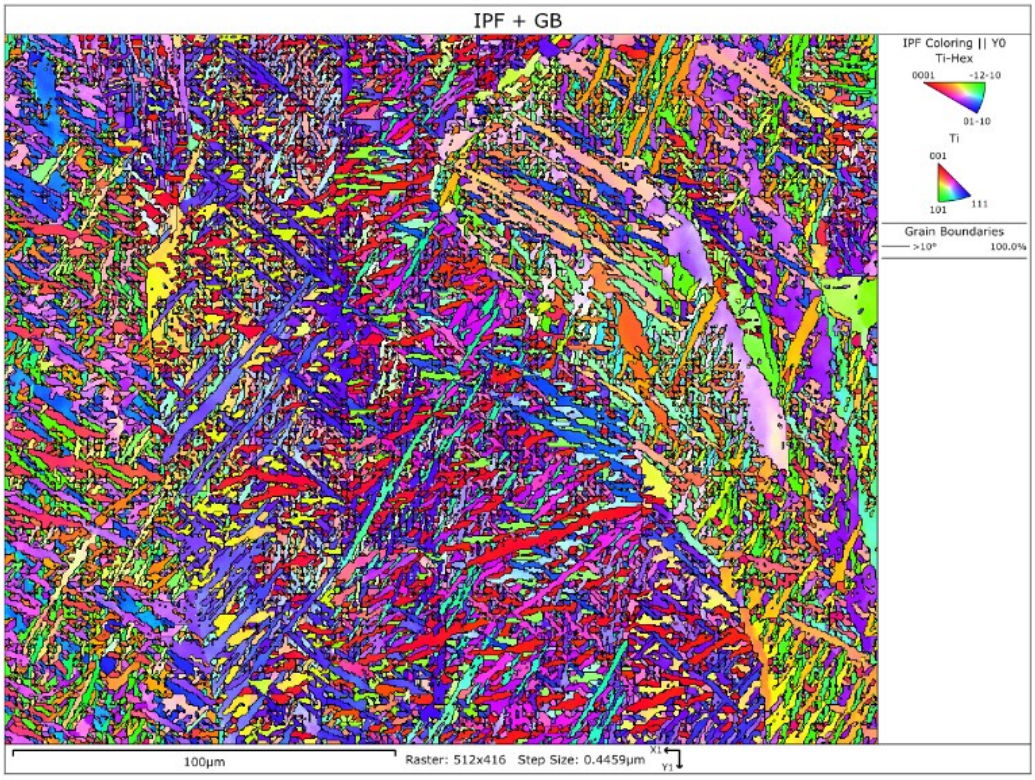

Figure 5.17 : Tensile sample 1 crystal orientation map.

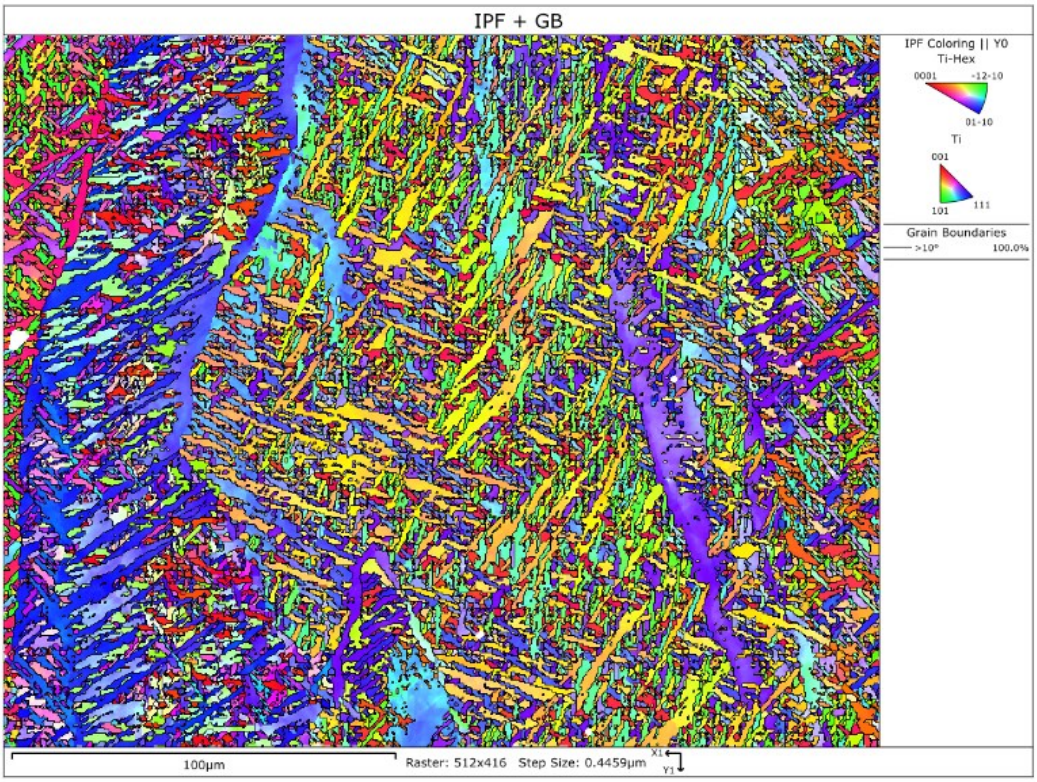

Figure 5.18 : Tensile sample 5 crystal orientation map.

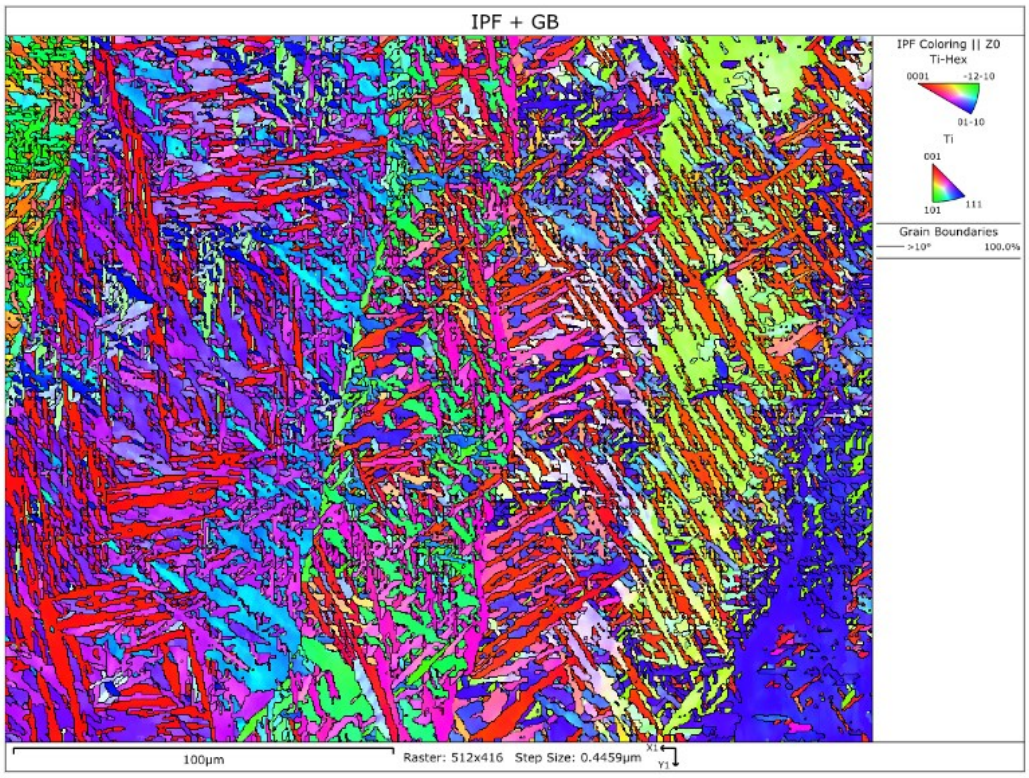

Figure 5.19 : Tensile sample 6 crystal orientation map.

Figure 5.20, Figure 5.21, and Figure 5.22 present the alpha lath thickness distribution obtained from the grain boundary maps of the crystal orientation plot of tensile samples 1, 5, and 6. The width of each column representing alpha lath thickness is 0.05µm.

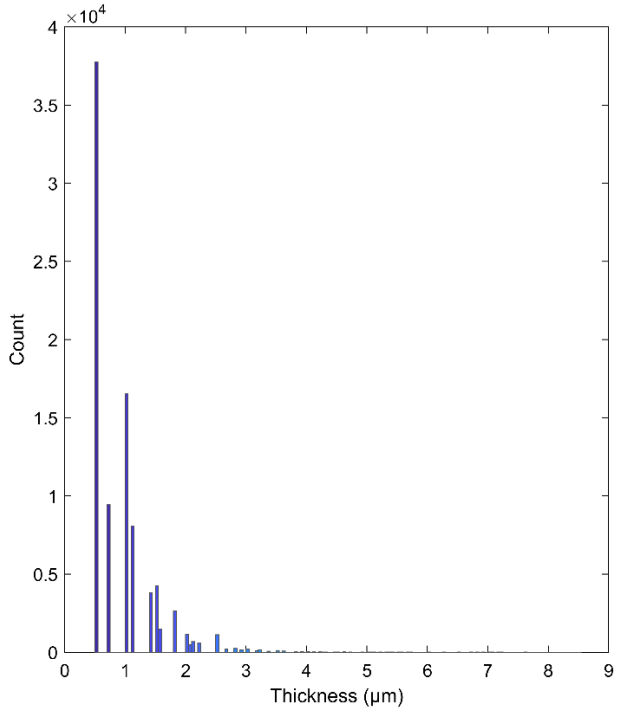

Figure 5.20 : Alpha lath thickness distribution for tensile sample 1 at 30VED.

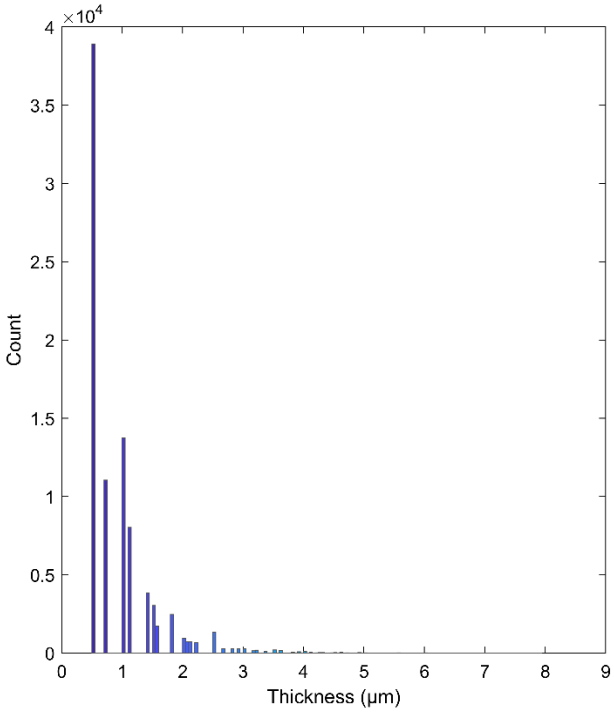

Figure 5.21 : Alpha lath thickness distribution for tensile sample 5 at 30VED.

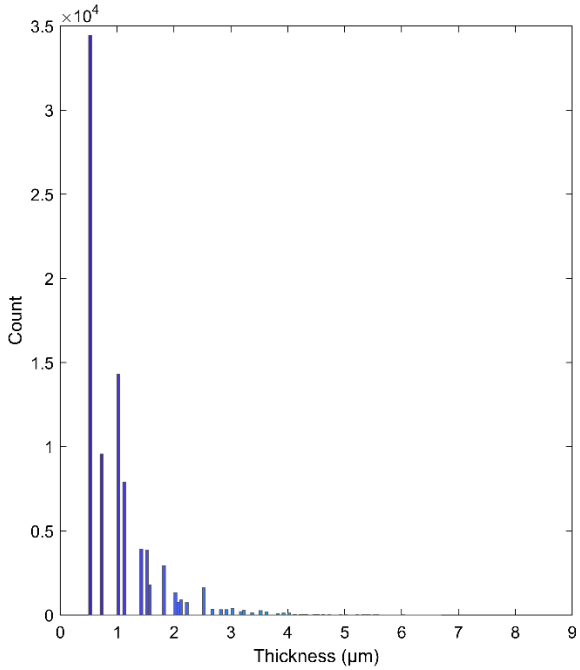

Figure 5.22 : Alpha lath thickness distribution for tensile sample 6 at 50VED.

Discussion

Figure 5.23 presents a visualization of the identification of the prior beta grain structure present in Ti64 EBM. For illustration purposes, a crystal orientation map for tensile sample 6 at a magnification of 200X was chosen. The prior beta grain boundaries are highlighted in white on a close-up view, where four separate prior-beta grains can be observed.

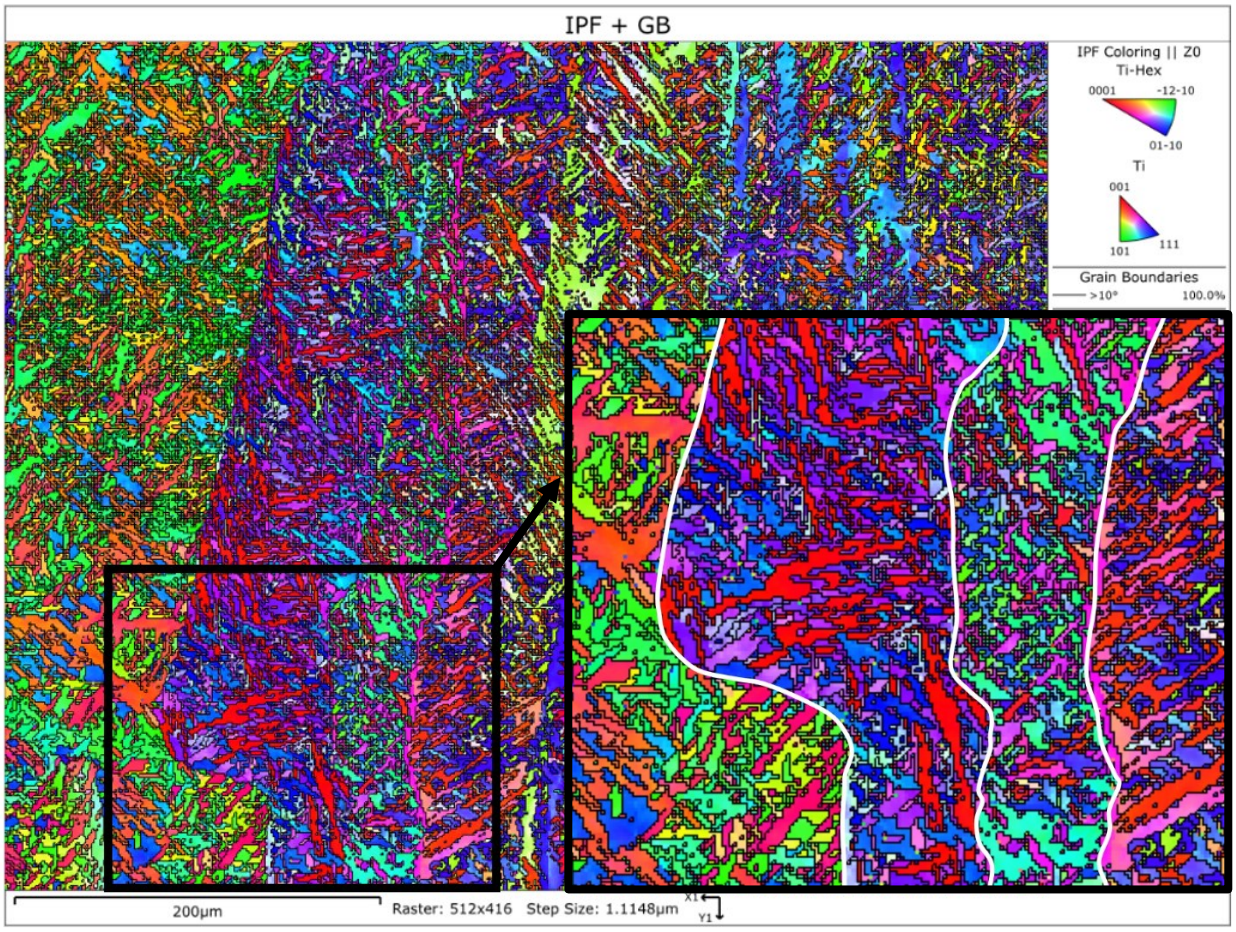

Figure 5.23 : Grain boundary identification in tensile sample 6 at 200X magnification.

The alpha lath thickness distribution for the 30 J/mm^3 VED and 50 J/mm^3 VED tensile samples are obtained from Figure 5.20 (sample 1), Figure 5.21 (sample 5), and Figure 5.22 (sample 6). Over 80,000 measurements were taken on each of the crystal orientation plots. Tensile sample 1 was printed at the extremity of the build surface, while tensile samples 5 and 6 were at the center of the build plate.

The thickness of the laths observed in all samples range from 0.525µm to 8.525 µm. In all cases, most of the measurements were on the lower bound of the histogram. The mode of the histogram is defined at the value that occurs most frequently in the data set. For sample 1, 90% of the measurements are between 0.525µm and 2.225µm, and the average taken in this range is 0.896 µm. The mode of the histogram for the alpha lath thickness of this sample is in the first column, between 0.525 µm and 0.530 µm. The results for all the tensile samples analysed through EBSD are presented in Table 5.4. Notably, there is no statistically significant difference observed in alpha lath thickness between the tensile samples with varying VED or between samples printed at the extremity and center of the build plate.

Table 5.4 : Tensile samples EBSD data from alpha lath thickness measurements

Tensile sample #	Measurement range	Mode	Average
1	0.525µm - 2.225µm	0.525 µm - 0.530 µm	0.896 µm
5	0.525µm - 2.825µm	0.525 µm - 0.530 µm	0.915 µm
6	0.525µm - 2.675µm	0.525 µm - 0.530 µm	0.959 µm

The alpha lath thickness determined through the Electron Backscatter Diffraction (EBSD) method yields similar values to those obtained using the method involving Kroll's reagent and scanning electron microscopy. The microstructure of a print, even with identical printing parameters, is influenced by geometrical features. The geometry of a sample impacts the cooling profile during printing, resulting in a distinct microstructure. This effect is particularly evident when small channels are present within a print, as they exhibit a faster cooling rate than the rest of the print. Given that the VED cubes and the tensile samples had different geometries, the alpha lath thickness might have varied slightly between the two sample types using the same method. However, significantly more grains have been measured using the EBSD method compared to the electron microscopy method. The automatic grain selection using MIIPAR also minimizes discrepancies in measurements between samples, as the user is not manually selecting and measuring individual grains. The accuracy of the grain measurements using MIPAR could be improved by scanning the samples at a higher magnification.

5.1.3 Fatigue samples microstructure

5.1.3.1 Optical microscopy porosity

Results

The porosity level for the fatigue samples was determined using the methodology outlined in Section 4.5.1. This is the same method used for the VED cubes, where the areas of the pores were compared with the image area using MIPAR. Figure 5.24 shows the area of the pores in a typical 50 J/mm^3 VED fatigue sample, while Figure 5.25 shows the pores in a typical 30 J/mm^3 VED fatigue sample.

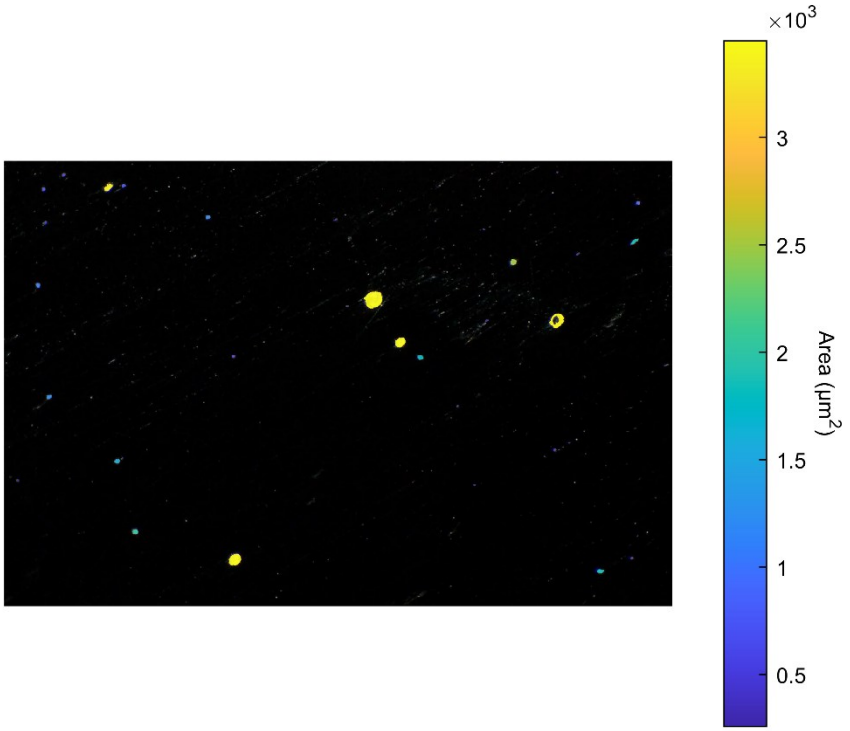

Figure 5.24 : Pores identification for 50 J/mm^3 fatigue sample at 200X magnification.

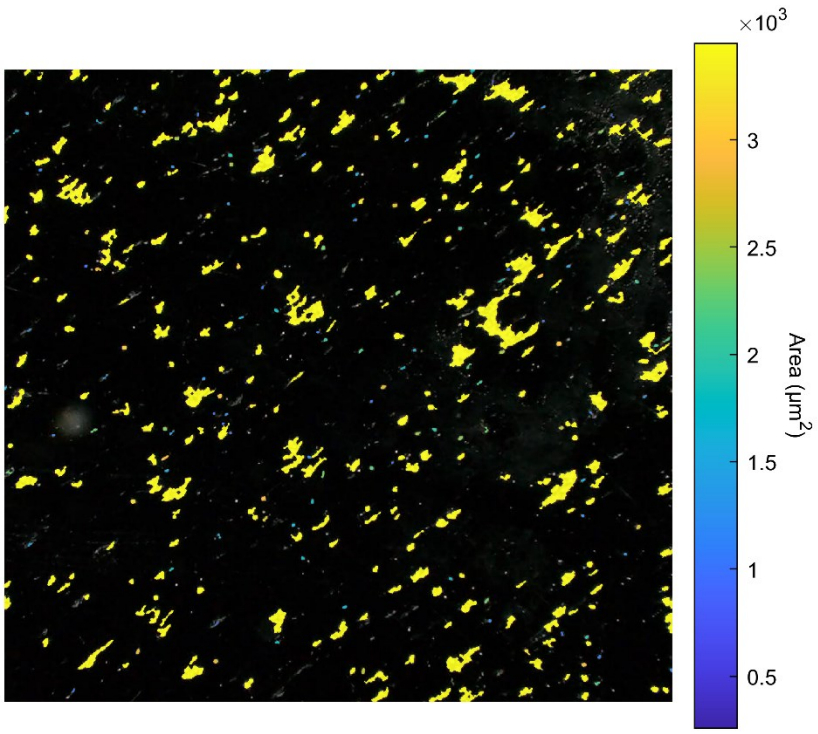

Figure 5.25 : Pores identification for 30 J/mm^3 fatigue sample at 50X magnification.

Fatigue coupons for porosity evaluation were extracted from the fatigue samples using the methodology outlined in Section 4.5.1. Five samples were selected at random for each VED level from the set of 24 fatigue samples. The maximum Feret diameter and root area parameters for the pores were also recorded and will be compared to the defect's parameters causing failure in Section 5.2.2.3 to follow. Table 5.5 and Table 5.6 present the porosity results for the 30VED and 50VED fatigue samples.

Table 5.5 : Fatigue Samples Porosity at 30 J/mm^3 VED

VED	Fatigue Sample No.	Image area (µm^2)	Pores Area (µm^2)	Porosity (%)	Maximum Feret Diameter (µm)	Maximum Equivalent Diameter (µm)	Average Feret Diameter (µm)	Average Equivalent Diameter (µm)
30 VED	7	7.87E+07	3.93E+06	4.99%	1345.42	574.82	162.82	97.45
	9	7.87E+07	2.56E+06	3.25%	689.90	300.92	149.58	86.85
	19	7.87E+07	1.70E+06	2.16%	560.58	265.68	136.26	80.51
	21	7.87E+07	1.88E+06	2.39%	709.81	266.63	130.08	76.41
	23	7.87E+07	2.55E+06	3.24%	662.30	277.39	145.82	87.09
Average	-	-	-	3.21%	793.60	337.09	144.91	85.66
STD DEV	-	-	-	0.99%	280.65	119.54	11.30	7.14

Table 5.6 : Fatigue Samples Porosity at 50 J/mm^3 VED

VED	Fatigue Sample No.	Image area (µm^2)	Pores Area (µm^2)	Porosity (%)	Maximum Feret Diameter (µm)	Maximum Equivalent Diameter (µm)	Average Feret Diameter (µm)	Average Equivalent Diameter (µm)
50VED	16	2.62E+07	8.37E+04	0.32%	129.82	79.11	39.42	28.94
	18	2.62E+07	6.83E+04	0.26%	169.58	98.99	59.58	45.96
	20	2.62E+07	9.77E+04	0.37%	184.05	148.07	68.98	46.27
	22	2.62E+07	6.94E+04	0.26%	123.94	103.53	54.29	42.58
	24	2.62E+07	7.19E+04	0.27%	186.33	161.35	51.90	40.06
Average	-	-	-	0.30%	158.74	118.21	54.83	40.76
STD DEV	-	-	-	0.04%	26.71	31.20	9.69	6.34

Table 5.5 and Table 5.6 give maximum and minimum measurements for total pore area, Feret diameter and Murakami's equivalent root area. However, individual measurements varied, and Figure 5.26 and Figure 5.27 present the distribution of the pore area obtained through MIPAR for the 50VED and 30VED samples, respectively. Figure 5.28 and Figure 5.29 present the Feret diameter of porosity observed in the 50VED and 30 VED samples, respectively. The width of the columns for the 50VED sample is 25µm, and 50µm for the 30 VED sample. Figure 5.30 and Figure 5.31 present Murakami's equivalent root area of porosity observed in the 50VED and 30 VED samples, respectively. The width of the columns for the 50VED sample is 25µm, and 50µm for the 30 VED sample. All the porosity distribution histograms for the fatigue sample coupons are presented in Appendix J.

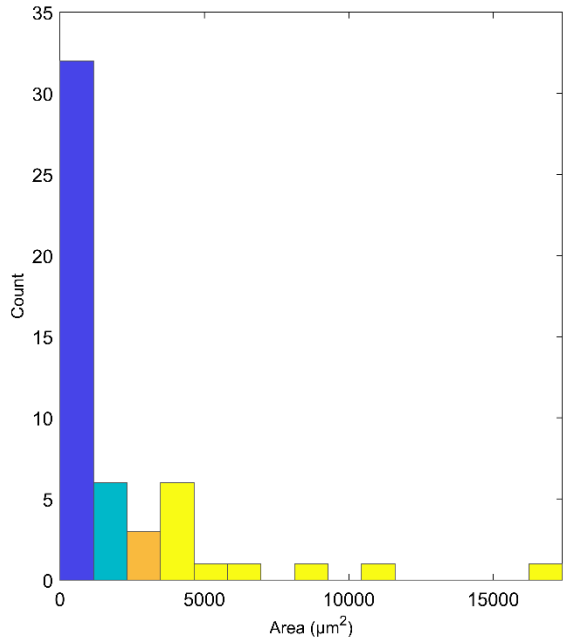

Figure 5.26 : Defect area distribution for 50 VED fatigue sample.

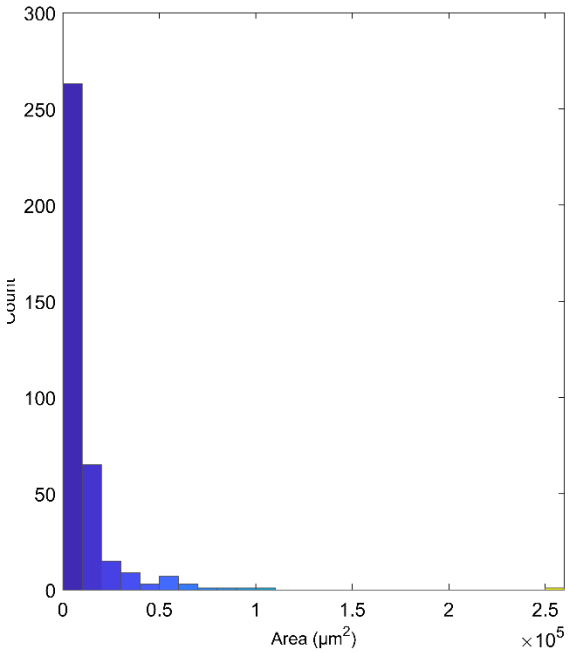

Figure 5.27 : Defect area distribution for 30 VED fatigue sample.

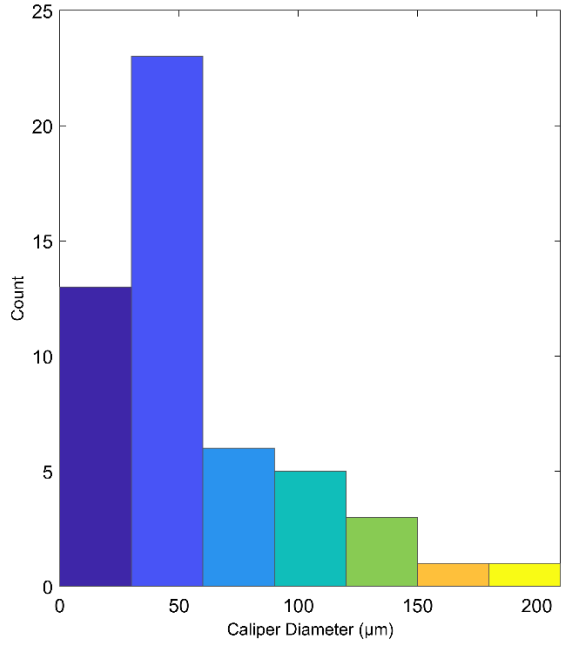

Figure 5.28 : Feret diameter distribution for 50VED fatigue sample.

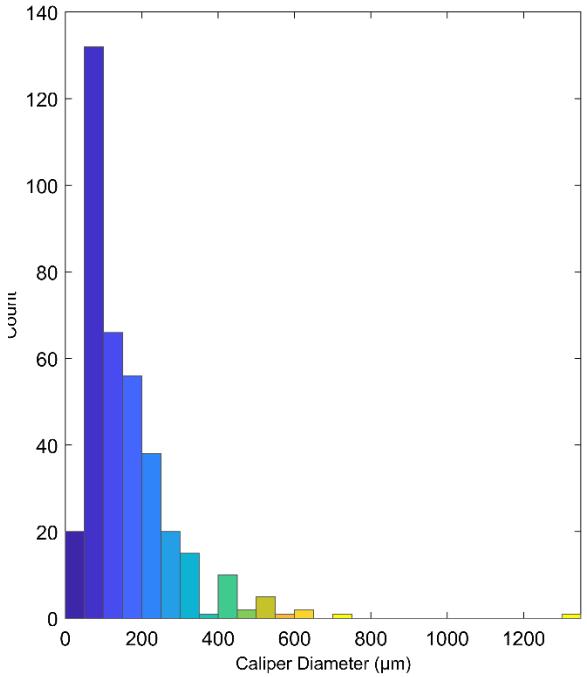

Figure 5.29 : Feret diameter distribution for 30VED fatigue sample.

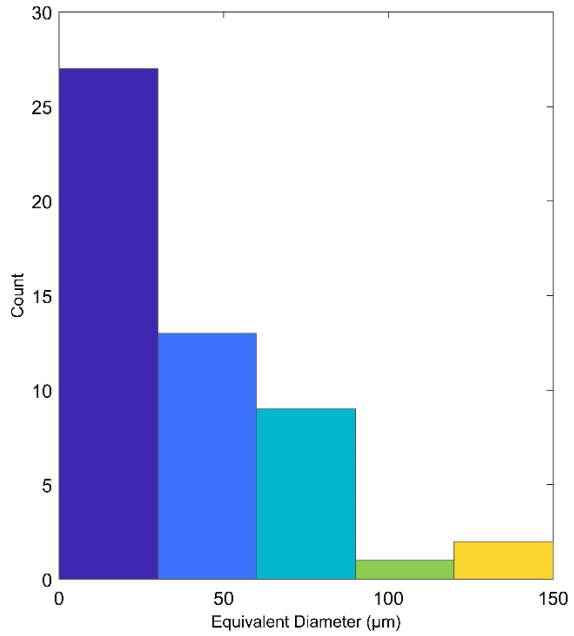

Figure 5.30 : Murakami's equivalent root area distribution for 50VED fatigue sample.

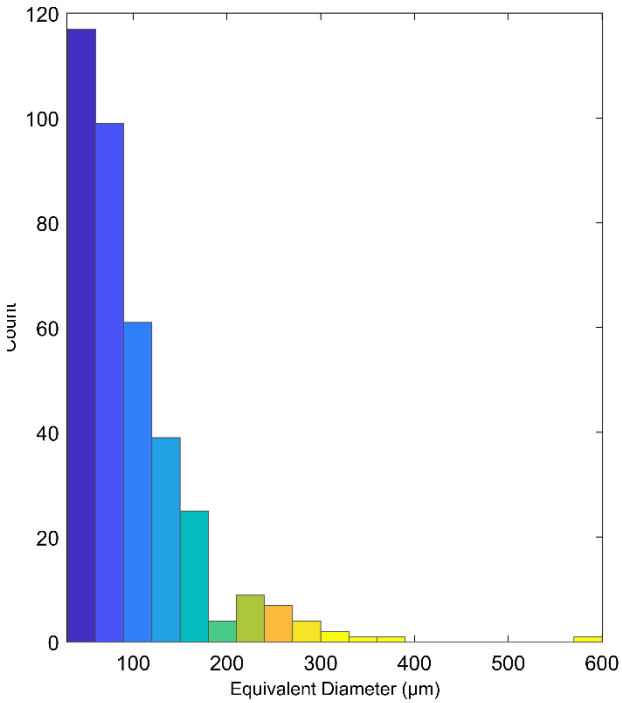

Figure 5.31 : Murakami's equivalent root area distribution for 50VED fatigue sample.

Discussion

The porosity calculations presented in Table 5.5 and Table 5.6 are obtained by assessing the area of all pores in relation to the overall image area to approximate the 2D porosity of the cross-section. While this approach does not provide information about pore size, it offers a reasonably accurate estimation for porosity measurements. The average porosity value for the 30VED samples is 3.21%, and the average porosity value for the 50VED samples is much smaller at 0.30%. This is likely attributable to the different types of defects between the 50VED samples and the 30VED sample. The porosity distributions presented in Figure 5.26 and Figure 5.27 show that the defects are concentrated in first column of the histogram, where most defects are between 150µm^2 and 1000µm^2 for the 50 VED sample, and between 1000µm^2 and 10000µm^2 for the 30VED samples.

For the 30VED sample, Feret diameter values presented in Table 5.5 are notably larger than those for the 50VED samples from Table 5.6. The maximum Feret diameter obtained through this method is considered fairly accurate, as it corresponds to the largest detected defect in optical microscopy, providing a reliable estimate for the maximum defect size at a specific location. However, larger defects may exist in other cross-sections of the sample. As opposed to the porosity area distribution, the Feret diameter distributions presented in Figure 5.28 and Figure 5.29 have most occurrences in the second column of the histogram. Most defects are between 25µm and 50µm for the 50VED sample, and between 50µm and 100µm for the 30VED sample.

Significant differences exist in Murakami's equivalent root area values between the 30VED and 50VED samples, but the Feret diameter exhibits a more substantial difference. The maximum value from Murakami's equivalent root area is also anticipated to be accurate, capturing the largest defect in the cross-section; larger defects may exist in other cross-sections of the sample. Similar to the porosity area distribution, the Feret diameter distributions shown in Figure 5.30 and Figure 5.31 have the most occurrences in the first column of the histogram, where the majority of defects are between 13µm and 50µm for the 50VED sample, and between 13µm and 100µm for the 30VED sample.

LOF defects in the VED samples were non-circular and irregular in size, and their Feret diameter values are expected to be higher, encompassing the entire defect therefore yielding larger values. In the 50VED samples where pores are predominantly circular, there is not a significant difference between the values obtained through Feret and Equivalent diameter methods.

Some circular defects in the 50VED samples have equivalent diameter and Feret diameter values larger than 150µm. The powder particle sizes supplied by ARCAM for Ti6Al4V range from 20µm to 150µm, measured by laser diffraction per ASTM B822 [66]. Gas porosity arises from the gas in between the powder particles, therefore defects caused by gas porosity must be smaller than 150µm. Accordingly, circular defects larger than 150µm can be classified as keyhole porosity. An example of a keyhole porosity with an equivalent diameter of 161µm is shown in Figure 5.32.

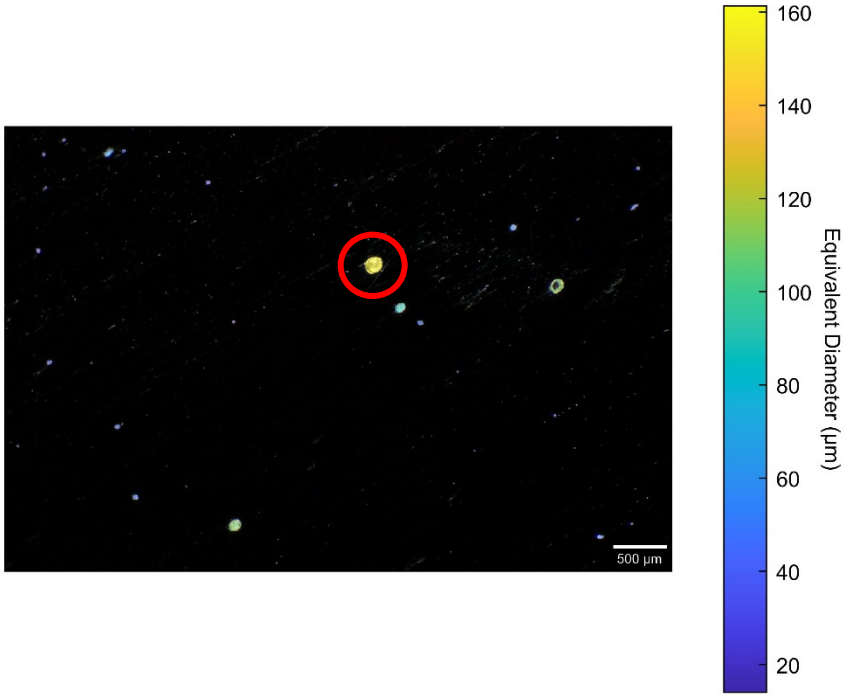

Figure 5.32 : Keyhole porosity in 50VED fatigue sample.

The histogram for Feret diameter has a mode at a higher value than Murakami's root area distribution. This could be attributed to the Feret diameter being shape-dependent, while Murakami's equivalent root area only considering the actual area of the porosity. Due to high standard deviations in both Feret and equivalent diameters, the average values lack statistical significance.

5.1.3.2 Fatigue samples mercury intrusion porosimetry

Results

Mercury intrusion porosimetry was performed on the same fatigue sample coupons used for the optical microscopy analysis with MIPAR in section 5.1.3.1. The method used for mercury intrusion porosimetry is outlined in Section 4.5.3.

Using MIP provides the opportunity to analyse the porosity of the full sample rather than a single cross-section. The results obtained from MIP provide the opportunity to evaluate the accuracy of 2D method presented in section 5.1.3.1. Five fatigue samples of 30VED and five fatigue samples of 50VED were used for MIP testing.

Figure 5.33 and Figure 5.34 illustrate the porosity spectra for the 30J/mm^3 and 50 J/mm^3 VED fatigue samples. The spectra show the maximum detectable pore size in the samples using a low-setting pressure of 2psia. The pore diameter is obtained using the Washburn equation in Equation (8) of section 4.5.3, assuming all pores are spherical. The low-pressure setting allows a maximum pore size of 90um to be detected with the equipment. For this reason, Figure 5.33 and Figure 5.34 only presents the data for the pores smaller than 90um. However, as presented in section 5.1.3.1, there are several pores viewed through optical microscopy that are greater than this value.

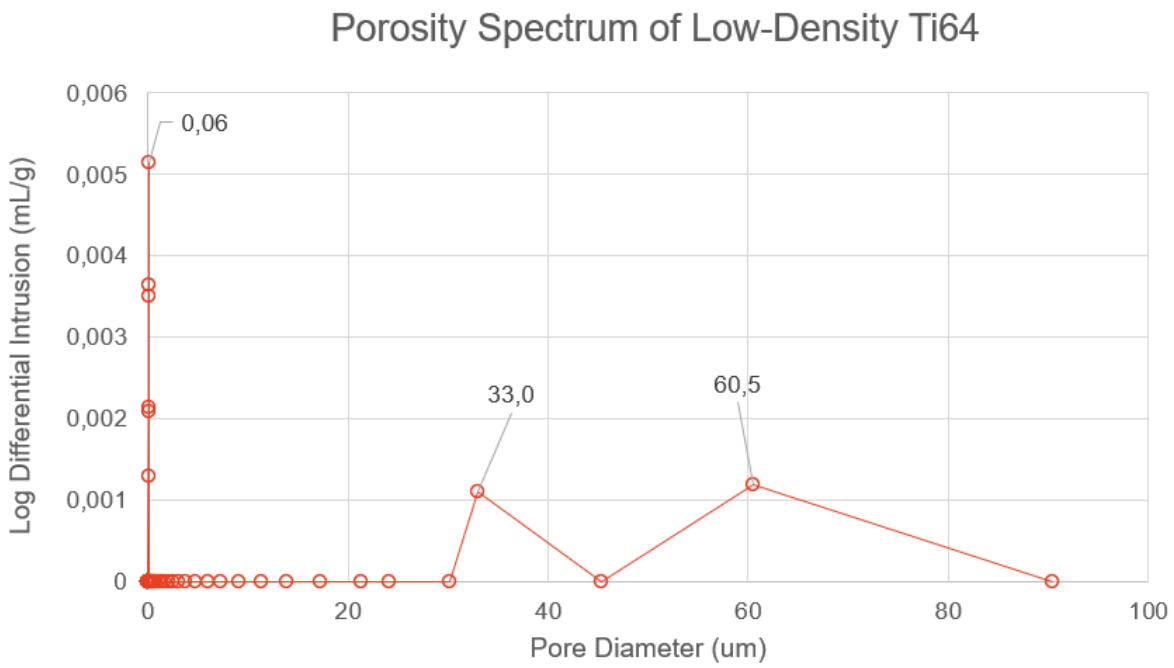

Figure 5.33 : Porosity spectrum for 30 J/mm^3 VED fatigue sample.

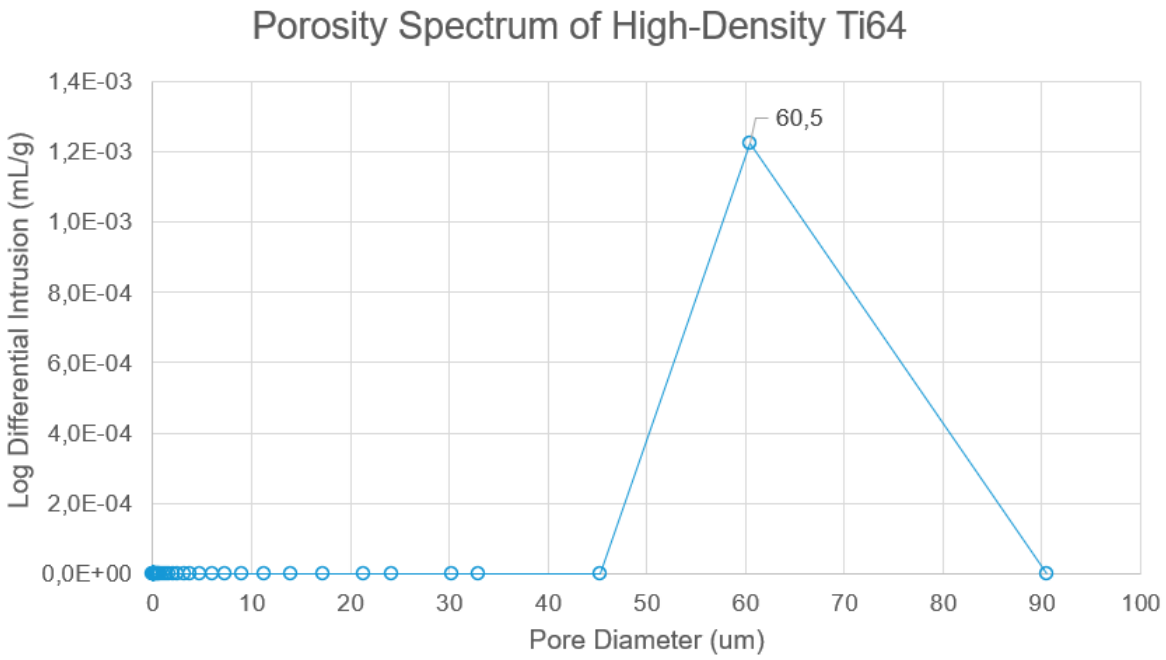

Figure 5.34 : Porosity spectrum for 50 J/mm^3 VED fatigue sample.

Table 5.7 and Table 5.8 provide a summary of the porosity and the average pore diameter of the fatigue samples analysed with the MIP technique. The porosity reported is the bulk porosity of the sample taken at 2psia.

Table 5.7 : 30 VED Porosity Results from MIP

30 VED Sample number	Porosity (%)	Total Intrusion Volume (mL/g)
7	0.44	1.10E-03
9	0.22	5.36E-04
19	0.19	4.77E-04
21	0.30	7.84E-04
23	1.01	2.60E-03
Average	0.43	1.10E-03
Standard Deviation	0.30	7.82E-04

Table 5.8 : 50 VED Porosity Results from MIP

50 VED Sample number	Porosity (%)	Total Intrusion Volume (mL/g)
16	0.19	4.73E-04
18	0.86	2.18E-03
20	0.30	7.48E-04
22	0.19	4.72E-04
24	0.25	6.23E-04
Average	0.36	8.99E-04
Standard Deviation	0.25	6.49E-04

Discussion

The porosity values for the 30VED samples in Table 5.7 are inconclusive, because pores over 90µm were not detected using this method. Optical microscopy measurements in Table 5.5 provide a maximum porosity defect size with an equivalent diameter of 574.82µm, which is significantly over the limit for this equipment.

The porosity reported using MIP for the 50VED samples is 0.36% on average, with a standard deviation of 0.25%. The porosity reported using MIPAR is 0.30% on average, with a standard deviation of 0.04%. The MIP method appears to yield smaller values than the MIPAR method upon a first examination, MIP has a pore detection range smaller than MIPAR. However, looking at sample 18 in Table 5.6, the porosity reported with MIP is significantly higher than the porosity reported with MIPAR. This suggests that the 2D analysis may not be as accurate, as some cross sections of the samples could contain larger porosity defects and have a higher porosity. Table 5.9 provides a comparison between porosity values obtained through MIP and values obtained through 2D analysis using MIPAR.

Table 5.9 : MIP and MIPAR porosity comparison

50 VED Sample number	MIP Porosity (%)	MIPAR Porosity (%)
16	0.19	0.32
18	0.86	0.26
20	0.30	0.37
22	0.19	0.26
24	0.25	0.27
Average	0.36	0.30
Standard Deviation	0.25	0.04

From the MIPAR data, the maximum Feret diameter is 158.74 µm for the 50VED, and the maximum equivalent diameter is 118.21 µm. The Micrometrics AutoPore IV at the low-pressure setting can detect pores up to 360µm in diameter at a pressure of 0.5psia. This range would be more adequate to measure the porosity of EBM samples, as some defects can be larger in size and could be detected using this equipment. Conversely, this equipment would not be adequate to determine the porosity of samples containing LOF defects, which are greater than 500um, as outlined by the 30VED samples. It can also be hypothesized that the MIP technique would not be efficient at detecting LOF pores, as the mercury would not be able to consider the loose powders as voids or defects.

5.1.3.3 Scanning electron microscopy

Results

The fatigue specimens were analysed using the electron backscatter diffraction (EBDS) technique. The process of obtaining the phase map and crystal orientation map is outlined in Section 4.5.4, and is the same method used for the tensile samples. Figure 5.35 and Figure 5.36 present the phase maps for fatigue samples 9 and 16, respectively.

The probe used in the EBSD technique captures the alpha and beta phases and presents them using different colors. The blue color represents the alpha phase, while the red color, shown in a close-up view, represents the beta phase. The zero-solution pixels, which are defects, are represented in white. All images are showing the samples on the plane parallel to the build direction, in the Y axis of the figures. The phases for acquisition are shown in Table 5.10, where the lattice parameters are given in angstroms.

Table 5.10 : EBSD Phases for Acquisition for Fatigue Samples

Phase	a	b	c	Alpha	Beta	Gamma	Space Group	Database
Ti-Hex (HCP)	2.95 Å	2.95 Å	4.73 Å	90.00 °	90.00 °	120.00 °	0	HKL
Ti (BCC)	3.31 Å	3.31 Å	3.31 Å	90.00 °	90.00 °	90.00 °	229	ICSD

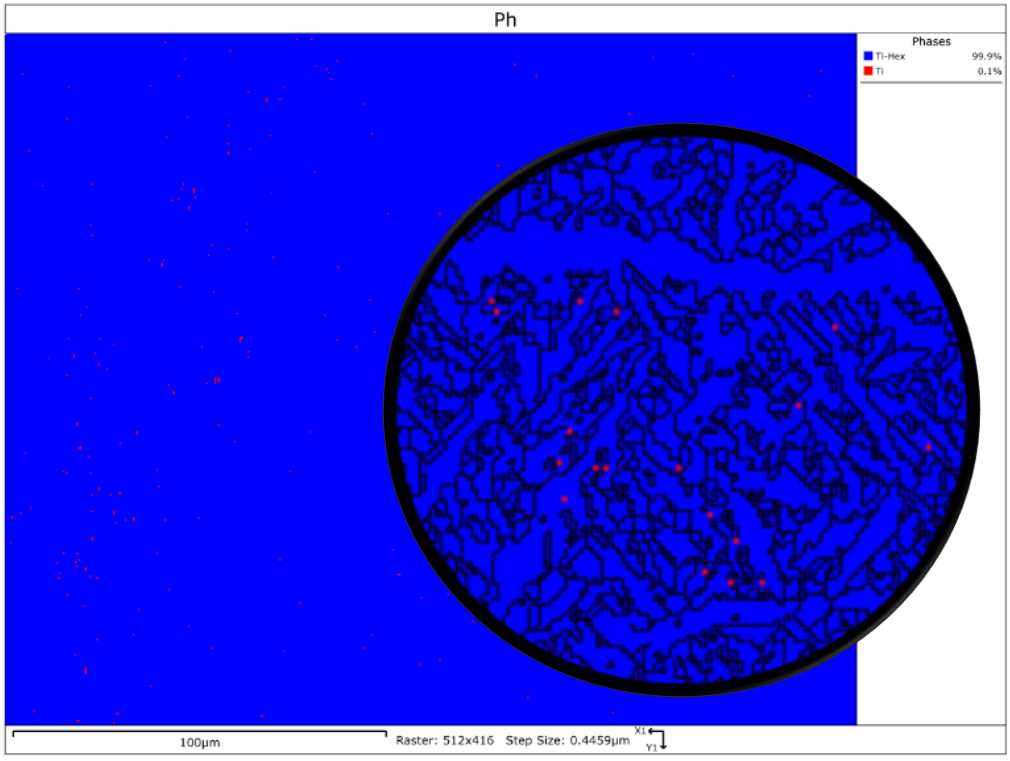

Figure 5.35 : Fatigue sample 9 phase map.

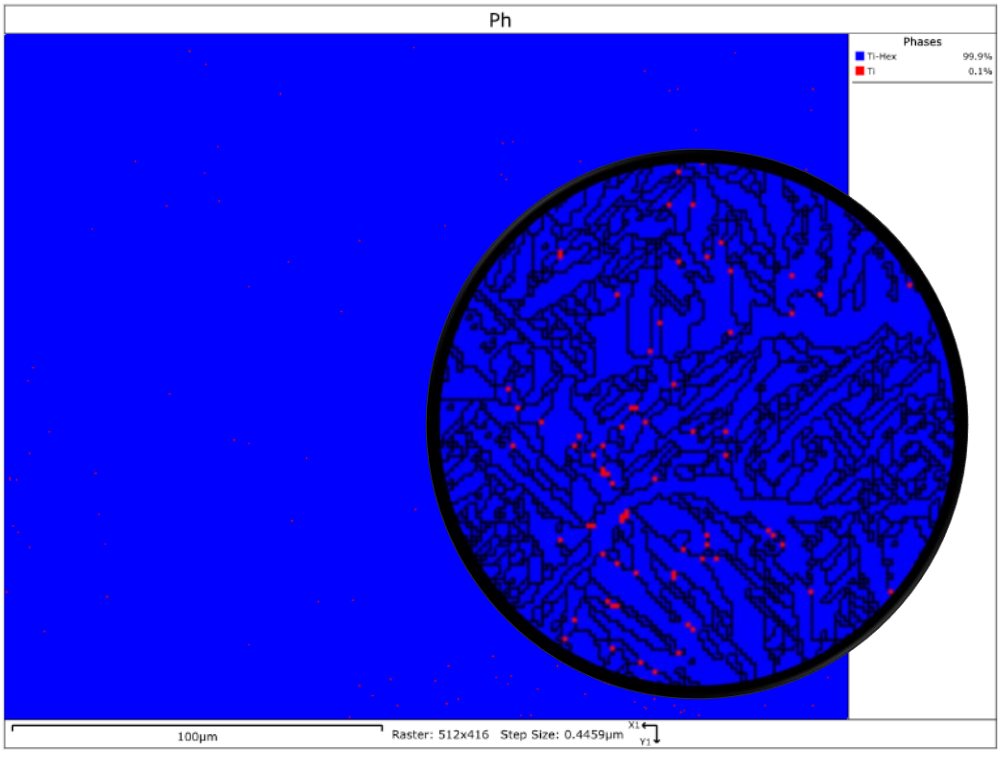

Figure 5.36 : Fatigue sample 16 phase map.

The hit rates for fatigue samples 9 and 16 are 80.00% and 82.62% respectively. To visualize the prior beta grain structure and the individual alpha lath orientation, the inverse pole figure (IPF) coloring is used. For fatigue samples 9 in Figure 5.37, the IPF coloring in the Z direction is used, and the IPF coloring in the Y direction is used for tensile sample 16 in Figure 5.38. These orientations are taken according to the sample main coordinate system, where the Z axis is out of plane on all the crystal orientation plots. The build direction for the fatigue samples was not recorded because the prints were machined in circular samples. The build direction (UP) could be along the X direction from Figure 5.37 and Figure 5.38 following the grain boundaries, but this information cannot be confirmed. The directions for the IPF coloring have been selected according to which direction showed the most visible contrast between the prior beta grains and their grain boundaries.

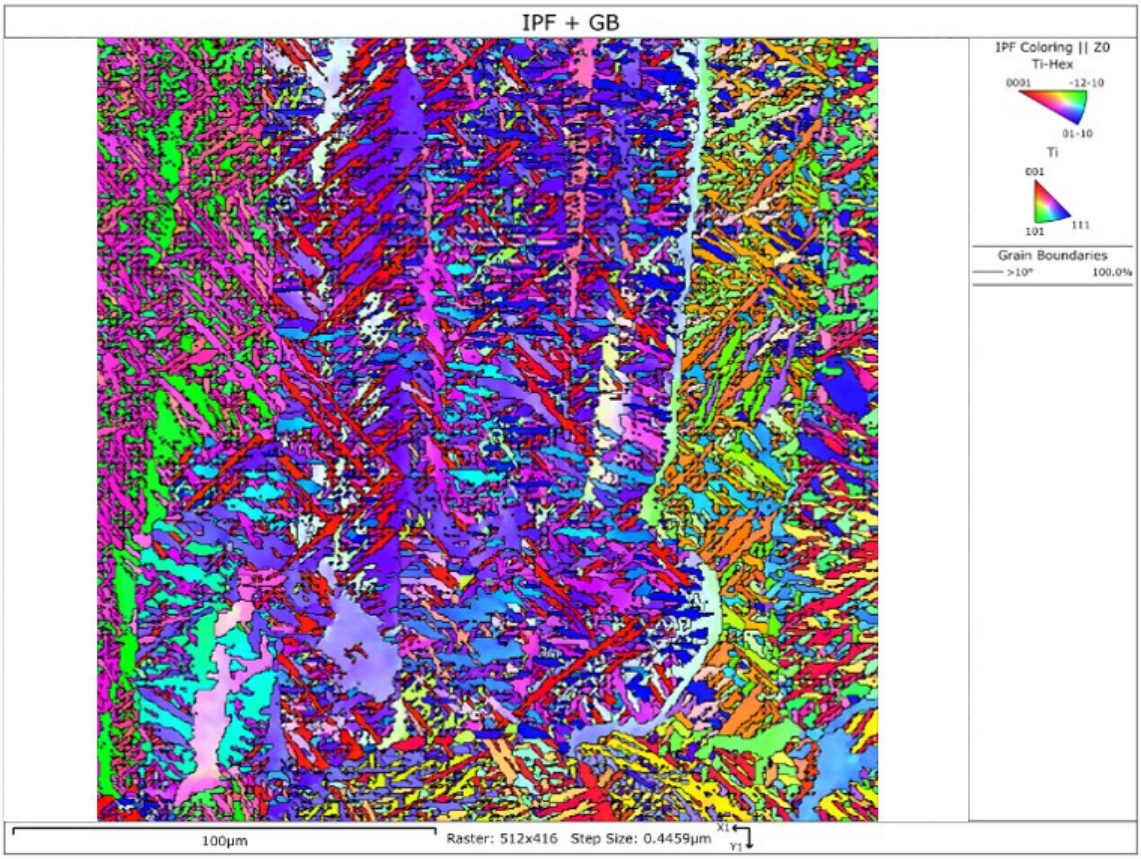

Figure 5.37 : Fatigue sample 9 crystal orientation map.

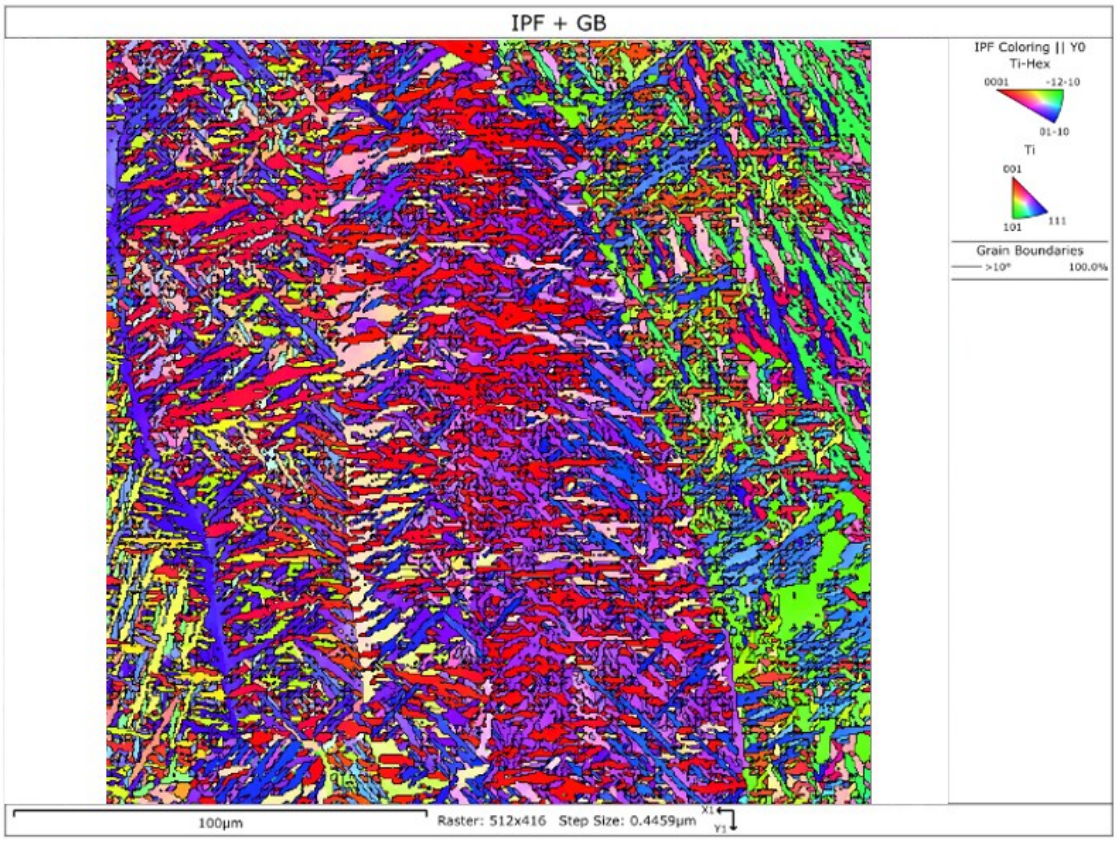

Figure 5.38 : Fatigue sample 16 crystal orientation map.

Figure 5.39 and Figure 5.40 presents the distribution of the alpha lath thickness measurements obtained from the grain boundary maps of the crystal orientation plot of fatigue samples 9 and 16. The width of each column representing alpha lath thickness is 0.05µm.

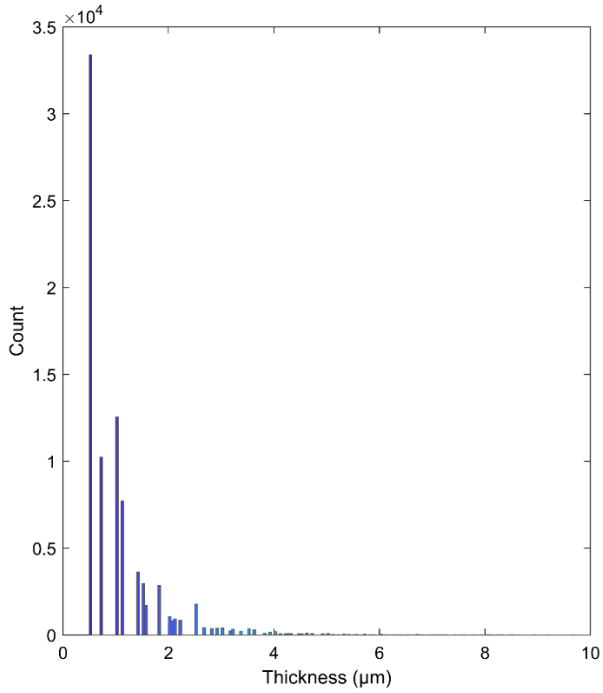

Figure 5.39 : Alpha lath thickness distribution for fatigue sample 9 at 30VED.

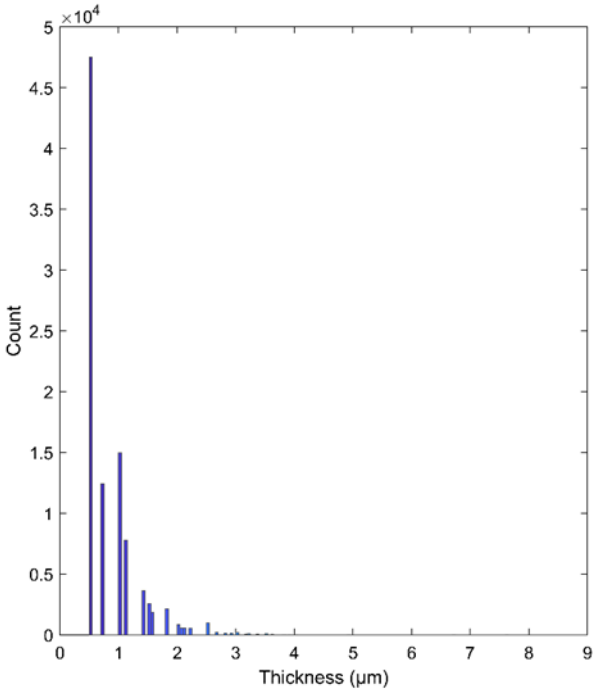

Figure 5.40 : Alpha lath thickness distribution for fatigue sample 16 at 50VED.

Discussion

The distribution of the alpha lath thickness measurements for the 30 J/mm^3 VED and 50 J/mm^3 VED fatigue samples are shown in Figure 5.39 for sample 9 and in Figure 5.40 for sample 16. Over 80000 measurements were taken on each of the crystal orientation plots. Fatigue sample 9 and 16 were both printed at the extremity of the build plate.

The thickness of the laths observed in all samples range from 0.525µm to 10.025 µm. In all cases, most of the measurements were on the lower bound of the histogram. The mode of the histogram for the alpha lath thickness of this sample is in the first column, between 0.525 µm and 0.530 µm. For sample 9, 90% of the measurements are between 0.525µm and 3.625µm, and the average in this range is 1.025 µm. The results for all the fatigue samples analysed through EBSD are presented in Table 5.11. Notably, there is no statistically significant difference observed in alpha lath thickness between the fatigue samples with varying VED.

Table 5.11 : Fatigue samples EBSD data from alpha lath thickness measurements

Fatigue sample #	Measurement range	Mode	Average
9	0.525µm - 3.625µm	0.525 µm - 0.530 µm	1.025 µm
16	0.525µm - 2.125µm	0.525 µm - 0.530 µm	0.823µm

In the analysis of the thickness of the alpha laths obtained through optical microscopy, detailed in Section 5.1.1, the 30 J/mm^3 VED cubes exhibit an average alpha lath thickness of 0.70µm, with a standard deviation of 0.03µm, while the 50 J/mm^3 VED cubes display an average thickness of 0.71µm, with a standard deviation of 0.04µm. In section 5.1.2.2, the average of the alpha lath thickness for 90% of the grain population from the EBSD analysis was 0.896 µm, 0.915 µm, and 0.959 µm, for tensile samples 1, 5, and 6, respectively. Notably, there is no statistically significant difference observed in alpha lath thickness between the tensile samples, VED cubes, and fatigue samples with varying VED, or between samples printed at the extremity and center of the build plate.

5.2 Mechanical properties

5.2.1 Tensile samples mechanical properties

Results

The mechanical properties of the tensile samples were obtained using the methodology for tensile testing presented in Section 4.6.1, and compared to the microstructural features identified in section 5.1.2. Table 5.12 provides reference mechanical properties for a solution heat treated and aged Ti64 sample with a microstructure of beta globules interspersed throughout a matrix of fully equiaxed alpha grains of mean diameter 2.5µm [85]. Table 5.13 and Table 5.14 present the mechanical properties for the 30 J/mm^3 VED and the 50 J/mm^3 VED tensile samples, respectively. Figure 5.41 and Figure 5.42 provide sample stress-strain curves for the 30VED and 50VED samples, respectively. The remaining stress-strain curves can be found in Appendix K.

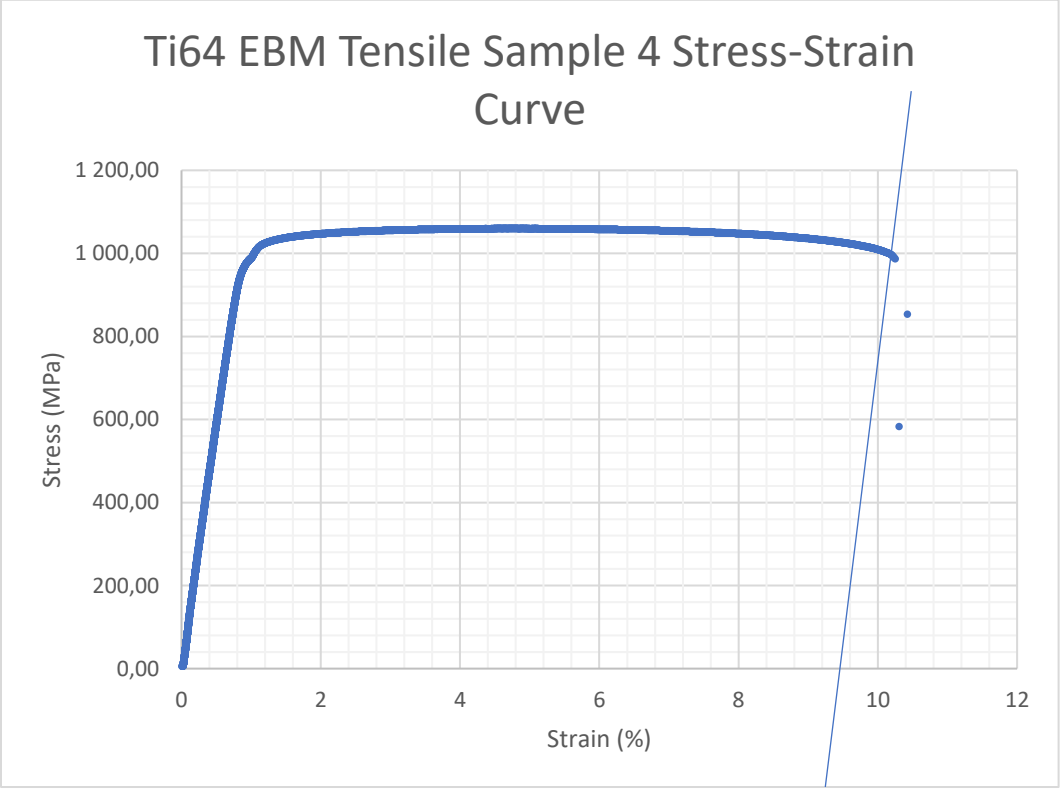

Figure 5.41 : Tensile sample 4 manufactured with 30VED stress-strain curve according to ASTM E8 standard.

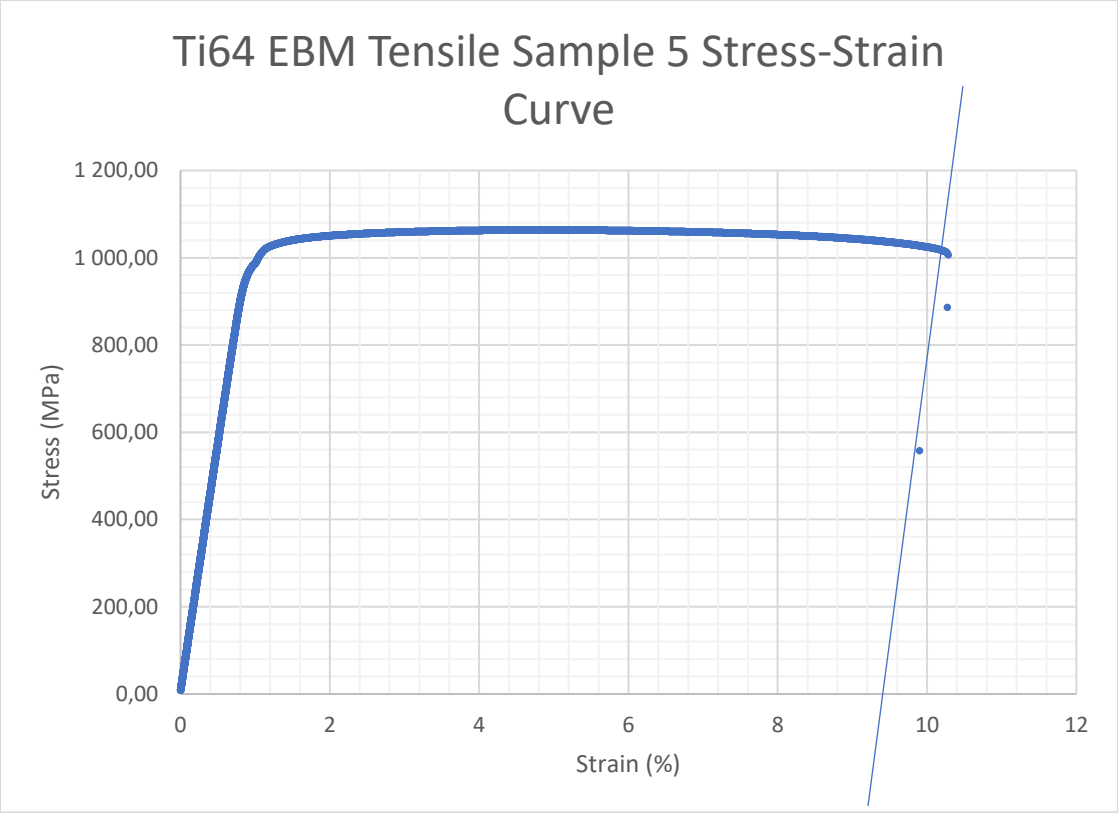

Figure 5.42 : Tensile sample 5 manufactured with 50VED stress-strain curve according to ASTM E8 standard.

Table 5.12 : Percent Elongation, Young's Modulus, Yield Strength, and Rockwell Hardness for Grade 5 Ti64 STA Samples.

Material	% EL at Fracture	% EL	Young's Modulus E (GPa)	Yield Strength (MPa)	UTS (MPa)	Hardness, Rockwell C
Grade 5 Ti64, STA	10	NA	114	1100	1170	41

Table 5.13 : Percent Elongation, Young's Modulus, Yield Strength, Ultimate Strength, and Rockwell Hardness for 30VED Ti64 EBM Tensile Samples.

VED	Tensile Sample #	% EL at Fracture	% EL	Young's Modulus E (GPa)	Yield Strength (MPa)	UTS (MPa)	Hardness, Rockwell C
30VED	1	9.2	3.7	114	1000	1079	35.1
	3	10.4	8.8	121	1035	1095	36.3
	5	10.1	8.7	115	1027	1080	35.3
	7	14.2	13.8	117	1021	1080	36.7
	9	14.3	13.4	119	1041	1100	37.3
	Average	11.6	9.7	117	1025	1087	36.1
	STD DEV	2.2	3.7	3	14	9	0.8
	% Deviation from baseline				6.8	7.1	11.9

Table 5.14: Percent Elongation, Young's Modulus, Yield Strength, Ultimate Strength, and Rockwell Hardness for 50VED Ti64 EBM Tensile Samples. *Indicates failure before yield.

VED	Tensile Sample #	% EL at Fracture	% EL	Young's Modulus E (GPa)	Yield Strength (MPa)	UTS (MPa)	Hardness, Rockwell C
50VED	2	10.8	8.4	114	1037	1093	36.7
	4	10.2	8.7	118	1014	1070	34.3
	6	14.4	13.3	117	1000	1065	37.0
	8	13.2	12.4	118	1023	1082	36.2
	10*	NA	NA	~~95~~	~~683~~	~~683~~	~~11.5~~
	Average	12.1	10.7	117	1018	1078	36.0
	STD DEV	1.7	2.2	1,3	14	11	1.1
	% Deviation from baseline				7.4	7.9	12.1

Discussion

Tensile sample 10 had a very high porosity level after being printed, and the sample's low hardness value supports the results of the visual examination. High levels of porosity were observed in samples from one extremity of the build plate, and one possible cause for this porosity could be the calibration of the build plate. The results of the tensile testing of sample 10 was not used to calculate the average values in Table 5.14. With reference to the results in Table 5.13 and Table 5.14, there is no statistically significant difference between the tensile properties of the 30VED and 50VED samples.

The results indicate that, although the print settings for the 30VED and 50VED samples is different, the tensile properties of the tensile samples are not affected by this difference. Another point of interest when comparing the EBM samples tensile properties to the baseline samples is the % elongation at fracture. Materials with a larger grain size are expected to have greater ductility [9]. However, in this study, the baseline sample with a grain size of 2.5µm has a 10% elongation at fracture, while the EBM samples with smaller grains have a % elongation of 11.6% +/- 2.2 and 12.1% +/- 1.7 for the 30VED and 50VED respectively. In section 5.1.2.2, the average of the alpha lath thickness for 90% of the grain population from the EBSD analysis was 0.896 µm, 0.915 µm, and 0.959 µm, for tensile samples 1 at 30VED, sample 5 at 30VED, and sample 6 at 50VED, respectively.

5.2.2 Fatigue samples mechanical properties

5.2.2.1 Tensile properties

Results

The tensile properties of all 24 fatigue samples were obtained following the methodology outlined in Section 4.6.3, and the results are presented in Table 5.15 for the 30VED fatigue specimens and Table 5.16 for the 50VED fatigue specimens. The Rockwell hardness values for the fatigue samples were obtained following the methodology outlined in section 4.6.2.

Of the 24 samples, the extensometer slipped during the testing for samples 1-4, and the results were incorrect. Figure 5.43 and Figure 5.44 provide sample stress-strain curves for the 30VED and 50VED samples, respectively. The remaining stress-strain curves can be found in Appendix L.

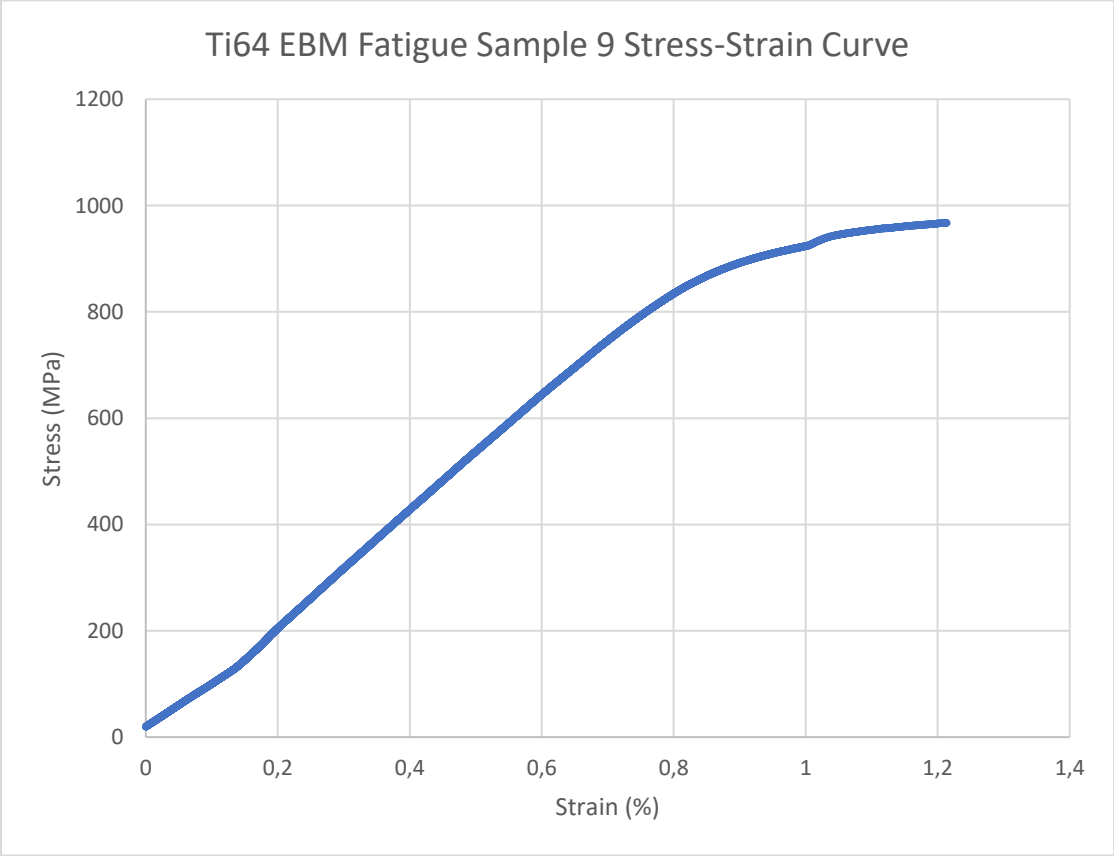

Figure 5.43 : Fatigue sample 9 manufactured with 30VED stress-strain curve according to ASTM E8 standard.

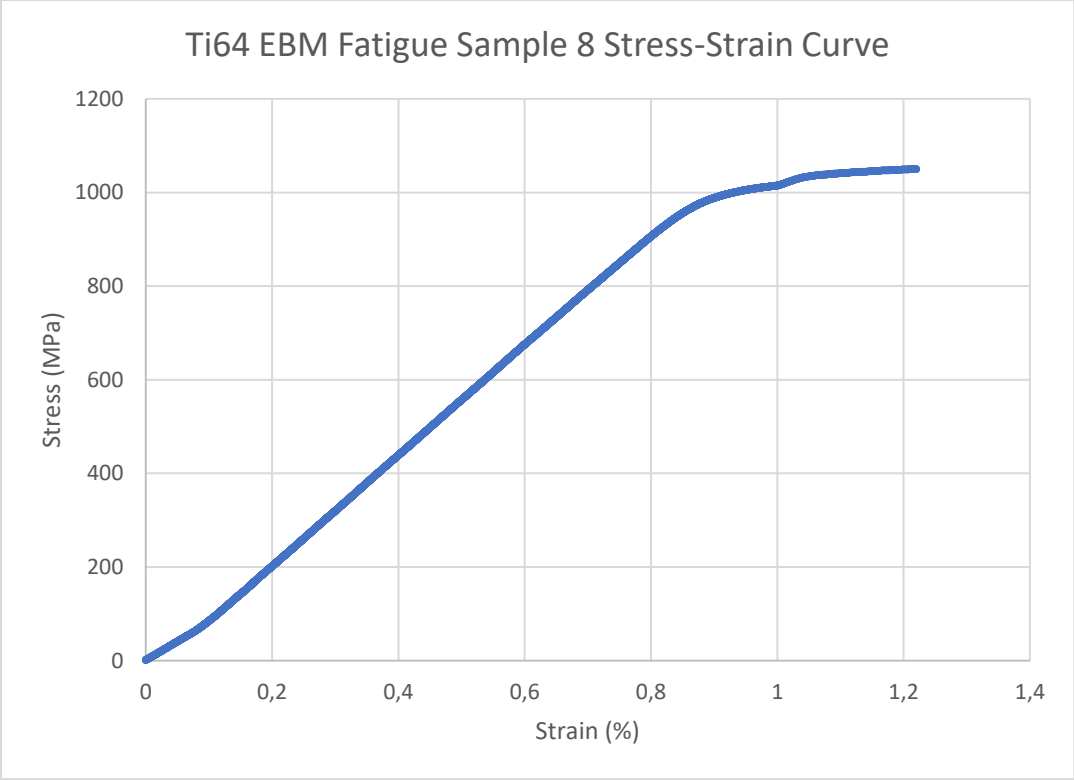

Figure 5.44 : Fatigue sample 8 manufactured with 50VED stress-strain curve according to ASTM E8 standard.

Table 5.15 : 30VED fatigue specimens Young's Modulus, Yield Strength, and Rockwell hardness. *Indicates extensometer slippage.

Fatigue Sample #	Young's Modulus E (GPa)	Yield Strength (MPa)	Hardness, Rockwell C
1*	~~102~~	953	33.9
3*	~~115~~	995	34.9
5	111	995	32.5
7	109	971	32.1
9	112	975	29.3
11	108	995	35.0
13	110	999	34.4
15	109	995	31.8
17	~~84~~	~~745~~	~~28.6~~
19	113	1015	35.2
21	116	1008	35.2
23	107	985	33.9
Average	110	990	33.5
STD DEV	4	17	1.8

Table 5.16 : 50VED fatigue specimens Young's Modulus, Yield Strength, and Rockwell hardness. *Indicates extensometer slippage.

Fatigue Sample #	Young's Modulus E (GPa)	Yield Strength (MPa)	Hardness, Rockwell C
2*	~~111~~	1 007	39.5
4*	~~118~~	1 017	39.8
6	141	1033	40.1
8	121	1071	40.5
10	116	1026	38.1
12	116	1036	39.3
14	116	1051	39.4
16	119	1062	39.6
18	119	1024	39.4
20	122	1027	39.3
22	117	1046	39.6
24	120	1075	40.0
Average	120	1 040	39.6
STD DEV	7	21	0.6

Discussion

Sample 17 from the 30VED set failed before reaching yield. Accordingly, the tensile property values for this sample were not used in the calculation of the averages for the 30VED fatigue samples. Sample 17, similarly to sample 10, was located at the extremity of the build plate. This adds support to the possibility that a problem with the calibration of the build plate contributed to the porosity and relatively poor properties of samples from this location.

The results for the Young's Modulus, Yield strength, and Rockwell hardness between the 30VED and 50 VED fatigue samples are similar but statistically significant using a 95% confidence interval. The porosity level reported in Section 5.1.3.1 for the two VED settings is different, and the tensile property results indicate that tensile properties may be slightly affected by differences in porosity.

Wilson-Heid et al. [53] found that the presence of a single pre-existing pore did not significantly affect the material's yield strength, ultimate tensile strength, or ductility until the pore diameter reached or exceeded 600μm, or 10% of the samples diameter. The maximum Feret diameter for the 30VED samples was 1345.42 μm, and the maximum size using Murakami's equivalent root area method is 574.82μm. The defects from gas porosity in the 50 VED samples had a Feret diameter of 186.33μm, and the maximum size using Murakami's equivalent root area method is 161.35um. For the sample geometry used, the samples have a diameter of 6.35mm. Using the Wilson-Heid et al. [53] 10% of diameter criteria, the defect diameter corresponding to 10% of the fatigue sample diameter, would be 635μm.

For the 50VED samples, both the Feret diameter values and Murakami's equivalent root area values were well below 635μm. For the 30VED values, the Feret diameter was much larger than 635μm cutoff, and Murakami's equivalent root area was slightly less than this value. However, Wilson-Heid et al. [53] examine a single large pore circular in size, whereas the porosity defects examined in this study are very irregular in size and located in a proximity to each other to possibly coalesce. Taking into consideration that Murakami's equivalent root area parameter does not consider adjacent defects and proximity to the surface, the actual defect diameter is probably greater than 574.82μm which was measured. According to the theory of Wilson-Heid et al. [53], the 30VED samples should show a decrease in tensile strength, whereas the 50VED samples should not.

5.2.2.2 Fatigue properties

Results

The fatigue properties of the 50VED and 30VED samples were obtained using the methodology outlined in Section 4.6.3. Results from the load-control fatigue testing are tabulated in Table 5.18 in terms of applied stress level and cycles to failure. Figure 5.45 is a plot of the applied stress level as a function of stress-cycles to failure for the baseline samples, the 50VED, and the 30VED fatigue samples, tested at a stress ratio R = 0.1.

For the baseline samples, 3 samples were tested at 1025MPa, 3 at 1000MPa, 3 at 975MPa, 3 at 950MPa and 1 sample was tested at 900MPa. The results were obtained to estimate the predicted fatigue behavior and are presented in Table 5.17.

Table 5.17 : Baseline Fatigue Samples Stress Level and Cycles to Failure

Item #	Stress (MPa)	Cycles to Failure (N_f)
1	700	5154910
2	900	1516600
3	1000	22152
4	1025	12856
5	975	28649
6	950	61206
7	950	93051
8	950	81231
9	975	28818
10	975	35655
11	1025	18921
12	1025	11334
13	1000	19286
14	1000	19149

Table 5.18 : Stress Level and Cycles to Failure for 30VED and 50VED EBM Fatigue Samples

VED	Fatigue Sample #	Stress Level (MPa)	Cycles to Failure (N_f)
30 VED	1	850	2494
	3	850	3524
	5	850	3916
	7	900	564
	9	800	2716
	11	700	5563
	13	650	8150
	15	625	6430
	19	600	12076
	21	500	32217
	23	400	41056
50 VED	2	800	119504
	4	800	206668
	6	900	9525
	8	750	19351
	10	700	148707
	12	650	607576
	14	625	988102
	16	600	367249
	18	575	1870760
	20	550	64970
	22	525	1571056
	24	500	5200000

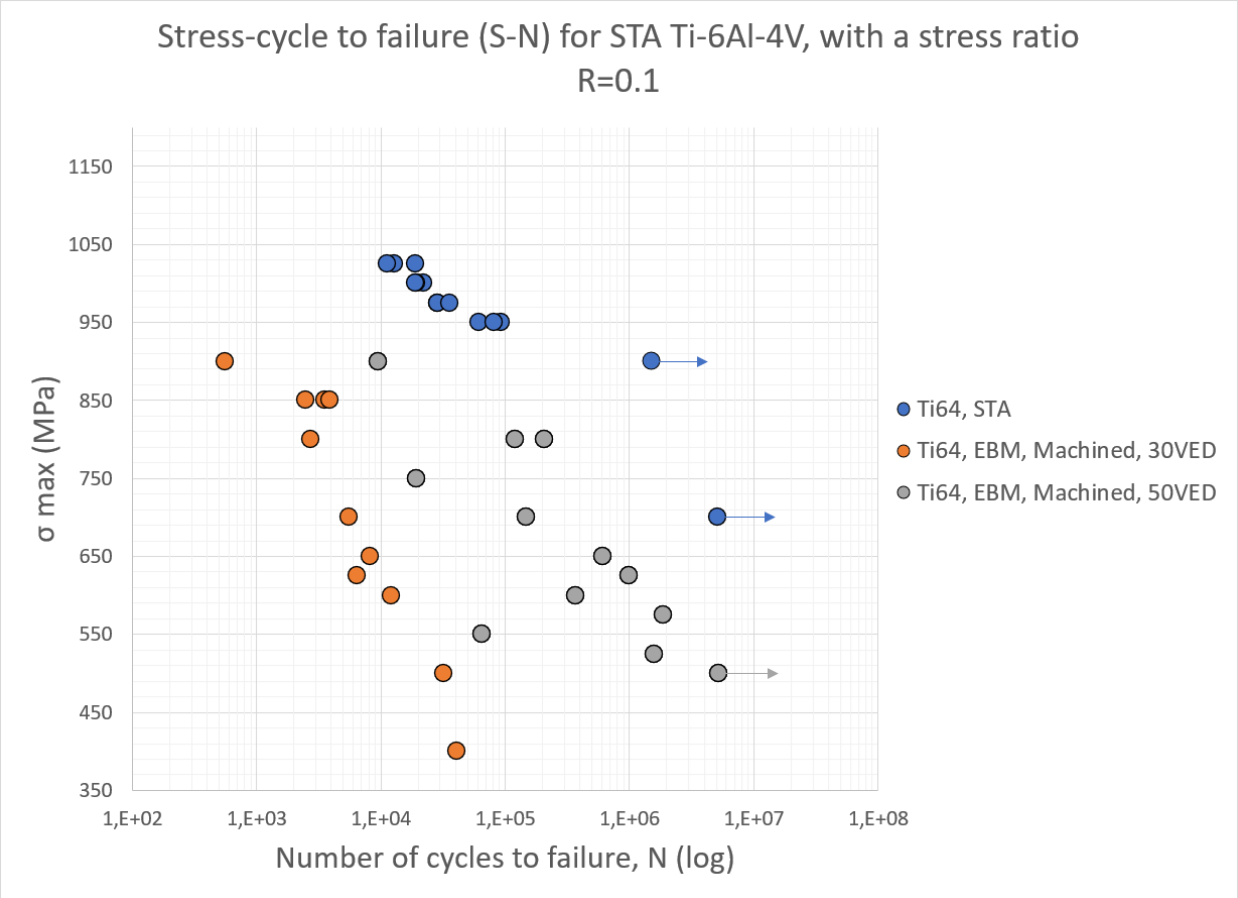

Figure 5.45 : Stress-cycle to failure (S-N) curve for STA Ti-6Al-4V at a stress ratio R of 0.1

The baseline results are represented by the blue circles in Figure 5.45, and one runout sample was tested at 900MPa. The 50VED samples results are represented by the grey circles in the figure, where one runout was observed at 500MPa. The 30VED samples results are represented by the orange circles, and no runout was obtained. More samples would have been necessary to obtain a conclusive fatigue limit for the 30VED and 50VED samples.

Discussion

One observation which can be made from Figure 5.45 is that the EBM samples fail at lower stress levels than the baseline sample. The EBM samples have been pre-strained to reduce data scatter, which is known to reduce fatigue life, whereas the baseline samples were not pre-strained. However, this alone may not account for the significant differences in fatigue strength observed and that the defects are contributing to the fatigue behaviour.

Additionally, the 30VED samples failed at lower stress levels than the 50VED samples. This supports the suggestion that defects are contributing to the fatigue behaviour of the EBM samples, and that the higher porosity level in the 30 VED samples is contributing to the shorter fatigue life observed.

Regardless of the pre-strain applied to the EBM specimens, the data points exhibit a large amount of scatter. The results suggest that the different magnitudes and locations for the maximum defect size in the EBM fatigue samples may be contributing to the scatter observed.

5.2.2.3 Fracture surface analysis

Results

The fracture surface of each failed fatigue sample was placed under the optical microscope to evaluate the fracture surfaces following the methodology outlined in Section 4.6.5. All the optical micrographs for the fatigue samples are presented in Appendix M. Results for fatigue sample 9 are provided here as an example to illustrate the process of quantifying the pore size according to two different techniques. In section 5.1.3.1, the two methods used to measure the defects were the Feret diameter and Murakami's equivalent root area. In the case of the fracture surface analysis, Murakami's *effective* root area method and the Feret diameter method were used. The difference between these two methods is that Murakami's *effective* root area method considers the proximity of the defect to the surface, while Murakami's equivalent root area method does not. Several areas can be visually identified from the sample and transferred to the microscope image, which is shown in Figure 5.46.

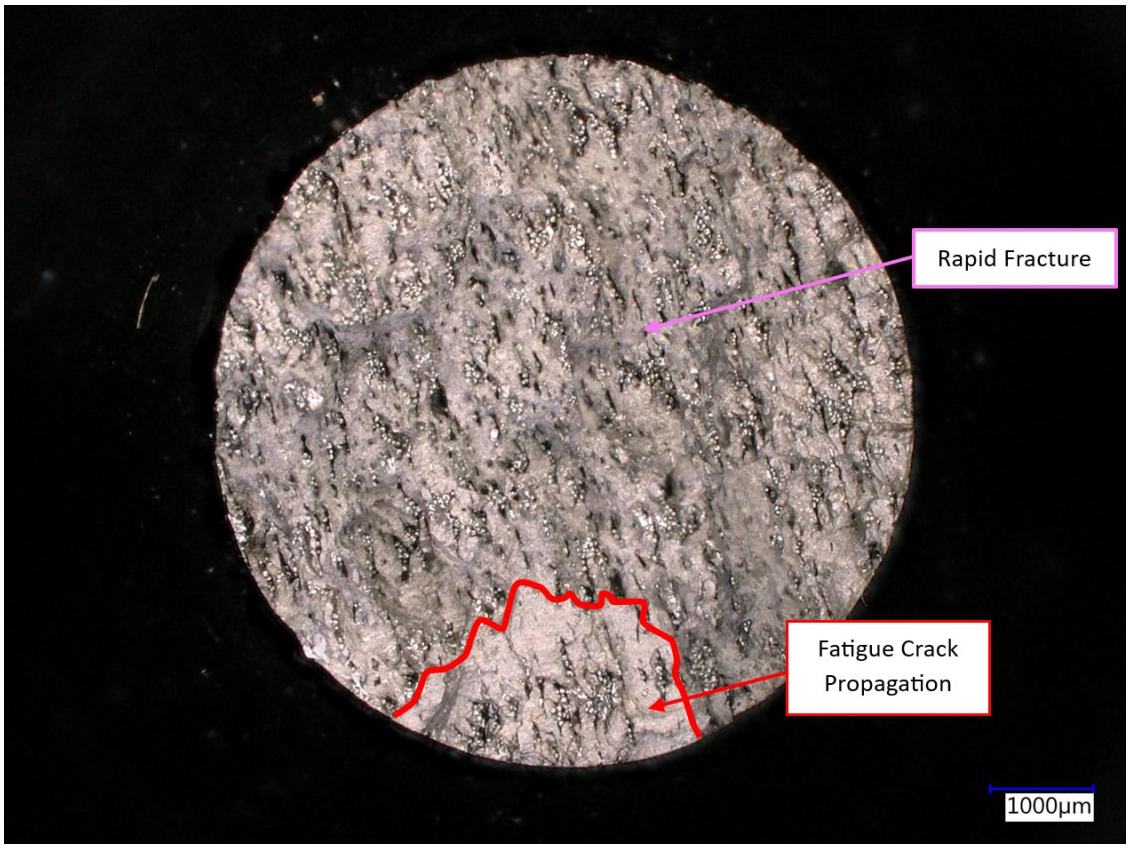

Figure 5.46 : Fatigue crack propagation and rapid fracture areas of fatigue sample 9 at 30X magnification.

The origin of the fracture is a lack of fusion defect. The fatigue crack propagation area can be identified as brighter than the rest of the surface which has undergone rapid fracture. It is possible that multiple cracks form on the surface, however only the biggest defect and neighboring defects within one diameter of the large defect are considered for this analysis. The image in Figure 5.47 is taken at 50X magnification, enlarging the fatigue crack propagation area; Murakami's effective root area method is used to determine the initial size of the crack-initiating defect. The image processing software Image J was used for this initial sizing process.

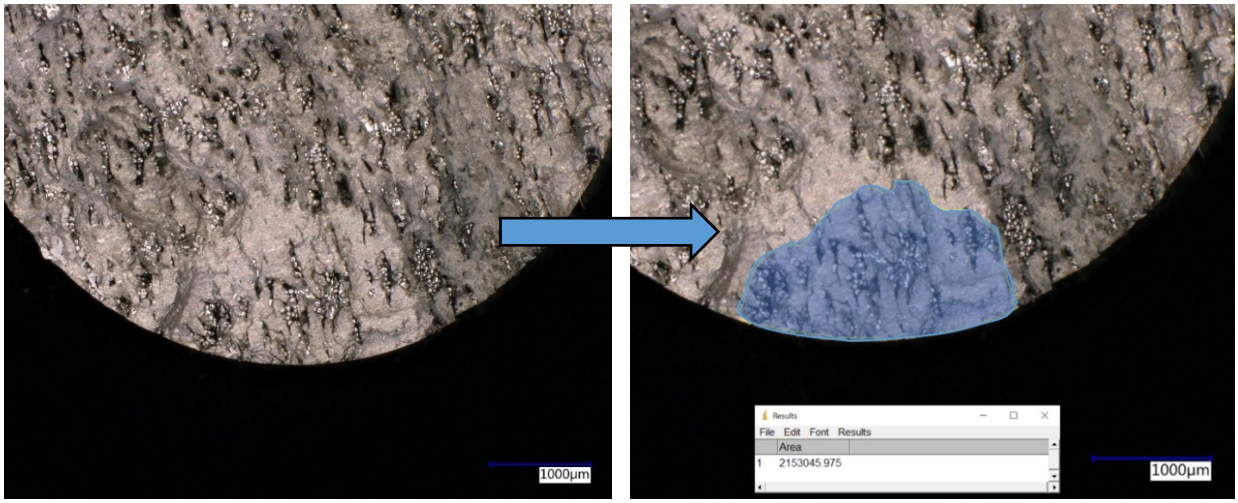

Figure 5.47 : Defect size determination from Murakami's effective root area method

According to Murakami's effective root area method, if multiple defects are close to each other, within one diameter of the largest defect, their areas are combined, as these defects could merge during the crack propagation and act as a single larger defect. In addition, with Murakami's effective root area method, the proximity to the sample surface is considered, because the initial defect can expand to the surface and cause a rapid fracture. The calculation of the defect area takes both these factors into account. The square root of the defect is calculated, which yields the root area parameter, in µm.

The next method investigated is the Feret diameter method. As opposed to Murakami's method, this method does not consider neighbor defects or proximity to the surface. The quantification of a defect using this method is shown in Figure 5.48.

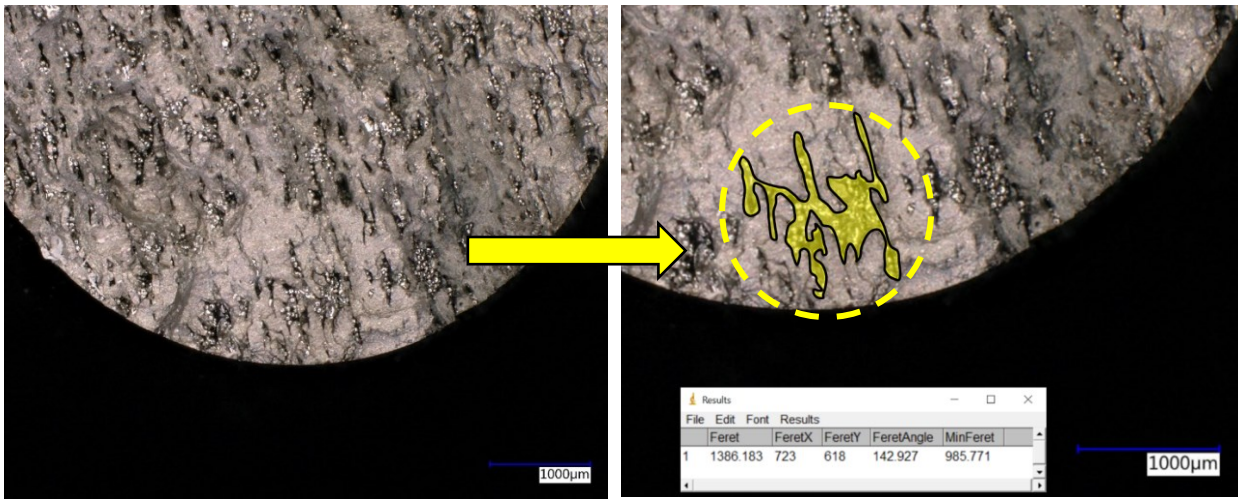

Figure 5.48 : Defect size determination from Feret diameter method

The same fracture surface analysis was performed on the 50 VED fatigue samples. Results for fatigue sample 20 are presented here as an example to illustrate the process. Visually identifiable regions on the fracture surface of sample 20 are illustrated in Figure 5.49, where the fatigue crack propagation segment is highlighted in red. This region is more easily discerned when observing the specimen outside the microscope, where the color contrast between crack propagation and rapid fracture is more pronounced. The crack propagation segment is highlighted in pink and exhibits a darker, more fibrous surface indicative of an unstable crack growth. The shear lip segment is outlined in blue. The lip is situated at a 45-degree angle on the sample's surface and corresponds to the maximum shear plane on the fracture surface.

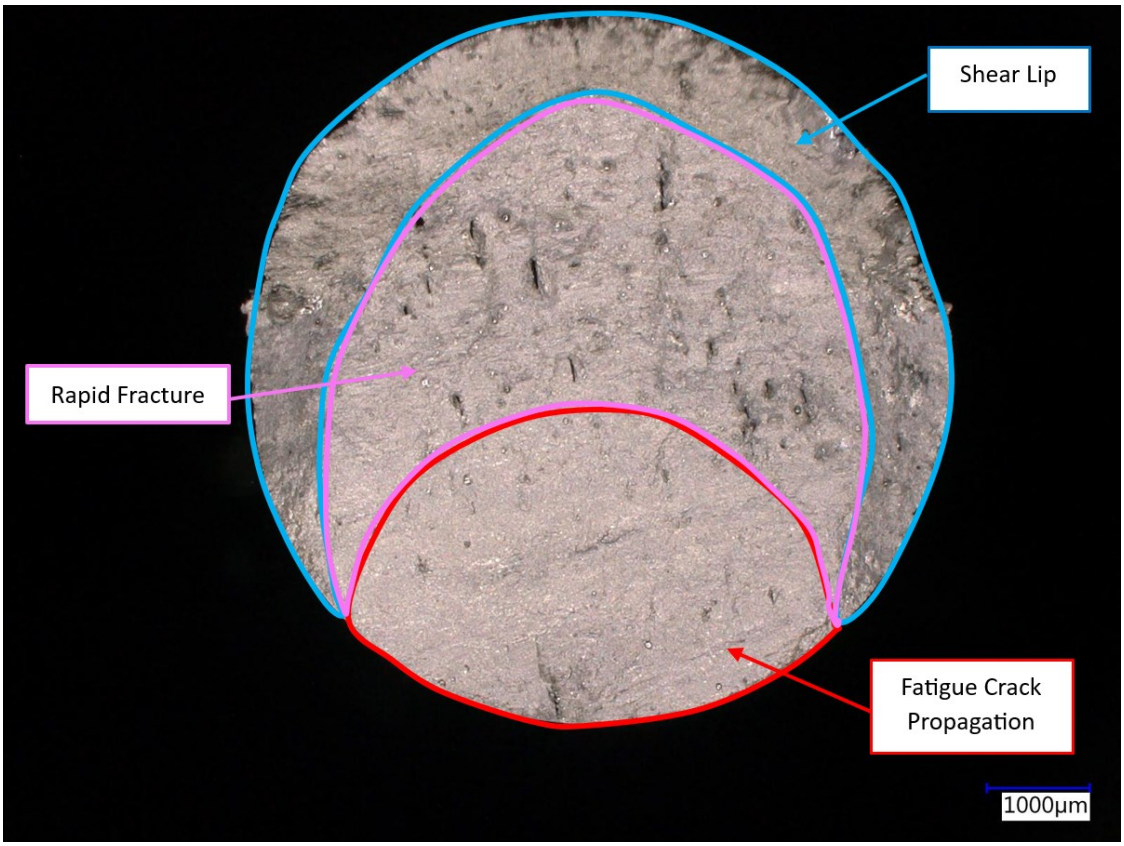

Figure 5.49 : Fatigue crack propagation, rapid fracture, and shear lip areas of fatigue sample 20.

In the case of sample 20, the origin of the fracture includes a lack of fusion defect in proximity to the surface. Following the method used for sample 9, this defect was quantified using two different methods: Murakami's root area and the Feret diameter methods. For Murakami's root area method, there is no surrounding defect, and the defect is within one diameter of the surface. The root area method therefore only includes the area extending to the surface as shown in Figure 5.50.

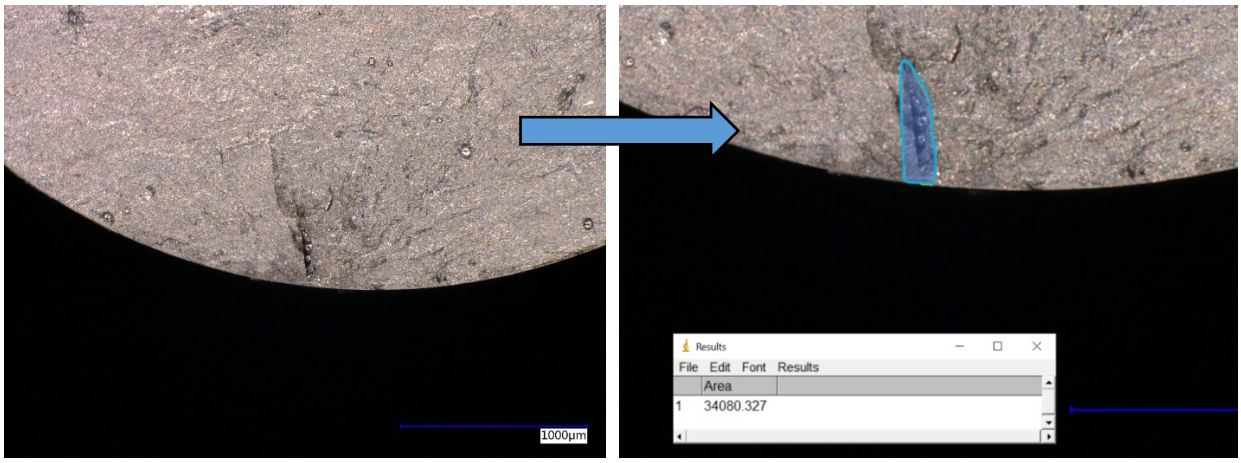

Figure 5.50 : Defect size determination from Murakami's effective root area method

The Feret diameter method does not consider neighboring defects or proximity to the surface. The quantification of a defect using this method is shown in Figure 5.51. It can be observed that in the case of isolated irregular defects, the Feret diameter method yields larger porosity defect sizes than in Murakami's effective root area method.

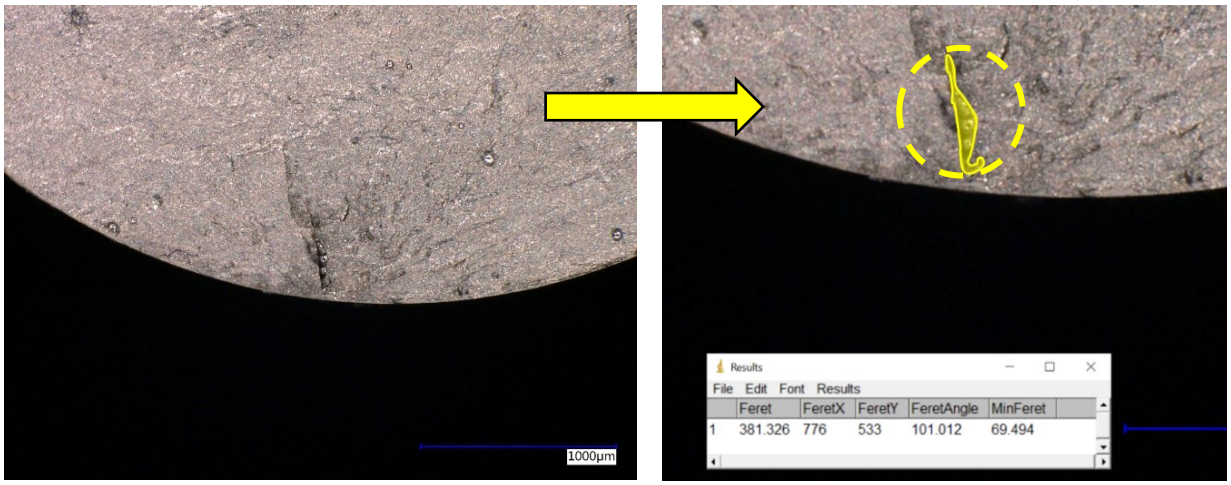

Figure 5.51 : Defect size determination from Feret diameter method

The fracture surface of fatigue sample 18, shown in Figure 5.52, is an example of a fatigue failure caused by an internal gas pore. The color contrast between the stable and unstable crack growth areas is more visible in the sample, as well as the origin of failure.

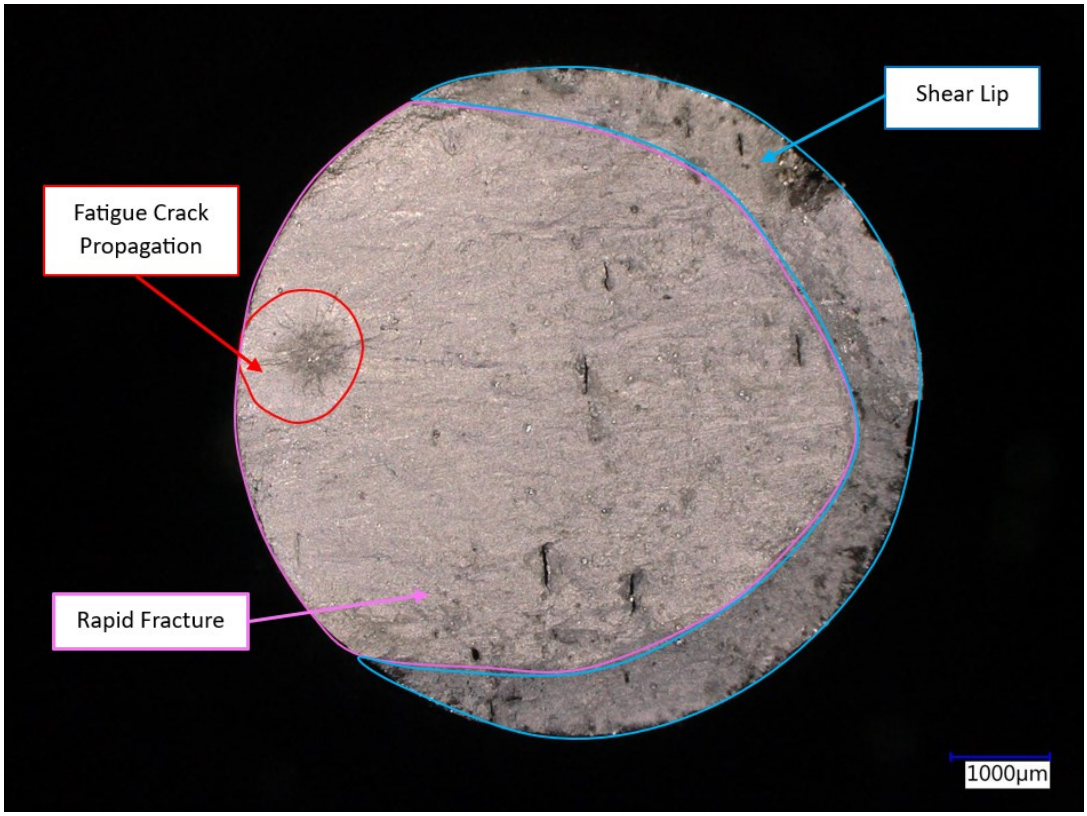

Figure 5.52 : Fatigue crack propagation, rapid fracture, and shear lip areas of fatigue sample 18.

The Feret diameter and Murakami's root area measurements are depicted in Figure 5.53 and Figure 5.54, respectively, for the case of this circular gas pore. In the case of this fatigue sample, both methods yield the same defect size.

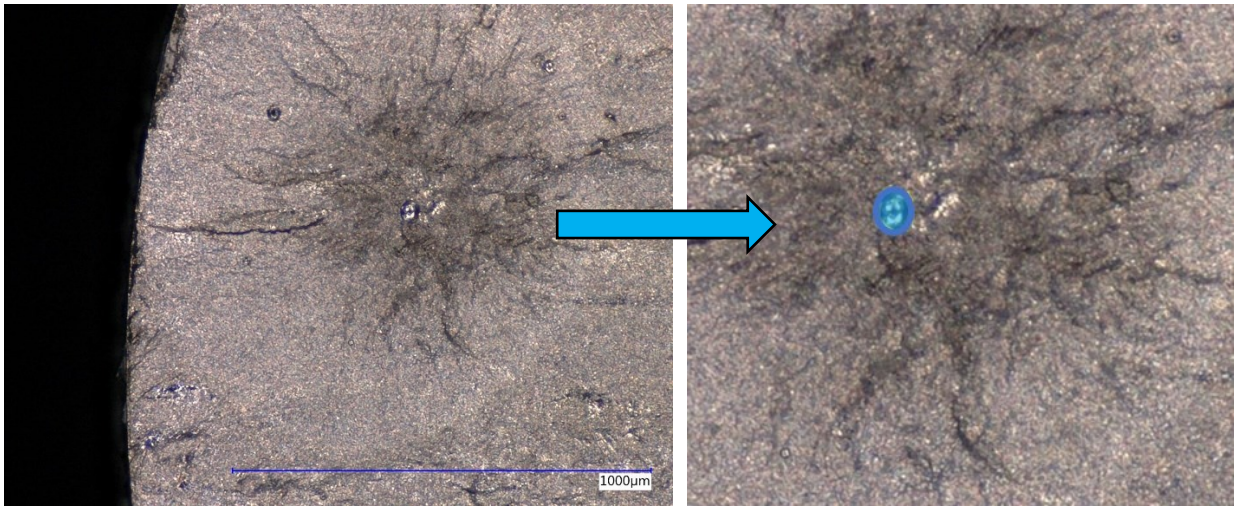

Figure 5.53 : Defect size determination from Murakami's effective root area method

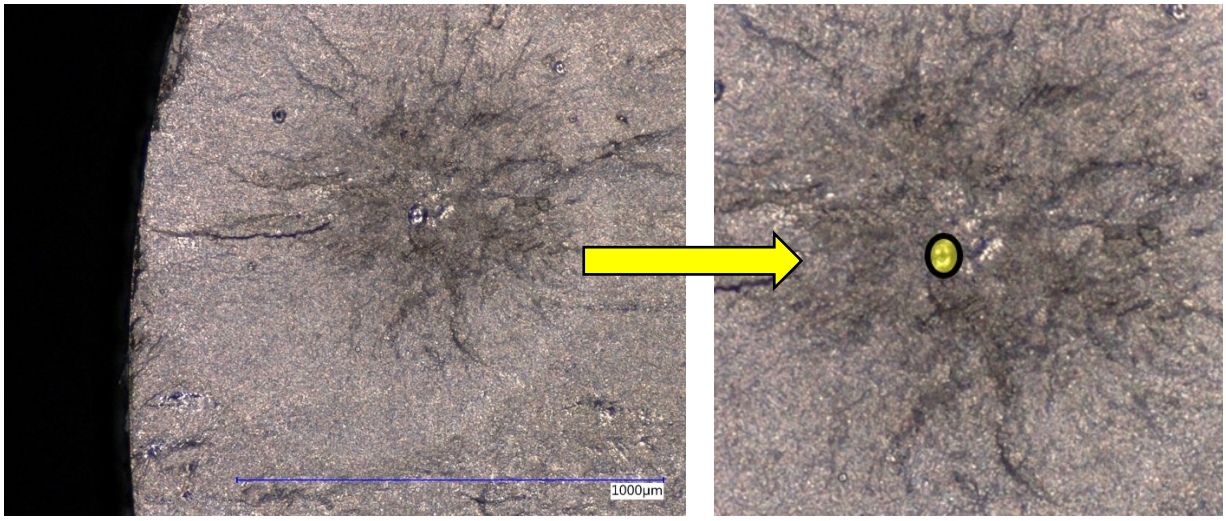

Figure 5.54 : Defect size determination from Feret diameter method

Table 5.19 presents the defect dimensions obtained using both Murakami's effective root area method and the Feret diameter method for all the fatigue samples, as well as the fatigue test stress level and cycles to failure. Each defect size is given a color coding, where red represents the largest defect size, and green the smallest.

Table 5.19 : Fatigue samples Feret Diameter and Root Area Parameters According to Cycles to Failure

VED	Fatigue Sample #	Stress (MPa)	Cycles to Failure (N_f)	Feret Diameter (µm)	$\sqrt{area_{eff}}$ (µm)
30 VED #	1	850	2494	1156.22	1255.81
	3	850	3524	1153.05	705.39
	5	850	3916	856.25	1598.33
	7	900	564	3434.72	1320.97
	9	800	2716	1386.18	1467.33
	11	700	5563	2941.56	2032.82
	13	650	8150	1242.68	1286.17
	15	625	6430	2502.16	2076.78
	19	600	12076	1035.90	1545.63
	21	500	32217	1206.85	1621.37
	23	400	41056	814.29	713.01
50 VED	2	800	119504	415.87	290.94
	4	800	206668	120.54	65.34
	6	900	9525	78.91	56.07
	8	750	19351	154.29	106.40
	10	700	148707	107.77	79.57
	12	650	607576	42.94	87.82
	14	625	988102	204.61	149.39
	16	600	367249	82.37	49.74
	18	575	1870760	59.85	45.30
	20	550	64970	381.33	184.61
	22	525	1571056	113.64	58.68

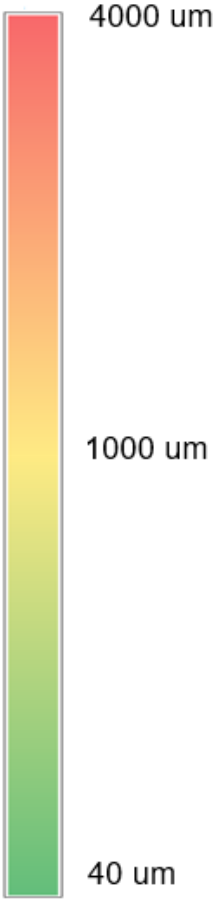

Discussion

According to the porosity analysis from MIPAR in section 5.1.3.1, the maximum Feret diameter was 186.33µm for the 50VED and 1345.42µm for the 30VED fatigue samples. The maximum equivalent diameter was 161.35 µm for the 50VED and 574.82 µm for the 30VED fatigue samples. The Feret diameter can be compared to the root area parameter because the root area parameter approximates the diameter of a circle which has the same area as the effective area determined using Murakami's method.

However, the fracture surface defect analysis yields a maximum Feret diameter of 415.87 µm for the 50VED and 3434.72 µm for the 30VED fatigue samples. The maximum equivalent root area is 290.94 µm for the 50VED samples, and 2076.78 µm for the 30VED samples.

Comparing the porosity analysis from MIPAR and fracture surface results, the estimates from MIPAR do not serve as an accurate defect size indication for the 30VED samples, where fracture surface results show that the actual defect size is more than double the estimated defect size obtained using MIPAR. The defect size estimation for the 50VED samples obtained using MIPAR also does not serve as an accurate defect size indication. Fracture surface images for samples 2 and 20 presented in Figure 5.55 and Figure 5.56 respectively, show significant LOF defects in the gauge section of the samples that were not detected in the coupons analysed with MIPAR.

Figure 5.55 : Fatigue sample 2 fracture surface with LOF defect at 50VED.

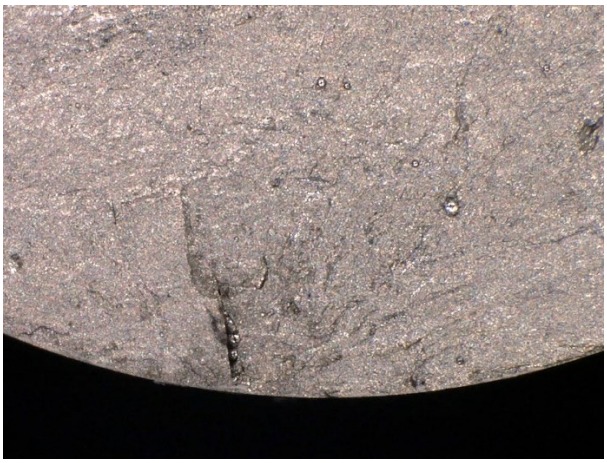

Figure 5.56 : Fatigue sample 20 fracture surface with LOF defect at 50VED.

Preliminary results from image analysis with MIPAR appear to indicate 50VED only contain gas pores, and 30VED only LOF. However, the fracture surface analysis results reveal that some of the 50VED samples had gas pores and LOF defects. This could account for the fact that some of the MIPAR estimations match the values from the fracture surface analysis, while others do not. Fatigue samples 2 and 20 are examples of fatigue samples containing isolated LOF defects. The fracture surface defect analysis yields a maximum Feret diameter of 415.87 µm and a maximum equivalent root area of 290.94 µm for sample 2. The fracture surface defect analysis yields a maximum Feret diameter of 381.33 µm and a maximum equivalent root area of 184.61 µm for sample 20. The MIPAR image analysis yields a maximum Feret diameter of 184.05 µm and a maximum equivalent root area of 148.07 µm.

The defect size estimation using MIPAR for the 50VED samples containing only gas pores offers better estimation. The fracture surface analysis yields a maximum Feret diameter of 204.61µm, and a maximum equivalent root area of 149.39µm for gas porosity in fatigue sample 14. The MIPAR image analysis yields a maximum Feret diameter of 184.05 µm and a maximum equivalent root area of 148.07 µm. Both the Feret diameter and Murakami's equivalent root area methods estimated from MIPAR for gas porosity are within 9% for the Feret Diameter and within 8% for the root area of the actual defect size on the fracture surface.

The color coding from Table 5.19 was combined with the stress-cycle to failure curve of Figure 5.45 to provide a visual representation of the effect of defect size on fatigue behavior. This technique is taken from the study by Tammas-Williams et al. [64] discussed in Section 2.6.2. Figure 5.57 presents the stress-cycle to failure curve with color gradients from the defect Feret diameter, while Figure 5.58 presents the stress-cycle to failure curve with color gradients from the root area method. Both Figure 5.57 and Figure 5.58 illustrate that larger defects yield a shorter fatigue life. Two clear trends can be observed for the 30 VED and 50 VED samples, as shown in Figure 5.59.

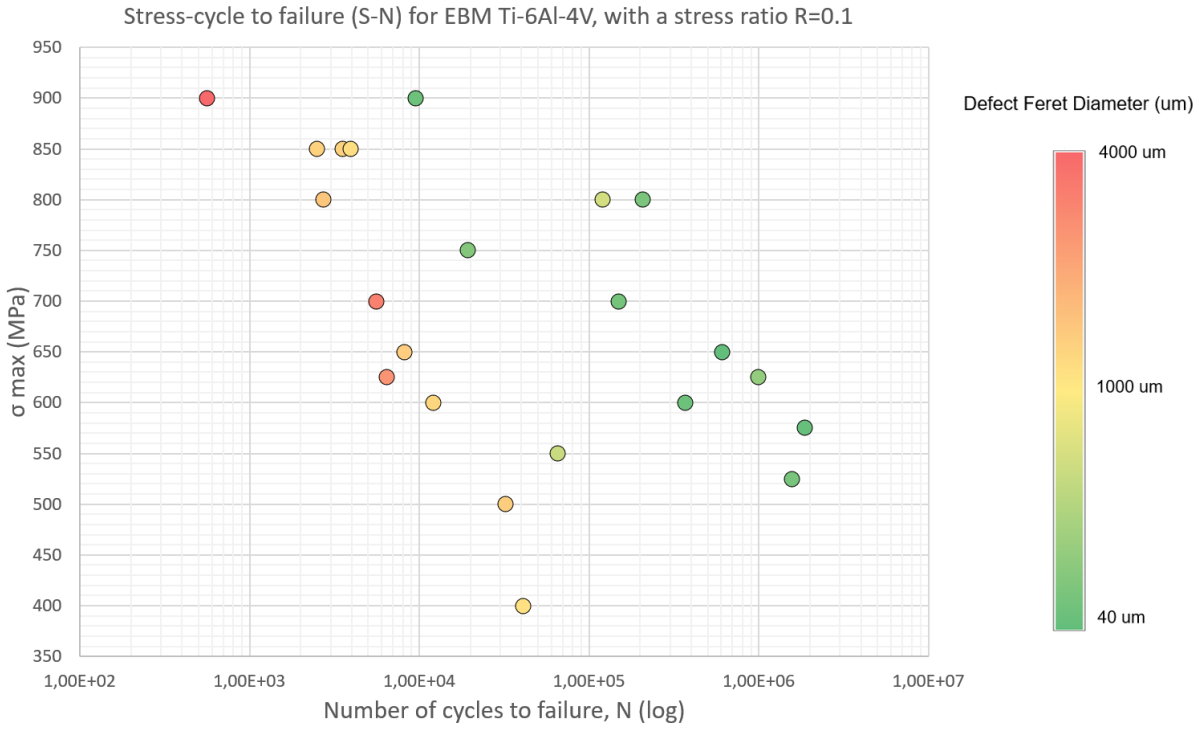

Figure 5.57 : Stress-cycle to failure (S-N) curve for EBM Ti64 at a stress ratio of R=0.1 with defect Feret diameter.

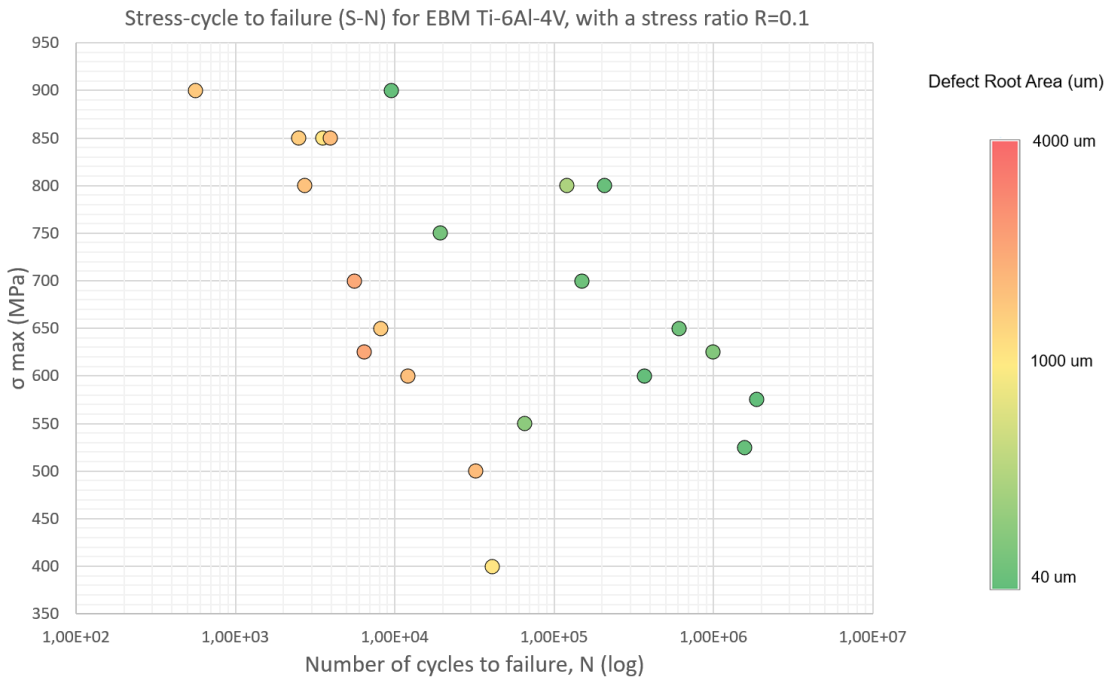

Figure 5.58 : Stress-cycle to failure (S-N) curve for EBM Ti64 at a stress ratio of R=0.1 with defect root area.

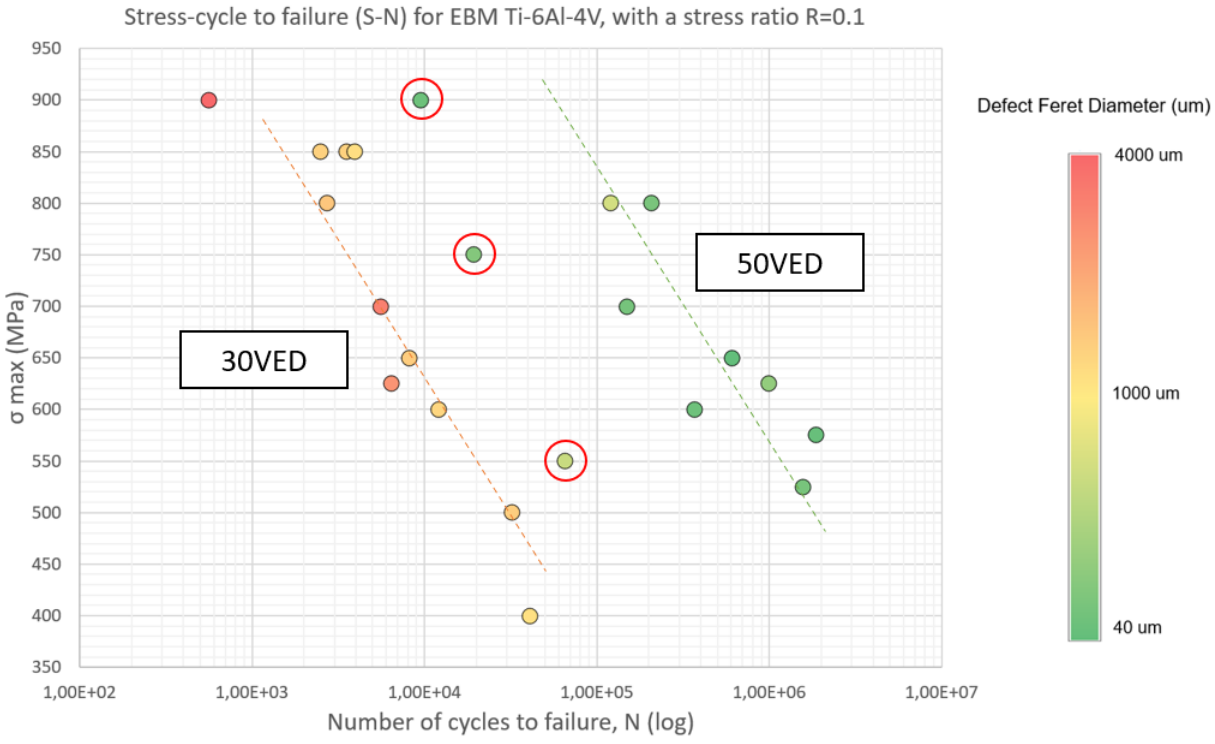

Figure 5.59 : 30VED, 50VED, and outlying individual samples in stress-cycle to failure curve.

Figure 5.57 and Figure 5.58 reveal a consistent trend in both the Feret diameter and Murakami's effective root area for the examined fatigue samples. Notably, larger defects in red and yellow demonstrate a shorter fatigue life compared to the smaller defects in green.

The fatigue curves presented for both 30VED and 50VED samples are estimations and should be interpreted as approximations, as the testing procedure for both 50VED and 30VED sample lacked the threefold repetitions at each load level required to yield precise values for fatigue behavior.

Three outliers are circled in red in Figure 5.59, denoting samples that experienced premature failure relative to others in the same VED category. These occurrences can be attributed to unique defects that could not be fully characterized using the Feret diameter or Murakami's effective root area measurements. Specifically, in the case of the 50VED samples deviating from the curve (samples 6, 8, and 20), samples 6 and 8 exhibited defects connecting to the surface, resulting in a shorter fatigue life despite possessing similar effective root areas or Feret diameters as other samples. Sample 8 featured a sharp near-surface defect, rendering it more susceptible to propagation and early failure despite its comparable size to other defects.

Given the incomplete characterization of surface-connected and sharp-contoured defect types and their fatigue failure criteria in the current experiment, further investigations are required to fully understand their influence on the behavior of Ti64 EBM prints. In the case of this experiment, each sample contained unique defects sizes and geometries, contributing to varying fatigue limits across the samples.

5.2.2.4 Energy-dispersive x-ray spectroscopy

Results

Energy dispersive x ray spectroscopy was performed on six fatigue samples to check for possible contamination at the fracture site. Three 50VED samples and three 30VED samples were analysed. Between 3 and 5 points, referred to as spectrums, were analysed for each specimen.

Figure 5.60 presents the five spectroscopy spectrums selected for fatigue sample 5, and Table 5.20 presents the elemental composition in weight percent for each spectrum.

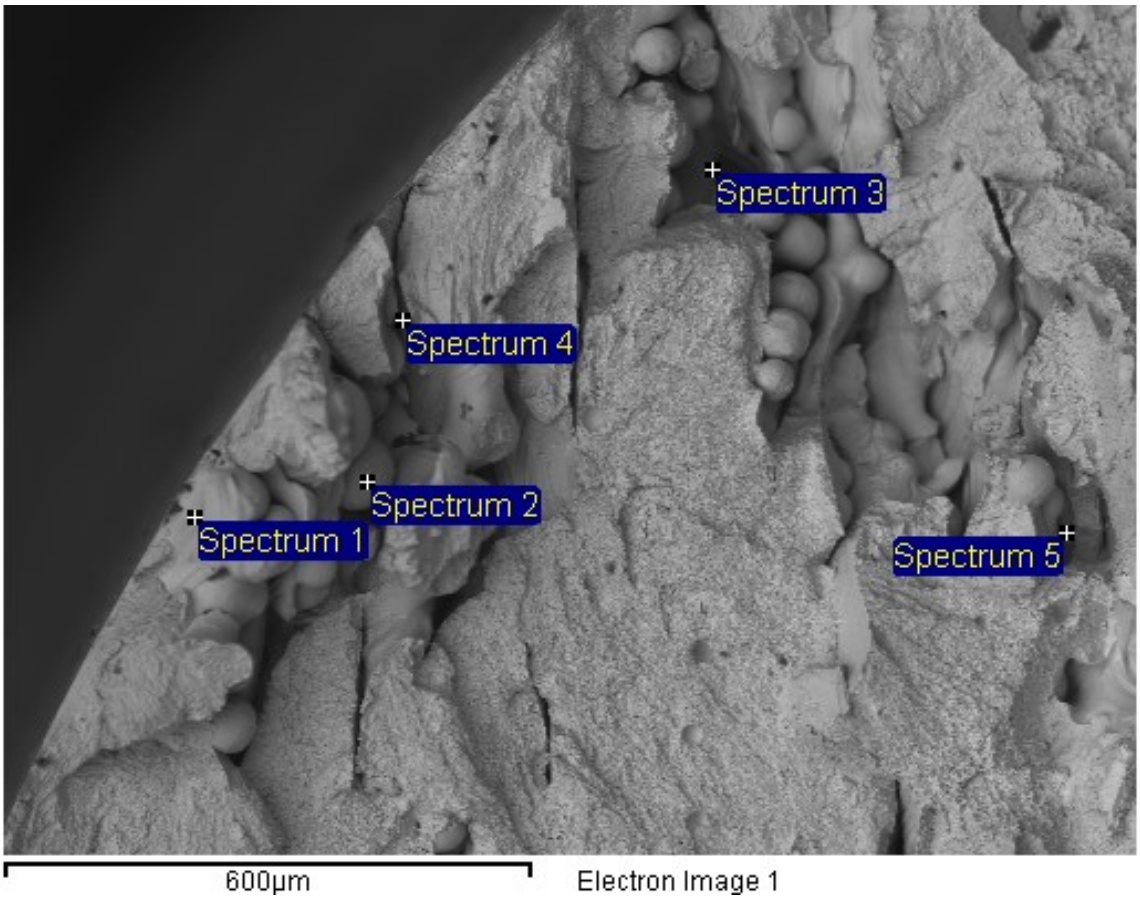

Figure 5.60 : Fatigue sample 5 energy-dispersive x-ray spectroscopy.

Table 5.20 : Elemental Composition per Spectrum for Fatigue Sample 5

Spectrum	Oxygen	Aluminum	Titanium	Vanadium	Total
Spectrum 1	3.4	4.9	87.8	3.9	100.0
Spectrum 2	0.0	3.2	89.9	6.9	100.0
Spectrum 3	0.0	5.8	88.3	5.9	100.0
Spectrum 4	0.0	1.4	84.8	13.8	100.0
Spectrum 5	0.0	5.3	87.4	7.3	100.0
Average	0.7	4.1	87.6	76	100.0

Figure 5.61 presents the five spectroscopy spectrums selected for fatigue sample 18, which also exhibited oxygen contamination. Table 5.21 presents the elemental composition in weight percent for each spectrum.

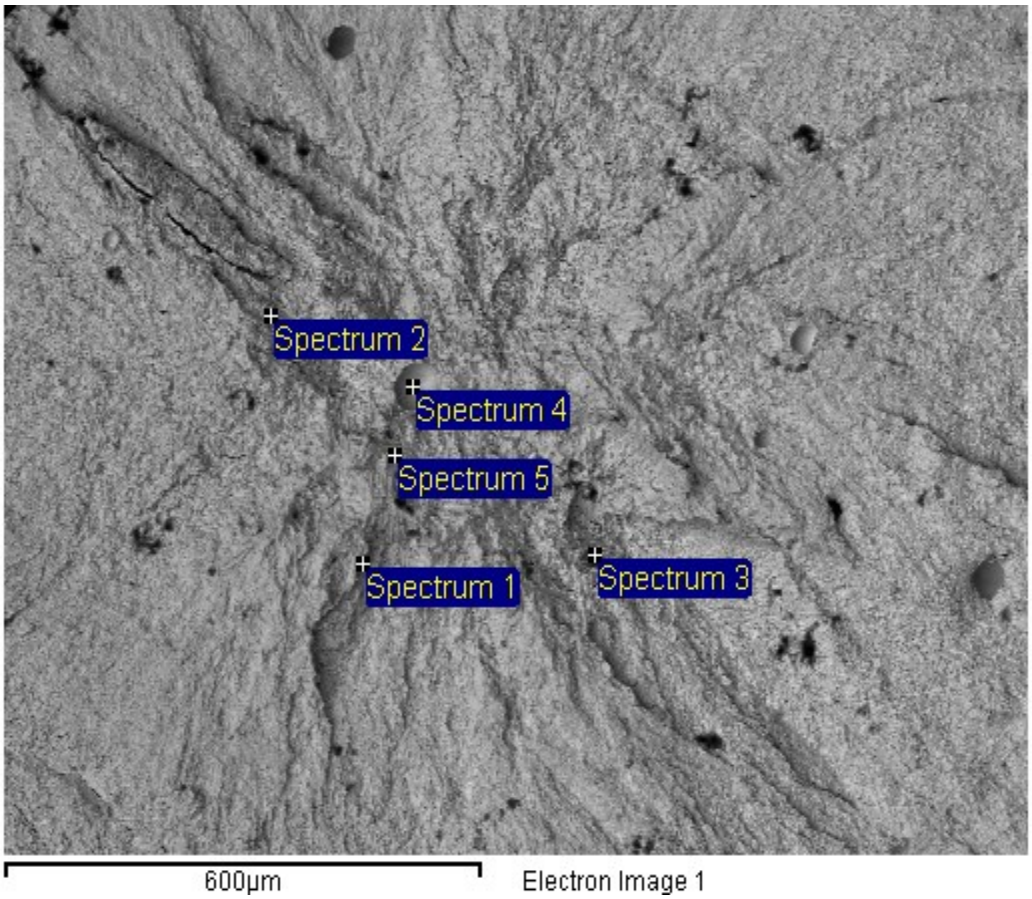

Figure 5.61 : Fatigue sample 20 energy-dispersive x-ray spectroscopy.

Table 5.21 : Elemental composition per spectrum for fatigue sample 20

Spectrum	Oxygen	Aluminum	Sulfur	Titanium	Vanadium	Chromium	Nickel	Total
Spectrum 1	0.0	0.5	0.0	96.9	2.6	0.0	0.0	100.0
Spectrum 2	0.0	0.3	0.0	96.3	3.5	0.0	0.0	100.0
Spectrum 3	15.4	4.9	0.3	71.2	5.1	0.8	2.2	100.0
Spectrum 4	0.0	0.4	0.0	96.9	2.7	0.0	0.0	100.0
Spectrum 5	0.0	3.6	0.0	92.7	3.7	0.0	0.0	100.0
Average	3.1	2.0	0.1	90.8	3.5	0.2	0.4	100.0

Discussion

Spectrum 1 of fatigue sample 5 had some oxygen contamination around the fracture origin. Although the EBM build process is performed under vacuum, it is possible that the oxygen contamination is a result of the powder production process, forming a titanium or vanadium oxide. Alternatively, the oxygen contamination could be due to some residual oxygen in the build chamber. Spectrum 3 of fatigue sample 20 has some oxygen contamination, with some nickel and chromium contamination in the same spectrum. The previous print in the EBM equipment used to print the fatigue samples was a nickel superalloy, which is most likely the cause of the presence of nickel-chromium oxide inside the print. The black dots visible on the electron microscope images are plastic particles from the transport storage bags the samples were placed in and are not contaminants. Two of the six fatigue samples analyzed using energy-dispersive x-ray spectroscopy contained some oxygen contamination. This contamination, along with the presence of surrounding defects, could be the cause of failure during the fatigue testing. One of the two samples also contained contamination from a previous print, which could highlight the importance of allocating one material to one machine in an industrial production setting.

In addition to the fatigue samples, several tensile samples were verified for contamination. A contamination area found on tensile sample 5 is shown in Figure 5.62. A particle of nickel was found on the prepared surface of the sample and can be seen in in Figure 5.62. A depletion of titanium can be observed in the contamination area.

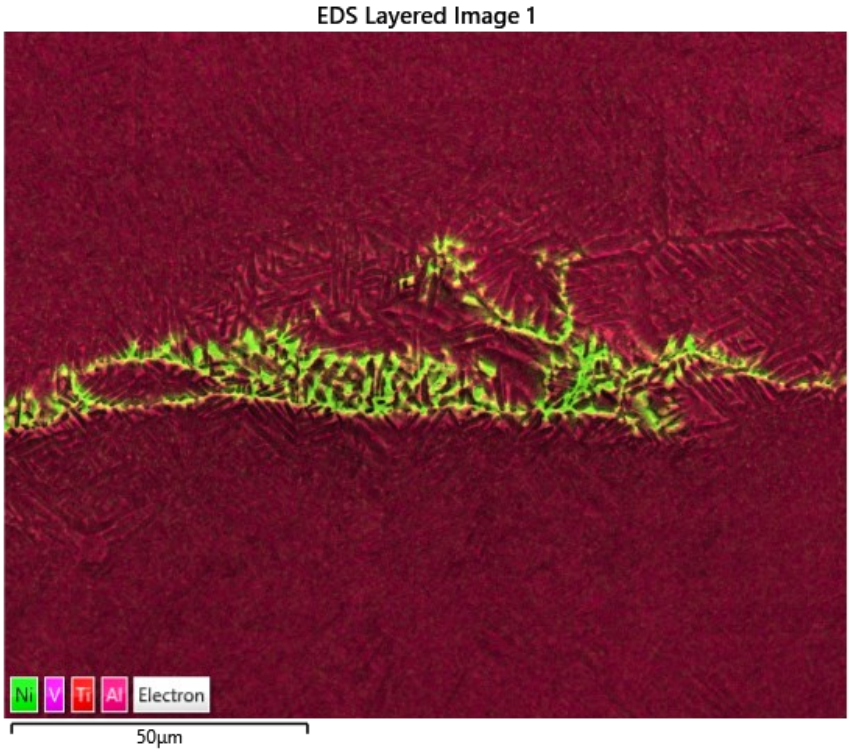

Figure 5.62 : Nickel contamination in tensile sample 5

Chapter 6 Conclusion

Tests and investigations conducted during this study lead to the following observations with respect to the research questions stated earlier.

- Individual process parameters have a distinct influence on the porosity of the prints printed with the same VED. VED cubes having the same energy density, but different beam currents and scan speeds have different levels of porosity. This suggests that the layer height and line offset should be adjusted for the types of defects present in the sample.

- VED alone is not a determining factor for alpha lath thickness, as shown by the examination of the VED cubes. Cubes printed with different volumetric energy densities have no statistically significant differences in terms of grain size. A study including the variation of individual parameters would be necessary to understand how each parameter affects the alpha lath thickness in Ti64.

- VED alone is not a determining factor for variations in tensile properties. Samples printed with different volumetric energy densities have no statistically significant differences in terms of tensile properties. A study including the variation of individual parameters would be necessary to understand how each parameter affects the tensile properties of Ti64.

- Porosity and the size of defects do significantly influence tensile properties. However, these factors significantly impact the fatigue life of EBM samples. Specifically, samples with larger defects exhibit a shorter fatigue life compared to a set of samples with smaller defects.

- Optical microscopy analysis of print coupons for the 50VED fatigue samples containing only gas porosity yield estimations within 9% for the Feret Diameter of defects and within 8% for the equivalent root area parameter. 50VED fatigue samples containing both gas porosity and LOF defects yield estimates which are significantly different from the actual values measured from the fracture surface. This suggests that, in the case of specimens containing only gas porosity defects, employing smaller coupons for larger prints with the aim of estimating print quality could serve as an efficient method to obtain an initial assessment of porosity without resorting to more expensive techniques such as CT scanning.

Chapter 7 Future work

This study offers a comprehensive overview of the microstructure, tensile properties, and fatigue properties of selected Ti64 samples produced using Electron Beam Melting (EBM). While providing a general understanding of these properties, further experimental work is necessary to gain a thorough comprehension of the microstructure, tensile properties, and fatigue properties of Ti64 EBM, and how print parameters affect these properties.

A primary recommendation to advance this investigation involves the printing of an additional set of cubes, focusing on individual parameters rather than Volumetric Energy Density (VED), to observe microstructural variations. In the current experiment, the simultaneous variation of beam current and scan speed to obtain different VEDs was employed. Conducting experiments with the variation of one parameter at a time would allow the understanding of how each parameter influences the printed microstructure. The sensitivity of each print parameter on microstructure could also be examined to allow a better understanding of the rationale in selecting specific print parameters to obtain a target alpha lath thickness according to the desired application.

Furthermore, the author proposes a better examination of porosity to ensure the full density of prints before testing. Notably, the porosity of the VED cubes in this experiment exhibited significant variations between samples. Observing defect types during the cube printing stage and evaluating intertrack or interlayer defects would enable adjustments with parameters such as layer height and line offset. After these adjustments, a comparative analysis between microscope examination and Mercury Intrusion Porosimetry (MIP) could be conducted to obtain a comprehensive understanding of porosity throughout the sample. It is important to note that if MIP is utilized, the chosen pressure should allow the detection of large pores. Other techniques to obtain defect geometries such as a Computed Tomography (CT) scan could also be used.

Finally, the author recommends conducting the fatigue experiments with a larger number of samples. Ensuring an adequate number of samples is available for each stress level, with at least three repetitions, including runout samples, is important to ensure the obtained data points are accurate. In the current experiment, the limited number of 12 samples for each VED prevented the determination of the fatigue limit, a critical design characteristic. For instance, in the 50VED experiment, starting stress levels at 900MPa with a first runout at 500MPa require testing samples for each 50MPa increment, resulting in a total of at least 30 samples per set to achieve a robust understanding of fatigue behavior.

Chapter 8 Bibliography

[1] *Metal Additive Manufacturing*, 1st ed. John Wiley & Sons, Ltd, 2021. doi: 10.1002/9781119210801.

[2] C. de Formanoir, S. Michotte, O. Rigo, L. Germain, and S. Godet, "Electron beam melted Ti–6Al–4V: Microstructure, texture and mechanical behavior of the as-built and heat-treated material," *Mater. Sci. Eng. A*, vol. 652, pp. 105–119, Jan. 2016, doi: 10.1016/j.msea.2015.11.052.

[3] P. Karimi, M. K. Keshavarz, E. Sadeghi, M. Habibnejad, and M. Vlasea, "Interplay of process, microstructure, and mechanical performance in electron beam-powder bed fusion of Ti48Al2Nb2Cr," *Addit. Manuf.*, vol. 77, p. 103811, Sep. 2023, doi: 10.1016/j.addma.2023.103811.

[4] T.-I. Hsu, Y.-T. Jhong, and M.-H. Tsai, "Effect of Gradient Energy Density on the Microstructure and Mechanical Properties of Ti6Al4V Fabricated by Selective Electron Beam Additive Manufacture," *Materials*, vol. 13, no. 7, p. 1509, Mar. 2020, doi: 10.3390/ma13071509.

[5] "OM Operation Manual Q10plus."

[6] C. Scott, "Arcam Opens EBM A2X 3D Printer's Development Mode to Academic Institutions," 3DPrint.com | The Voice of 3D Printing / Additive Manufacturing. Accessed: Nov. 21, 2023. [Online]. Available: https://3dprint.com/218545/arcam-ebm-a2x-development/

[7] "HI-AM Themes," HI-AM. Accessed: Nov. 28, 2023. [Online]. Available: https://nserc-hi-am.ca/themes/

[8] N. Hrabe and T. Quinn, "Effects of processing on microstructure and mechanical properties of a titanium alloy (Ti–6Al–4V) fabricated using electron beam melting (EBM), Part 2: Energy input, orientation, and location," *Mater. Sci. Eng. A*, vol. 573, pp. 271–277, Jun. 2013, doi: 10.1016/j.msea.2013.02.065.

[9] T. Scharowsky, V. Juechter, R. F. Singer, and C. Körner, "Influence of the Scanning Strategy on the Microstructure and Mechanical Properties in Selective Electron Beam Melting of Ti–6Al–4V," *Adv. Eng. Mater.*, vol. 17, no. 11, pp. 1573–1578, 2015, doi: 10.1002/adem.201400542.

[10] K. Puebla, L. E. Murr, S. M. Gaytan, E. Martinez, F. Medina, and R. B. Wicker, "Effect of Melt Scan Rate on Microstructure and Macrostructure for Electron Beam Melting of Ti-6Al-4V," *Mater. Sci. Appl.*, vol. 3, no. 5, Art. no. 5, May 2012, doi: 10.4236/msa.2012.35038.

[11] N. Hrabe, T. Gnäupel-Herold, and T. Quinn, "Fatigue properties of a titanium alloy (Ti–6Al–4V) fabricated via electron beam melting (EBM): Effects of internal defects and residual stress," *Int. J. Fatigue*, vol. 94, pp. 202–210, Jan. 2017, doi: 10.1016/j.ijfatigue.2016.04.022.

[12] J. Ran, F. Jiang, X. Sun, Z. Chen, C. Tian, and H. Zhao, "Microstructure and Mechanical Properties of Ti-6Al-4V Fabricated by Electron Beam Melting," *Crystals*, vol. 10, no. 11, Art. no. 11, Nov. 2020, doi: 10.3390/cryst10110972.

[13] S. S. Al-Bermani, M. L. Blackmore, W. Zhang, and I. Todd, "The Origin of Microstructural Diversity, Texture, and Mechanical Properties in Electron Beam Melted Ti-6Al-4V," *Metall. Mater. Trans. A*, vol. 41, no. 13, pp. 3422–3434, Dec. 2010, doi: 10.1007/s11661-010-0397-x.

[14] M. Galati, “Electron beam melting process,” 2021, pp. 277–301. doi: 10.1016/B978-0-12-818411-0.00014-8.
[15] M. Madeja and R. Dziedzic, “Speed function effects on properties of Ti-5Al-5Mo-5 V-1Cr-1Fe alloy manufactured by electron beam melting,” *Int. J. Adv. Manuf. Technol.*, vol. 128, pp. 1–14, Sep. 2023, doi: 10.1007/s00170-023-12213-3.
[16] E. Sadeghi *et al.*, “A state-of-the-art review on fatigue performance of powder bed fusion-built alloy 718,” *Prog. Mater. Sci.*, vol. 133, p. 101066, Mar. 2023, doi: 10.1016/j.pmatsci.2022.101066.
[17] P. Karimi, E. Sadeghi, J. Ålgårdh, and J. Andersson, “EBM-manufactured single tracks of Alloy 718: Influence of energy input and focus offset on geometrical and microstructural characteristics,” *Mater. Charact.*, vol. 148, pp. 88–99, Feb. 2019, doi: 10.1016/j.matchar.2018.11.033.
[18] “Post-Processing for Metal 3D Printing | Design Tip.” Accessed: Jan. 30, 2024. [Online]. Available: https://www.protolabs.com/resources/design-tips/post-processing-for-metal-3d-printing/
[19] M. Ahlfors, F. Bahbou, and U. Ackelid, “Optimizing HIP and printing parameters for EBM Ti-6Al-4V,” Sep. 2018.
[20] S. Liu and Y. C. Shin, “Additive manufacturing of Ti6Al4V alloy: A review,” *Mater. Des.*, vol. 164, p. 107552, Feb. 2019, doi: 10.1016/j.matdes.2018.107552.
[21] S. Tammas-Williams, P. J. Withers, I. Todd, and P. B. Prangnell, “The Effectiveness of Hot Isostatic Pressing for Closing Porosity in Titanium Parts Manufactured by Selective Electron Beam Melting,” *Metall. Mater. Trans. A*, vol. 47, no. 5, pp. 1939–1946, May 2016, doi: 10.1007/s11661-016-3429-3.
[22] C. Liu *et al.*, “Effect of Hot Isostatic Pressing on Microstructures and Mechanical Properties of Ti6Al4V Fabricated by Electron Beam Melting,” *Metals*, vol. 10, no. 5, Art. no. 5, May 2020, doi: 10.3390/met10050593.
[23] S. L. Lu *et al.*, “Intensified texture in selective electron beam melted Ti-6Al-4V thin plates by hot isostatic pressing and its fundamental influence on tensile fracture and properties,” *Mater. Charact.*, vol. 152, pp. 162–168, Jun. 2019, doi: 10.1016/j.matchar.2019.04.019.
[24] S. L. Lu, H. P. Tang, Y. P. Ning, N. Liu, D. H. StJohn, and M. Qian, “Microstructure and Mechanical Properties of Long Ti-6Al-4V Rods Additively Manufactured by Selective Electron Beam Melting Out of a Deep Powder Bed and the Effect of Subsequent Hot Isostatic Pressing,” *Metall. Mater. Trans. A*, vol. 46, no. 9, pp. 3824–3834, Sep. 2015, doi: 10.1007/s11661-015-2976-3.
[25] T. Persenot, G. Martin, R. Dendievel, J.-Y. Buffiére, and E. Maire, “Enhancing the tensile properties of EBM as-built thin parts: Effect of HIP and chemical etching,” *Mater. Charact.*, vol. 143, pp. 82–93, Sep. 2018, doi: 10.1016/j.matchar.2018.01.035.
[26] J. Wang, H. P. Tang, K. Yang, N. Liu, L. Jia, and M. Qian, “Selective Electron Beam Manufacturing of Ti-6Al-4V Strips: Effect of Build Orientation, Columnar Grain Orientation, and Hot Isostatic Pressing on Tensile Properties,” *JOM*, vol. 70, no. 5, pp. 638–643, May 2018, doi: 10.1007/s11837-018-2794-3.
[27] V. Popov, A. Katz-Demyanetz, A. Garkun, G. Muller, E. Strokin, and H. Rosenson, “Effect of Hot Isostatic Pressure treatment on the Electron-Beam Melted Ti-6Al-4V specimens,” *Procedia Manuf.*, vol. 21, pp. 125–132, Jan. 2018, doi: 10.1016/j.promfg.2018.02.102.

[28] G. Mirone, R. Barbagallo, and S. Di Bella, “Effect of process parameters on the mechanical properties of a Titanium alloy fabricated by Electron Beam Melting (EBM),” *IOP Conf. Ser. Mater. Sci. Eng.*, vol. 1214, no. 1, p. 012001, Jan. 2022, doi: 10.1088/1757-899X/1214/1/012001.
[29] K.-H. Chang, “Rapid Prototyping,” in *e-Design*, Elsevier, 2015, pp. 743–786. doi: 10.1016/B978-0-12-382038-9.00014-4.
[30] A. Kirchner, B. Klöden, J. Luft, T. Weißgärber, and B. Kieback, “Process window for electron beam melting of Ti-6Al-4V,” *Powder Metall.*, vol. 58, no. 4, pp. 246–249, Aug. 2015, doi: 10.1179/0032589915Z.000000000244.
[31] C. R. Pobel, C. Arnold, F. Osmanlic, Z. Fu, and C. Körner, “Immediate development of processing windows for selective electron beam melting using layerwise monitoring via backscattered electron detection,” *Mater. Lett.*, vol. 249, pp. 70–72, Aug. 2019, doi: 10.1016/j.matlet.2019.03.048.
[32] X. Ding, Y. Koizumi, D. Wei, and A. Chiba, “Effect of process parameters on melt pool geometry and microstructure development for electron beam melting of IN718: A systematic single bead analysis study,” *Addit. Manuf.*, vol. 26, pp. 215–226, Mar. 2019, doi: 10.1016/j.addma.2018.12.018.
[33] S. Ghosh *et al.*, “Single-Track Melt-Pool Measurements and Microstructures in Inconel 625,” *JOM*, vol. 70, no. 6, pp. 1011–1016, Jun. 2018, doi: 10.1007/s11837-018-2771-x.
[34] H. Helmer, A. Bauereiß, R. F. Singer, and C. Körner, “Grain structure evolution in Inconel 718 during selective electron beam melting,” *Mater. Sci. Eng. A*, vol. 668, pp. 180–187, Jun. 2016, doi: 10.1016/j.msea.2016.05.046.
[35] W. Sames, “Additive Manufacturing of Inconel 718 using Electron Beam Melting: Processing, Post-Processing, & Mechanical Properties,” Thesis, 2015. Accessed: Nov. 29, 2023. [Online]. Available: https://oaktrust.library.tamu.edu/handle/1969.1/155230
[36] I. Yadroitsev, P. Krakhmalev, I. Yadroitsava, S. Johansson, and I. Smurov, “Energy input effect on morphology and microstructure of selective laser melting single track from metallic powder,” *J. Mater. Process. Technol.*, vol. 213, no. 4, pp. 606–613, Apr. 2013, doi: 10.1016/j.jmatprotec.2012.11.014.
[37] J. Moritz *et al.*, “Influence of Electron Beam Powder Bed Fusion Process Parameters at Constant Volumetric Energy Density on Surface Topography and Microstructural Homogeneity of a Titanium Aluminide Alloy,” *Adv. Eng. Mater.*, vol. 25, no. 15, p. 2201871, Aug. 2023, doi: 10.1002/adem.202201871.
[38] X. Gong, J. Lydon, K. Cooper, and K. Chou, “Beam speed effects on Ti–6Al–4V microstructures in electron beam additive manufacturing,” *J. Mater. Res.*, vol. 29, no. 17, pp. 1951–1959, Sep. 2014, doi: 10.1557/jmr.2014.125.
[39] A. T. Silvestri, S. Foglia, R. Borrelli, S. Franchitti, C. Pirozzi, and A. Astarita, “Electron beam melting of Ti6Al4V: Role of the process parameters under the same energy density,” *J. Manuf. Process.*, vol. 60, pp. 162–179, Dec. 2020, doi: 10.1016/j.jmapro.2020.10.065.
[40] A. Mostafaei *et al.*, “Defects and anomalies in powder bed fusion metal additive manufacturing,” *Curr. Opin. Solid State Mater. Sci.*, vol. 26, no. 2, p. 100974, Apr. 2022, doi: 10.1016/j.cossms.2021.100974.
[41] H. Gong, K. Rafi, H. Gu, T. Starr, and B. Stucker, “Analysis of defect generation in Ti–6Al–4V parts made using powder bed fusion additive manufacturing processes,” *Addit. Manuf.*, vol. 1–4, pp. 87–98, Oct. 2014, doi: 10.1016/j.addma.2014.08.002.

[42] S. L. Lu *et al.*, “Prior β grain evolution and phase transformation of selective laser melted Ti6Al4V alloy during heat treatment,” *J. Alloys Compd.*, vol. 914, p. 165235, Sep. 2022, doi: 10.1016/j.jallcom.2022.165235.
[43] X. Tan *et al.*, “Graded microstructure and mechanical properties of additive manufactured Ti–6Al–4V via electron beam melting,” *Acta Mater.*, vol. 97, pp. 1–16, Sep. 2015, doi: 10.1016/j.actamat.2015.06.036.
[44] Z. Fang *et al.*, “Powder metallurgy of titanium – past, present, and future,” *Int. Mater. Rev.*, vol. 63, pp. 1–53, Aug. 2017, doi: 10.1080/09506608.2017.1366003.
[45] U. Prisco, A. Astarita, A. El Hassanin, and S. Franchitti, “Influence of processing parameters on microstructure and roughness of electron beam melted Ti-6Al-4V titanium alloy,” *Mater. Manuf. Process.*, vol. 34, no. 15, pp. 1753–1760, Nov. 2019, doi: 10.1080/10426914.2019.1683576.
[46] T. Pasang *et al.*, “Directionally-Dependent Mechanical Properties of Ti6Al4V Manufactured by Electron Beam Melting (EBM) and Selective Laser Melting (SLM),” *Materials*, vol. 14, no. 13, Art. no. 13, Jan. 2021, doi: 10.3390/ma14133603.
[47] P. Karimi and E. Sadeghi, “private communication,” Sep. 18, 2023.
[48] H. Galarraga, D. A. Lados, R. R. Dehoff, M. M. Kirka, and P. Nandwana, “Effects of the microstructure and porosity on properties of Ti-6Al-4V ELI alloy fabricated by electron beam melting (EBM),” *Addit. Manuf.*, vol. 10, pp. 47–57, Apr. 2016, doi: 10.1016/j.addma.2016.02.003.
[49] P. Zelinski, “Carnegie Mellon University and Argonne National Laboratory Seek to Understand Gas-Driven Micro Defects in Metal AM Parts.” Accessed: Dec. 05, 2023. [Online]. Available: https://www.additivemanufacturing.media/articles/carnegie-mellon-university-and-argonne-national-laboratory-seek-to-understand-gas-driven-micro-defects-in-metal-am-parts
[50] A. Abu-Issa *et al.*, “Effects of altered hot isostatic pressing treatments on the microstructures and mechanical performance of electron beam melted Ti-6Al-4V,” *J. Mater. Res. Technol.*, vol. 9, pp. 8735–8743, Jul. 2020, doi: 10.1016/j.jmrt.2020.06.019.
[51] A. B. Spierings, M. Schneider, and R. Eggenberger, “Comparison of density measurement techniques for additive manufactured metallic parts,” *Rapid Prototyp. J.*, vol. 17, no. 5, pp. 380–386, Jan. 2011, doi: 10.1108/13552541111156504.
[52] MCA Services, “Mercury Intrusion Porosimetry.” Accessed: Jan. 30, 2024. [Online]. Available: http://www.mcaservices.co.uk/mercury%20porosimetry.htm
[53] A. E. Wilson-Heid, T. C. Novak, and A. M. Beese, “Characterization of the Effects of Internal Pores on Tensile Properties of Additively Manufactured Austenitic Stainless Steel 316L,” *Exp. Mech.*, vol. 59, no. 6, pp. 793–804, Jul. 2019, doi: 10.1007/s11340-018-00465-0.
[54] G. Kasperovich and J. Hausmann, “Improvement of fatigue resistance and ductility of TiAl6V4 processed by selective laser melting,” *J. Mater. Process. Technol.*, vol. 220, pp. 202–214, Jun. 2015, doi: 10.1016/j.jmatprotec.2015.01.025.
[55] P. Wang *et al.*, “Scanning optical microscopy for porosity quantification of additively manufactured components,” *Addit. Manuf.*, vol. 21, pp. 350–358, May 2018, doi: 10.1016/j.addma.2018.03.019.
[56] “CT Basics.” Accessed: Dec. 02, 2023. [Online]. Available: https://case.edu/med/neurology/NR/CT%20Basics.htm

[57] A. du Plessis, I. Yadroitsava, and I. Yadroitsev, “Effects of defects on mechanical properties in metal additive manufacturing: A review focusing on X-ray tomography insights,” *Mater. Des.*, vol. 187, p. 108385, Feb. 2020, doi: 10.1016/j.matdes.2019.108385.
[58] Y. Murakami, “Additive manufacturing: effects of defects,” in *Metal Fatigue*, Elsevier, 2019, pp. 453–483. doi: 10.1016/B978-0-12-813876-2.00018-2.
[59] Sympatec GmbH, “Particle Shape,” Sympatec. Accessed: Feb. 08, 2024. [Online]. Available: https://www.sympatec.com/en/particle-measurement/glossary/particle-shape/
[60] H. Gong, K. Rafi, H. Gu, G. D. Janaki Ram, T. Starr, and B. Stucker, “Influence of defects on mechanical properties of Ti–6Al–4V components produced by selective laser melting and electron beam melting,” *Mater. Des.*, vol. 86, pp. 545–554, Dec. 2015, doi: 10.1016/j.matdes.2015.07.147.
[61] Radlof, Benz, Heyer, and Sander, “Monotonic and Fatigue Behavior of EBM Manufactured Ti-6Al-4V Solid Samples: Experimental, Analytical and Numerical Investigations”.
[62] J. Günther *et al.*, “Fatigue life of additively manufactured Ti–6Al–4V in the very high cycle fatigue regime,” *Int. J. Fatigue*, vol. 94, pp. 236–245, Jan. 2017, doi: 10.1016/j.ijfatigue.2016.05.018.
[63] V. Sandell, “Defects in E-PBF Ti-6Al-4V and their effect on fatigue behaviour:”.
[64] S. Tammas-Williams, P. Withers, I. Todd, and P. Prangnell, “The Influence of Porosity on Fatigue Crack Initiation in Additively Manufactured Titanium Components,” *Sci. Rep.*, vol. 7, Aug. 2017, doi: 10.1038/s41598-017-06504-5.
[65] F. Pantuso, “Un modèle pour prédire la durée de vie à la fatigue des composants métalliques à gradation fonctionnelle fabriqués de manière additive.”.
[66] “Ti-6AI-4V Gr. 5,” Advanced Powders. Accessed: Mar. 13, 2024. [Online]. Available: https://www.ge.com/powders/titanium/ti-6al-4v-5
[67] Buehler, “Polishing Application Guide.” [Online]. Available: https://www.buehler.com/assets/Brochures/English/Consumables/FN01465_0216_Polishing_Application_Guide_WEB.pdf
[68] J. Guo *et al.*, “Investigation on surface integrity of electron beam melted Ti-6Al-4 V by precision grinding and electropolishing,” *Chin. J. Aeronaut.*, vol. 34, no. 12, pp. 28–38, Dec. 2021, doi: 10.1016/j.cja.2020.08.014.
[69] F. Pantuso, “private communication.”
[70] MIPAR, “Local Measurements - MIPAR User Manual - v4.4,” MIPAR. Accessed: Jan. 30, 2024. [Online]. Available: https://www.manula.com/manuals/mipar/user-manual/latest/en/topic/local-measurements
[71] “Mercury Intrusion Porosimetry,” Particle Technology Labs. Accessed: Dec. 19, 2023. [Online]. Available: https://particletechlabs.com/analytical-testing/mercury-intrusion-porosimetry/
[72] Micromeritics, “Bulk and Skeletal Density Computations for the AutoPore.” Accessed: Jan. 30, 2024. [Online]. Available: https://www.micromeritics.com/resources/library/
[73] E. W. Washburn, “The Dynamics of Capillary Flow,” *Phys. Rev.*, vol. 17, no. 3, pp. 273–283, Mar. 1921, doi: 10.1103/PhysRev.17.273.
[74] Micromeritics Instrument Corporation, “AutoPoreIV Operators Manual.”
[75] “EBSD - Electron Backscatter Diffraction - Nanoanalysis,” Oxford Instruments. Accessed: Dec. 19, 2023. [Online]. Available: https://nano.oxinst.com/products/ebsd/

[76] R. Schwarzer and J. Hjelen, “Backscattered Electron Imaging with an EBSD Detector,” *Microsc. Today*, vol. 23, pp. 12–17, Jan. 2015, doi: 10.1017/S1551929514001333.
[77] “Ion Milling | Nanoscience Instruments.” Accessed: Dec. 19, 2023. [Online]. Available: https://www.nanoscience.com/techniques/ion-milling/
[78] ASTM, “E8/E8M Standard Test Methods for Tension Testing of Metallic Materials.” Accessed: Jan. 24, 2024. [Online]. Available: https://www.astm.org/e0008_e0008m-22.html
[79] D. L. DuQuesnay, “private communication,” Jan. 24, 2023.
[80] M. A. Pompetzki, T. H. Topper, and D. L. DuQuesnay, “The effect of compressive underloads and tensile overloads on fatigue damage accumulation in SAE 1045 steel,” *Int. J. Fatigue*, vol. 12, no. 3, pp. 207–213, May 1990, doi: 10.1016/0142-1123(90)90097-X.
[81] ASTM, “ASTM E 466 - Standard Practice for Conducting Force Controlled Constant Amplitude Axial Fatigue Tests of Metallic Materials.”
[82] X. Zhang, H. Wang, and L. Luo, “Comparison Analysis of the Calculation Methods for Particle Diameter,” Aug. 2022, Accessed: Jan. 24, 2024. [Online]. Available: https://www.mdpi.com/2073-4352/12/8/1107
[83] “What is EDS/EDX? - Nanoanalysis,” Oxford Instruments. Accessed: Dec. 19, 2023. [Online]. Available: https://nano.oxinst.com/campaigns/what-is-eds/edx
[84] “Extreme Tips & Tricks – Things to Remember During Extreme Operation - Nanoanalysis,” Oxford Instruments. Accessed: Dec. 14, 2023. [Online]. Available: https://nano.oxinst.com/library/past-blogs/extreme-tips-and-tricks
[85] A. K. Lynn and D. L. DuQuesnay, “Hydroxyapatite-coated Ti–6Al–4V: Part 1: the effect of coating thickness on mechanical fatigue behaviour,” *Biomaterials*, vol. 23, no. 9, pp. 1937–1946, May 2002, doi: 10.1016/S0142-9612(01)00321-0.

Appendix A Tensile specimen blank drawing

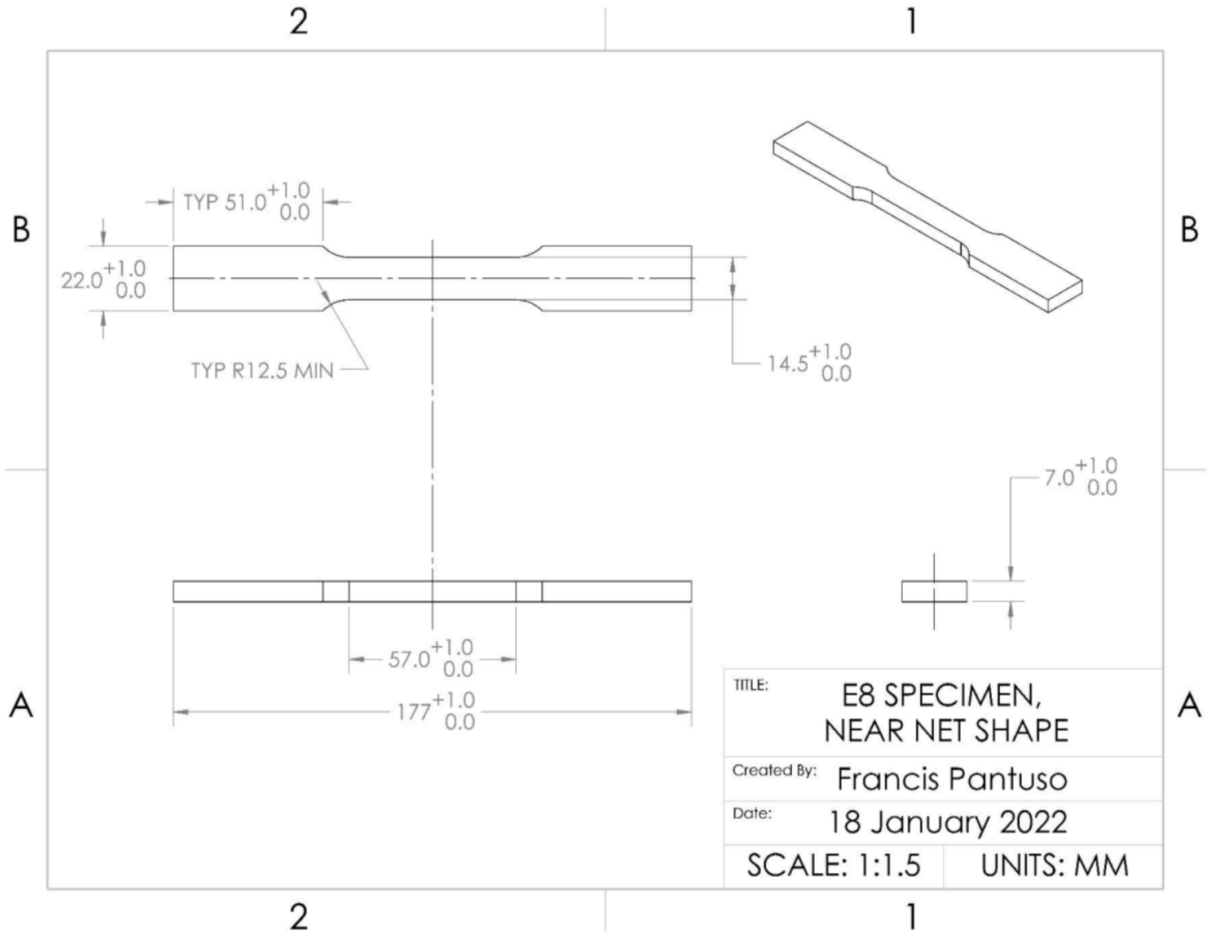

Appendix B Strain-controlled fatigue specimen blank drawing

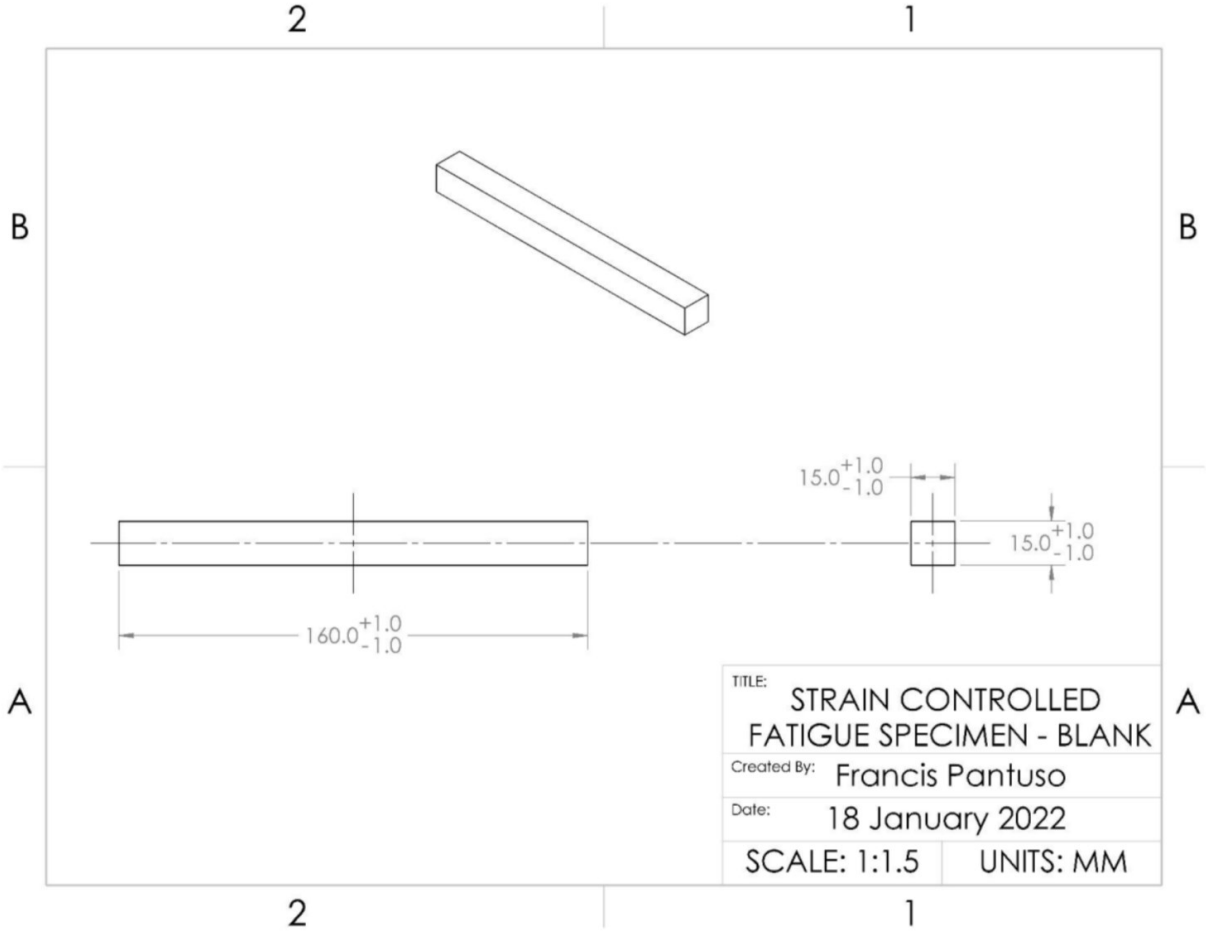

Appendix C Tensile specimen drawing

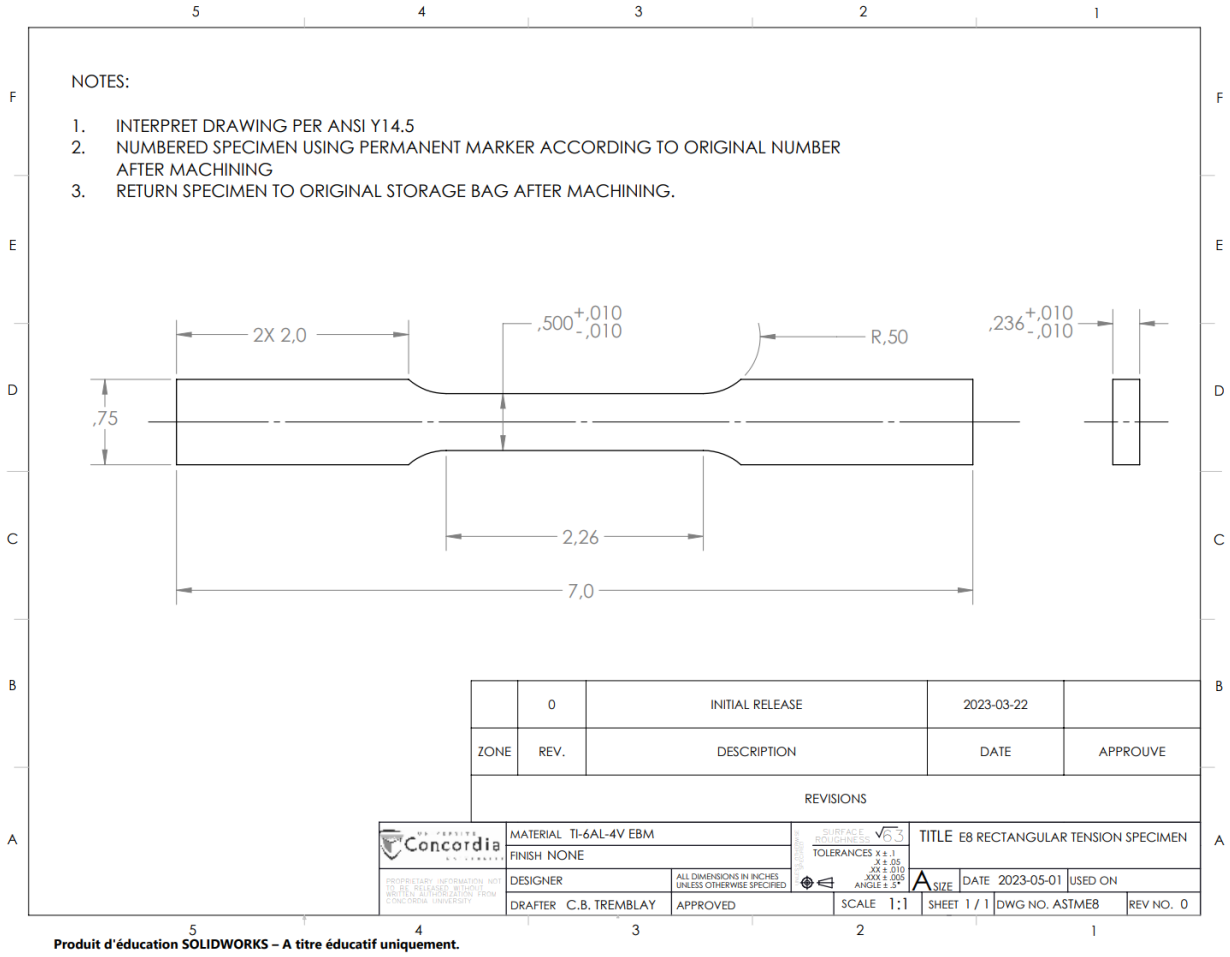

Appendix D Low-cycle EBM fatigue specimen drawing

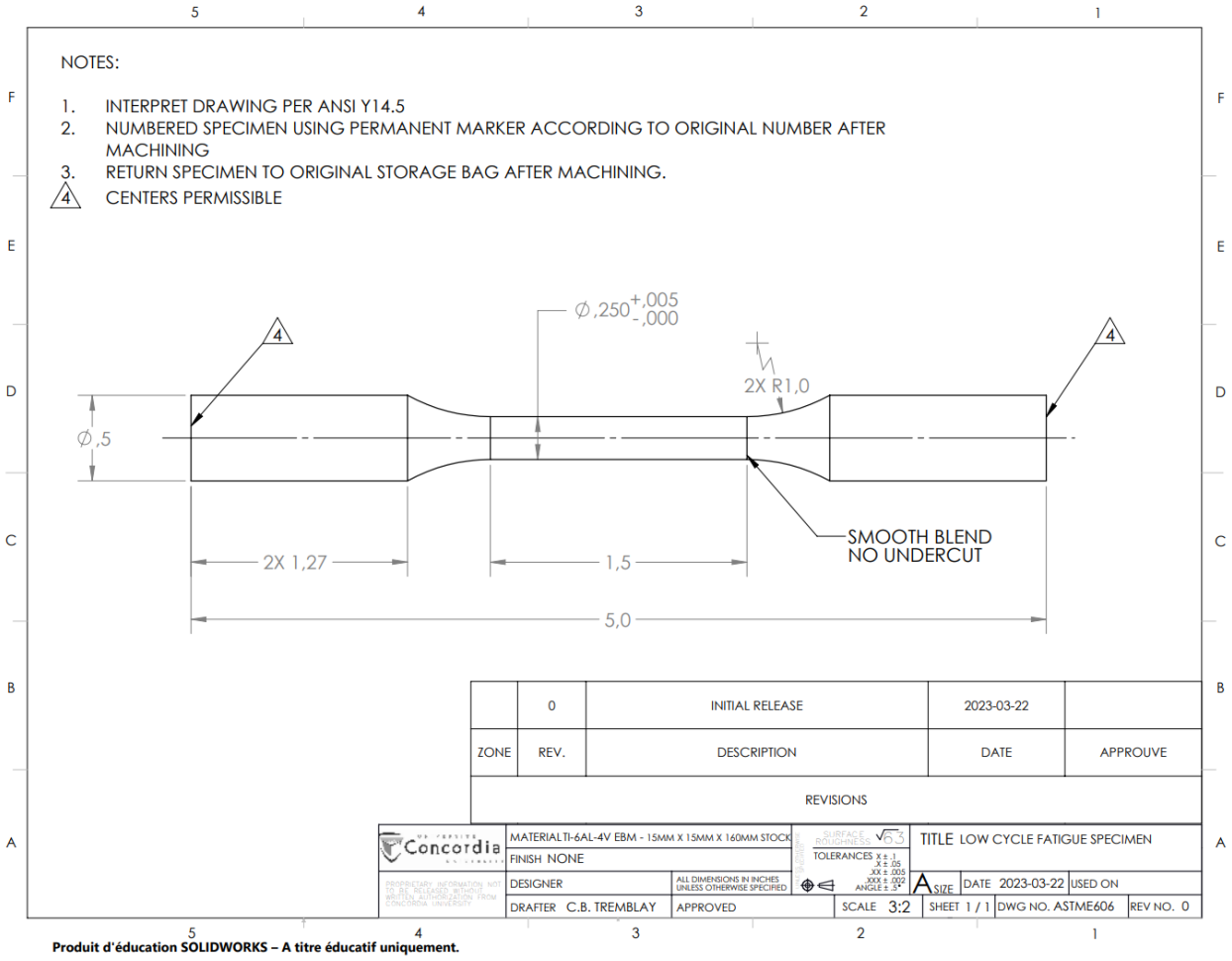

Produit d'éducation SOLIDWORKS – A titre éducatif uniquement.

Appendix E Baseline fatigue specimen drawing

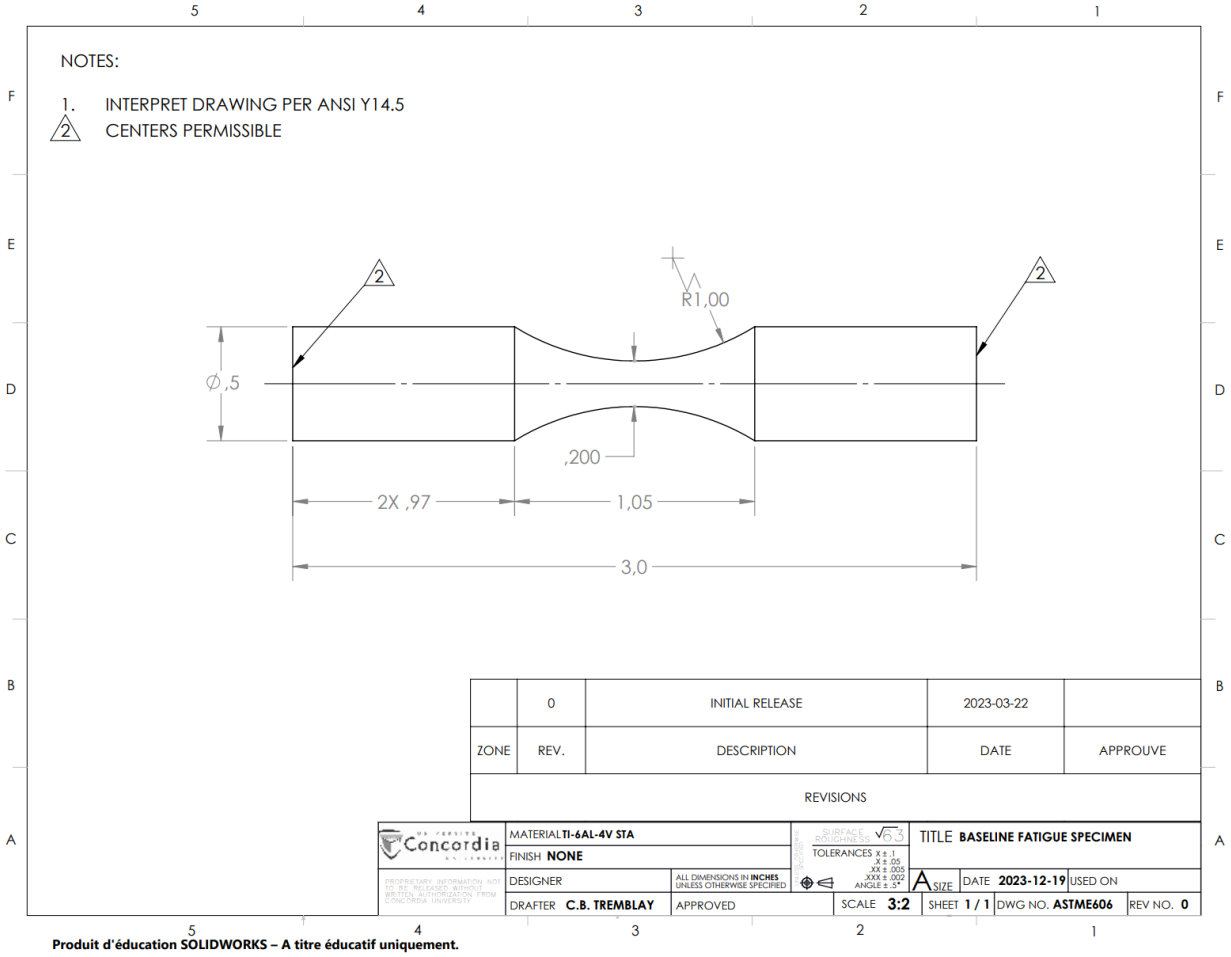

Appendix F Tensile specimens inspection report

Inspection Report

Part Name	Tensile Specimens	Inspector	C.B. TREMBLAY
Part Number	ASTM E8	Date	April 29th 2023
Revision	0	Ambient Temperature	21°C

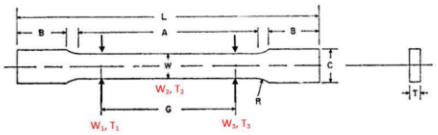

Dimension Inspected	W	T
DWG Dimension	0,5	0,236
Tolerance	+0,010 -0,010	+0,010 -0,010
Limits	0,510 0,490	0,246 0,226

Item #	T1	W1	T2	W2	T3	W3	MEASUREMENT METHOD	ACCEPT / REJECT	REMARKS
1	0,2401	0,5019	0,2401	0,4998	0,2389	0,5003	MICROMETER	ACCEPT	
2	0,2424	0,4993	0,2428	0,4994	0,2421	0,499	MICROMETER	ACCEPT	
3	0,2415	0,5033	0,2418	0,5042	0,2405	0,5034	MICROMETER	ACCEPT	
4	0,2345	0,5024	0,237	0,5039	0,2365	0,5034	MICROMETER	ACCEPT	
5	0,2404	0,4994	0,2398	0,4992	0,2379	0,4976	MICROMETER	ACCEPT	
6	0,24	0,4998	0,2398	0,5009	0,2397	0,5006	MICROMETER	ACCEPT	
7	0,24	0,5039	0,2403	0,5036	0,2398	0,5038	MICROMETER	ACCEPT	
8	0,2421	0,4996	0,2406	0,4998	0,238	0,4998	MICROMETER	ACCEPT	
9	0,2446	0,4996	0,2444	0,5004	0,2423	0,5004	MICROMETER	ACCEPT	

Inspection Report

Part Name	Tensile Specimens	Inspector	C.B. TREMBLAY
Part Number	ASTM E8	Date	April 29th 2023
Revision	0	Ambient Temperature	21°C

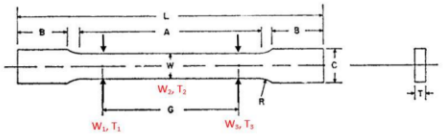

Dimension Inspected	W	T
DWG Dimension	0,5	0,236
Tolerance	+0,010 -0,010	+0,010 -0,010
Limits	0,510 0,490	0,246 0,226

Item #	T1	W1	T2	W2	T3	W3	MEASUREMENT METHOD	ACCEPT / REJECT	REMARKS
10	0,2387	0,5021	0,2393	0,5031	0,2377	0,5023	MICROMETER	ACCEPT	VISIBLE POROSITY ON NECK SURFACE - SEVERE

Appendix G Fatigue specimens inspection report

Inspection Report

Part Name	Fatigue Specimens	Inspector	C.B. TREMBLAY
Part Number	ASTM E466	Date	April 4th 2023
Revision	0	Ambient Temperature	22°C

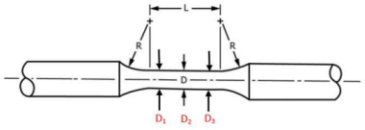

Dimension Inspected	D
DWG Dimension	0.25
Tolerance	+0.005 0
Limits	0,255 0,25

Item #	D1	D2	D3	D AVERAGE	MEASUREMENT METHOD	ACCEPT / REJECT	REMARKS
1	0,2532	0,254	0,2546	0,2539	MICROMETER	ACCEPT	VISIBLE POROSITY ON NECK SURFACE - MILD
2	0,2526	0,25355	0,2539	0,2534	MICROMETER	ACCEPT	
3	0,2521	0,25275	0,2532	0,2527	MICROMETER	ACCEPT	VISIBLE POROSITY ON NECK SURFACE - MILD
4	0,2525	0,25325	0,25375	0,2532	MICROMETER	ACCEPT	
5	0,252	0,2523	0,2525	0,2523	MICROMETER	ACCEPT	VISIBLE POROSITY ON NECK SURFACE - MILD
6	0,25215	0,2529	0,2533	0,2528	MICROMETER	ACCEPT	
7	0,2513	0,252	0,25295	0,2521	MICROMETER	ACCEPT	VISIBLE POROSITY ON NECK SURFACE - MILD
8	0,2522	0,253	0,2534	0,2529	MICROMETER	ACCEPT	
9	0,252	0,25285	0,25315	0,2527	MICROMETER	ACCEPT	

Inspection Report

Part Name	Fatigue Specimens	Inspector	C.B. TREMBLAY
Part Number	ASTM E466	Date	April 4th 2023
Revision	0	Ambient Temperature	22°C

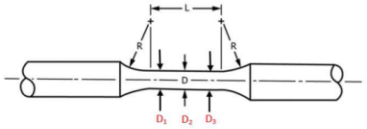

Dimension Inspected	D
DWG Dimension	0.25
Tolerance	+0.005 0
Limits	0,255 0,25

Item #	D1	D2	D3	D AVERAGE	MEASUREMENT METHOD	ACCEPT / REJECT	REMARKS
10	0,2518	0,2525	0,25265	0,2523	MICROMETER	ACCEPT	
11	0,2515	0,2529	0,2533	0,2526	MICROMETER	ACCEPT	
12	0,25265	0,2533	0,2539	0,2533	MICROMETER	ACCEPT	
13	0,252	0,2529	0,25315	0,2527	MICROMETER	ACCEPT	
14	0,25225	0,25275	0,25315	0,2527	MICROMETER	ACCEPT	
15	0,252	0,25275	0,25315	0,2526	MICROMETER	ACCEPT	VISIBLE POROSITY ON NECK SURFACE - MILD
16	0,25195	0,2529	0,25295	0,2526	MICROMETER	ACCEPT	
17	0,2525	0,25315	0,2535	0,2531	MICROMETER	ACCEPT	VISIBLE POROSITY ON NECK SURFACE - SEVERE SEVERE SPECIMEN WARPAGE BEFORE MACHINING
18	0,25205	0,2528	0,2531	0,2527	MICROMETER	ACCEPT	

Inspection Report

Part Name	Fatigue Specimens	Inspector	C.B. TREMBLAY
Part Number	ASTM E466	Date	April 4th 2023
Revision	0	Ambient Temperature	22°C

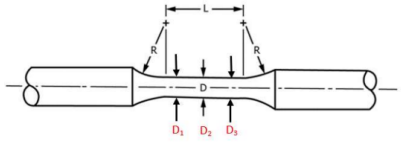

Dimension Inspected	D
DWG Dimension	0.25
Tolerance	+0.005 0
Limits	0,255 0,25

Item #	D1	D2	D3	D AVERAGE	MEASUREMENT METHOD	ACCEPT / REJECT	REMARKS
19	0,2521	0,2527	0,25305	0,2526	MICROMETER	ACCEPT	
20	0,2521	0,25265	0,25305	0,2526	MICROMETER	ACCEPT	
21	0,2521	0,2528	0,25315	0,2527	MICROMETER	ACCEPT	VISIBLE POROSITY ON NECK SURFACE - MILD
22	0,2521	0,25265	0,25295	0,2526	MICROMETER	ACCEPT	
23	0,25195	0,2526	0,25295	0,2525	MICROMETER	ACCEPT	
24	0,25275	0,2536	0,254	0,2535	MICROMETER	ACCEPT	

Appendix H VED cubes porosity

Cube 1, 50X Magnification

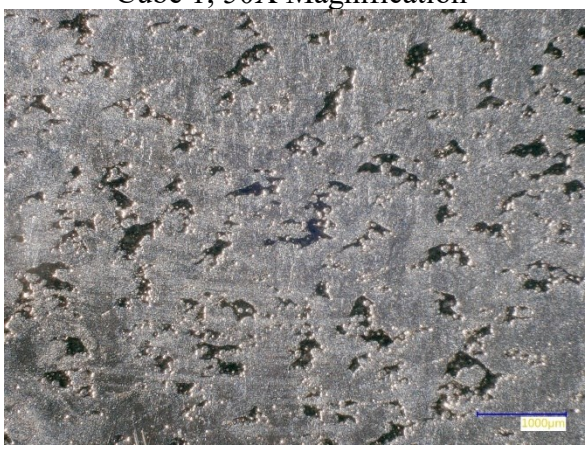

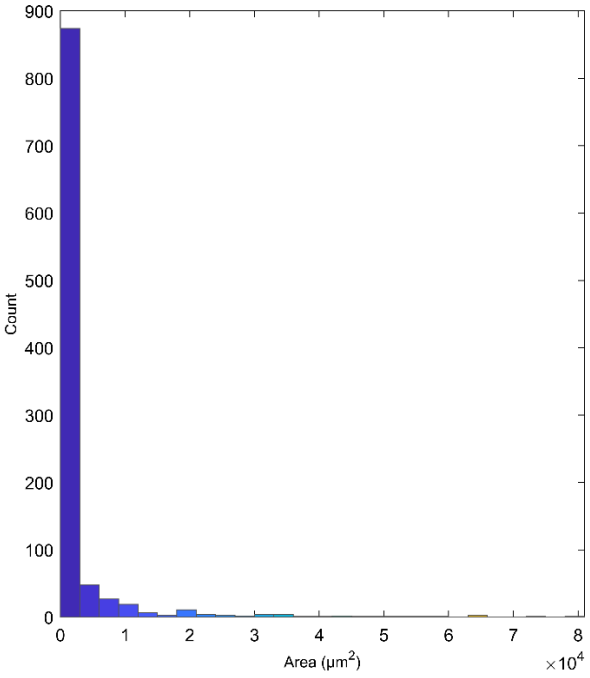

Cube 2, 50X Magnification

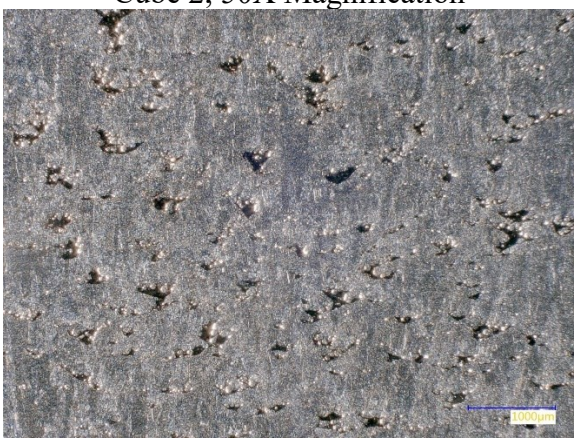

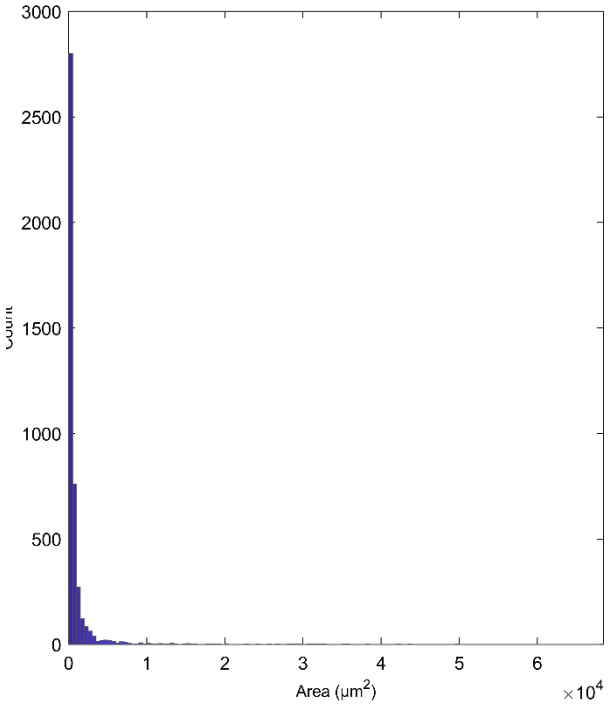

Cube 3, 50X Magnification

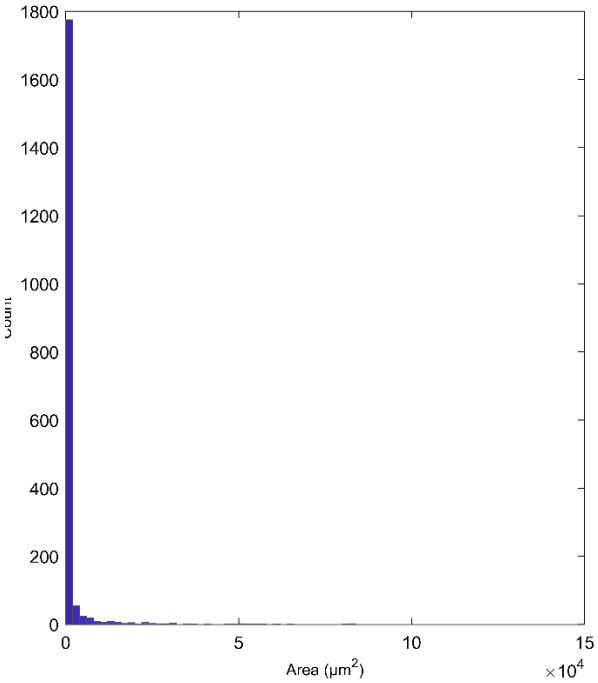

Cube 4, 50X Magnification

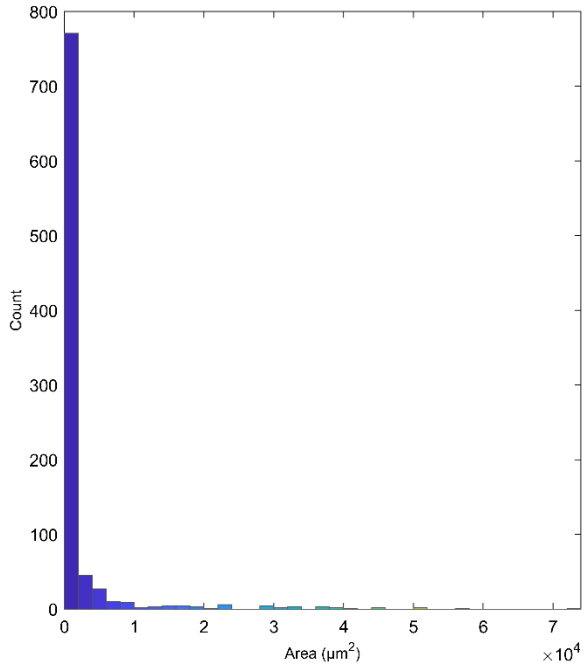

Cube 5, 50X Magnification

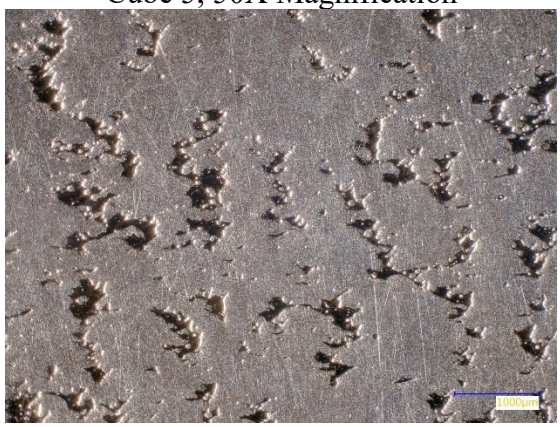

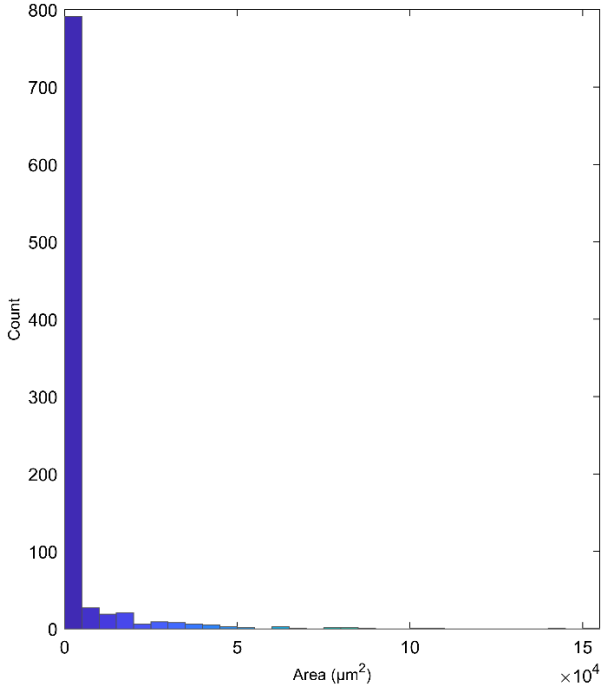

Cube 6, 50X Magnification

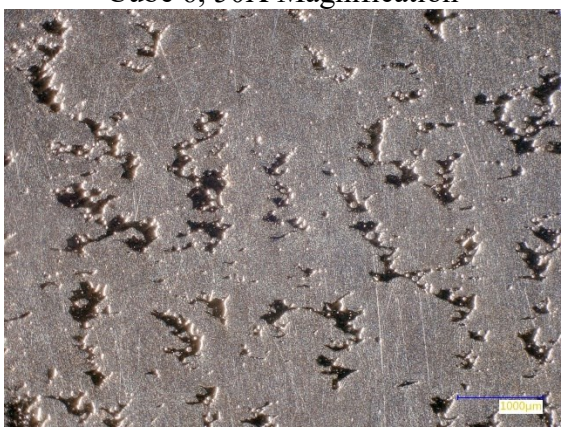

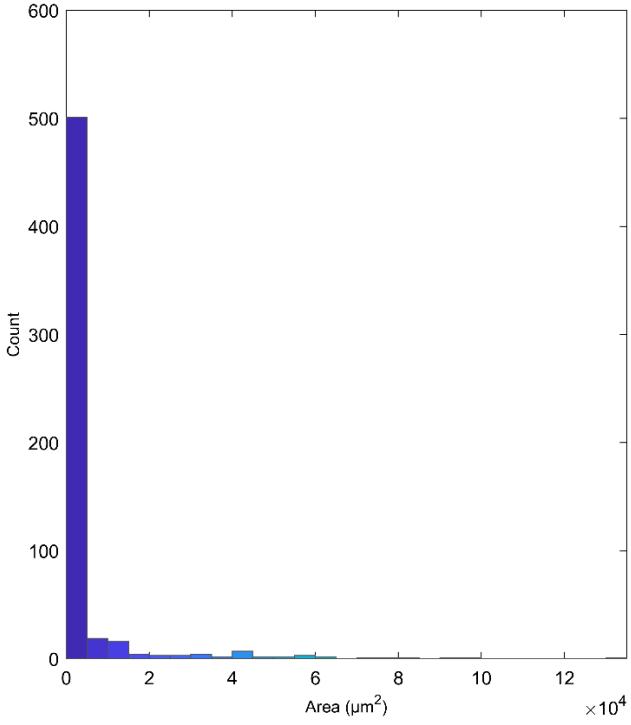

Cube 7, 50X Magnification

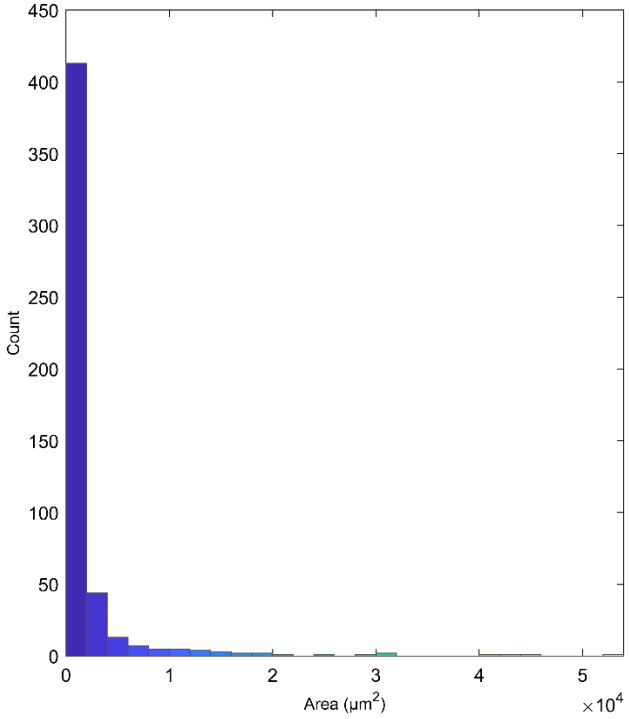

Cube 8, 50X Magnification

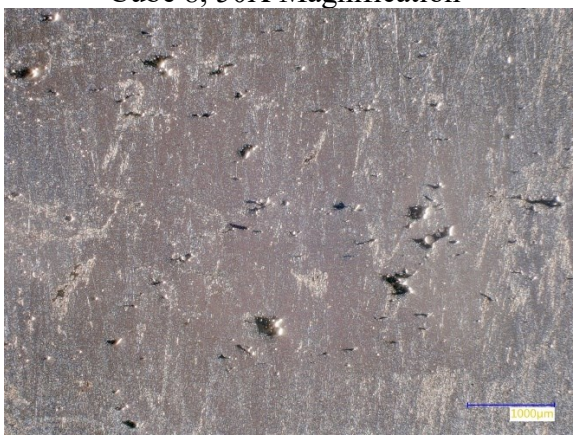

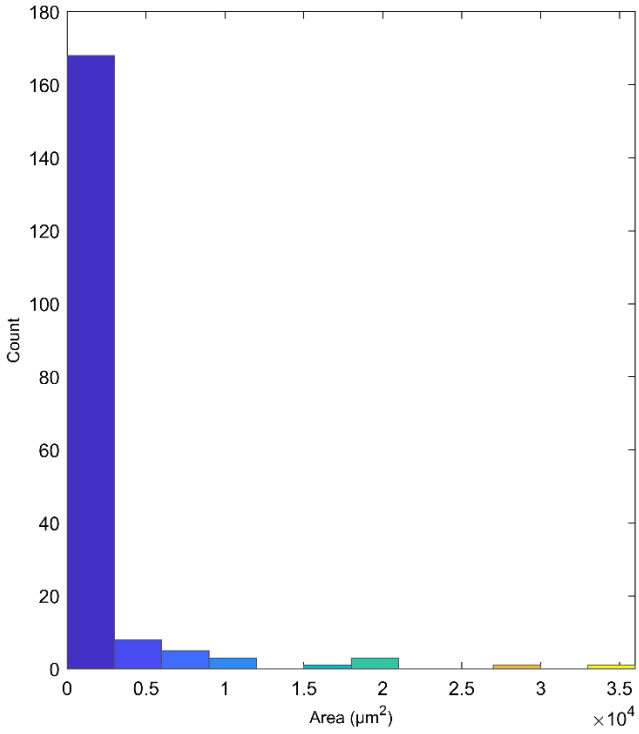

Cube 9, 50X Magnification

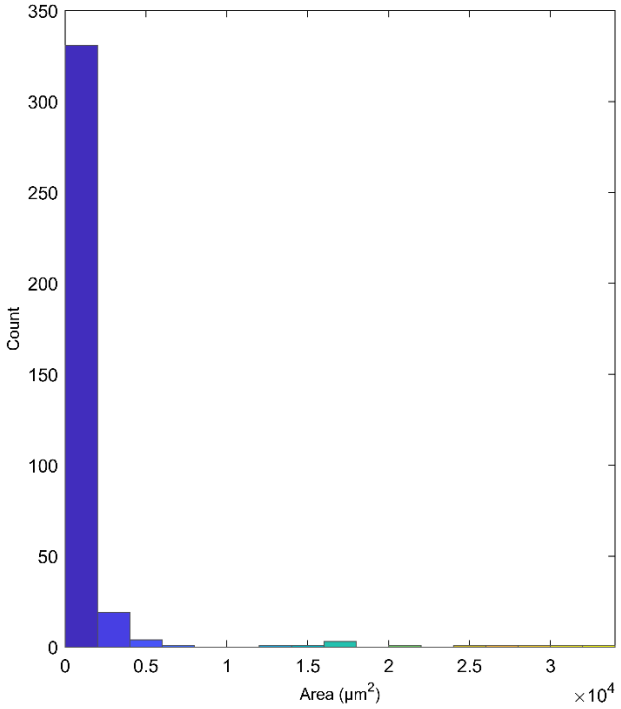

Cube 10, 50X Magnification

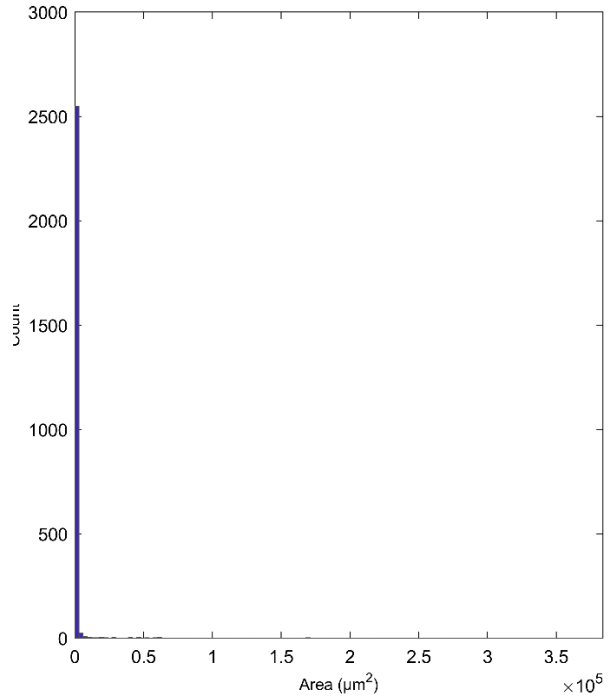

Cube 11, 50X Magnification

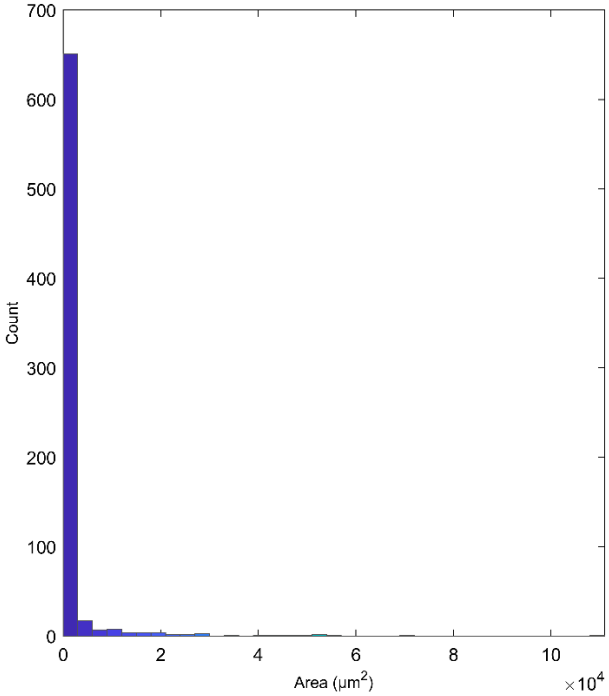

Cube 12, 50X Magnification

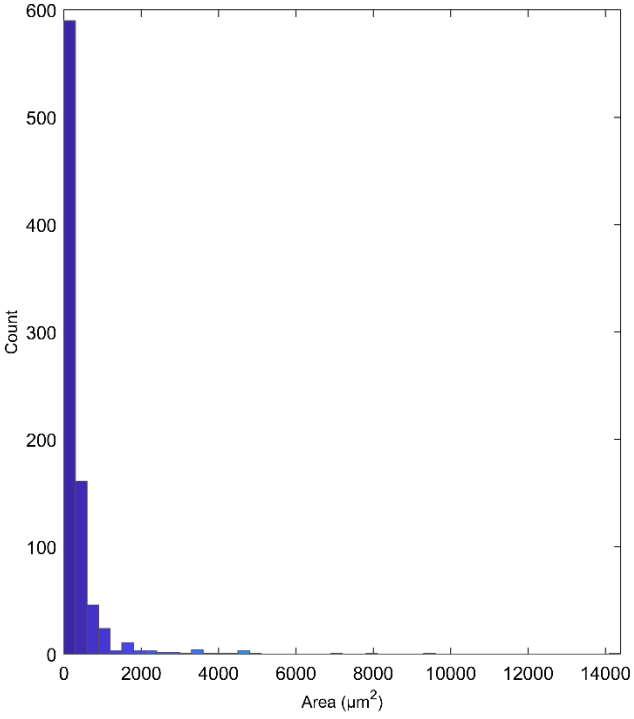

Cube 13, 200X Magnification

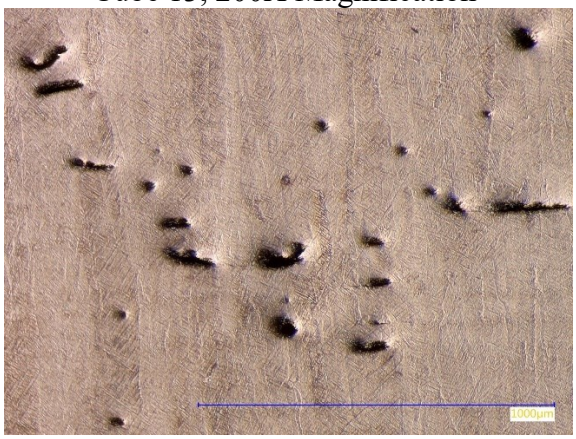

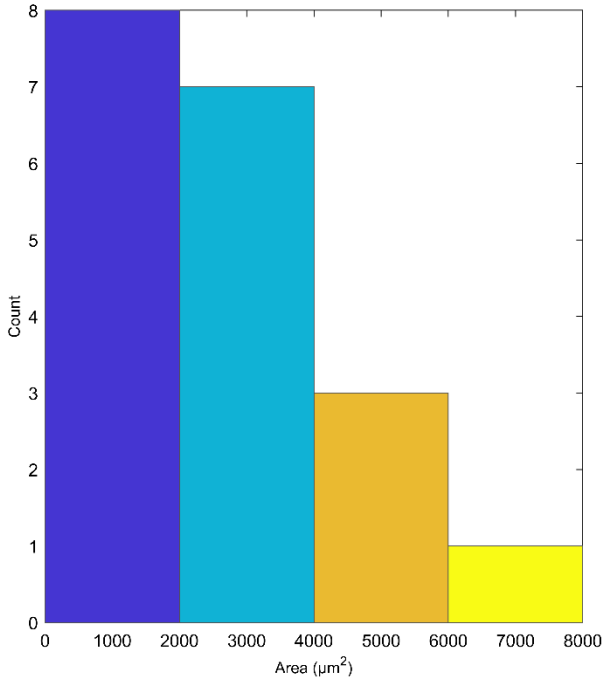

Cube 14, 200X Magnification

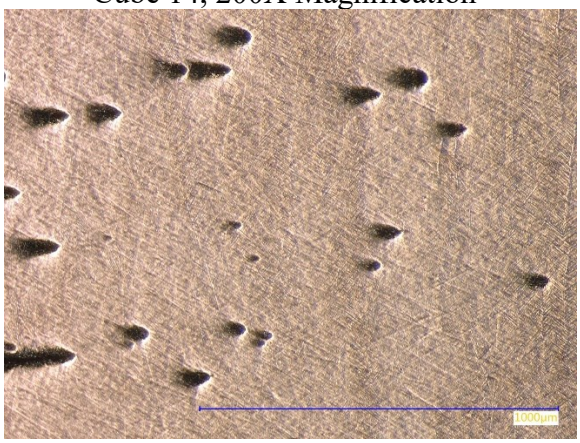

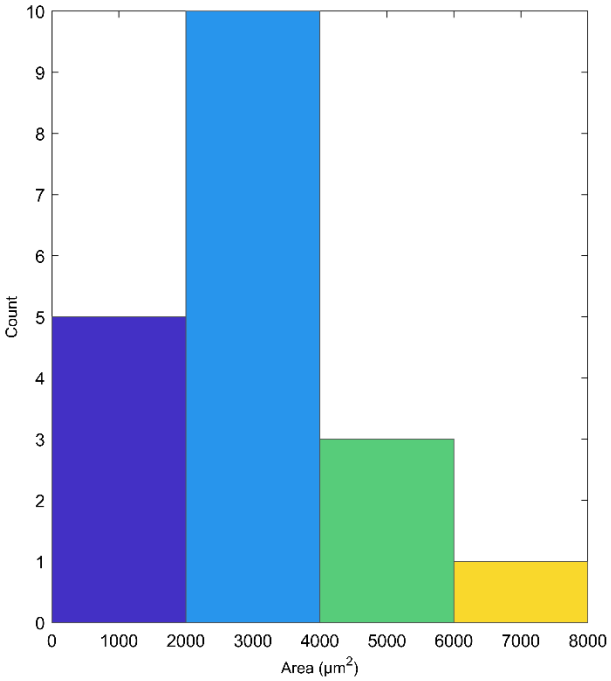

Cube 15, 50X Magnification

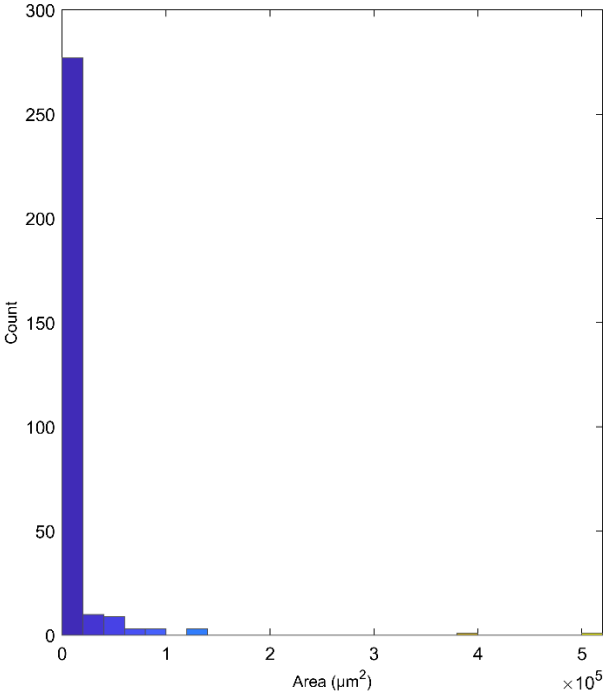

Cube 16, 50X Magnification

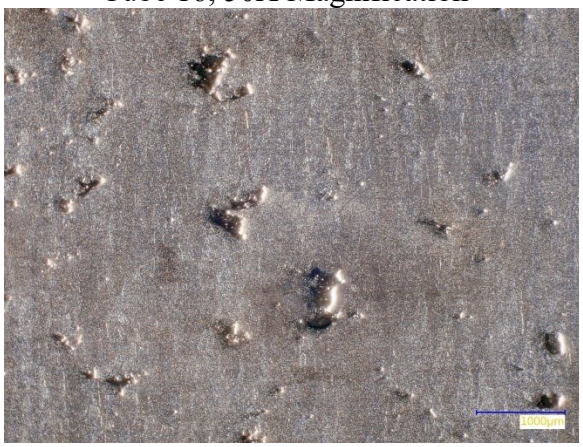

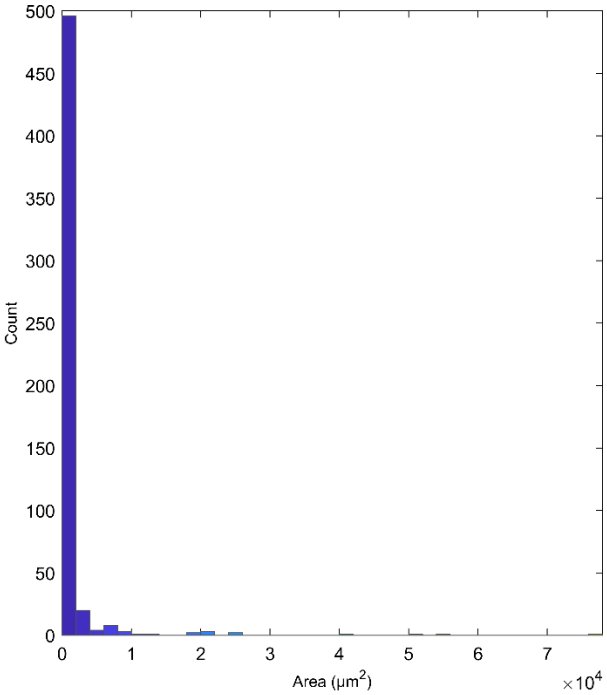

Cube 17, 200X Magnification

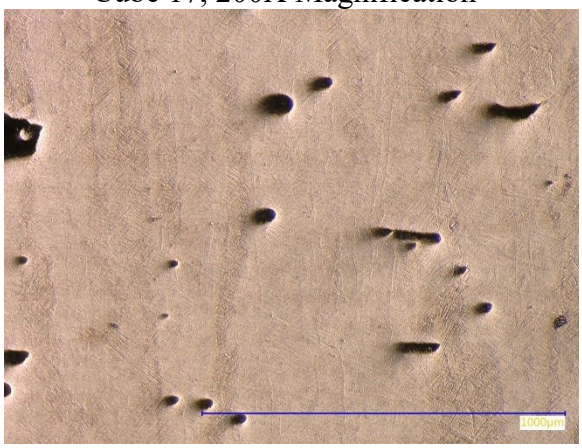

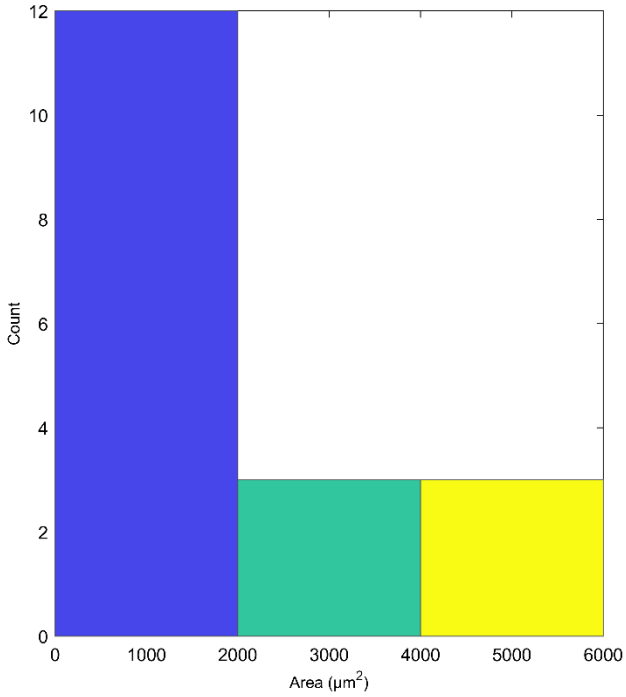

Cube 18, 150X Magnification

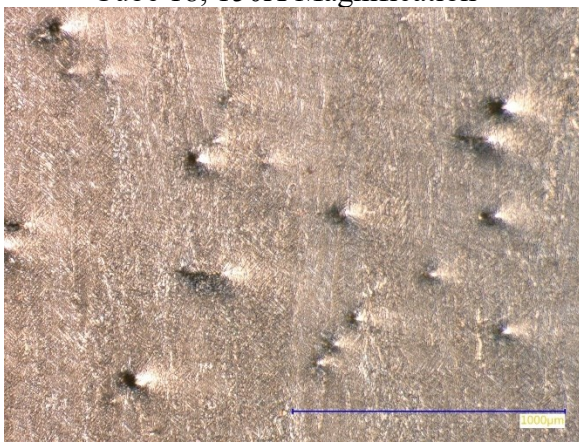

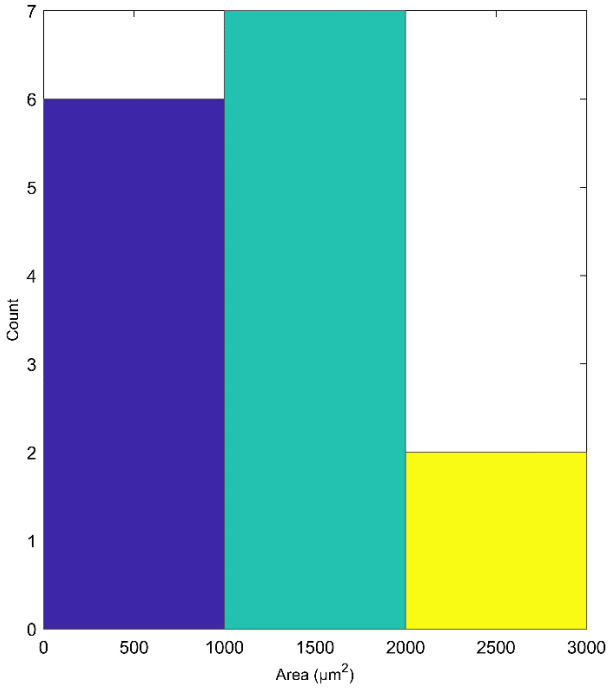

Cube 19, 200X Magnification

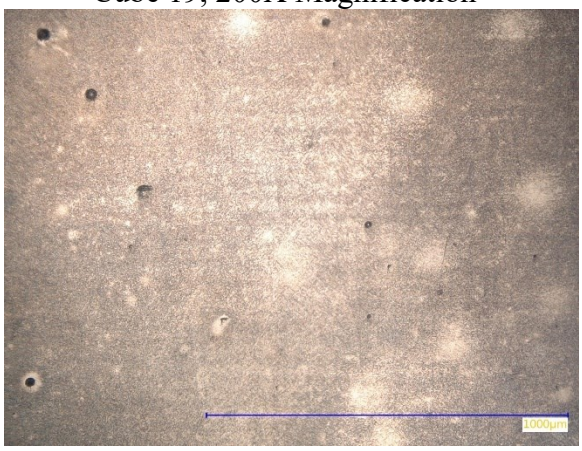

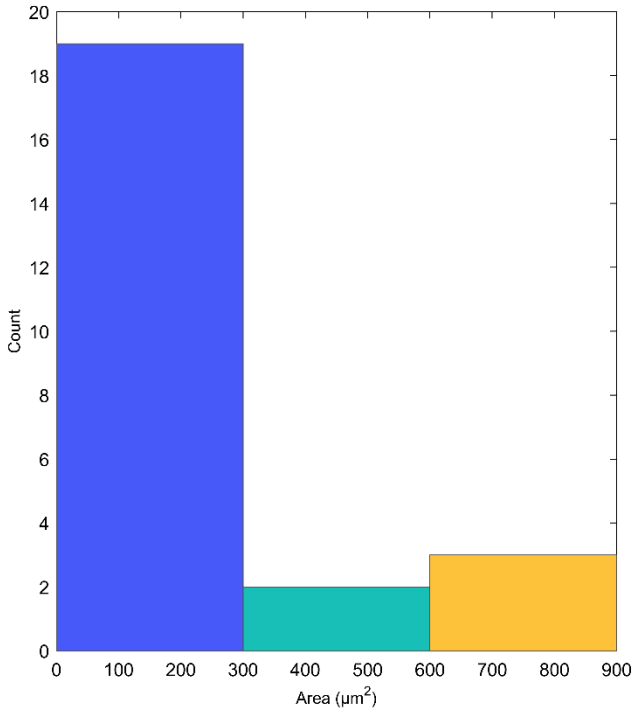

Cube 20, 50X Magnification

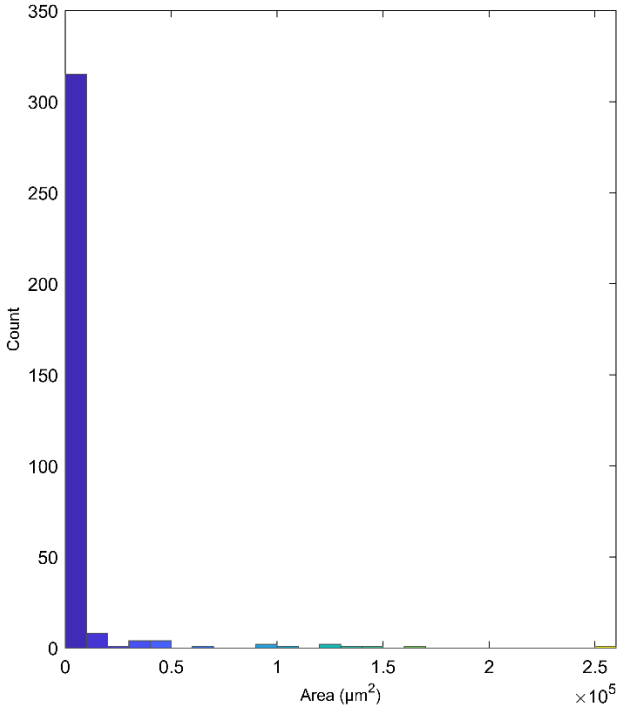

Cube 21, 200X Magnification

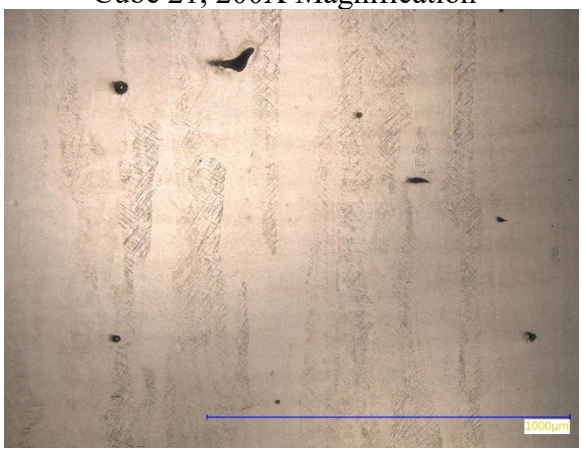

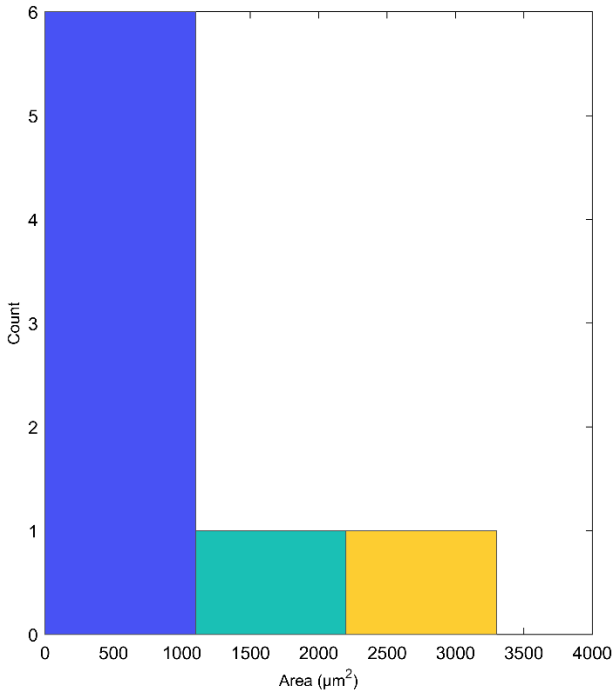

Cube 22, 200X Magnification

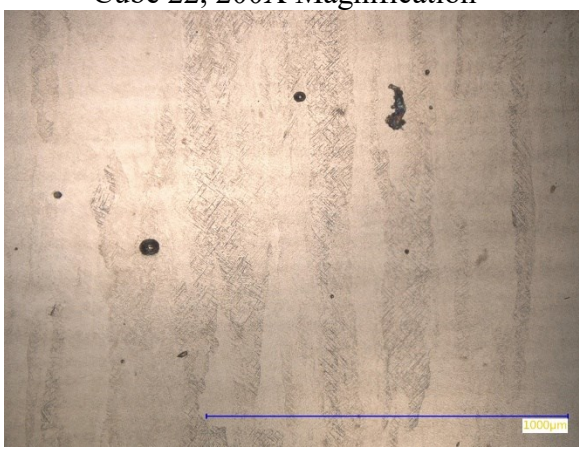

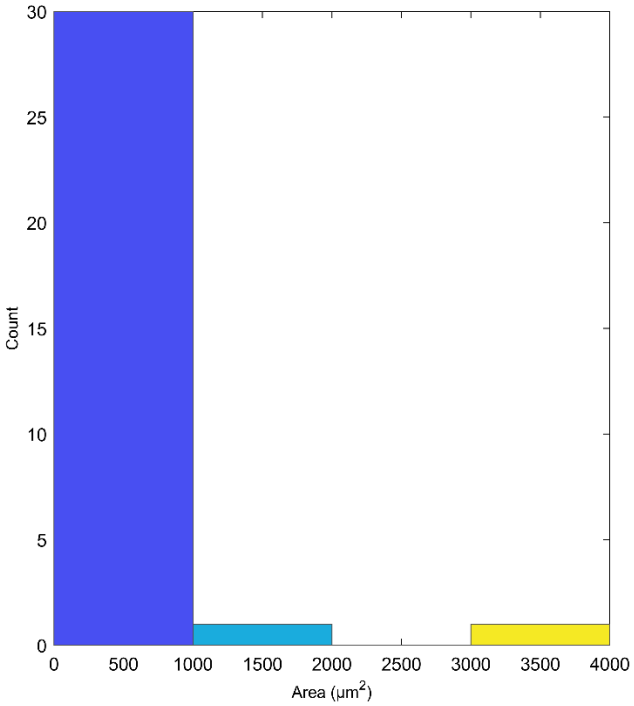

Cube 23, 200X Magnification

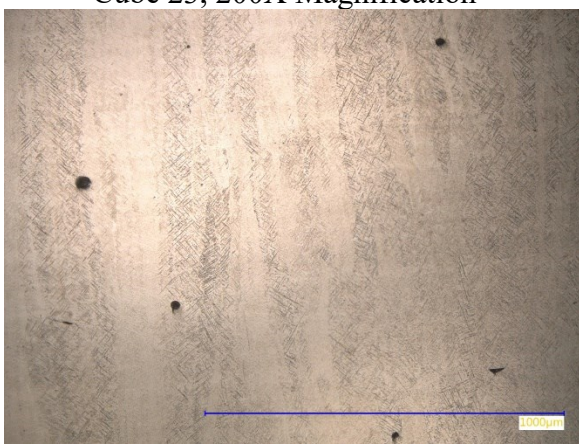

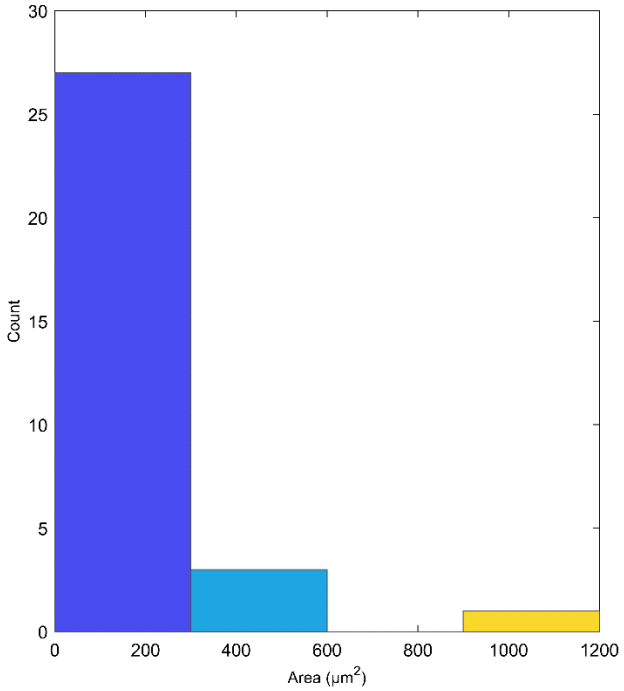

Cube 24, 200X Magnification

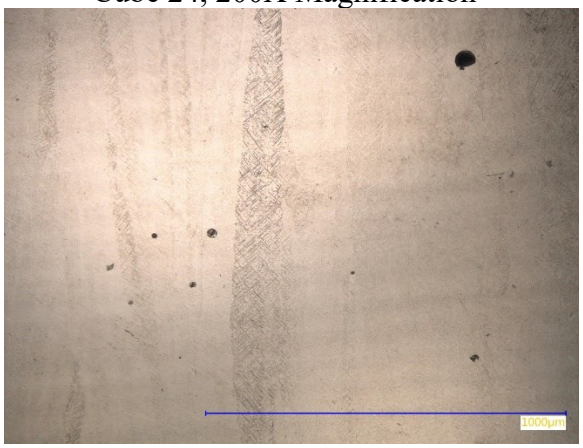

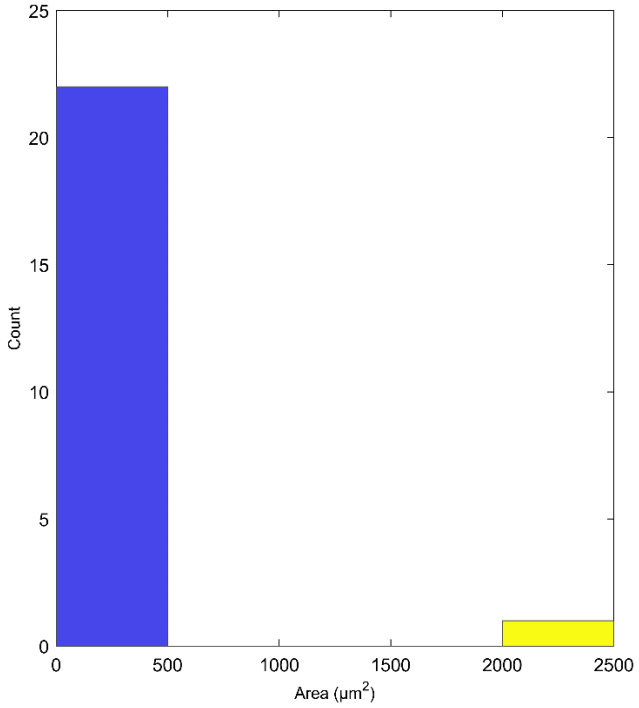

Cube 25, 50X Magnification

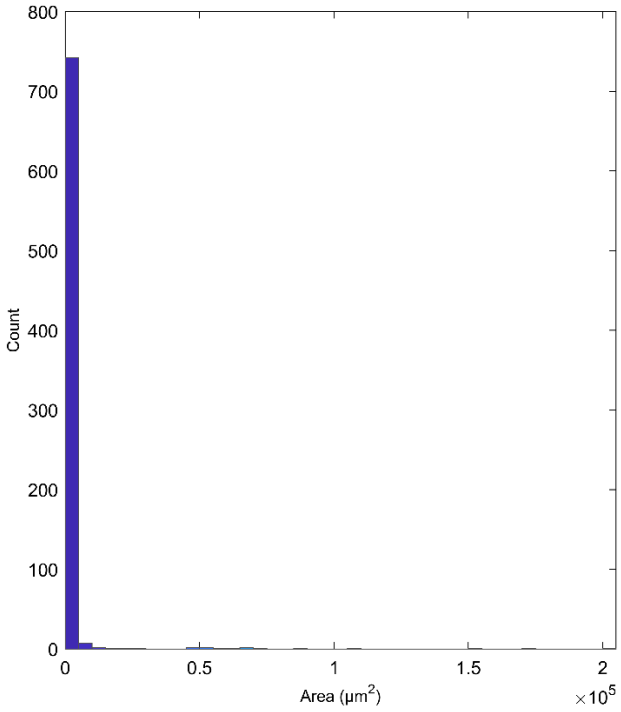

Cube 26, 200X Magnification

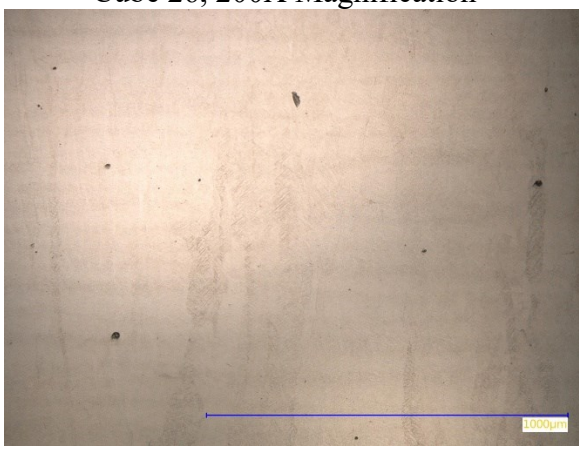

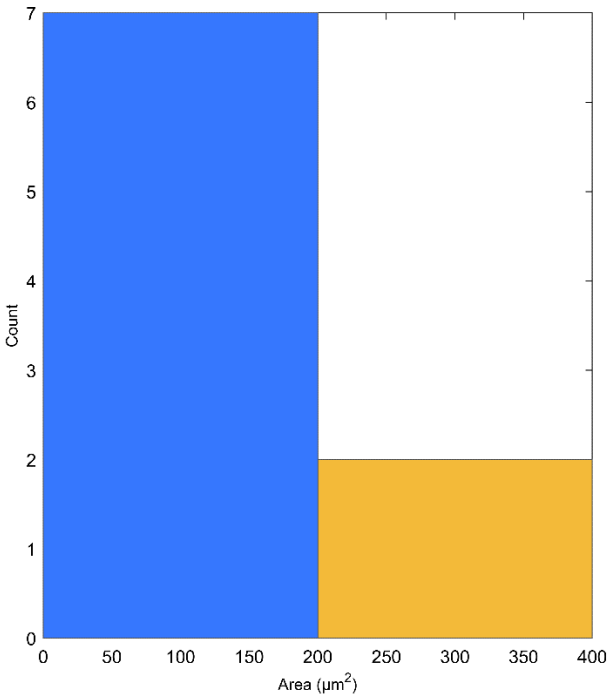

Cube 27, 200X Magnification

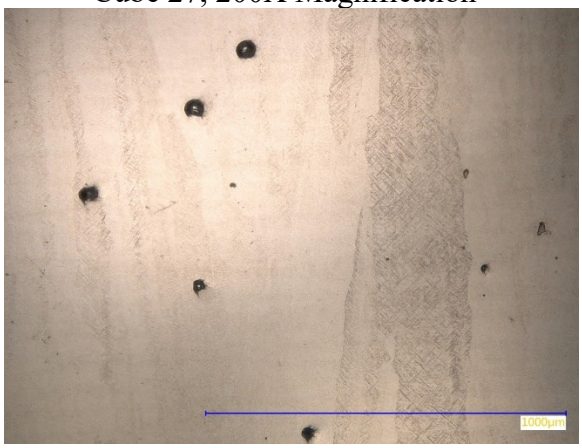

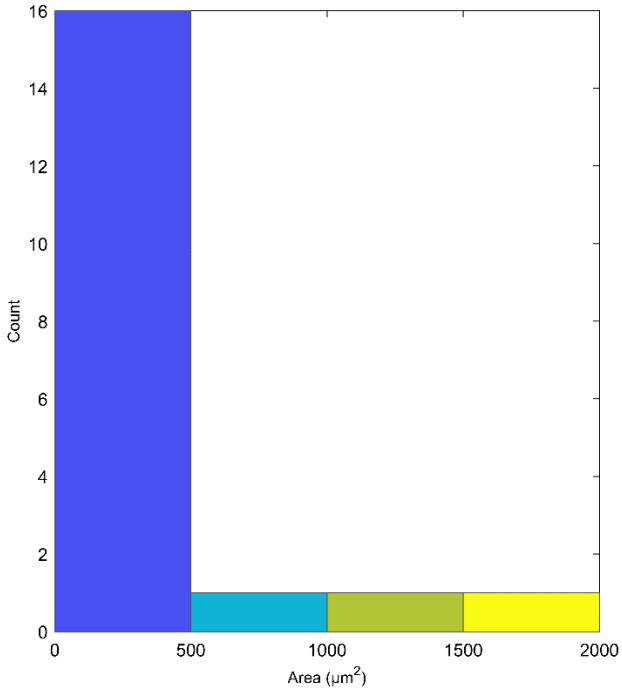

Cube 28, 200X Magnification

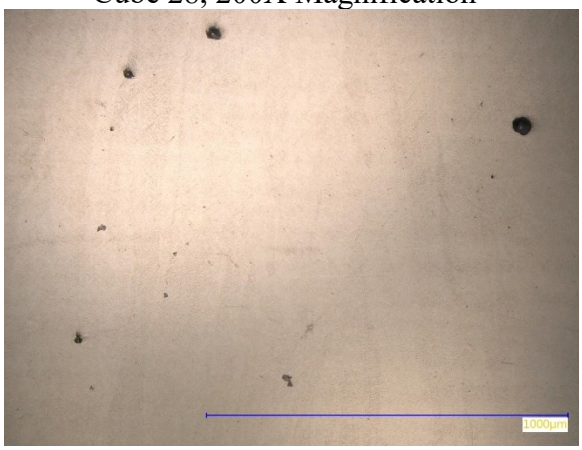

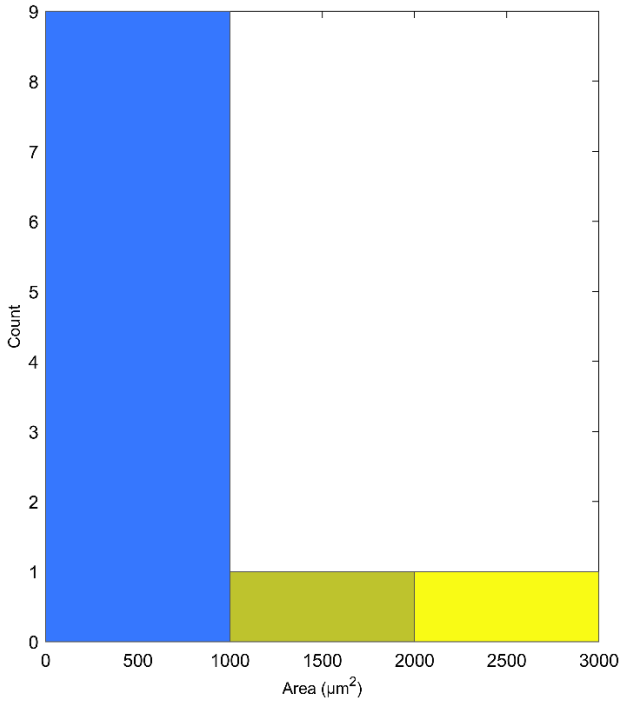

Cube 29, 200X Magnification

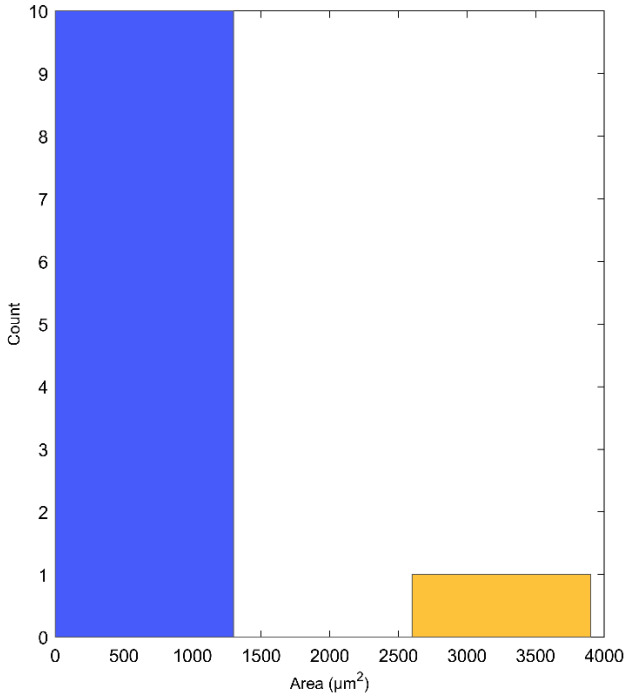

Cube 30, 200X Magnification

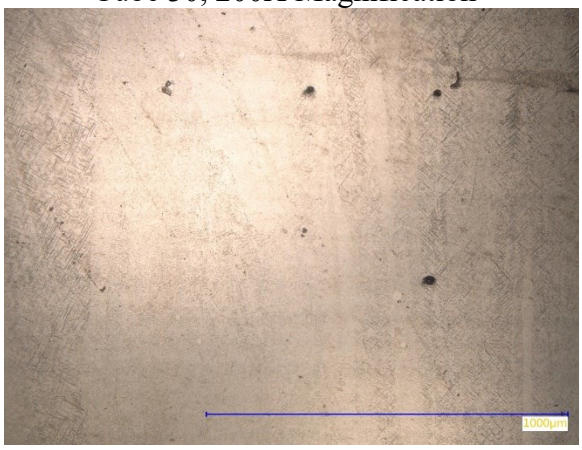

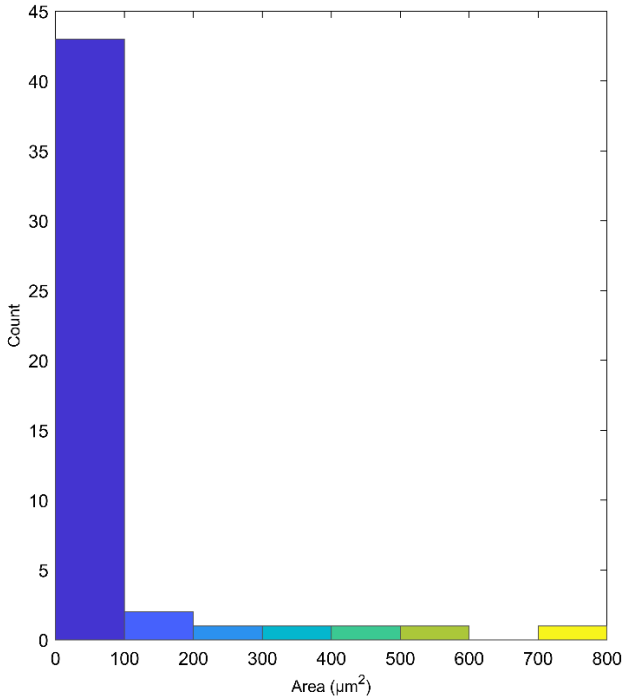

Appendix I VED cubes scanning electron microscopy photographs.

Cube 7

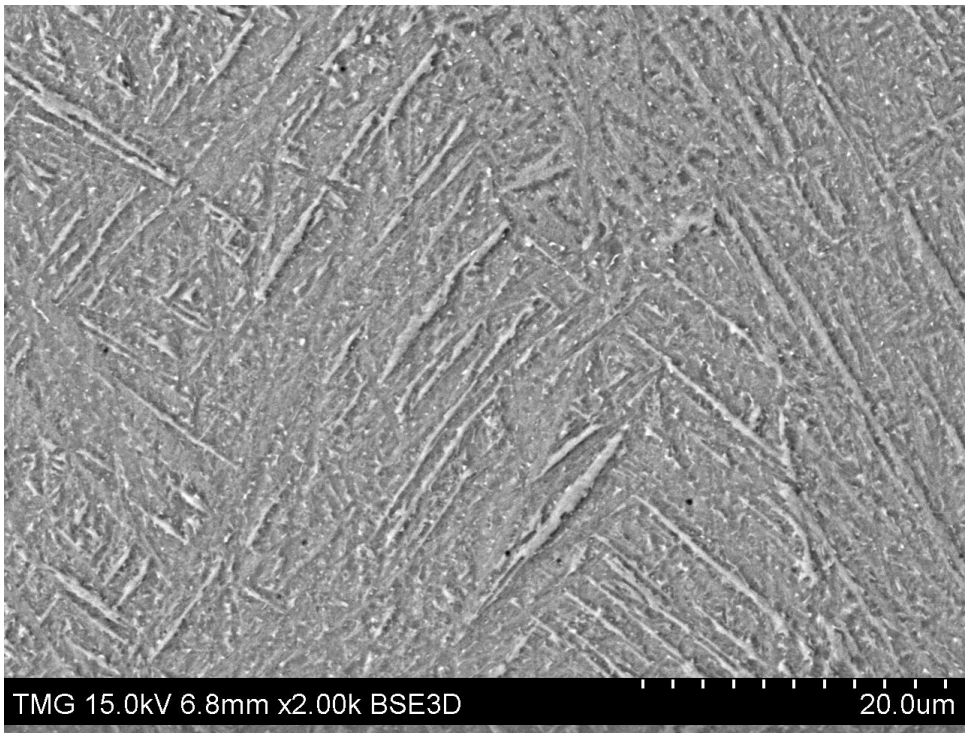

Cube 8

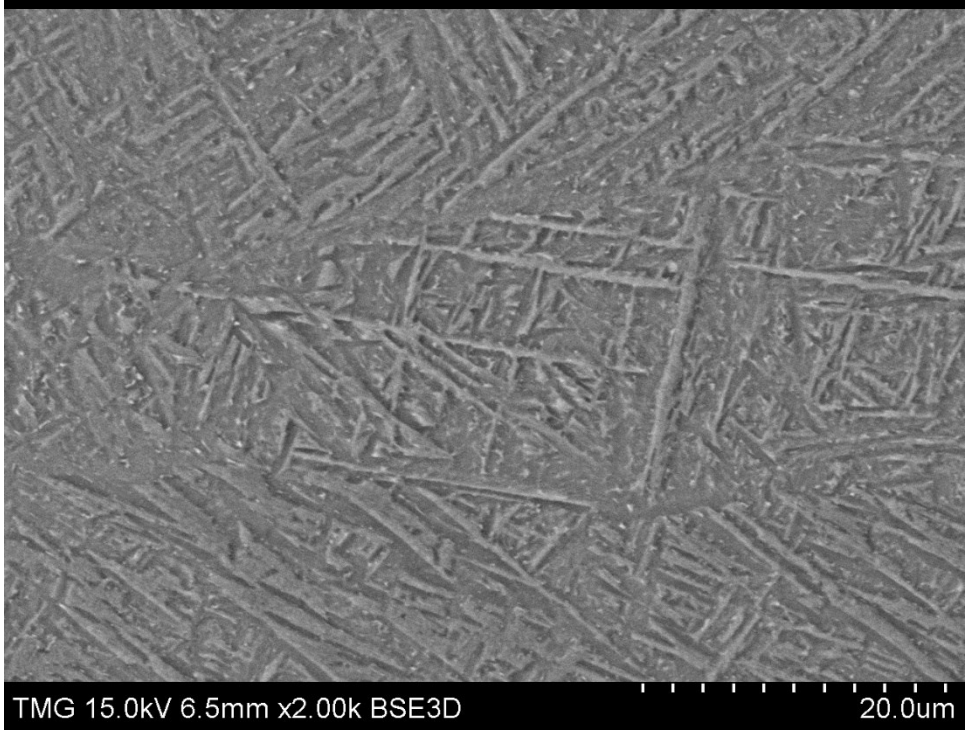

Cube 9

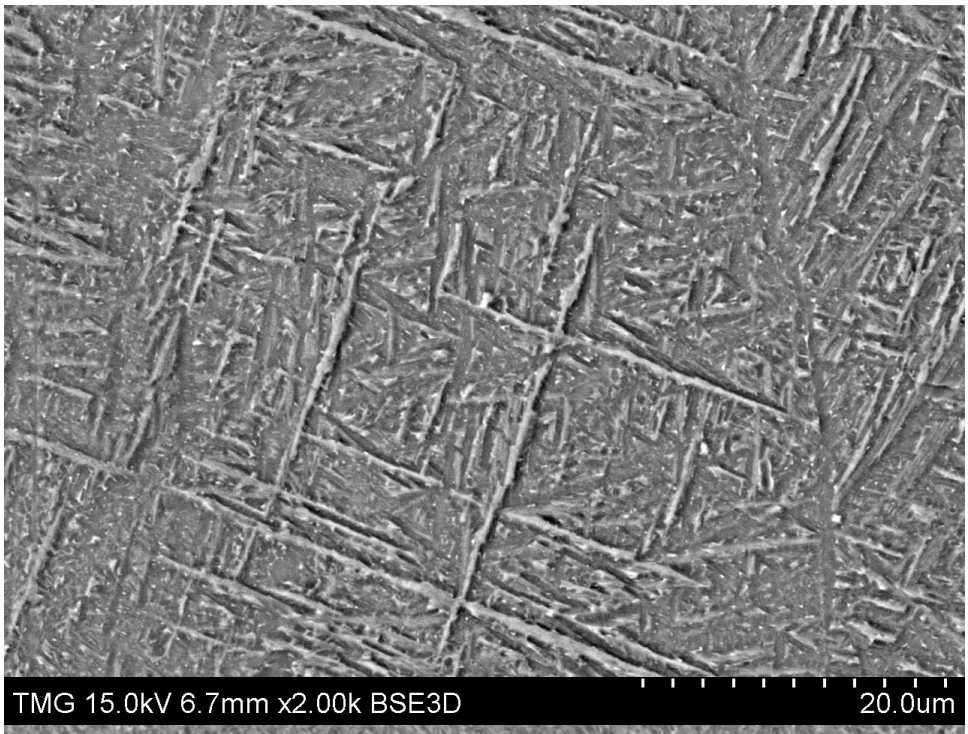

Cube 10

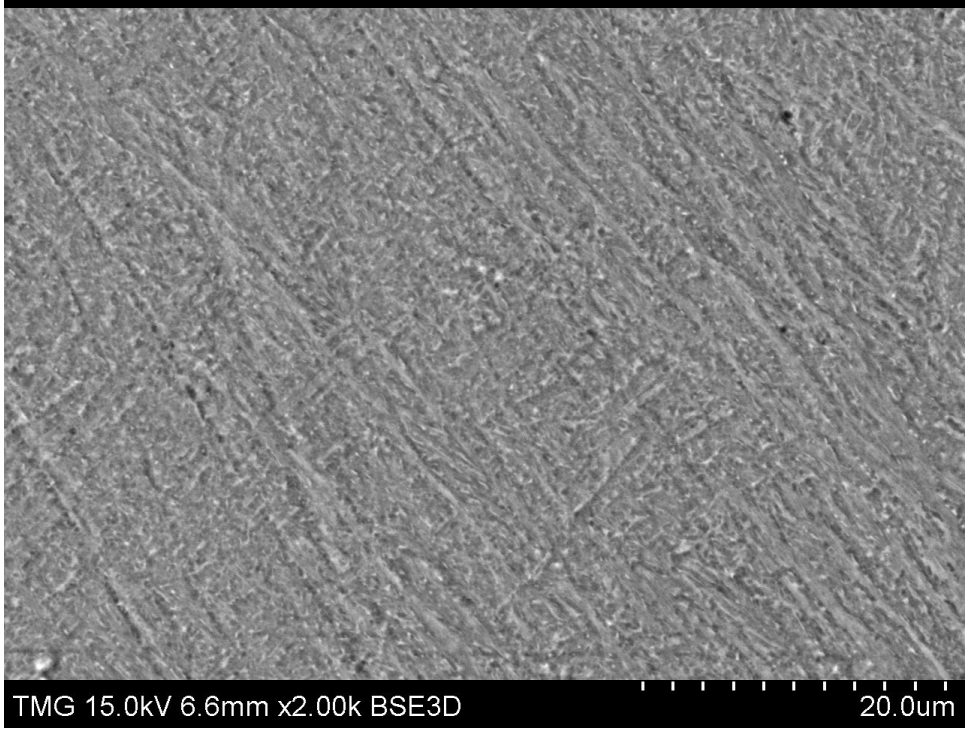

Cube 13

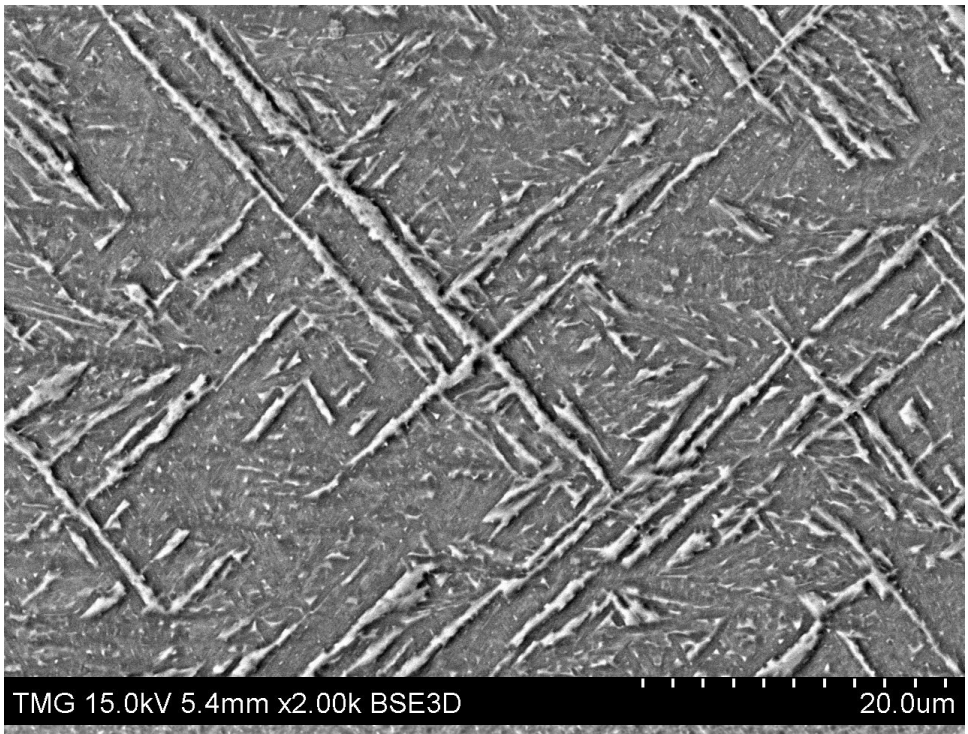

Cube 14

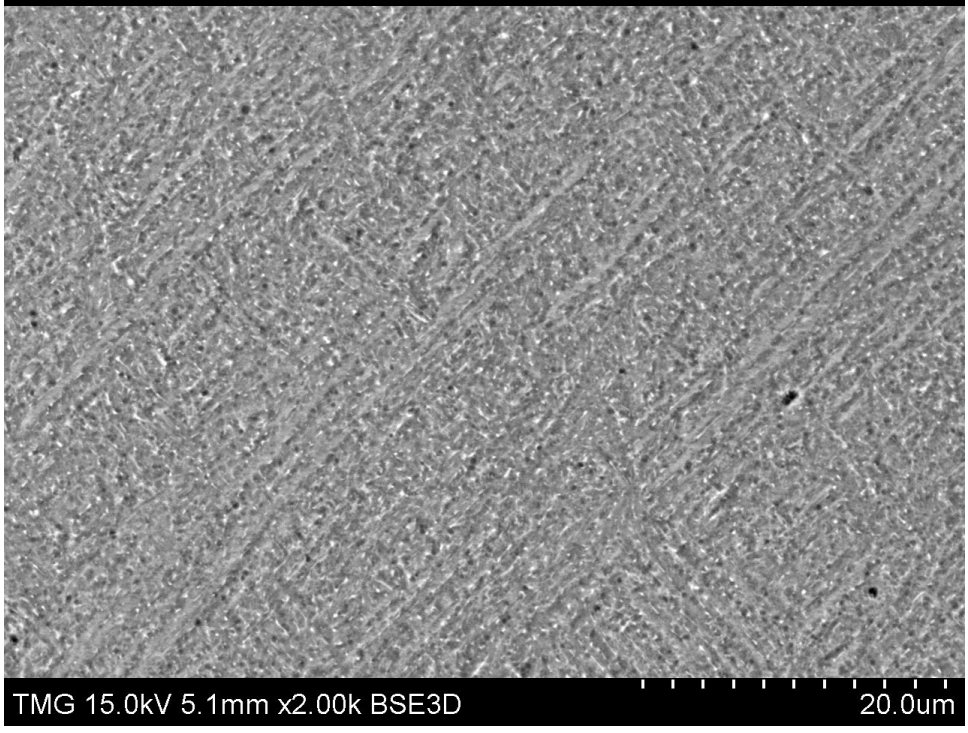

Cube 17

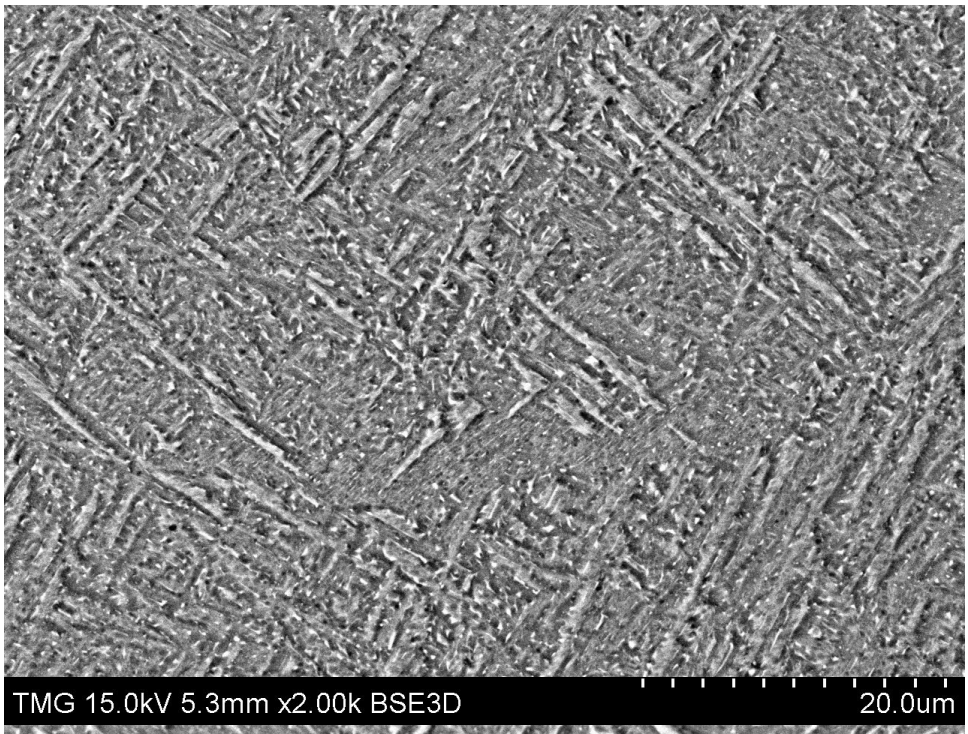

Cube 21

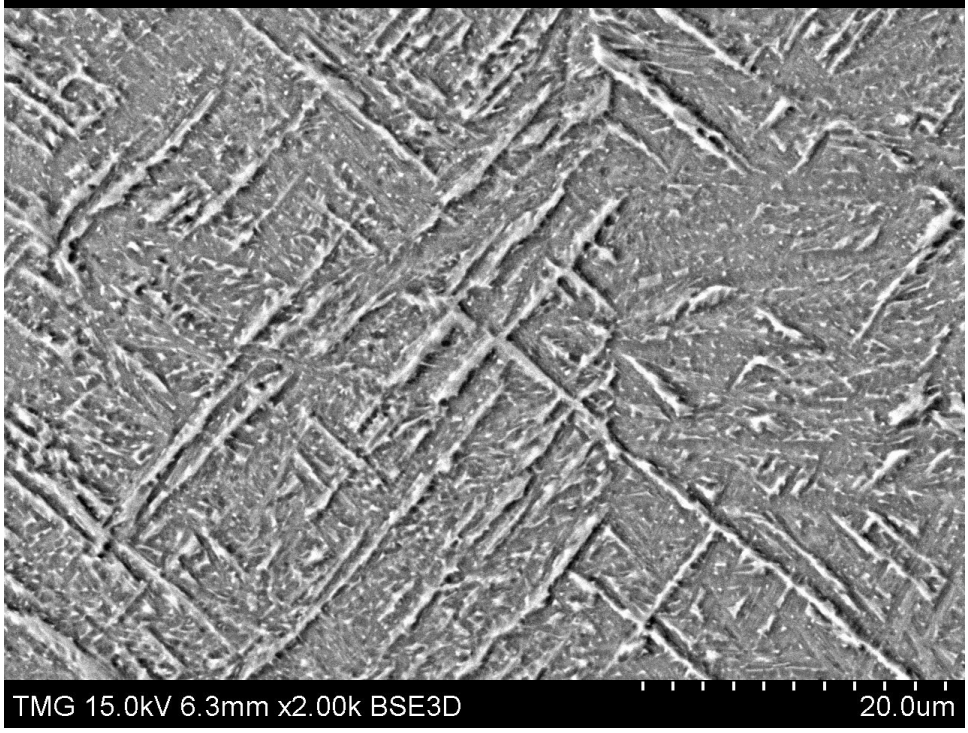

Cube 22

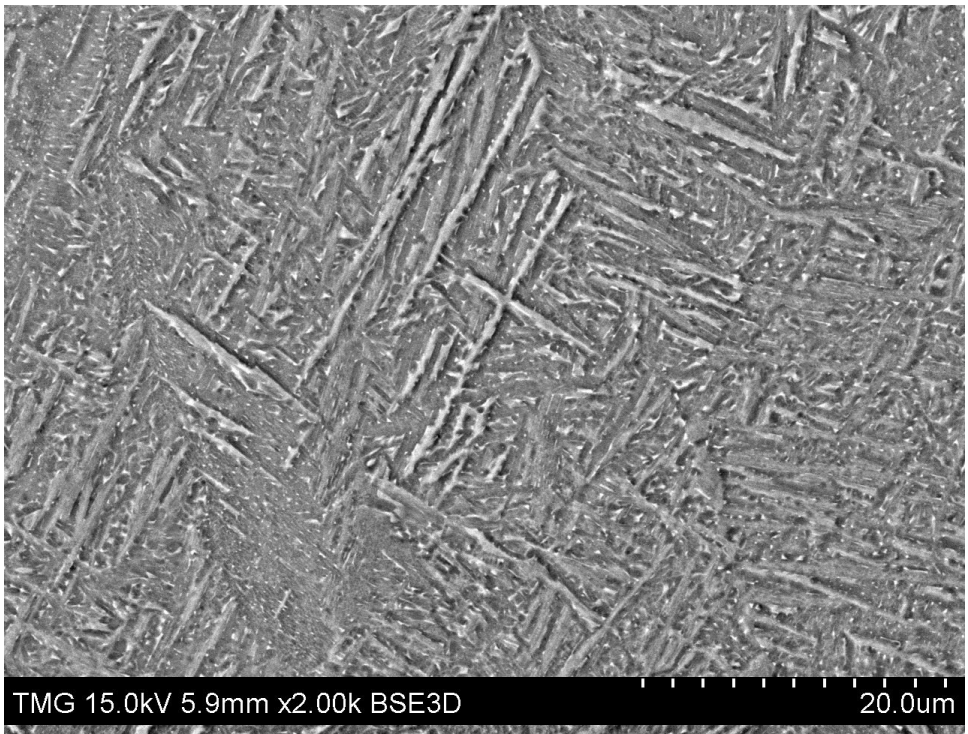

Cube 23

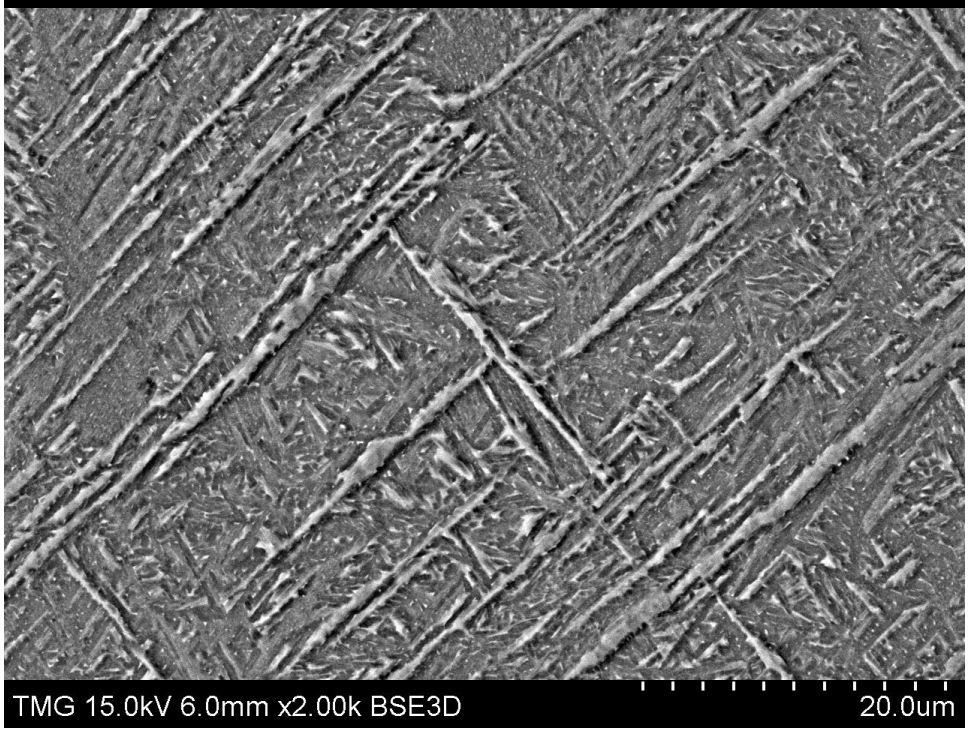

Cube 24

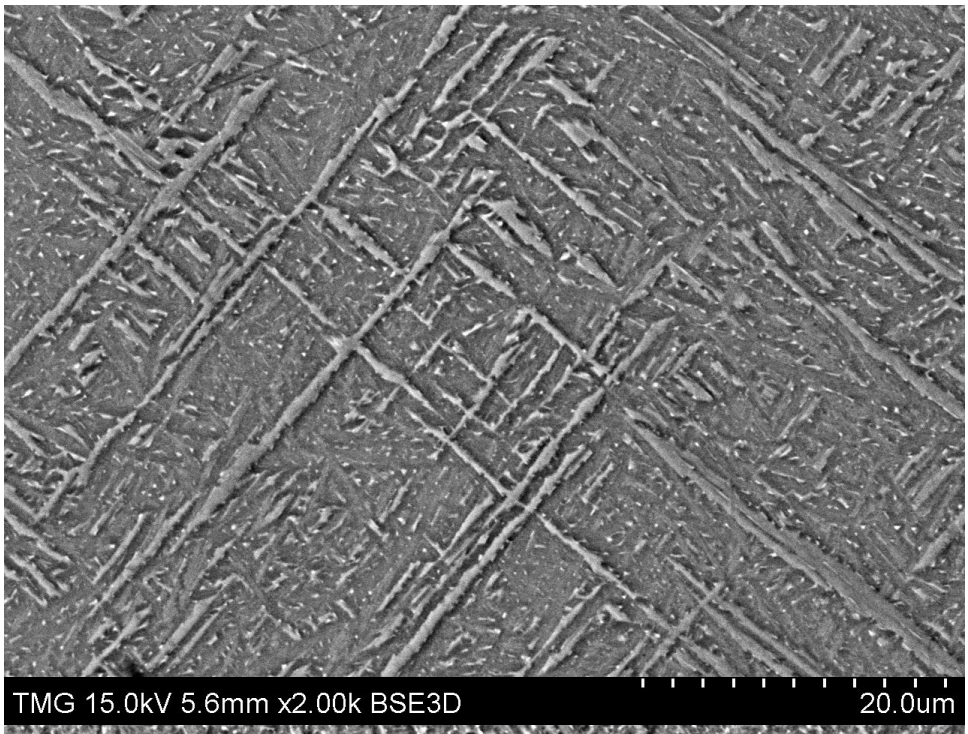

Cube 26

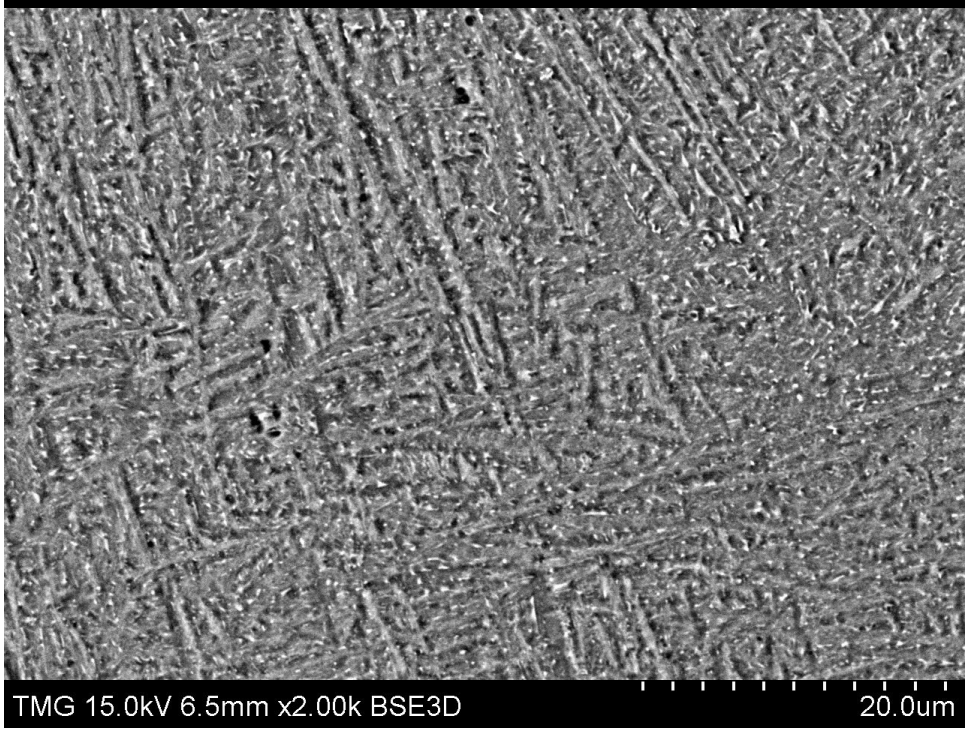

Cube 27

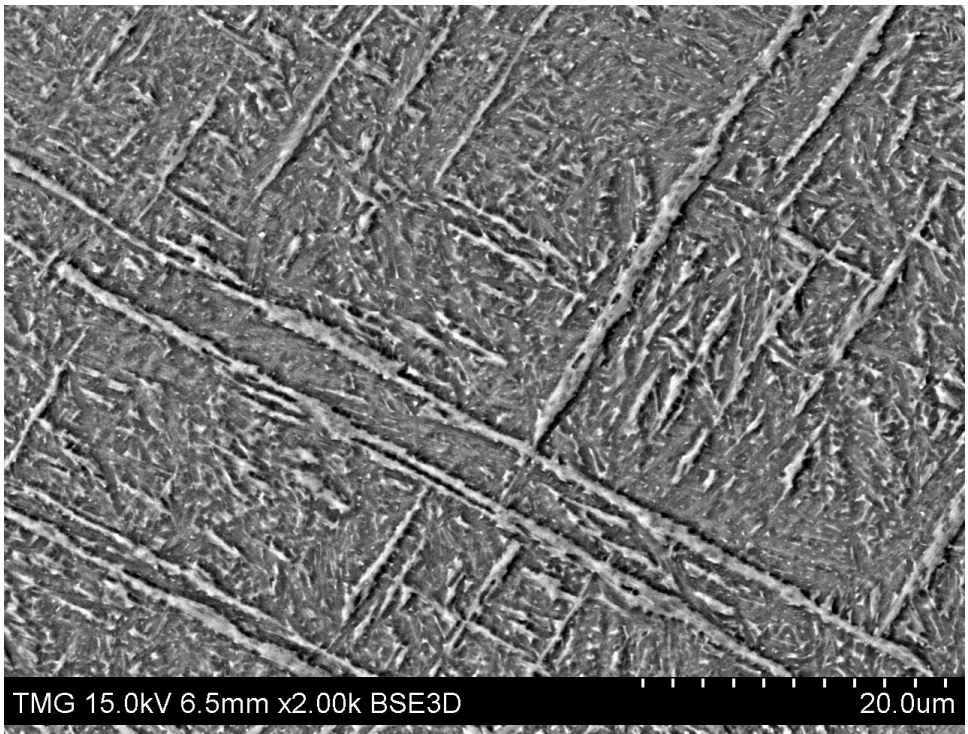

Cube 28

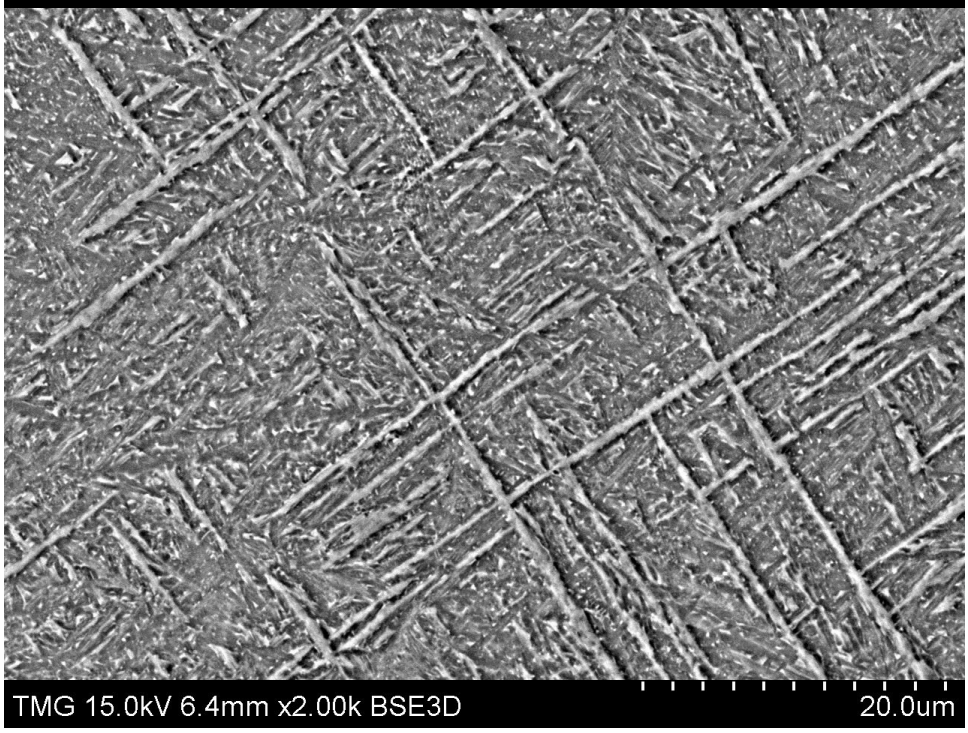

Cube 29

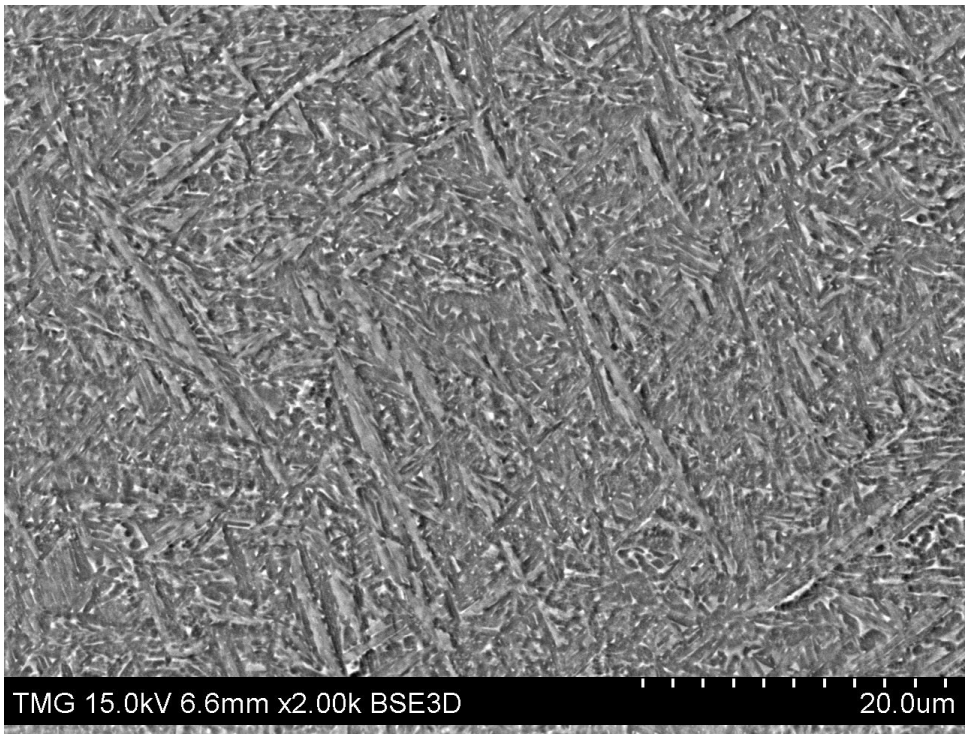

Cube 30

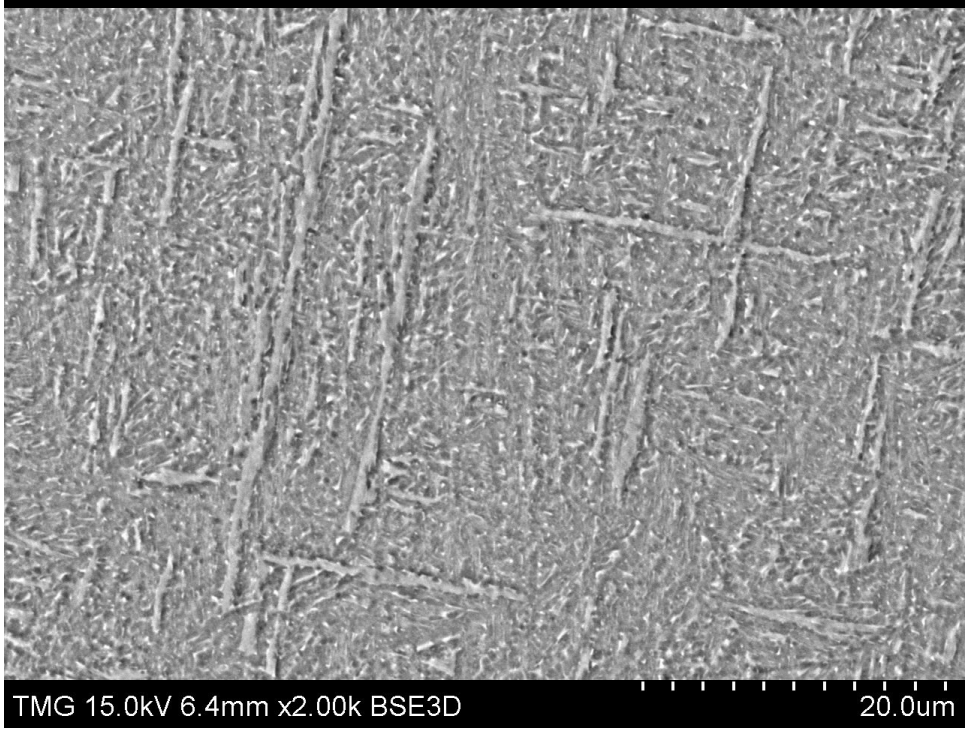

Appendix J Fatigue coupons porosity distributions

Fatigue sample 7

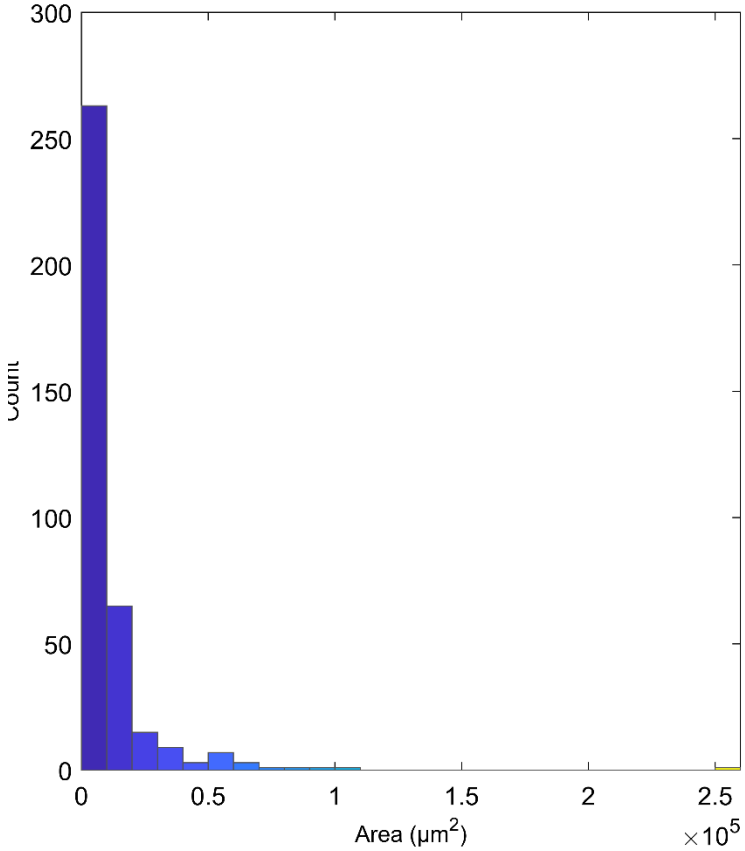

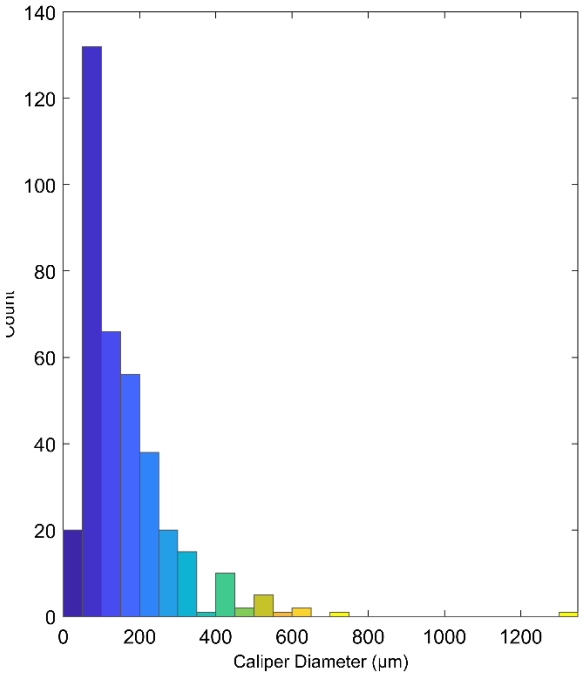

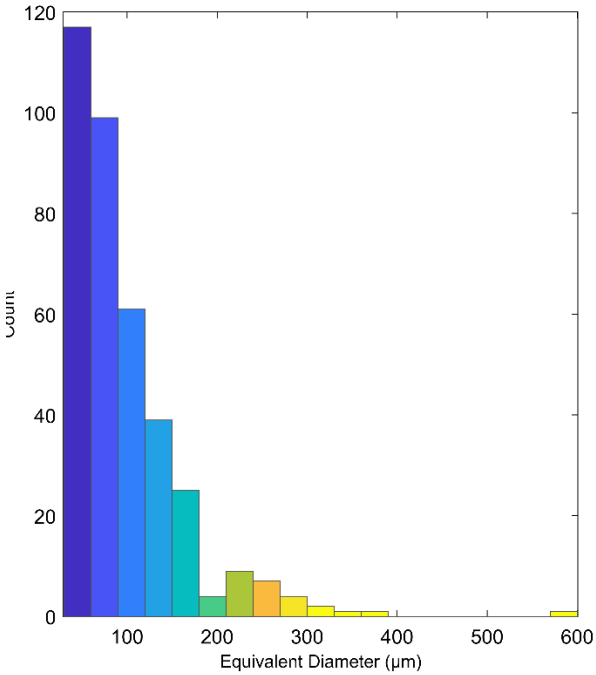

Fatigue sample 9

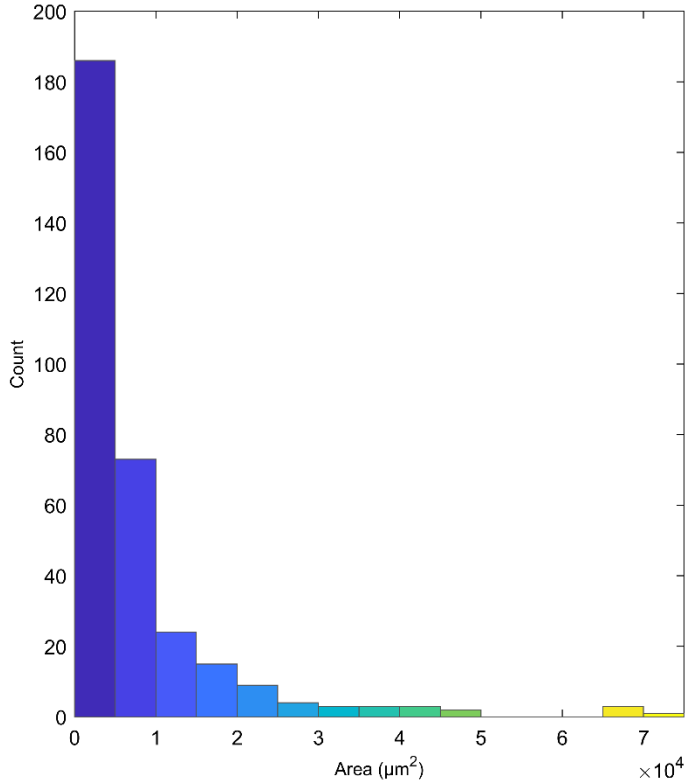

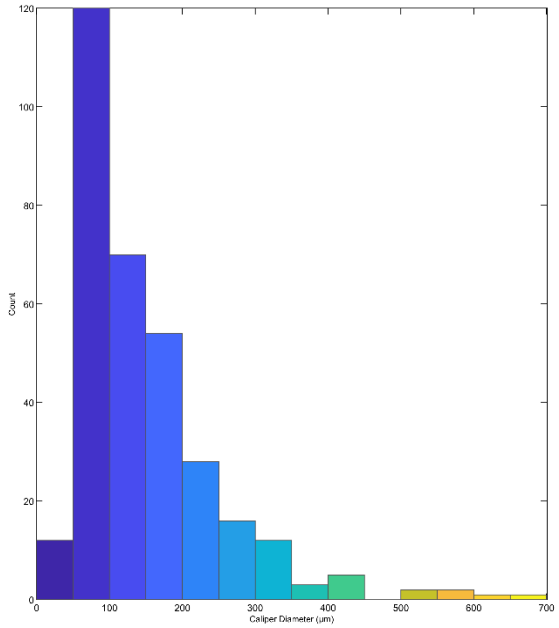

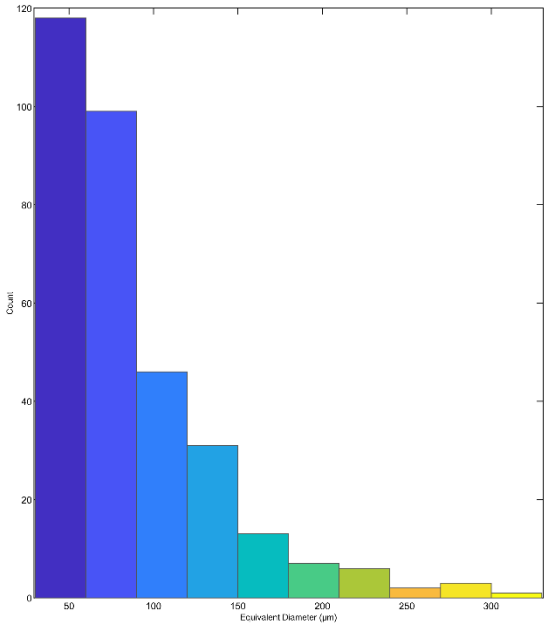

Fatigue sample 16

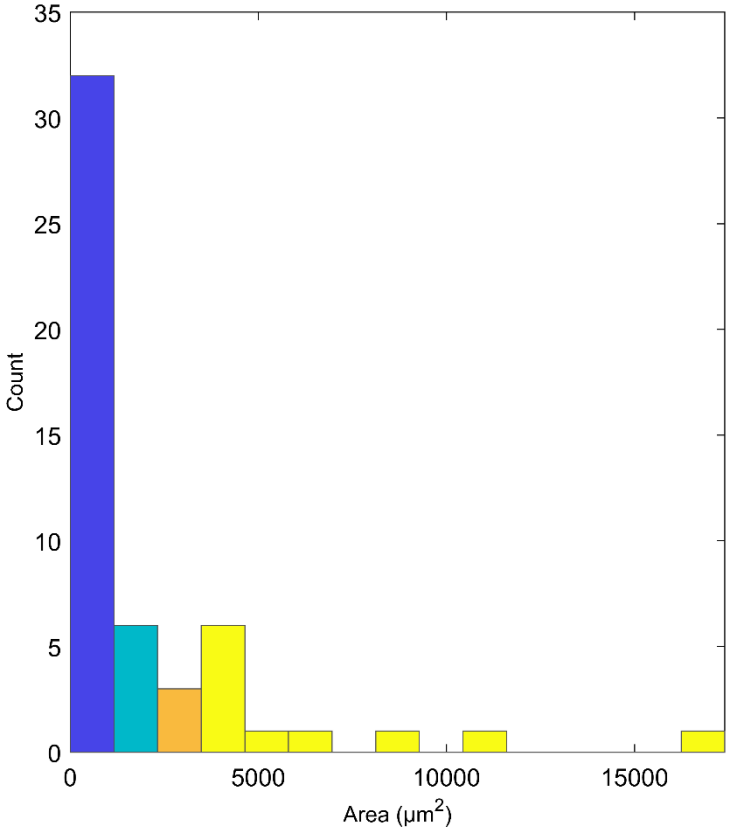

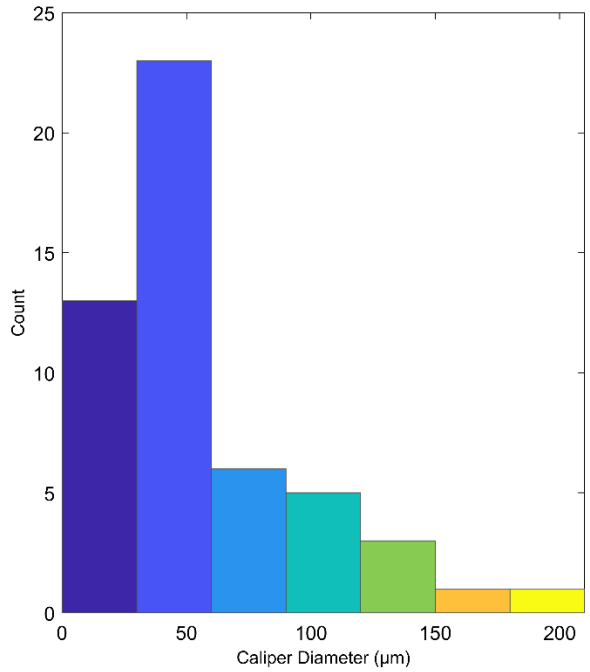

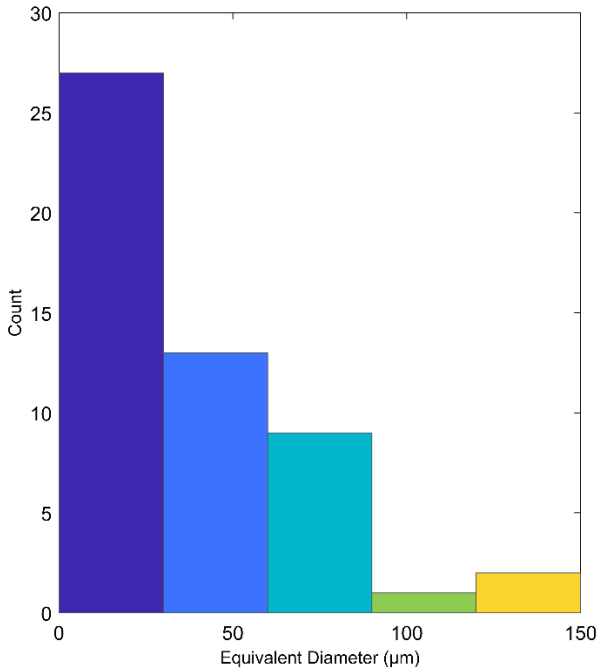

Fatigue sample 18

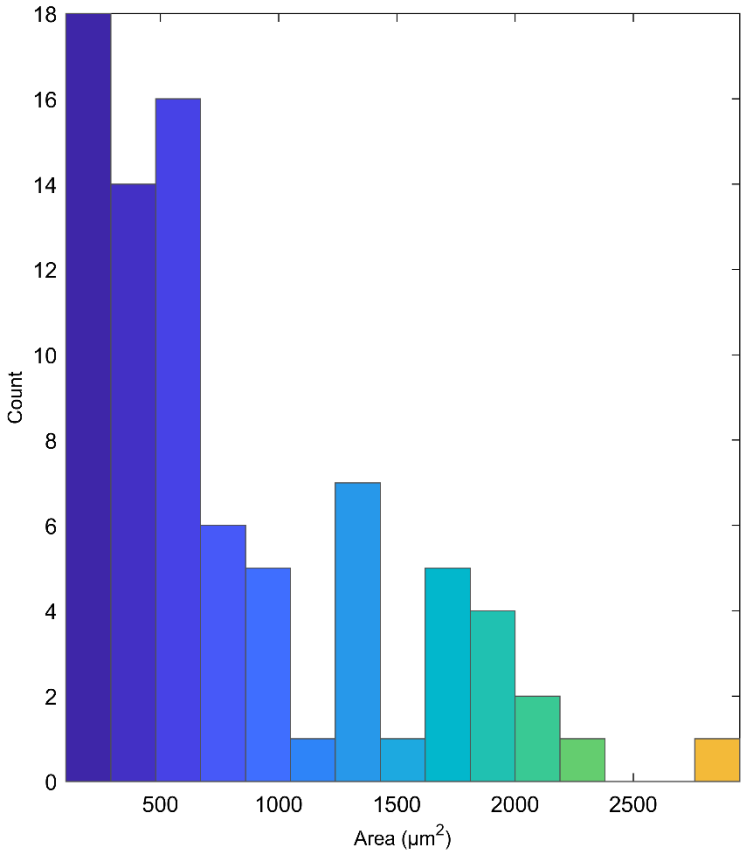

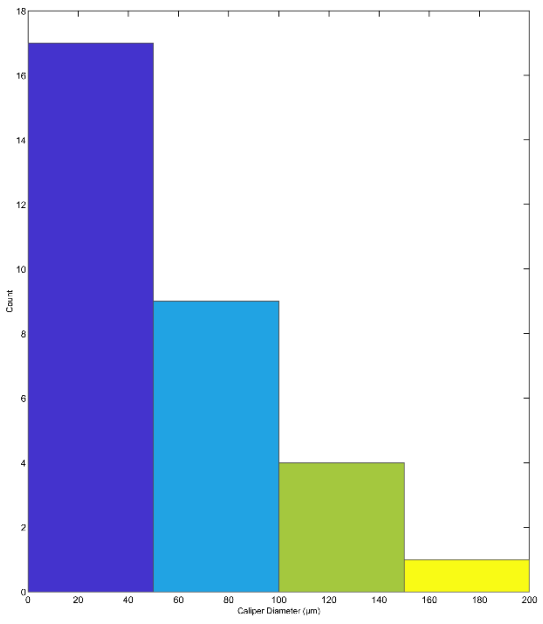

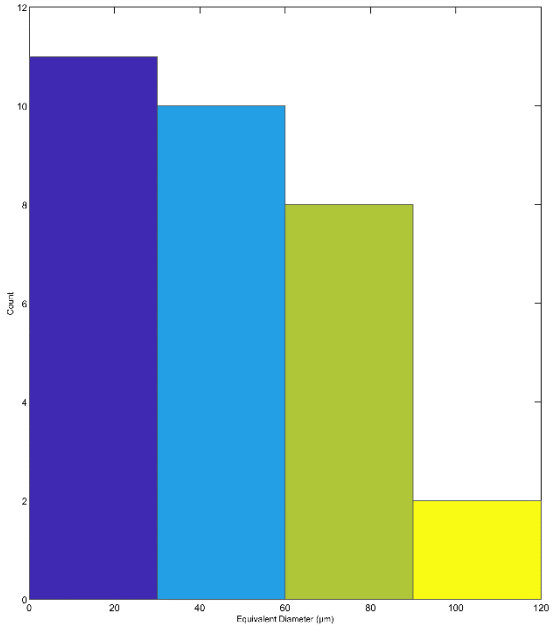

Fatigue sample 19

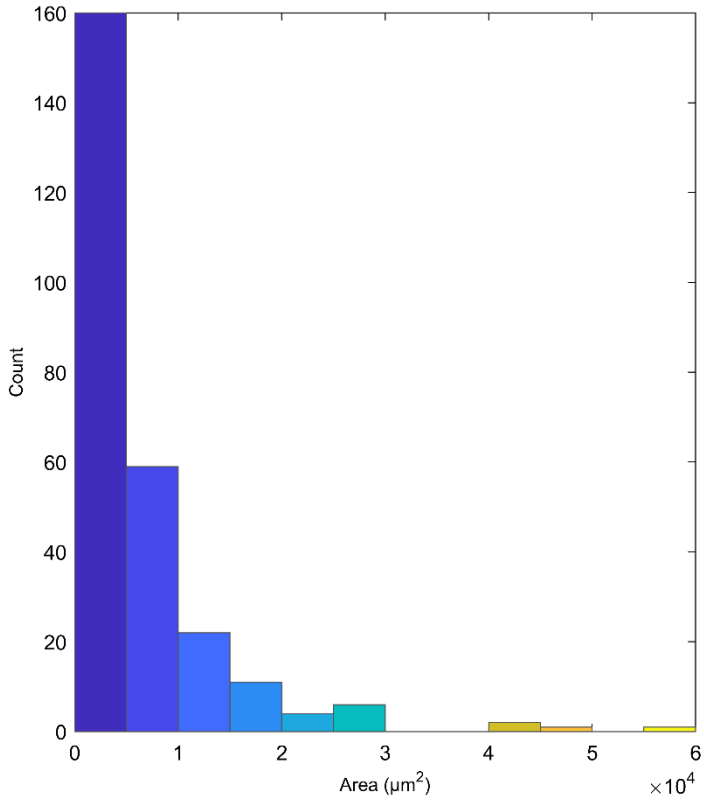

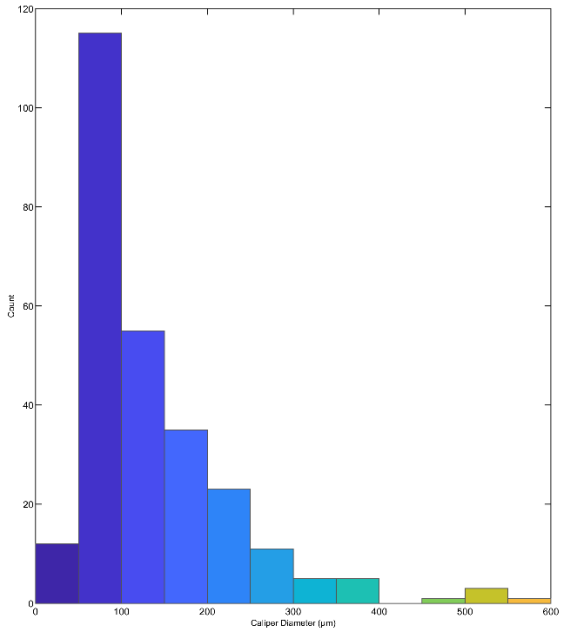

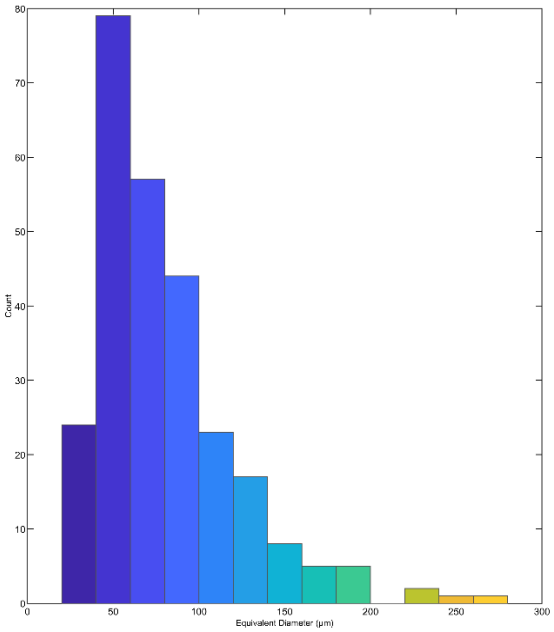

Fatigue sample 20

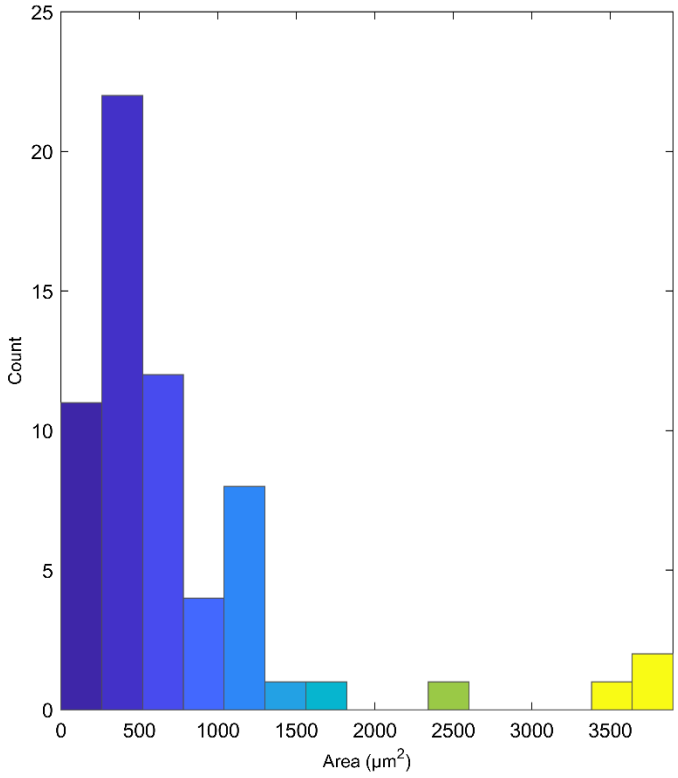

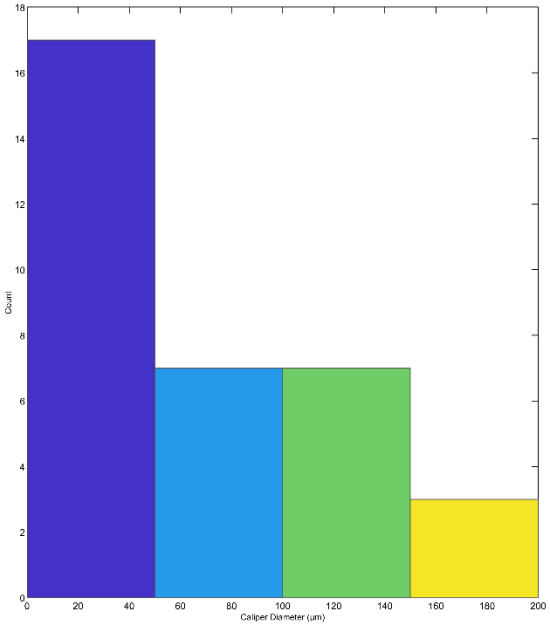

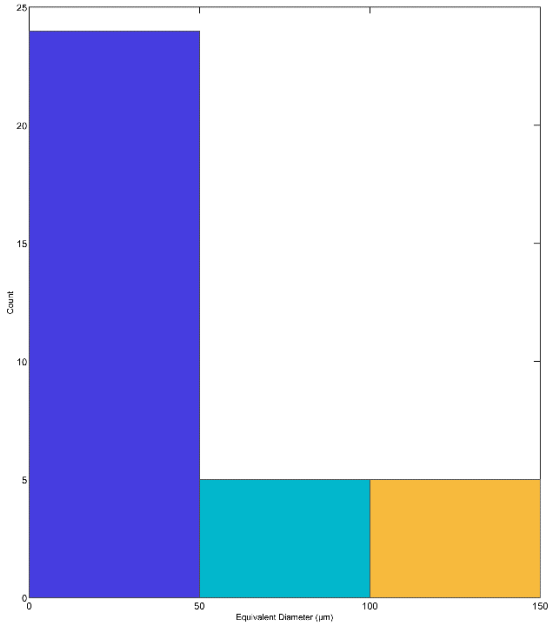

Fatigue sample 21

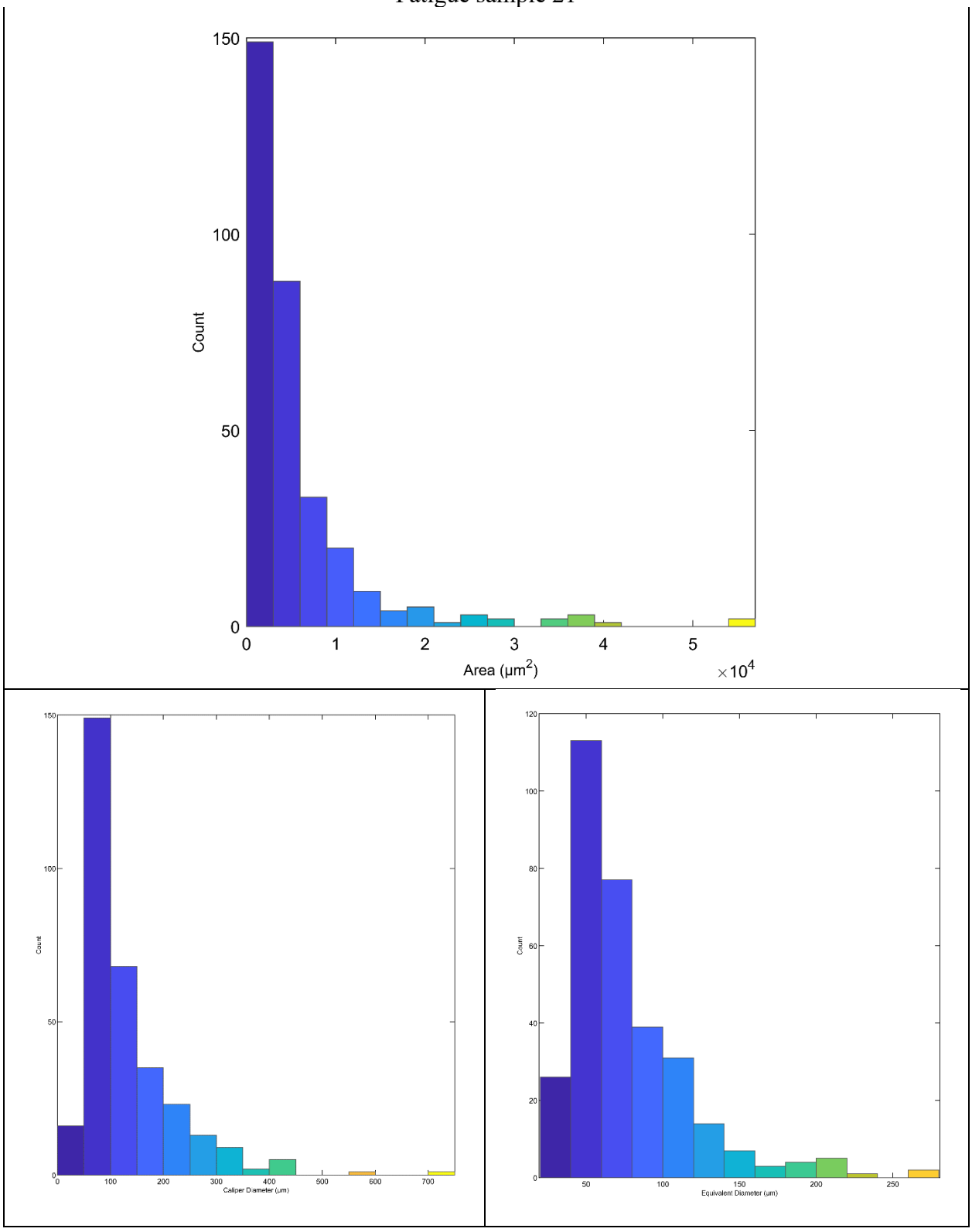

Fatigue sample 22

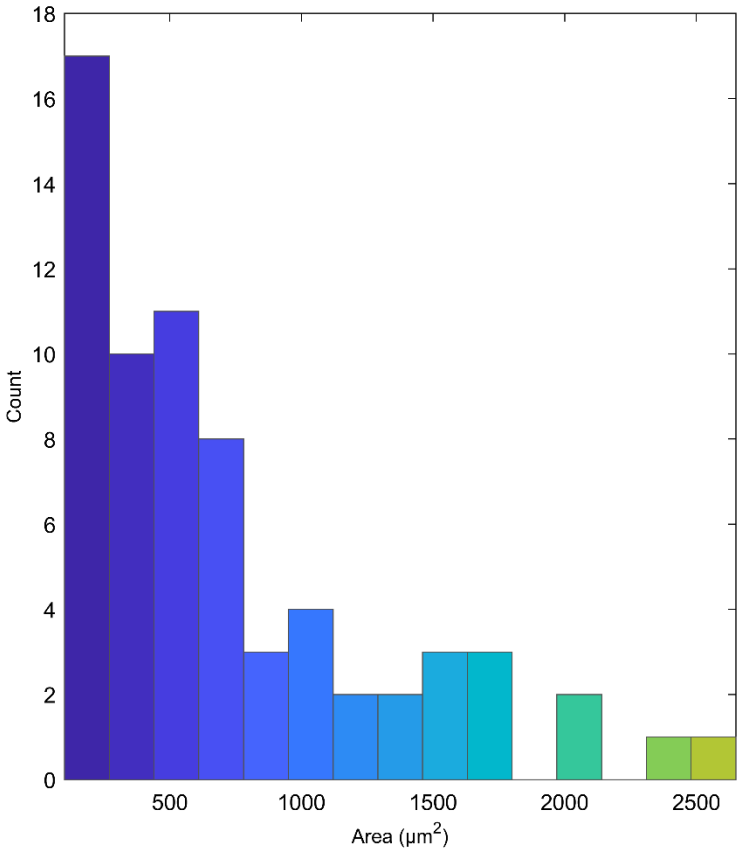

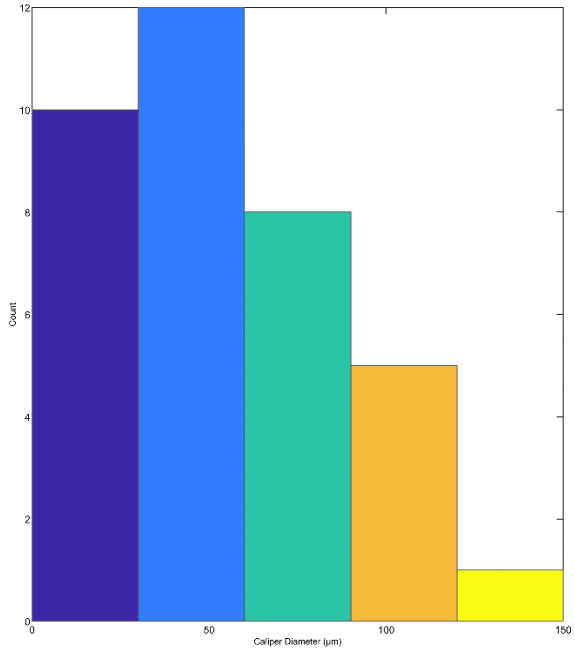

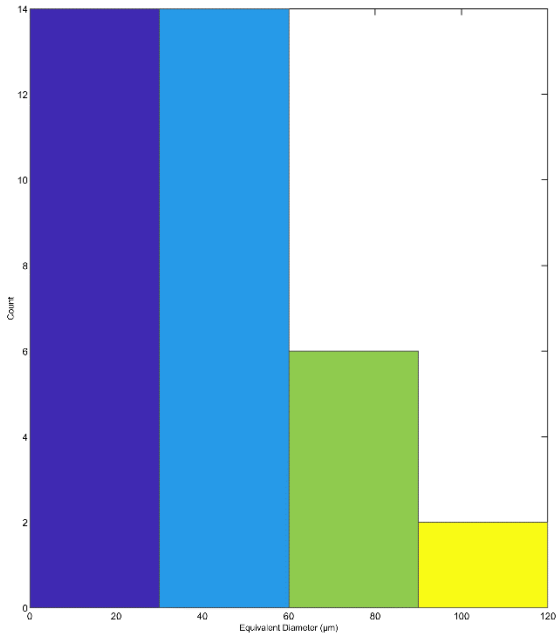

Fatigue sample 23

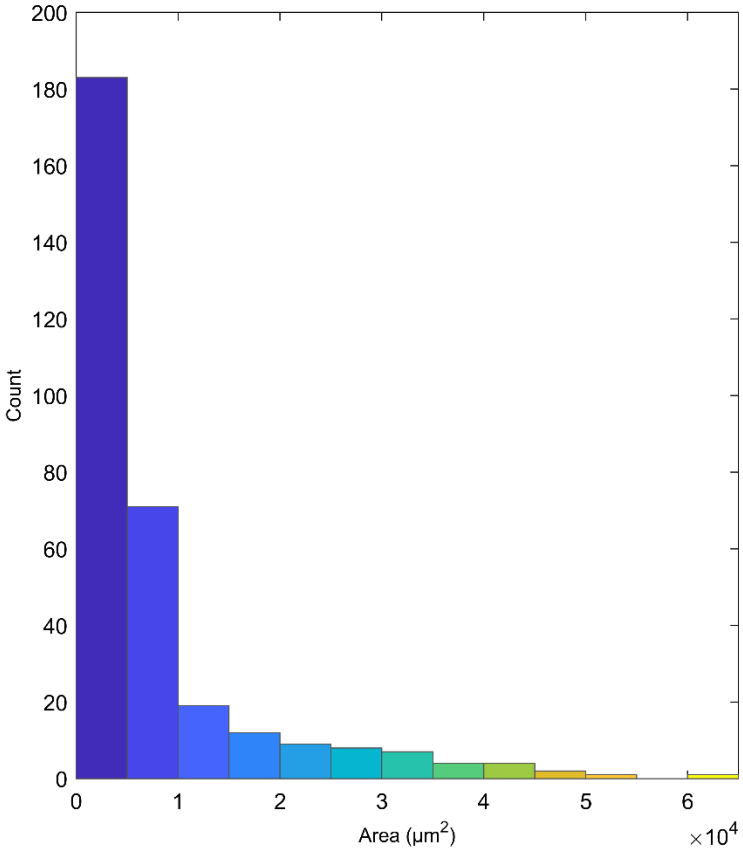
Count
Area (μm²)
×10⁴

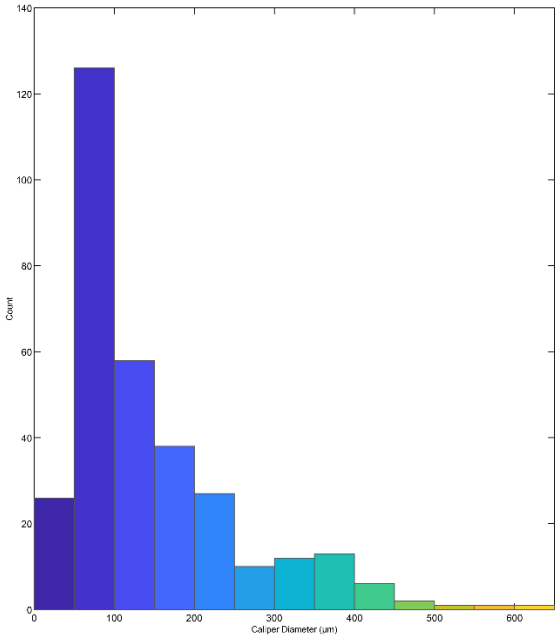
Count
Caliper Diameter (μm)

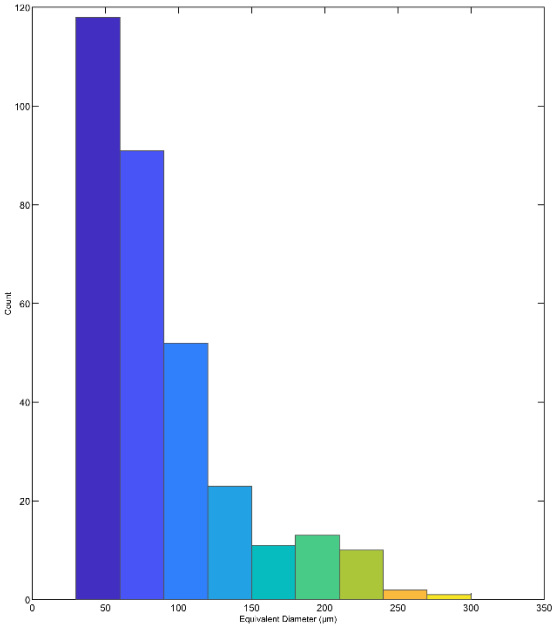
Count
Equivalent Diameter (μm)

Fatigue sample 24

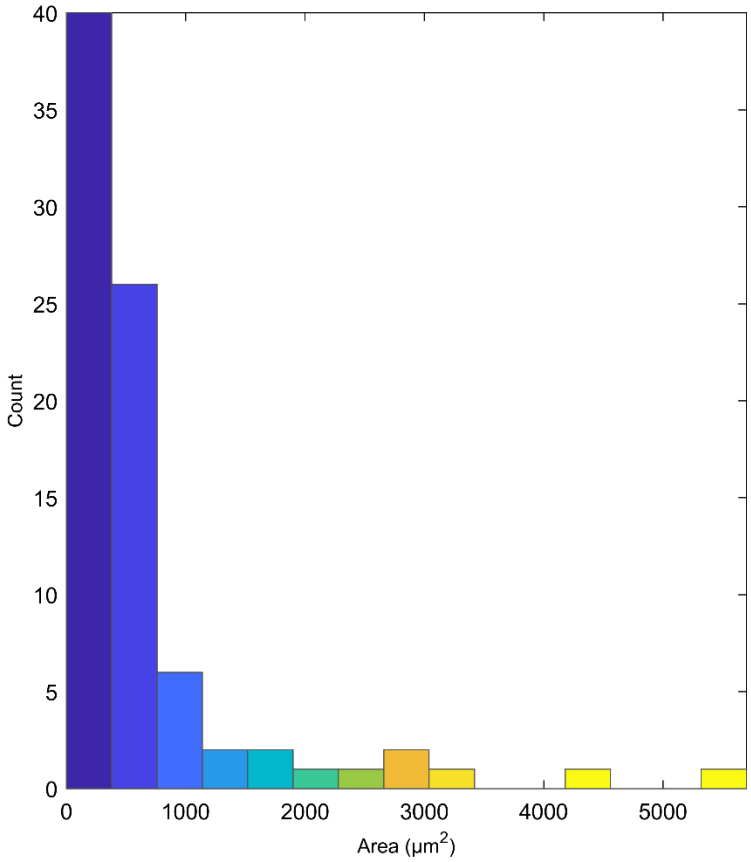

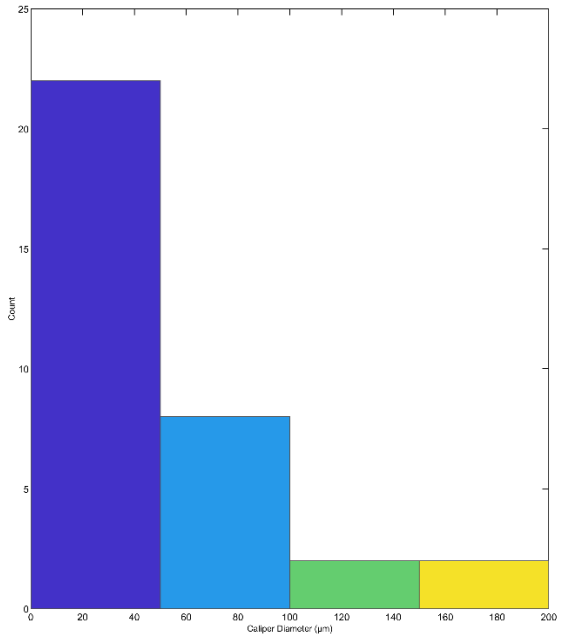

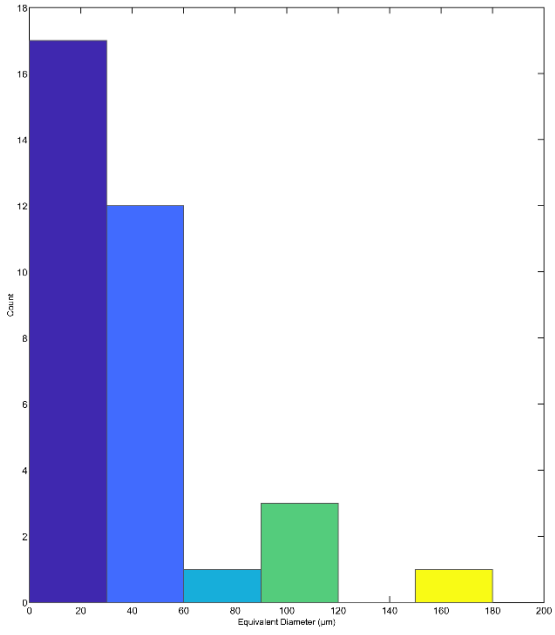

Appendix K Tensile samples stress-strain curves.

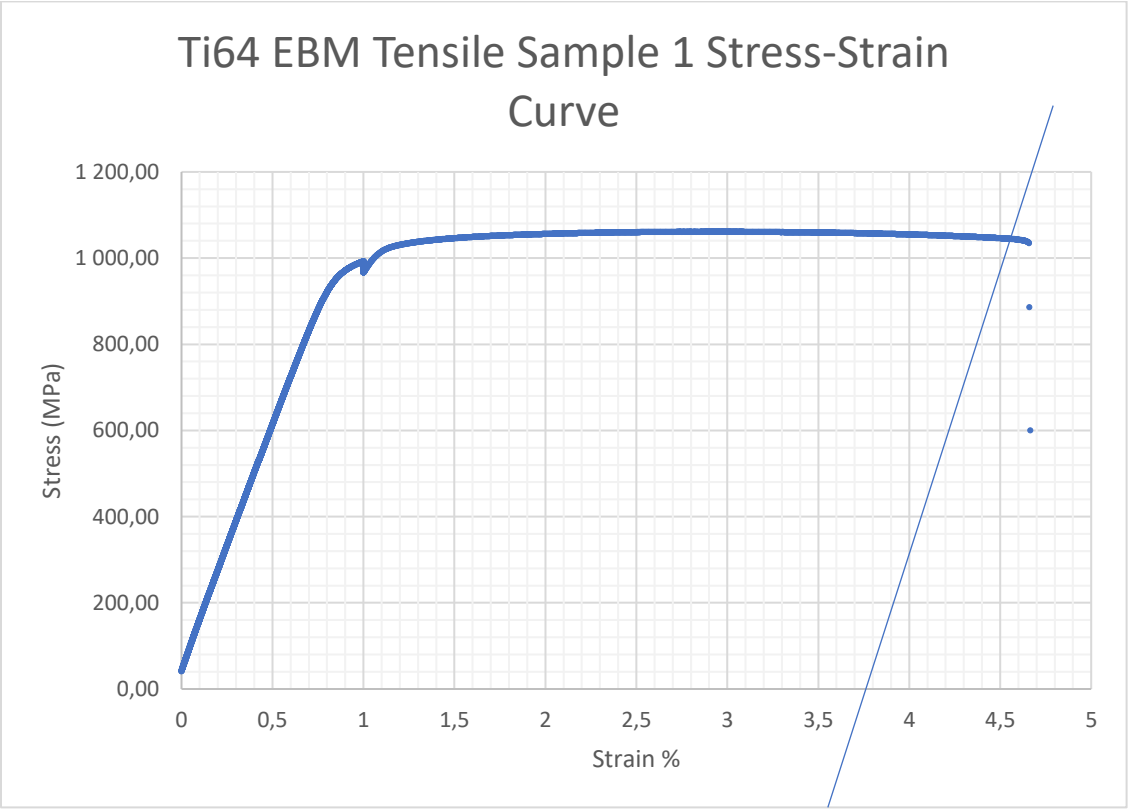

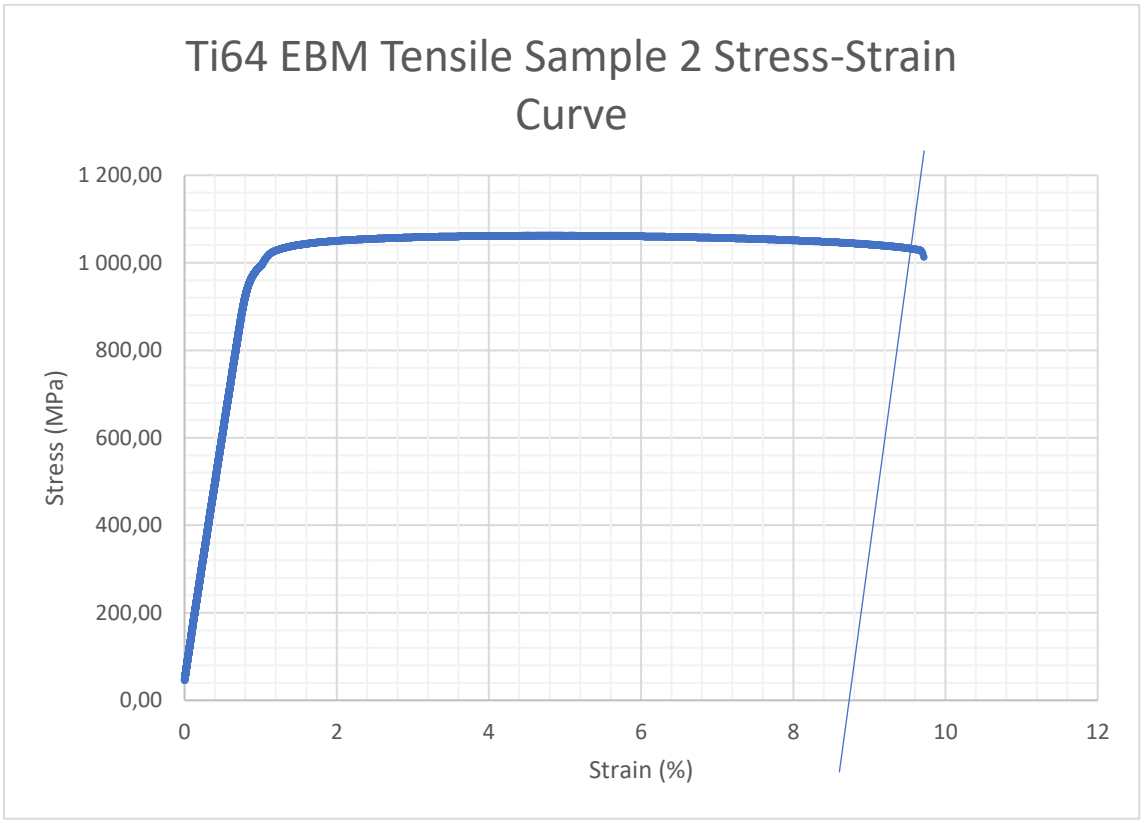

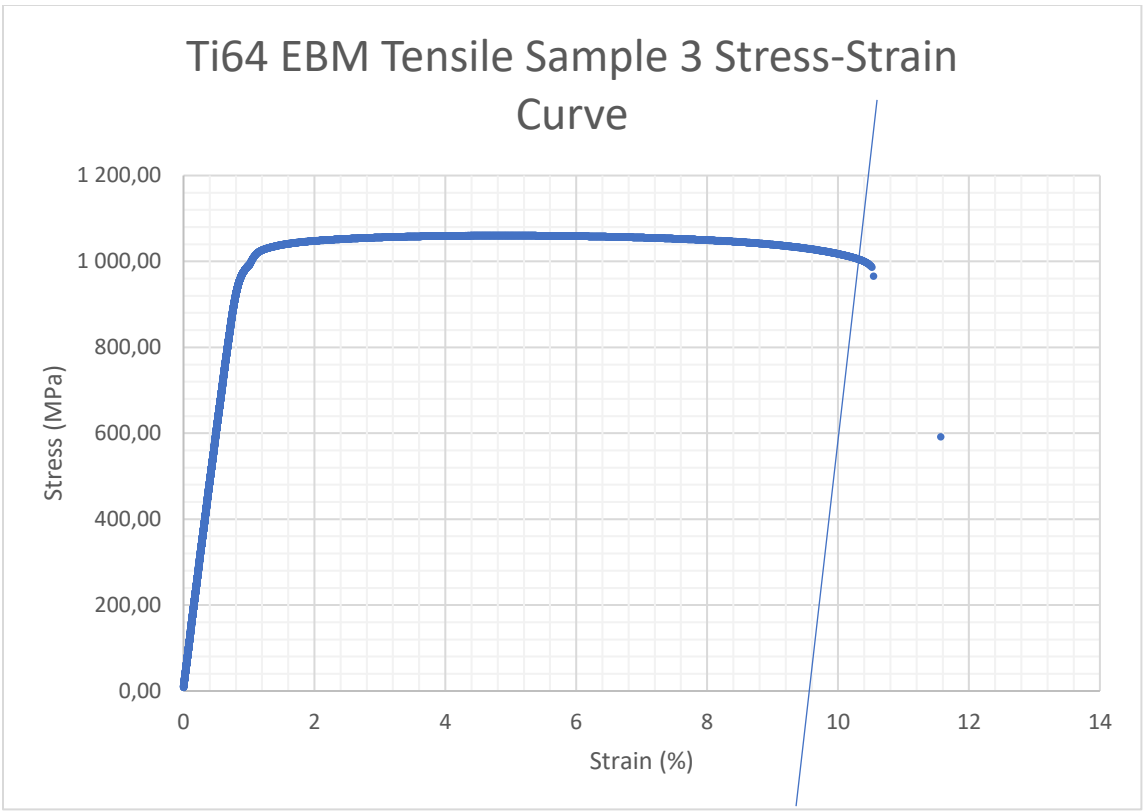
Ti64 EBM Tensile Sample 3 Stress-Strain Curve
1 200,00
1 000,00
800,00
600,00
400,00
200,00
0,00
Stress (MPa)
0
2
4
6
8
10
12
14
Strain (%)

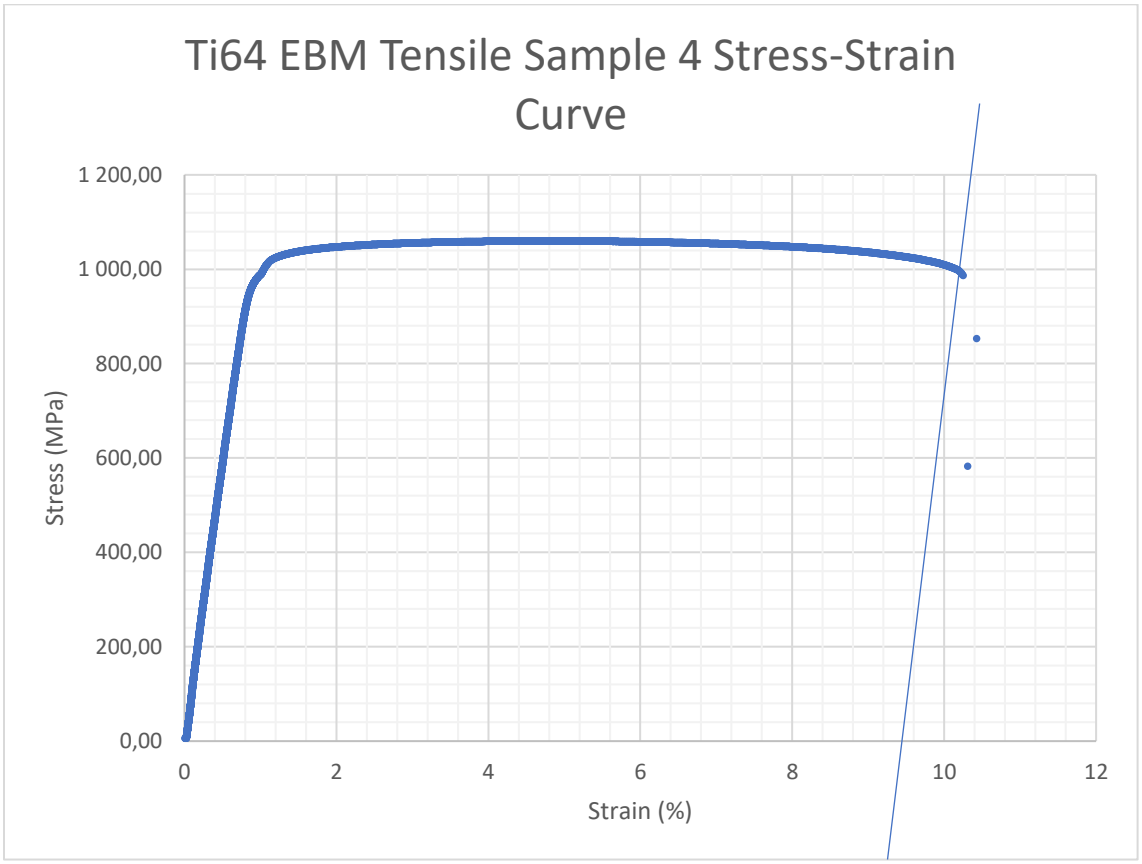
Ti64 EBM Tensile Sample 4 Stress-Strain Curve
1 200,00
1 000,00
800,00
600,00
400,00
200,00
0,00
Stress (MPa)
0
2
4
6
8
10
12
Strain (%)

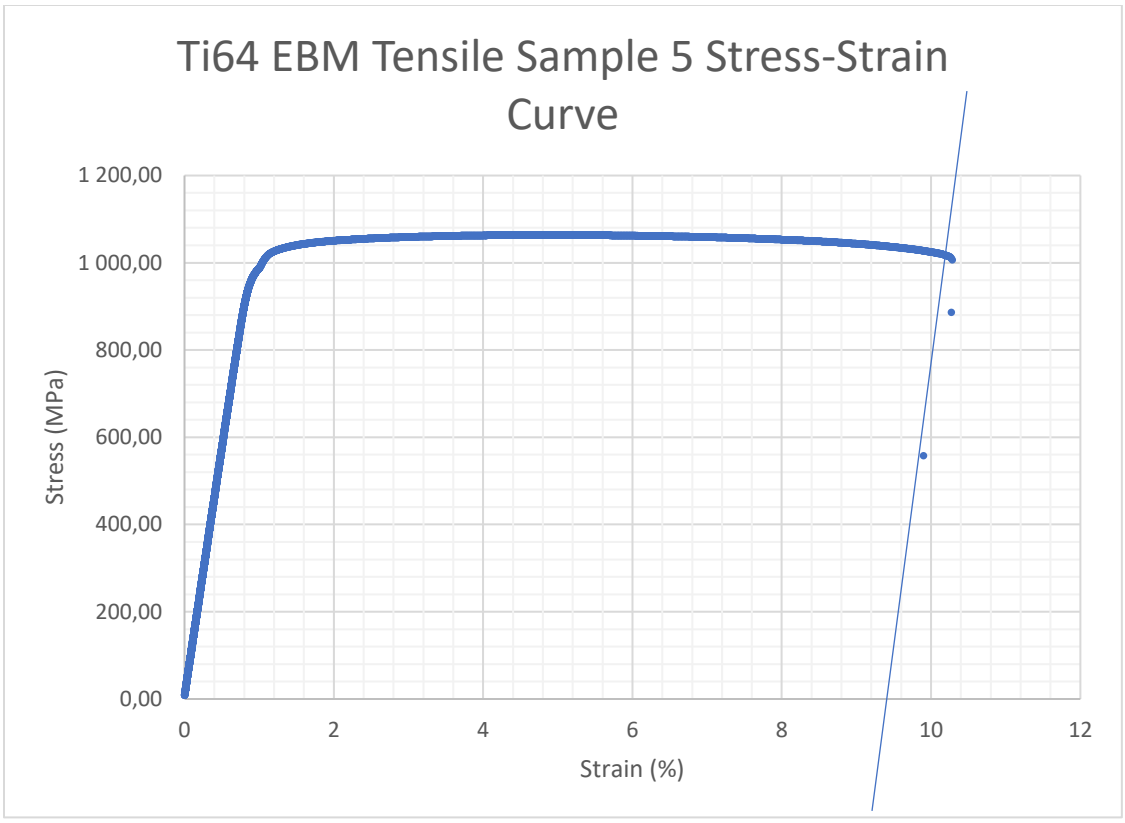
Ti64 EBM Tensile Sample 5 Stress-Strain Curve
1 200,00
1 000,00
800,00
600,00
400,00
200,00
0,00
Stress (MPa)
0
2
4
6
8
10
12
Strain (%)

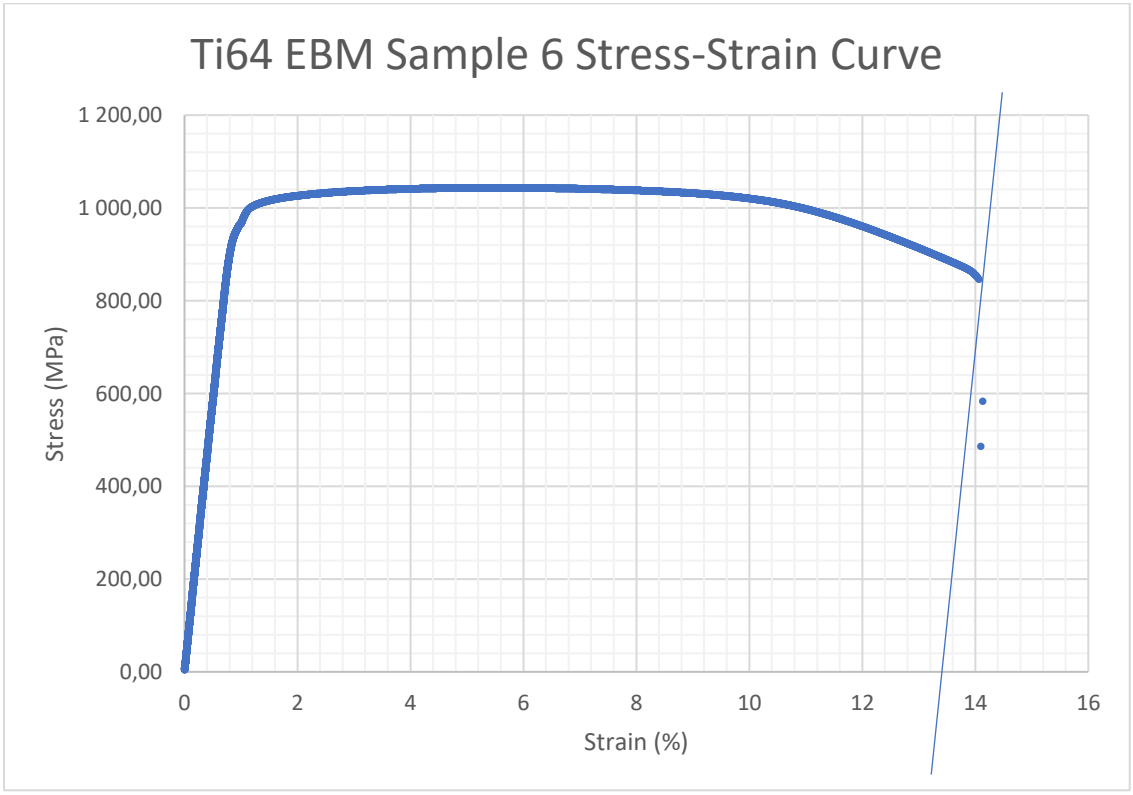
Ti64 EBM Sample 6 Stress-Strain Curve
1 200,00
1 000,00
800,00
600,00
400,00
200,00
0,00
Stress (MPa)
0
2
4
6
8
10
12
14
16
Strain (%)

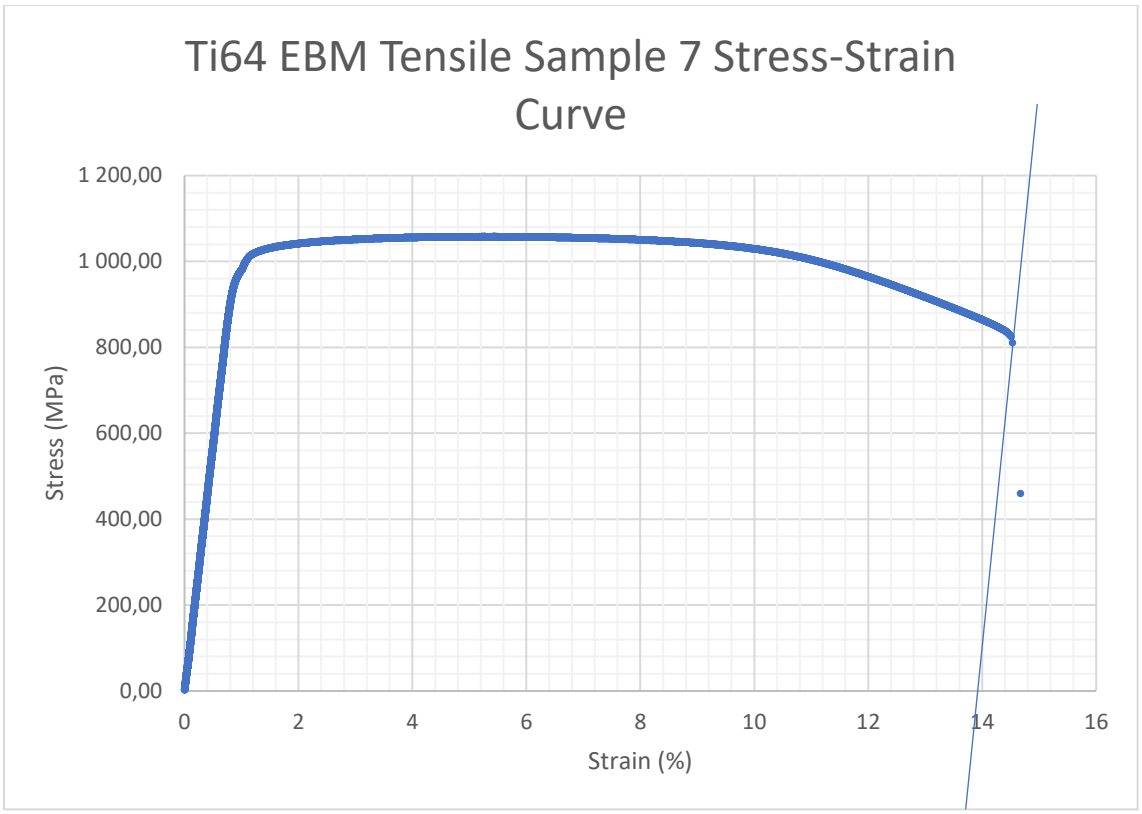
Ti64 EBM Tensile Sample 7 Stress-Strain Curve
1 200,00
1 000,00
800,00
600,00
400,00
200,00
0,00
Stress (MPa)
0
2
4
6
8
10
12
14
16
Strain (%)

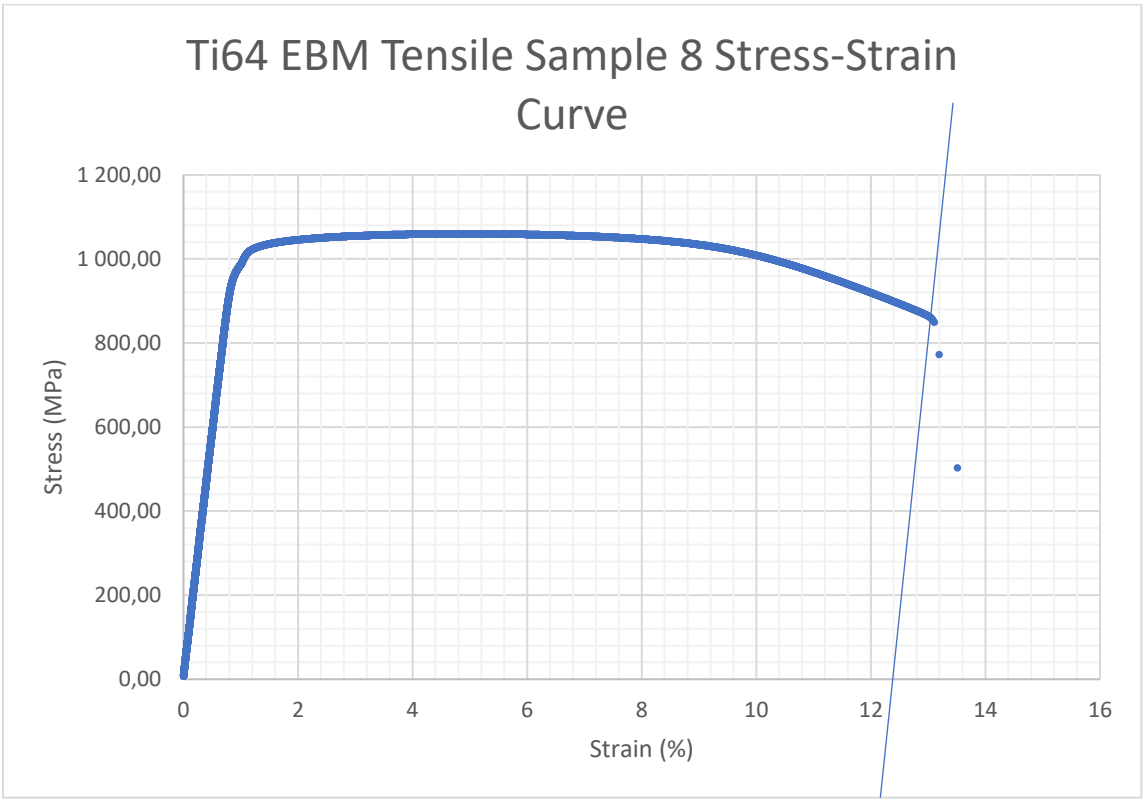
Ti64 EBM Tensile Sample 8 Stress-Strain Curve
1 200,00
1 000,00
800,00
600,00
400,00
200,00
0,00
Stress (MPa)
0
2
4
6
8
10
12
14
16
Strain (%)

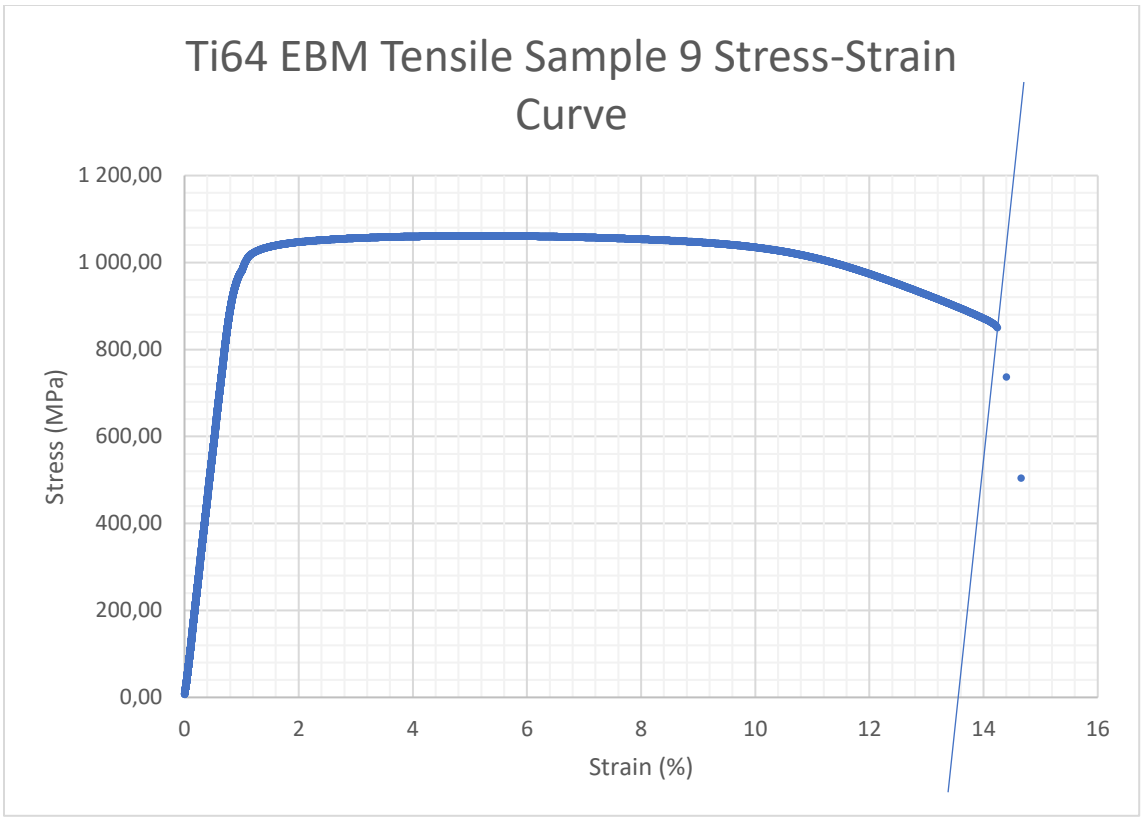
Ti64 EBM Tensile Sample 9 Stress-Strain Curve
1 200,00
1 000,00
800,00
600,00
400,00
200,00
0,00
Stress (MPa)
0
2
4
6
8
10
12
14
16
Strain (%)

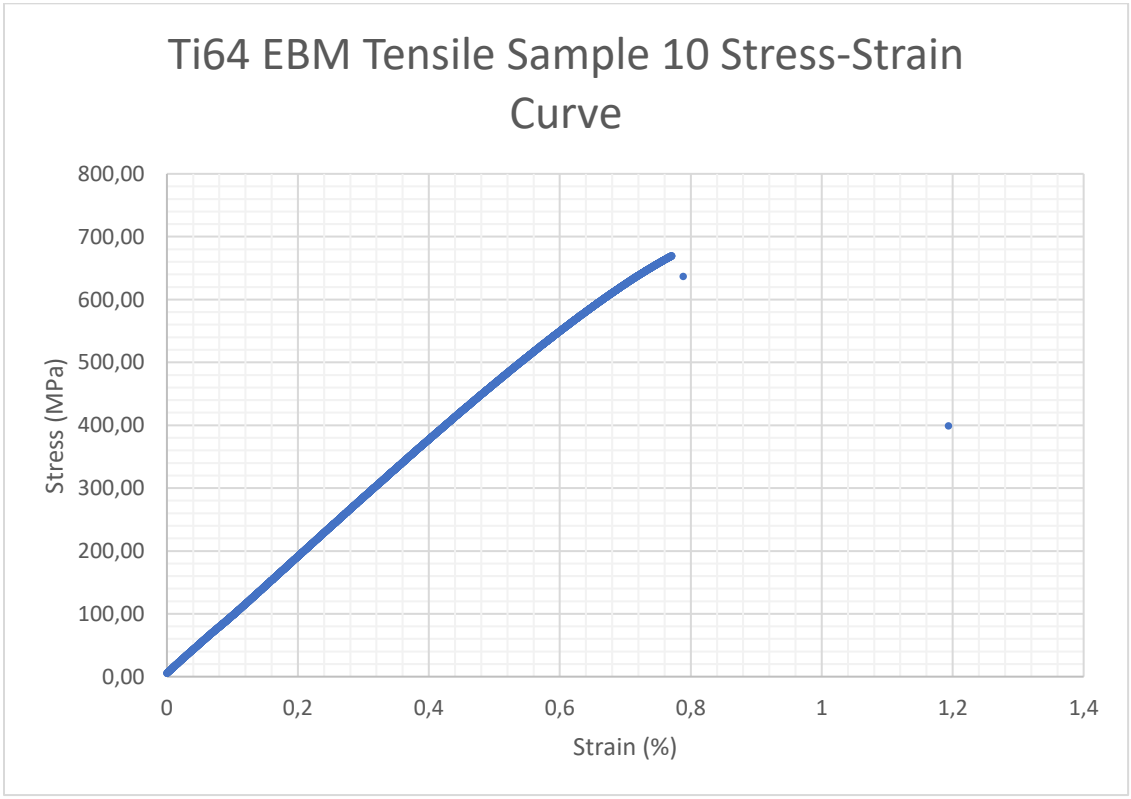
Ti64 EBM Tensile Sample 10 Stress-Strain Curve
800,00
700,00
600,00
500,00
400,00
300,00
200,00
100,00
0,00
Stress (MPa)
0
0,2
0,4
0,6
0,8
1
1,2
1,4
Strain (%)

Appendix L Fatigue samples stress-strain curves.

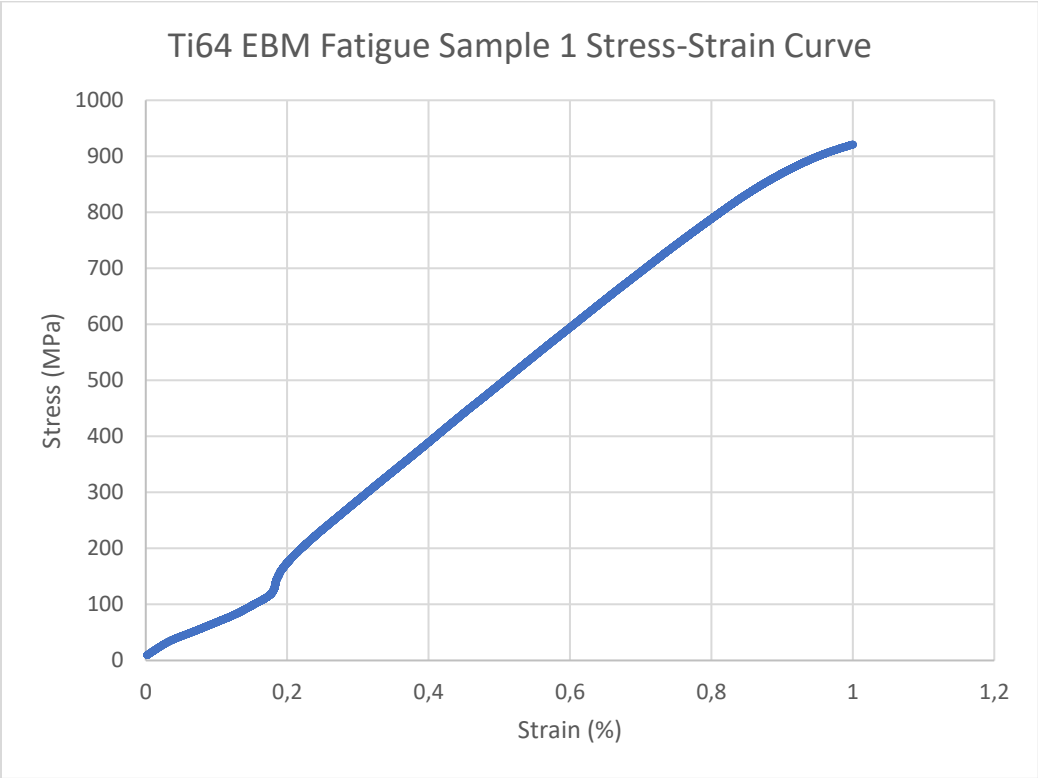

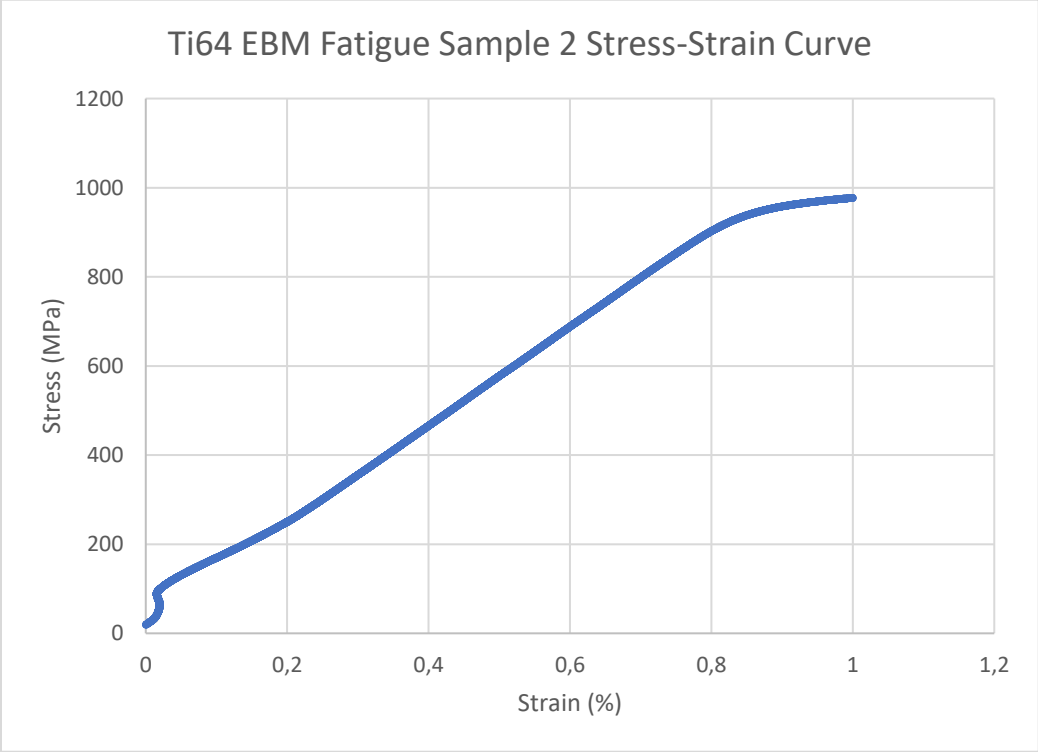

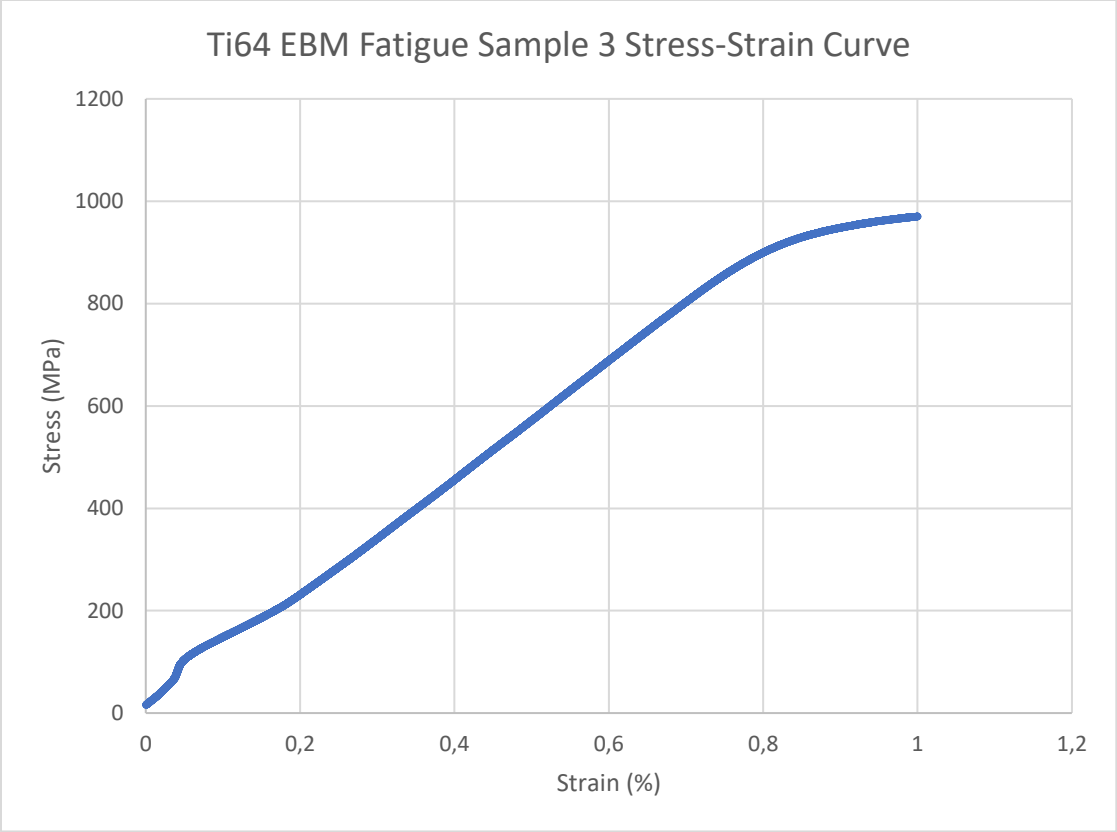
Ti64 EBM Fatigue Sample 3 Stress-Strain Curve
Stress (MPa)
1200
1000
800
600
400
200
0
0
0,2
0,4
0,6
0,8
1
1,2
Strain (%)

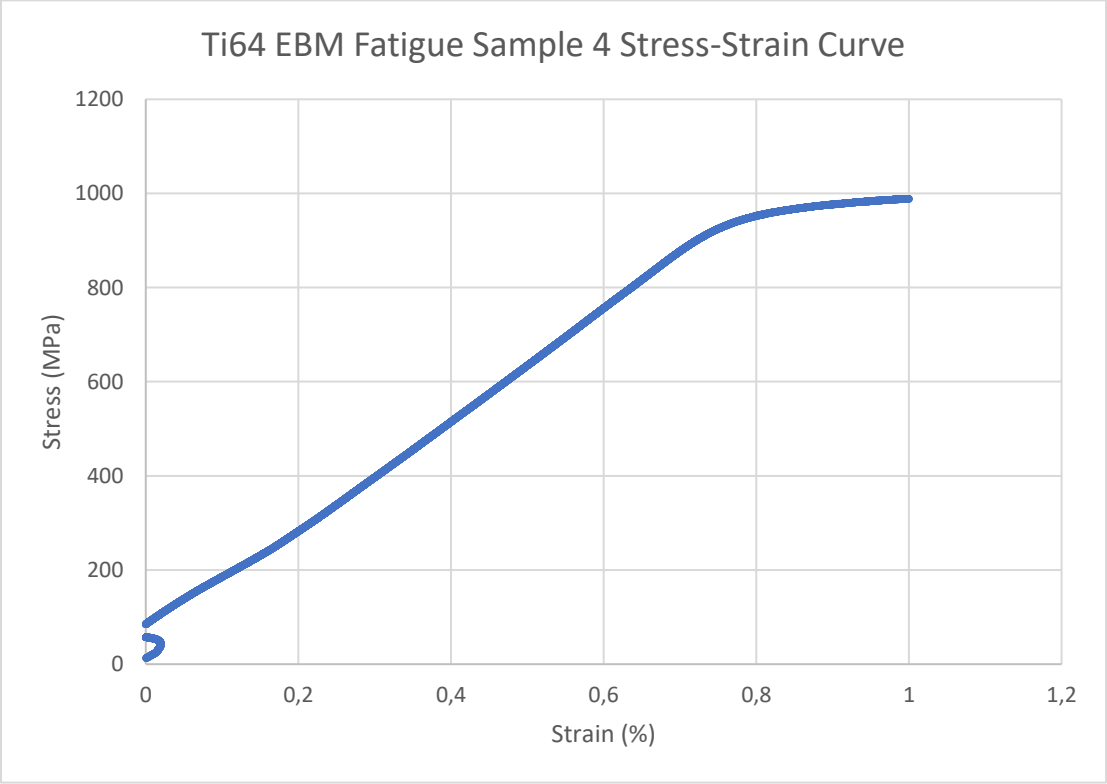
Ti64 EBM Fatigue Sample 4 Stress-Strain Curve
Stress (MPa)
1200
1000
800
600
400
200
0
0
0,2
0,4
0,6
0,8
1
1,2
Strain (%)

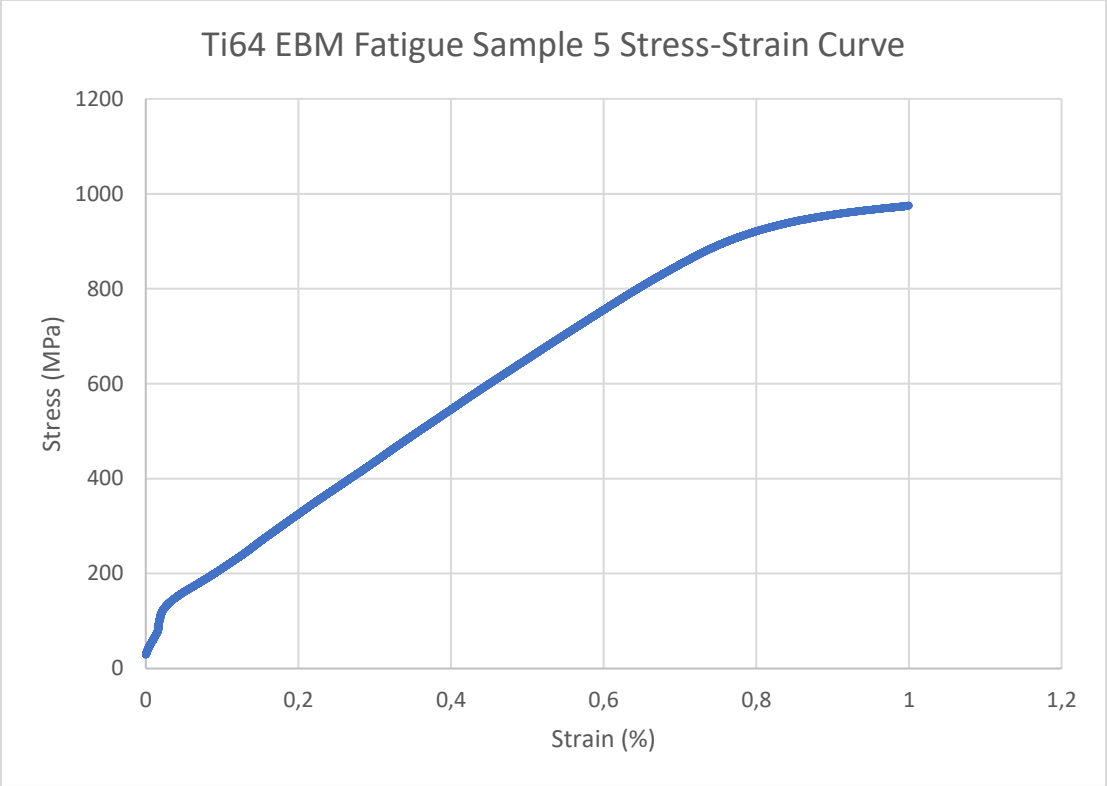
Ti64 EBM Fatigue Sample 5 Stress-Strain Curve
Stress (MPa)
1200
1000
800
600
400
200
0
0
0,2
0,4
0,6
0,8
1
1,2
Strain (%)

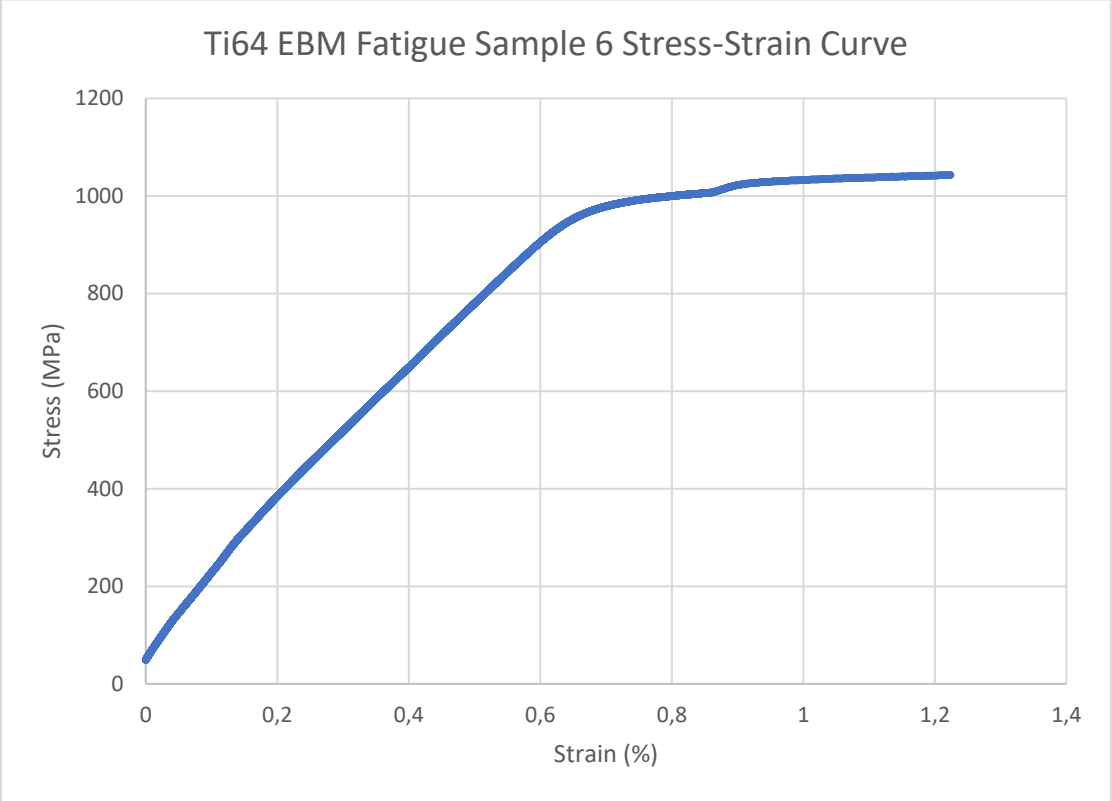
Ti64 EBM Fatigue Sample 6 Stress-Strain Curve
Stress (MPa)
1200
1000
800
600
400
200
0
0
0,2
0,4
0,6
0,8
1
1,2
1,4
Strain (%)

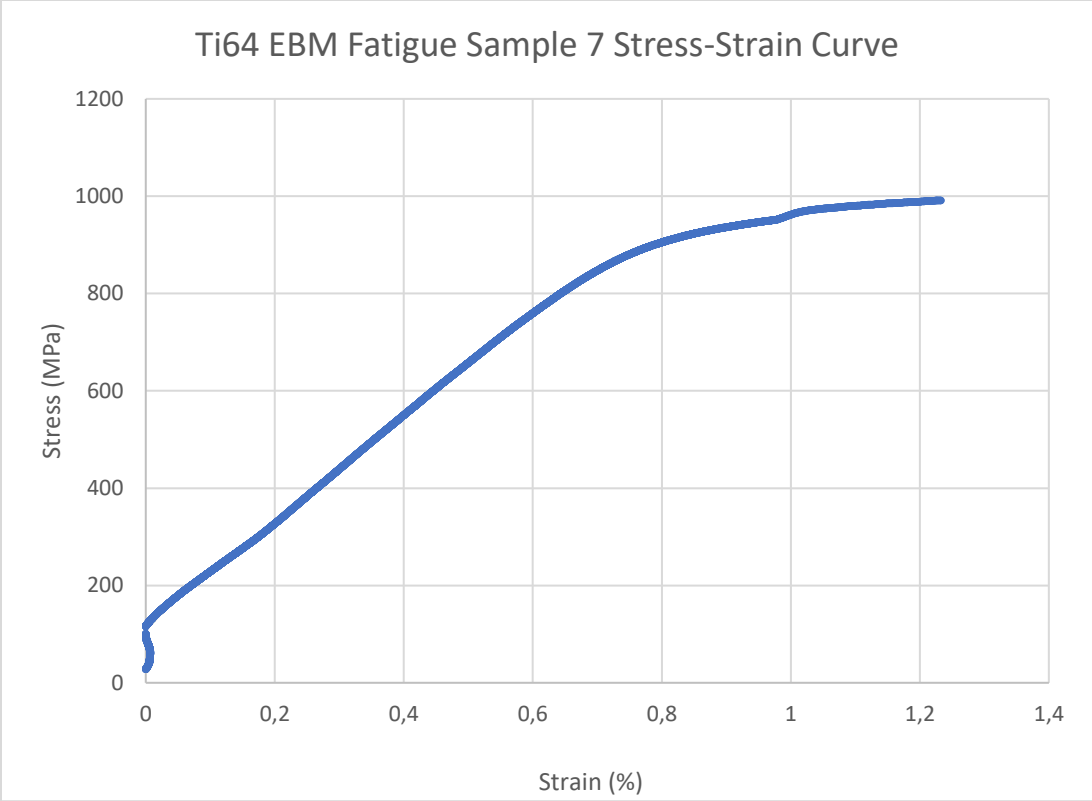
Ti64 EBM Fatigue Sample 7 Stress-Strain Curve
Stress (MPa)
1200
1000
800
600
400
200
0
0
0,2
0,4
0,6
0,8
1
1,2
1,4
Strain (%)

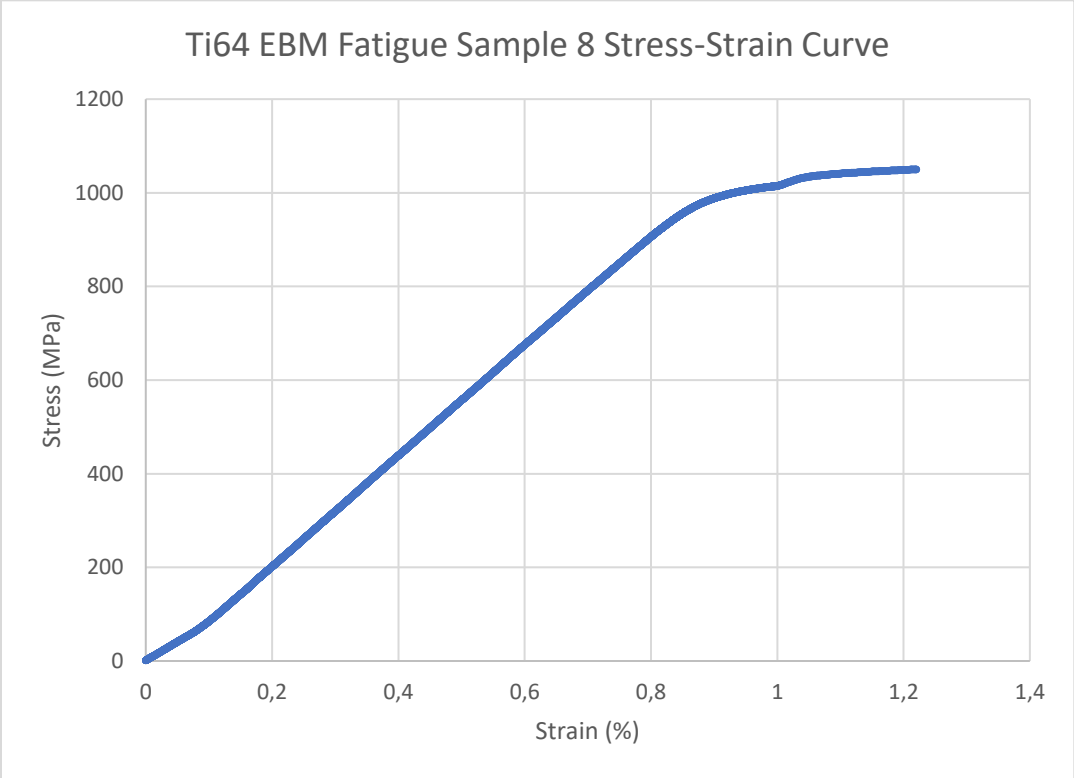
Ti64 EBM Fatigue Sample 8 Stress-Strain Curve
Stress (MPa)
1200
1000
800
600
400
200
0
0
0,2
0,4
0,6
0,8
1
1,2
1,4
Strain (%)

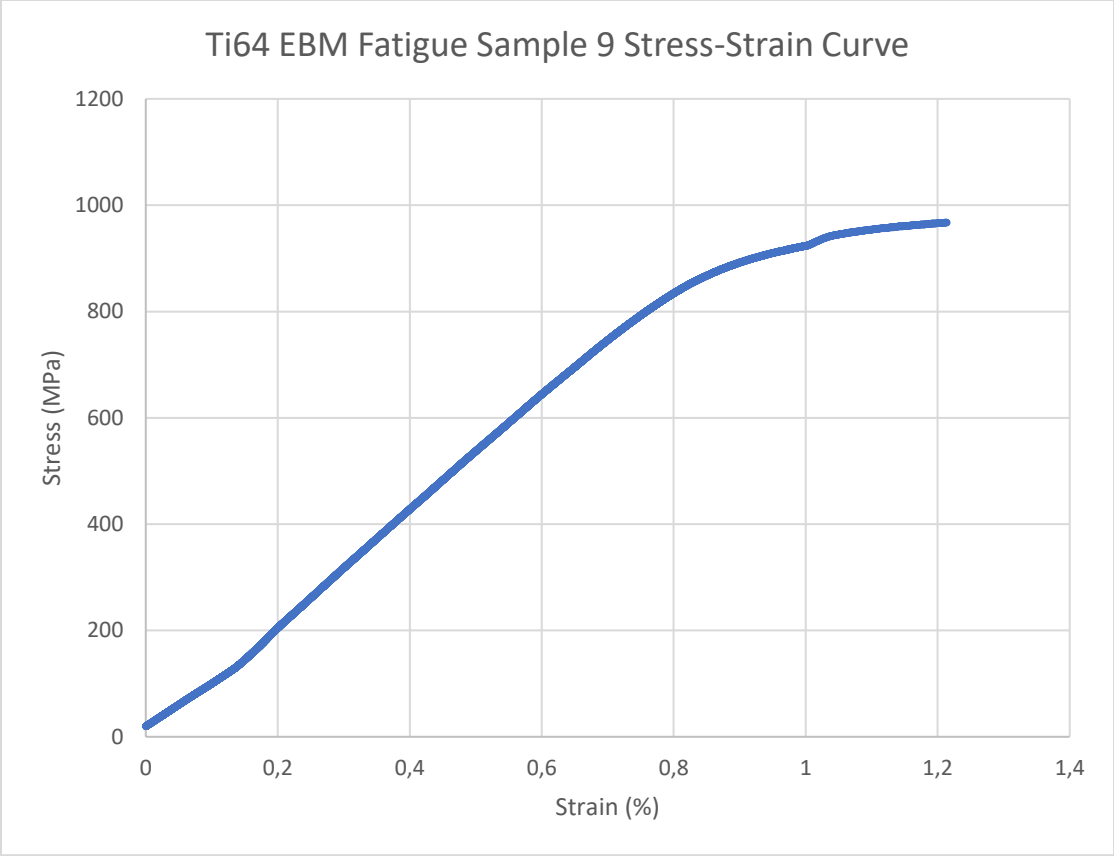
Ti64 EBM Fatigue Sample 9 Stress-Strain Curve
Stress (MPa)
1200
1000
800
600
400
200
0
0
0,2
0,4
0,6
0,8
1
1,2
1,4
Strain (%)

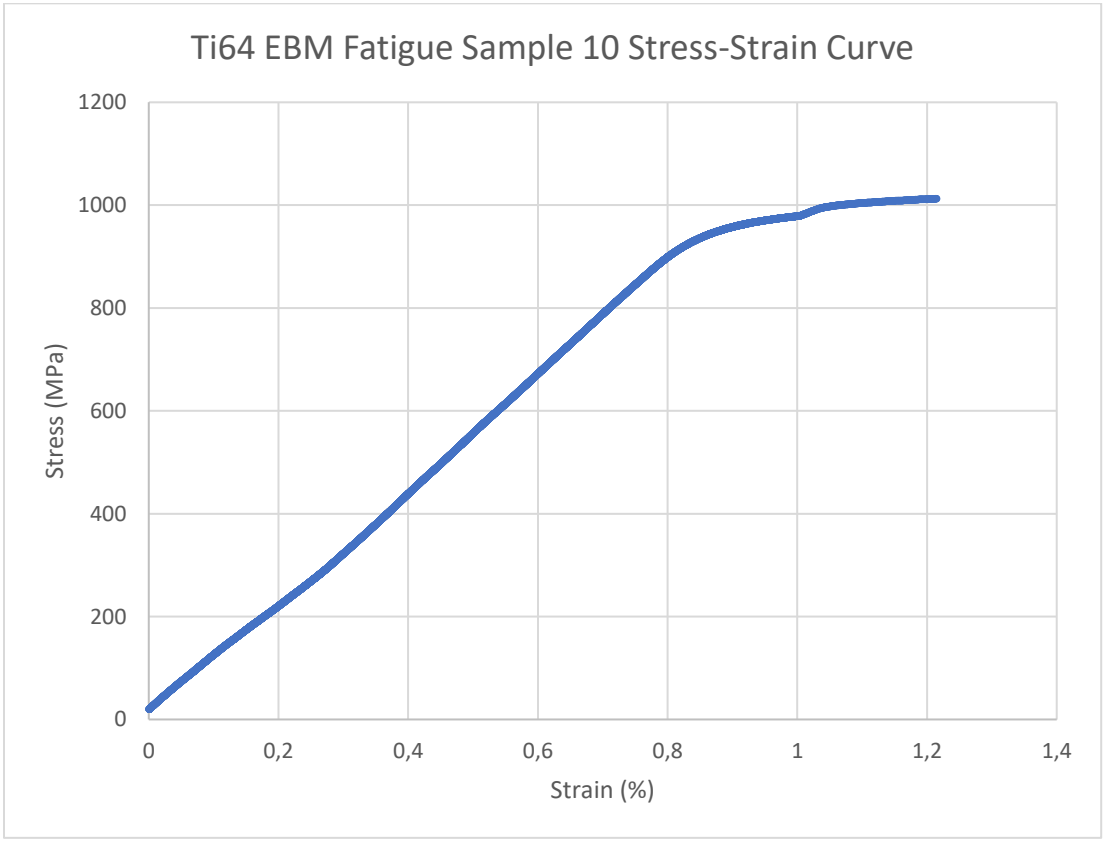
Ti64 EBM Fatigue Sample 10 Stress-Strain Curve
Stress (MPa)
1200
1000
800
600
400
200
0
0
0,2
0,4
0,6
0,8
1
1,2
1,4
Strain (%)

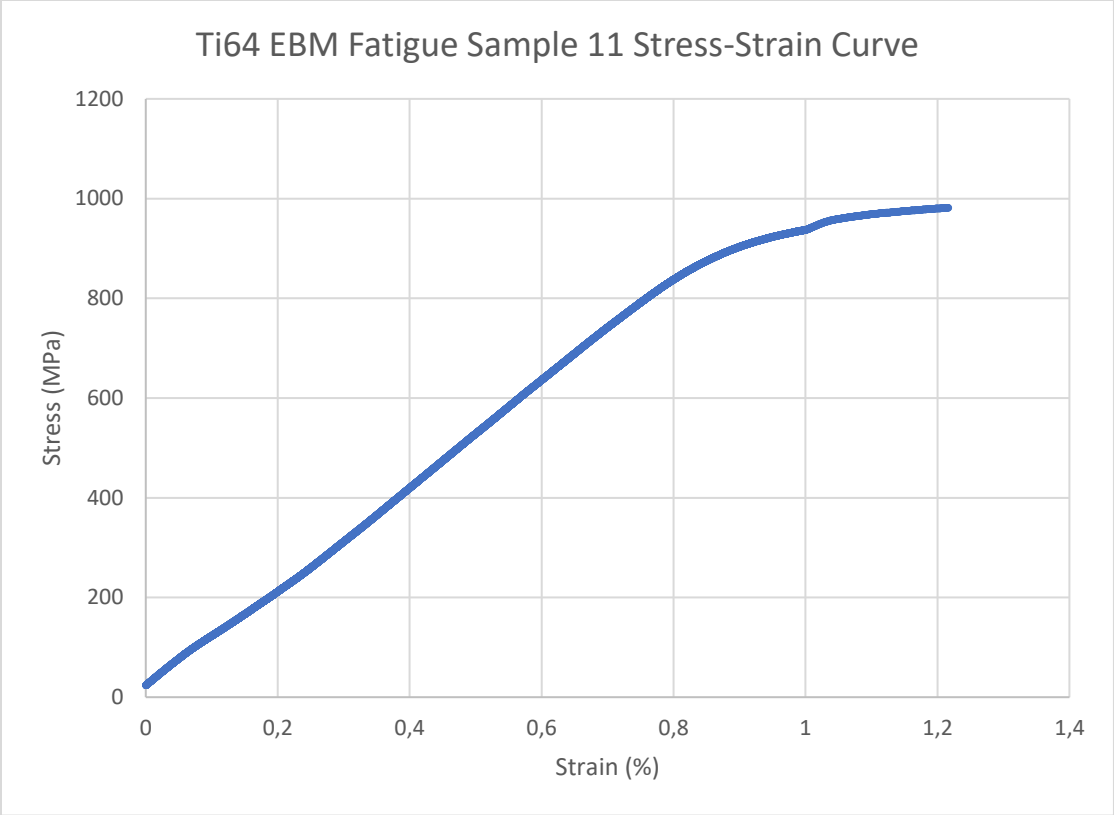
Ti64 EBM Fatigue Sample 11 Stress-Strain Curve
Stress (MPa)
1200
1000
800
600
400
200
0
0
0,2
0,4
0,6
0,8
1
1,2
1,4
Strain (%)

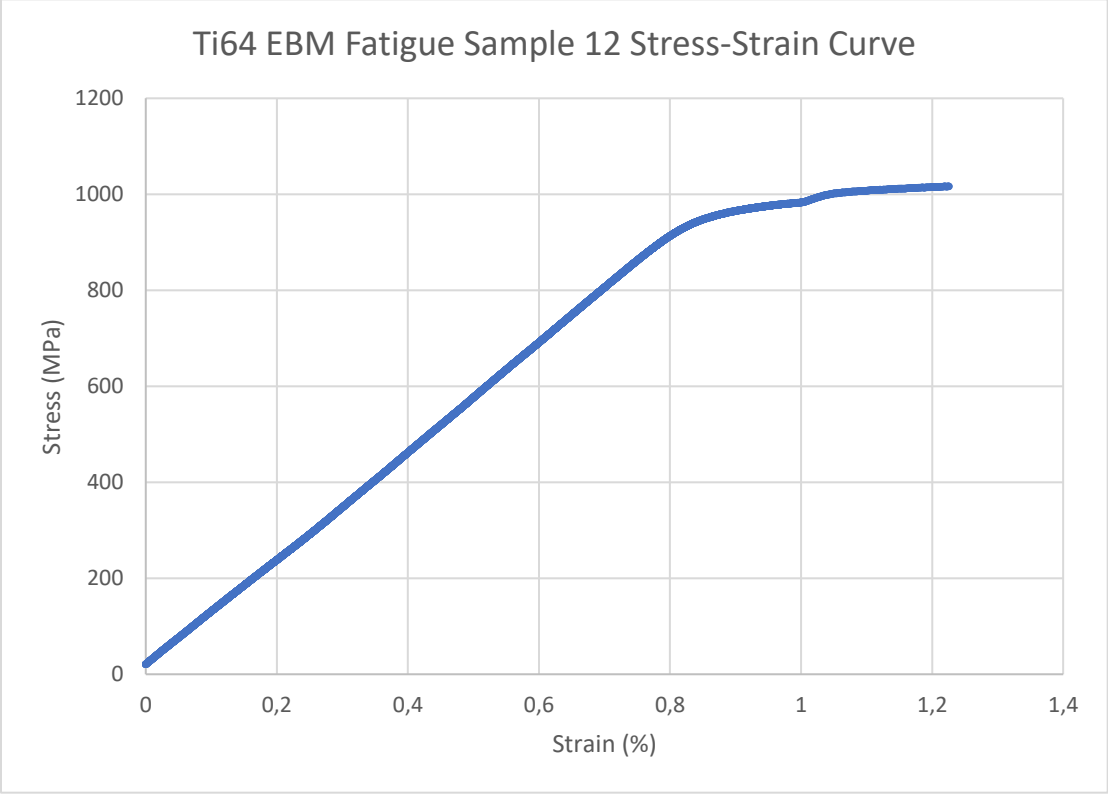
Ti64 EBM Fatigue Sample 12 Stress-Strain Curve
Stress (MPa)
1200
1000
800
600
400
200
0
0
0,2
0,4
0,6
0,8
1
1,2
1,4
Strain (%)

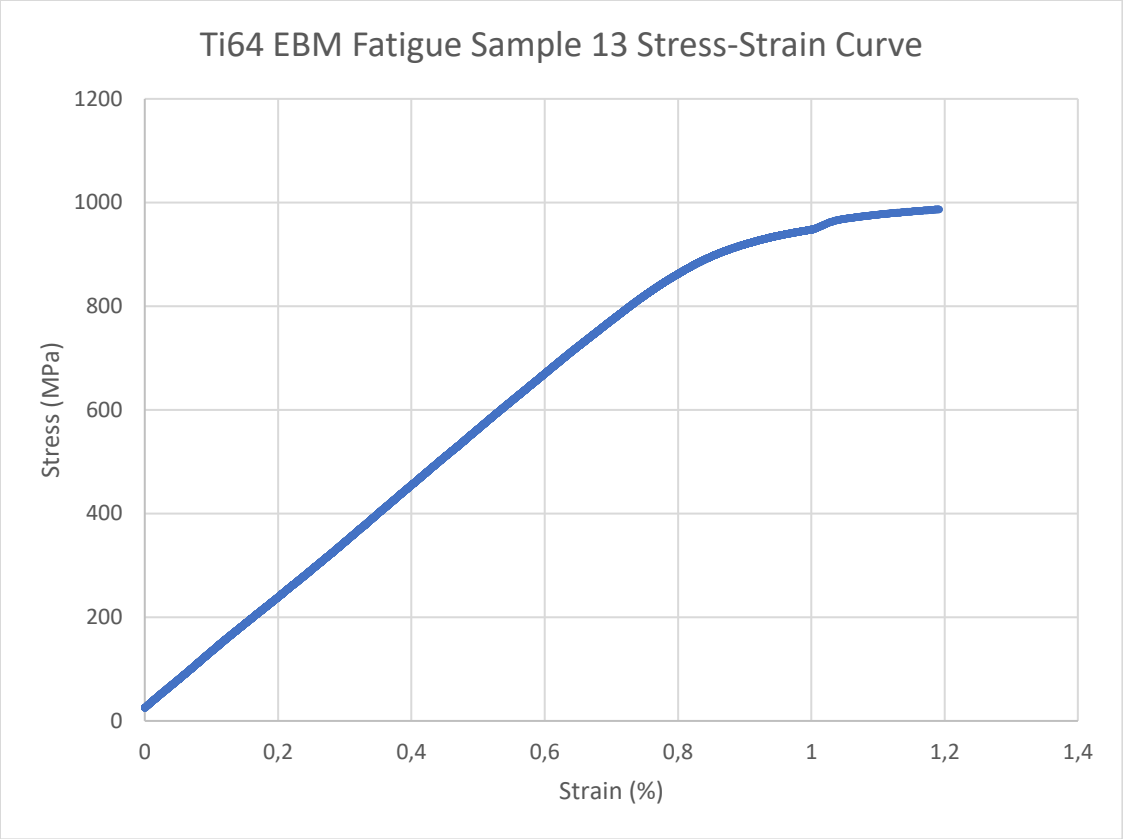
Ti64 EBM Fatigue Sample 13 Stress-Strain Curve
Stress (MPa)
1200
1000
800
600
400
200
0
0
0,2
0,4
0,6
0,8
1
1,2
1,4
Strain (%)

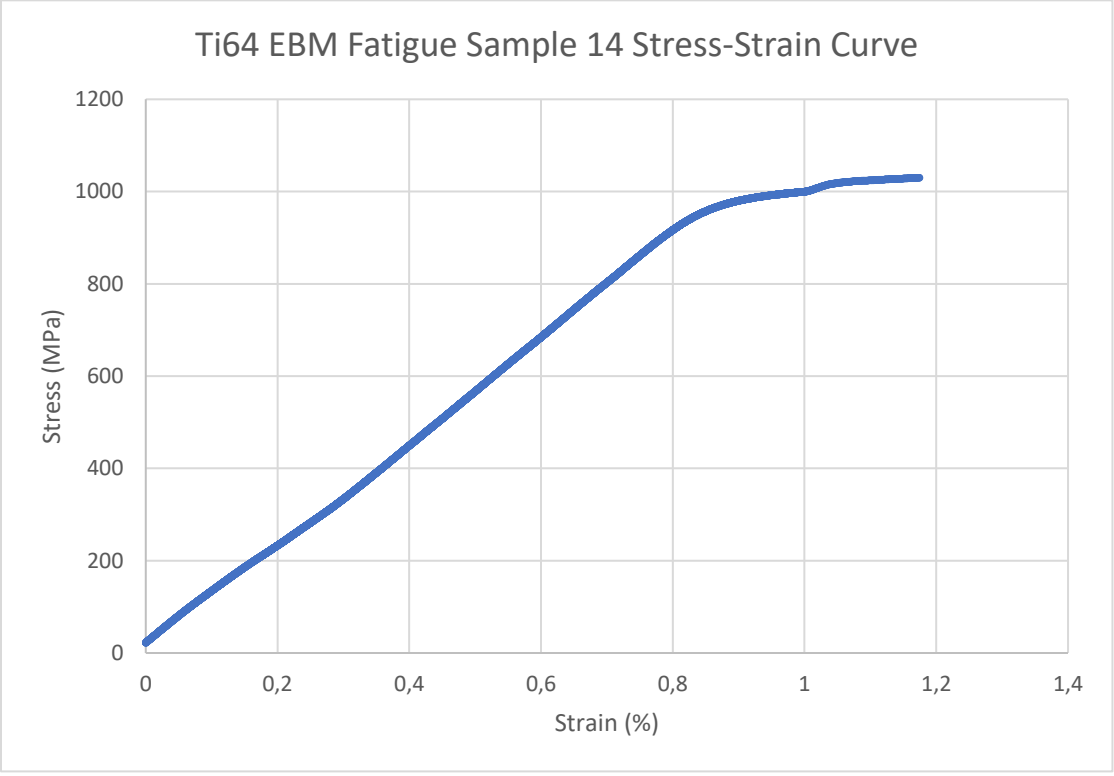
Ti64 EBM Fatigue Sample 14 Stress-Strain Curve
Stress (MPa)
1200
1000
800
600
400
200
0
0
0,2
0,4
0,6
0,8
1
1,2
1,4
Strain (%)

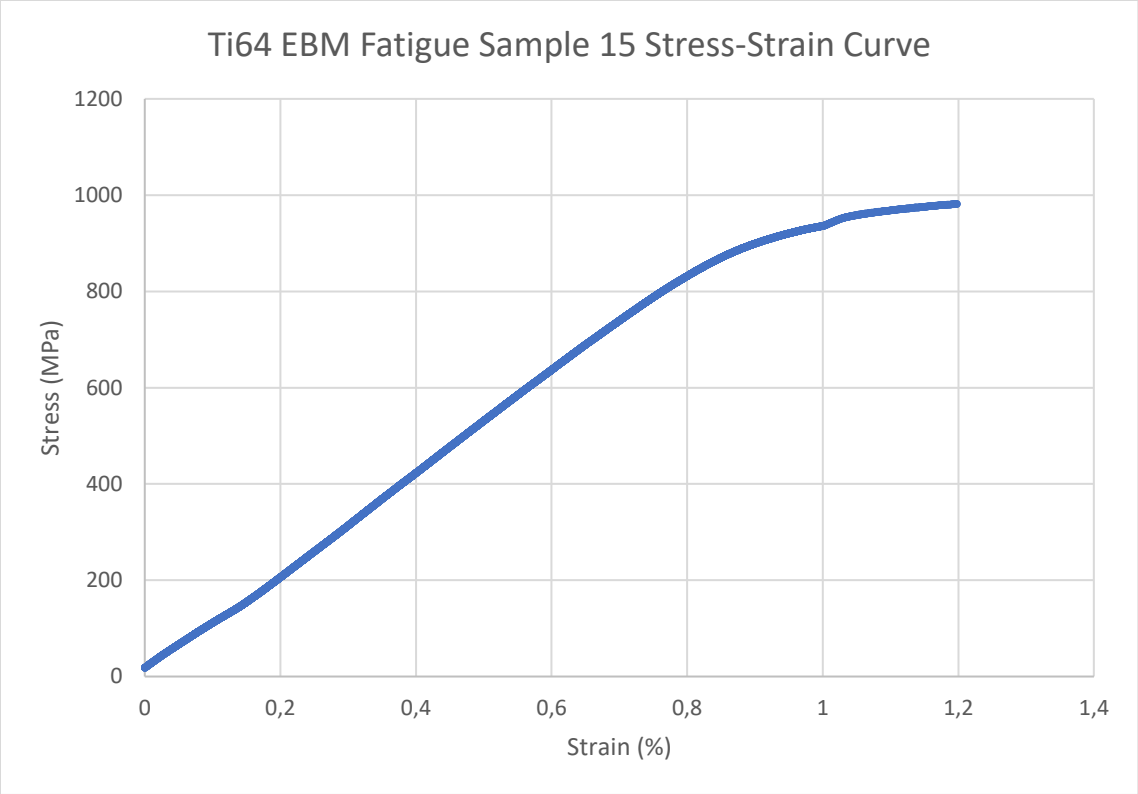
Ti64 EBM Fatigue Sample 15 Stress-Strain Curve
Stress (MPa)
1200
1000
800
600
400
200
0
0
0,2
0,4
0,6
0,8
1
1,2
1,4
Strain (%)

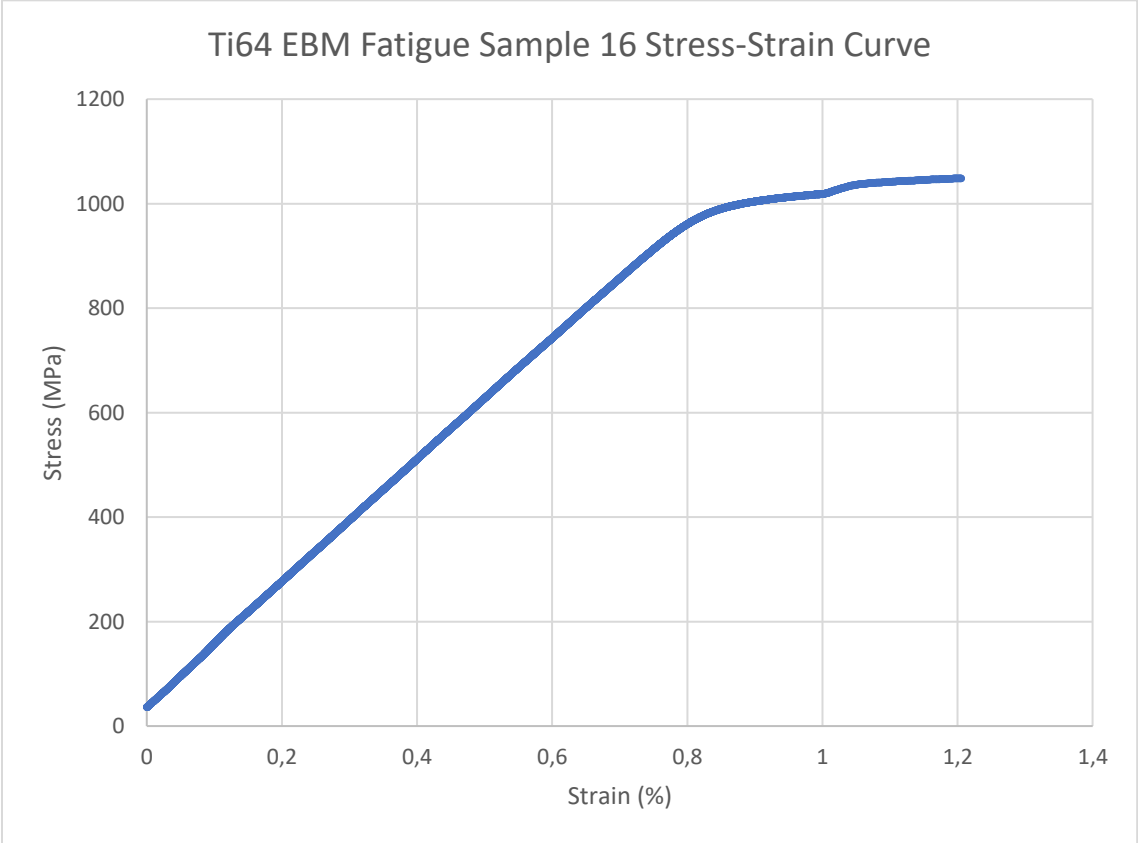
Ti64 EBM Fatigue Sample 16 Stress-Strain Curve
Stress (MPa)
1200
1000
800
600
400
200
0
0
0,2
0,4
0,6
0,8
1
1,2
1,4
Strain (%)

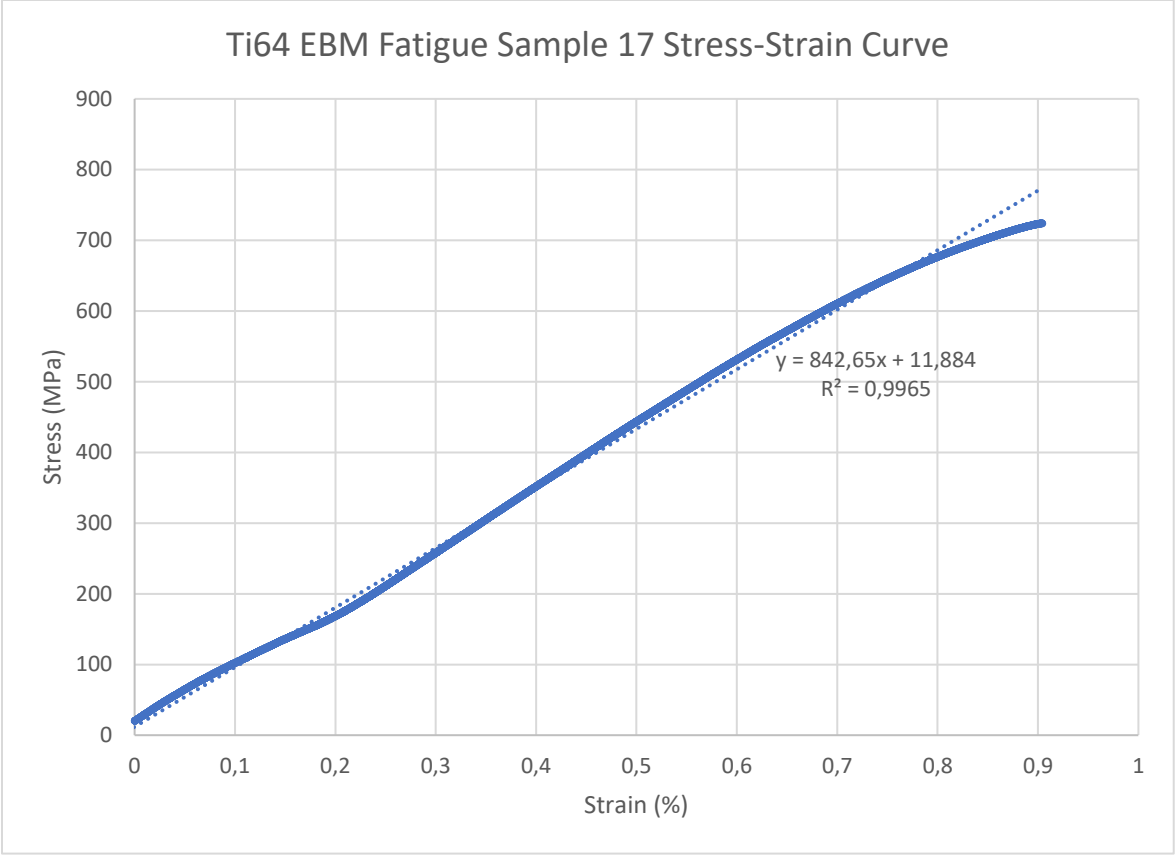
Ti64 EBM Fatigue Sample 17 Stress-Strain Curve
Stress (MPa)
900
800
700
600
500
400
300
200
100
0
0
0,1
0,2
0,3
0,4
0,5
0,6
0,7
0,8
0,9
1
Strain (%)
y = 842,65x + 11,884
R² = 0,9965

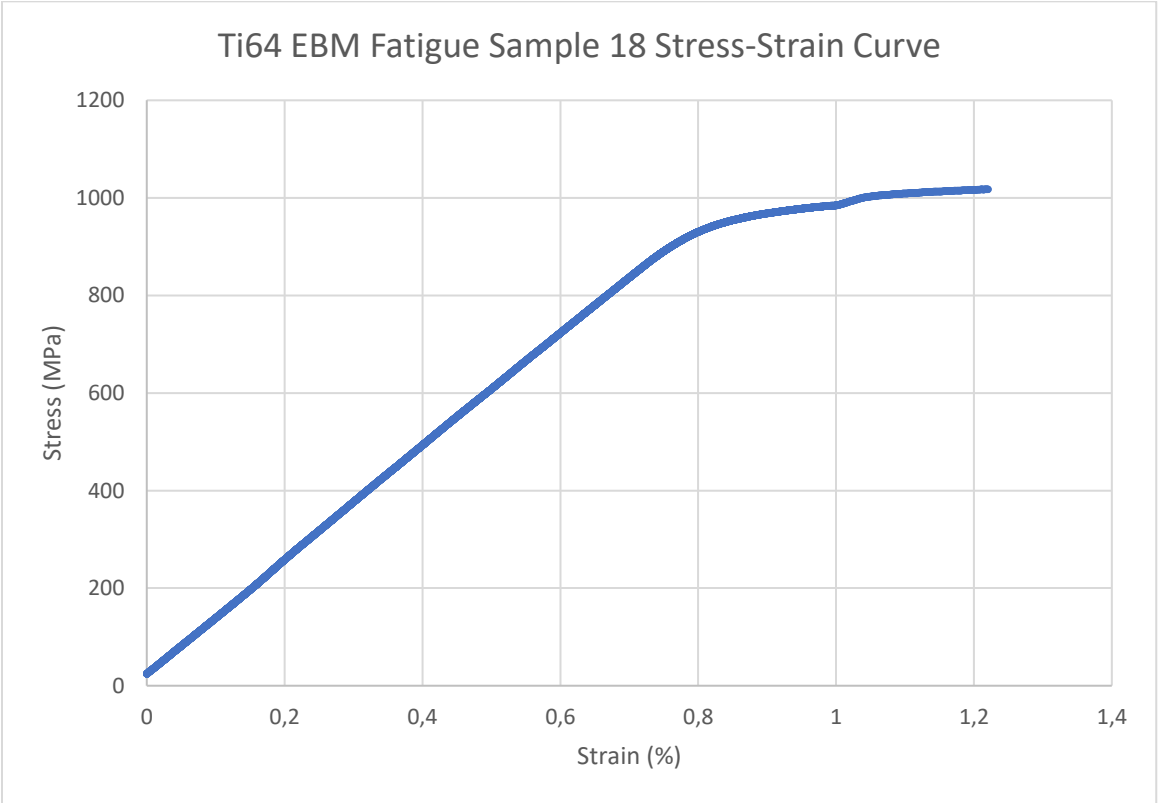
Ti64 EBM Fatigue Sample 18 Stress-Strain Curve
Stress (MPa)
1200
1000
800
600
400
200
0
0
0,2
0,4
0,6
0,8
1
1,2
1,4
Strain (%)

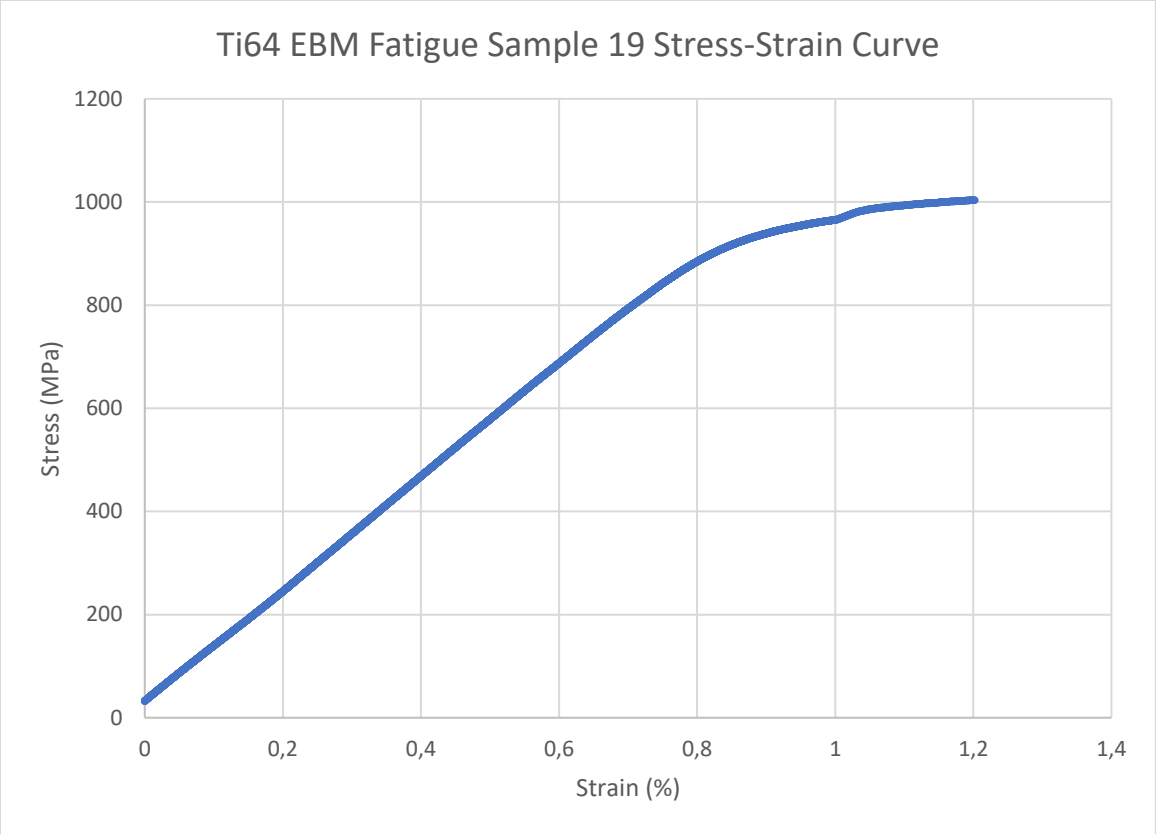
Ti64 EBM Fatigue Sample 19 Stress-Strain Curve
Stress (MPa)
1200
1000
800
600
400
200
0
0
0,2
0,4
0,6
0,8
1
1,2
1,4
Strain (%)

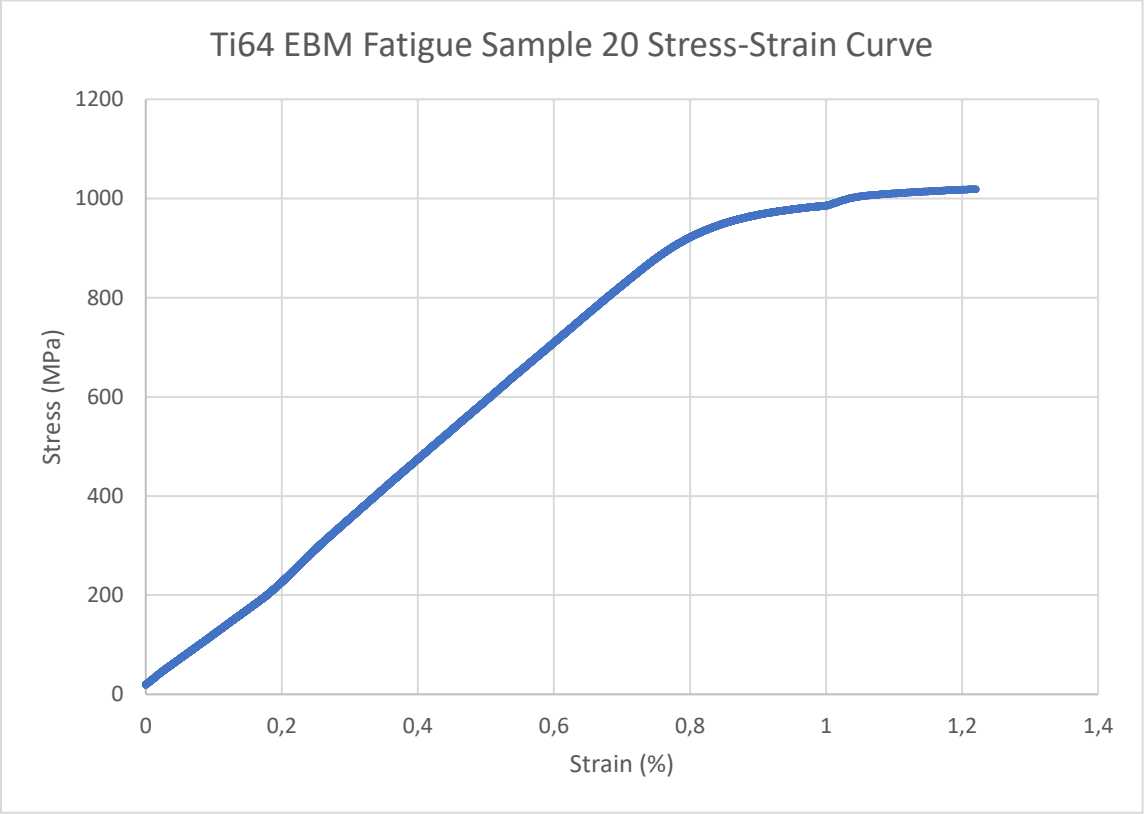
Ti64 EBM Fatigue Sample 20 Stress-Strain Curve
Stress (MPa)
1200
1000
800
600
400
200
0
0
0,2
0,4
0,6
0,8
1
1,2
1,4
Strain (%)

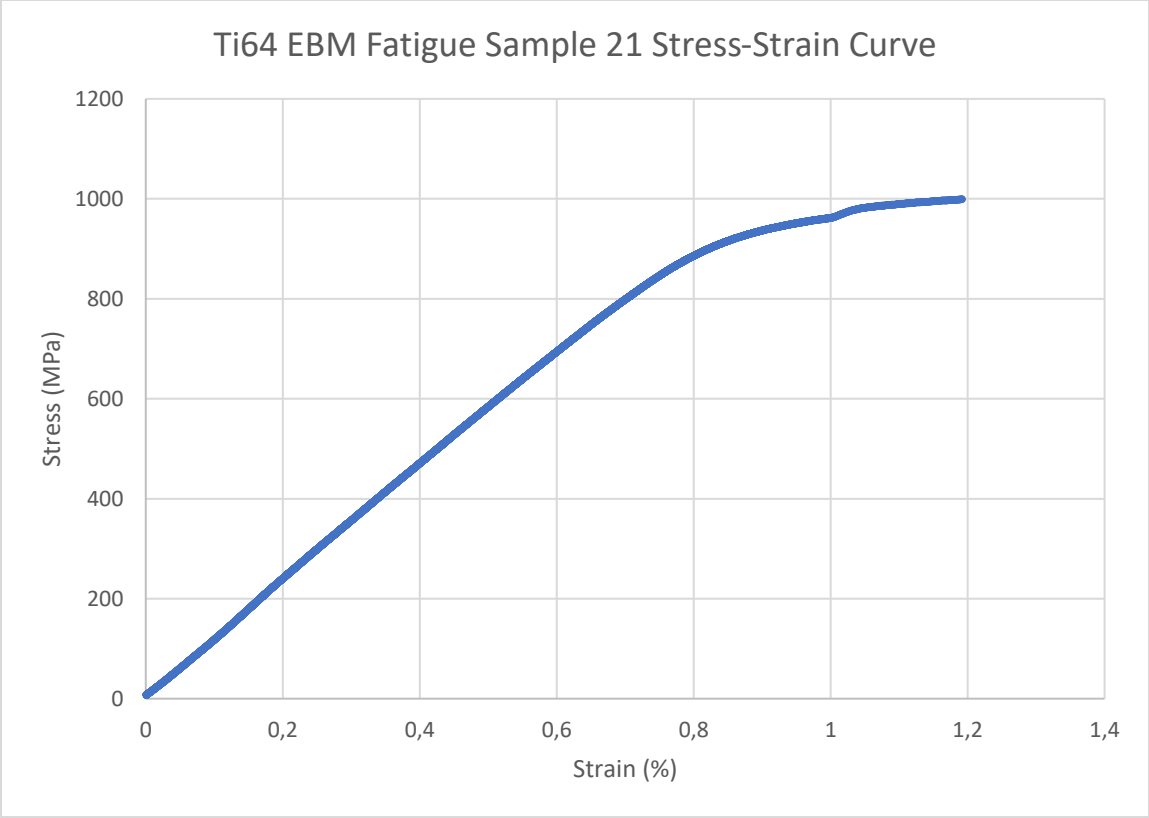
Ti64 EBM Fatigue Sample 21 Stress-Strain Curve
Stress (MPa)
1200
1000
800
600
400
200
0
0
0,2
0,4
0,6
0,8
1
1,2
1,4
Strain (%)

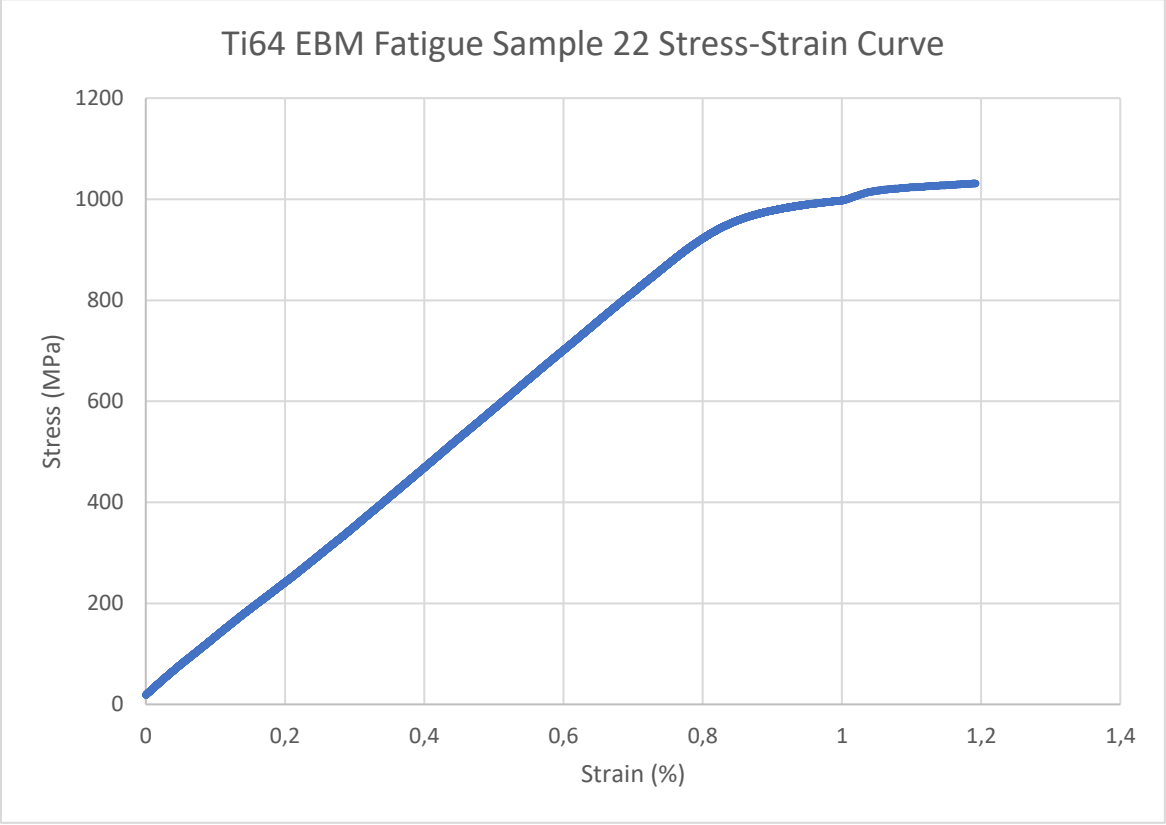
Ti64 EBM Fatigue Sample 22 Stress-Strain Curve
Stress (MPa)
1200
1000
800
600
400
200
0
0
0,2
0,4
0,6
0,8
1
1,2
1,4
Strain (%)

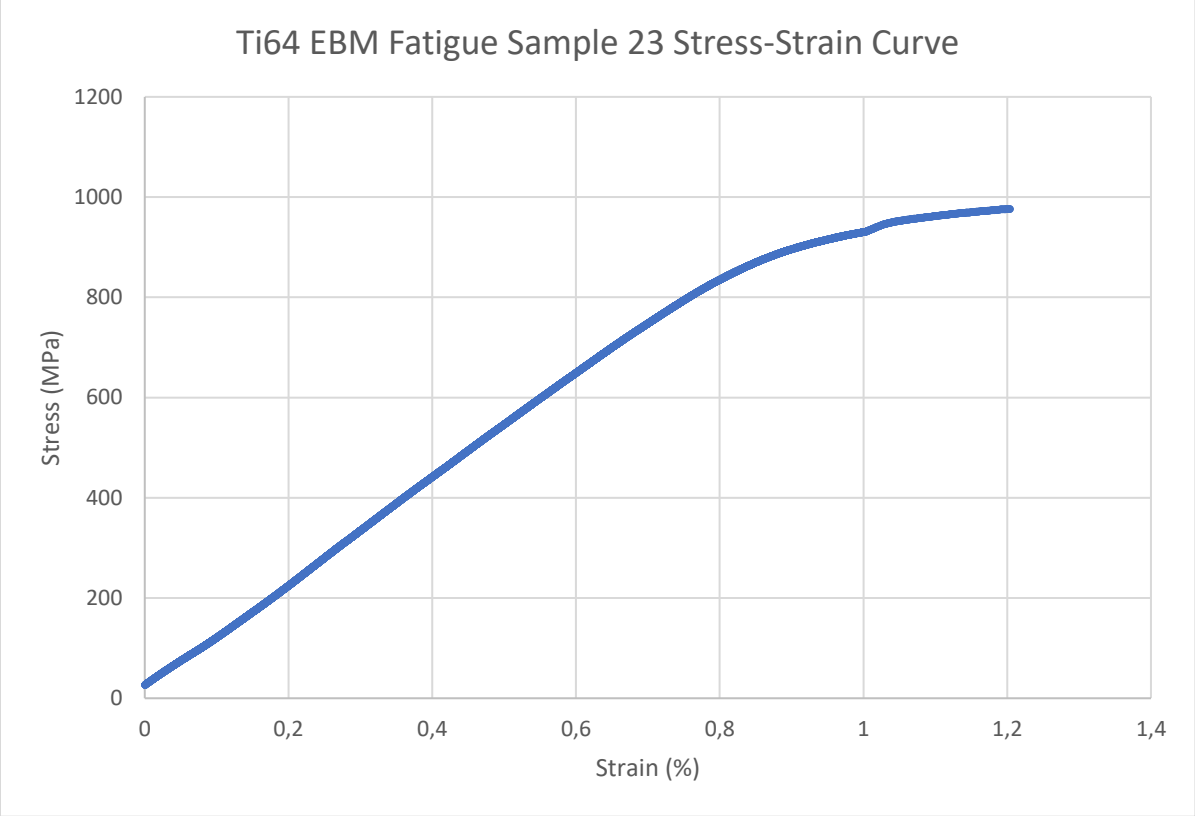
Ti64 EBM Fatigue Sample 23 Stress-Strain Curve
Stress (MPa)
1200
1000
800
600
400
200
0
0
0,2
0,4
0,6
0,8
1
1,2
1,4
Strain (%)

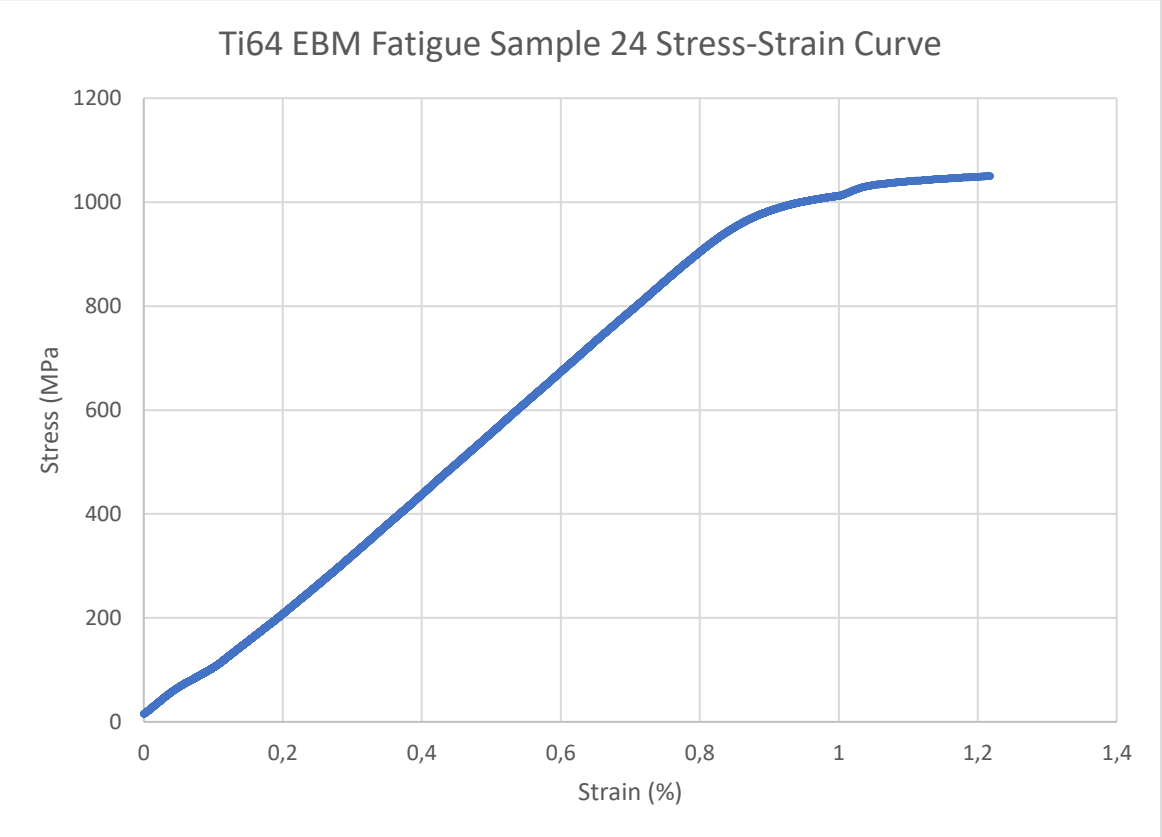
Ti64 EBM Fatigue Sample 24 Stress-Strain Curve
Stress (MPa
1200
1000
800
600
400
200
0
0
0,2
0,4
0,6
0,8
1
1,2
1,4
Strain (%)

Appendix M Fatigue samples fracture surface

Fatigue Sample 1 : Feret Diameter

Fatigue Sample 1 : Murakami's effective root area

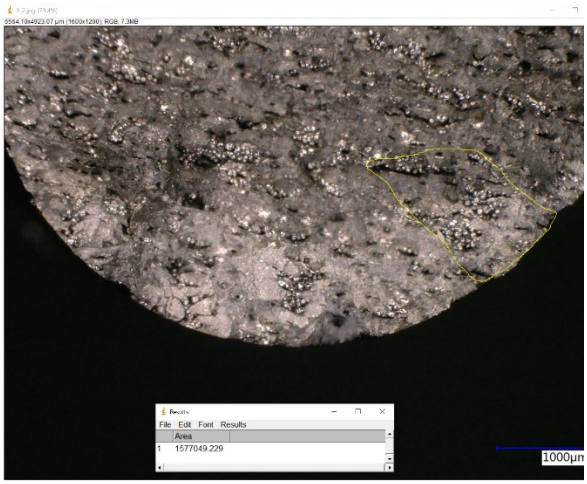

Fatigue Sample 2 : Feret Diameter

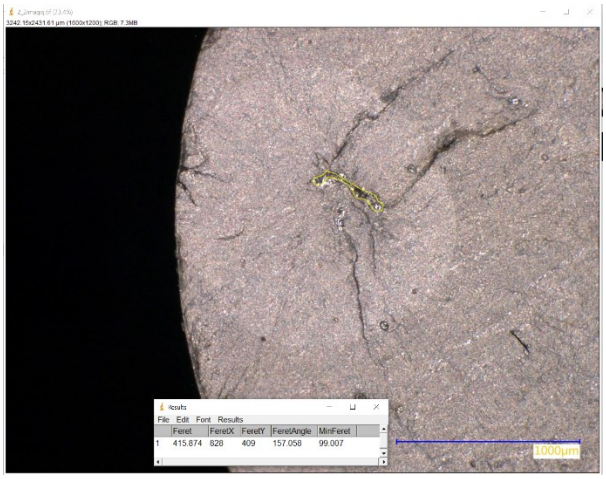

Fatigue Sample 2 : Murakami's effective root area

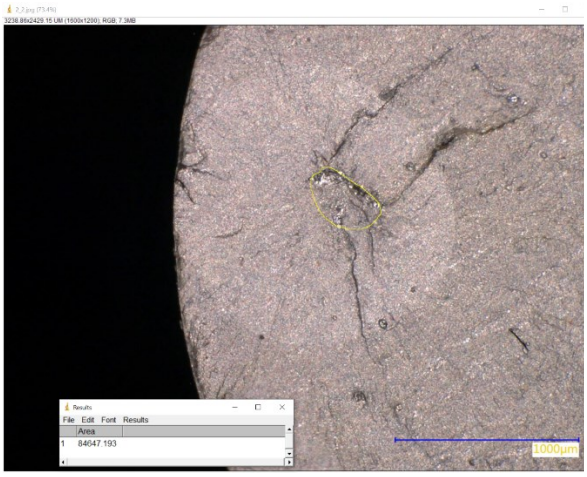

Fatigue Sample 3 : Feret Diameter

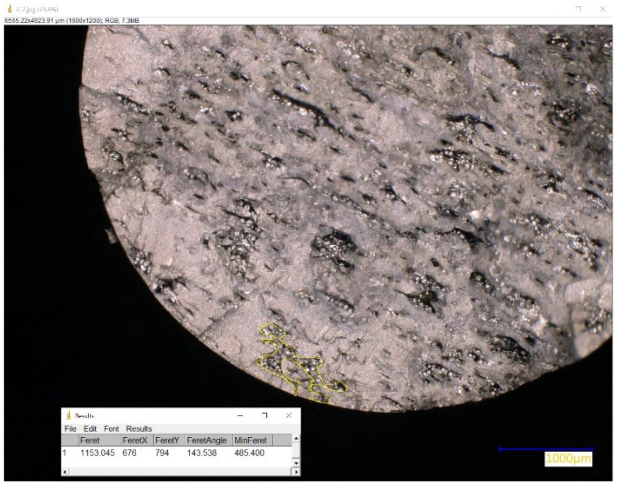

Fatigue Sample 3 : Murakami's effective root area

Fatigue Sample 4 : Feret Diameter

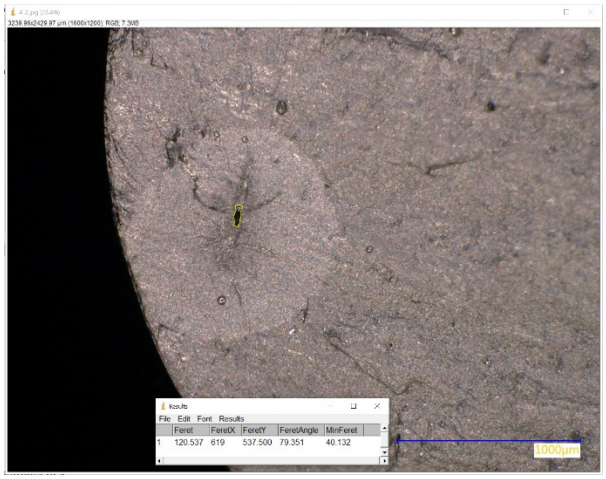

Fatigue Sample 4 : Murakami's effective root area

Fatigue Sample 5 : Feret Diameter

Fatigue Sample 5 : Murakami's effective root area

Fatigue Sample 6 : Feret Diameter

Fatigue Sample 6 : Murakami's effective root area

Fatigue Sample 7 : Feret Diameter

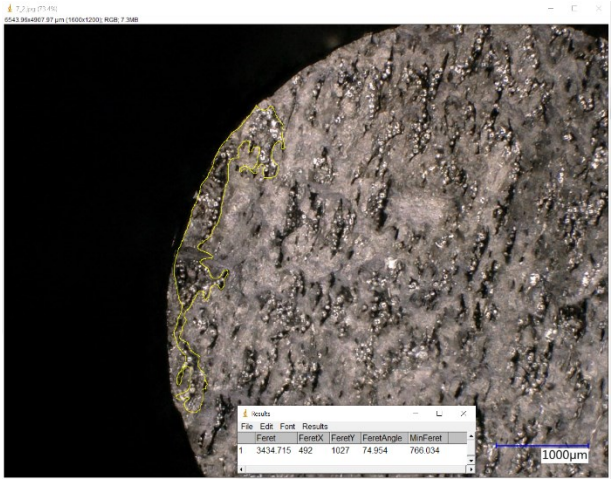

Fatigue Sample 7 : Murakami's effective root area

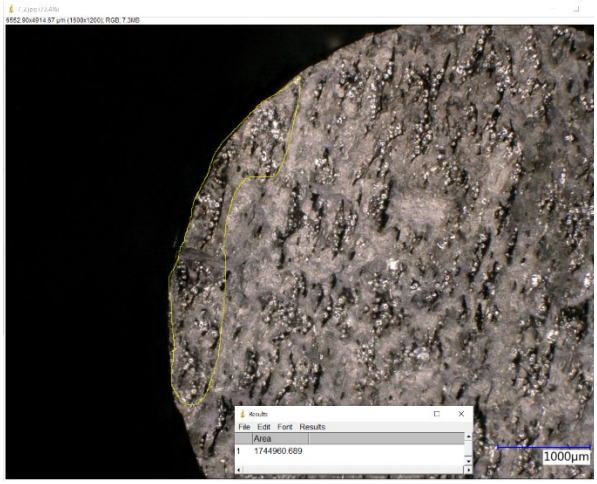

Fatigue Sample 8: Feret Diameter

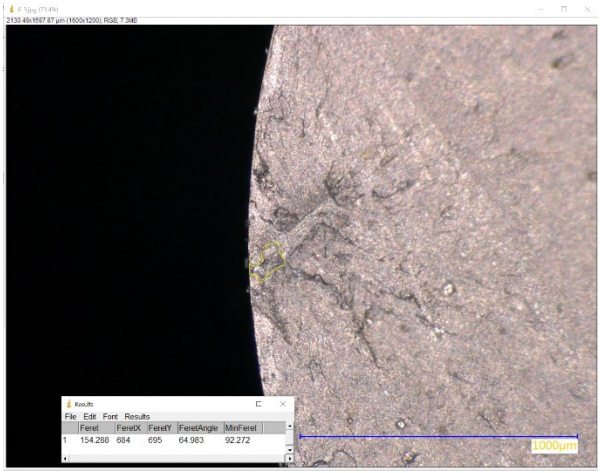

Fatigue Sample 8 : Murakami's effective root area

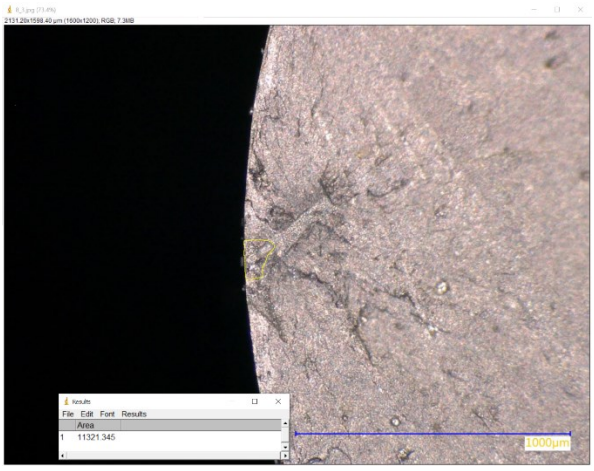

Fatigue Sample 9 : Feret Diameter

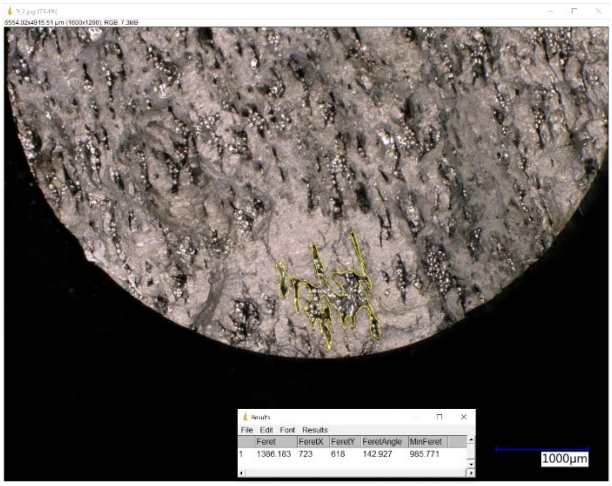

Fatigue Sample 9 : Murakami's effective root area

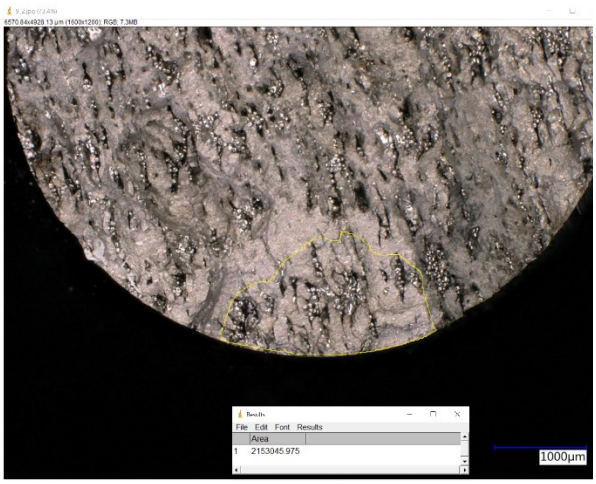

Fatigue Sample 10 : Feret Diameter

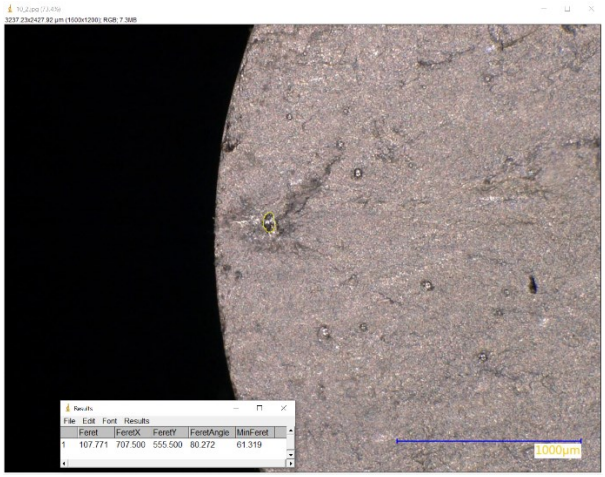

Fatigue Sample 10 : Murakami's effective root area

Fatigue Sample 11 : Feret Diameter

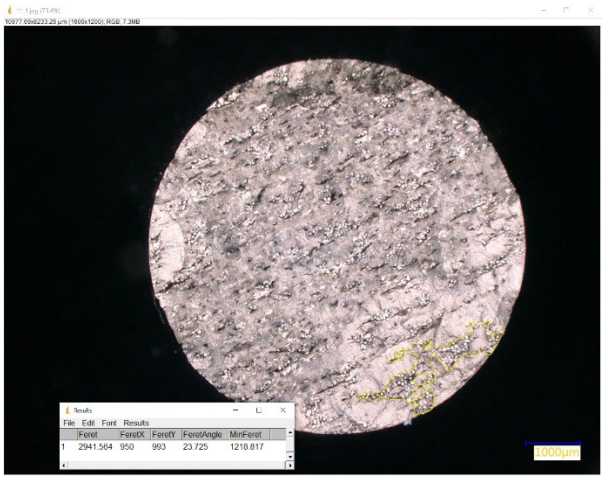

Fatigue Sample 11 : Murakami's effective root area

Fatigue Sample 12 : Feret Diameter

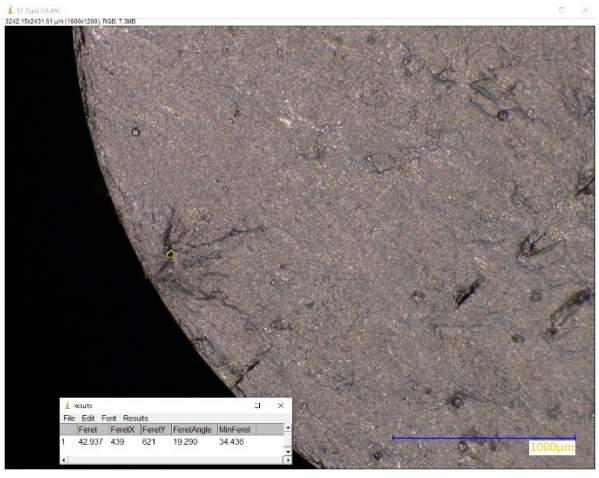

Fatigue Sample 12 : Murakami's effective root area

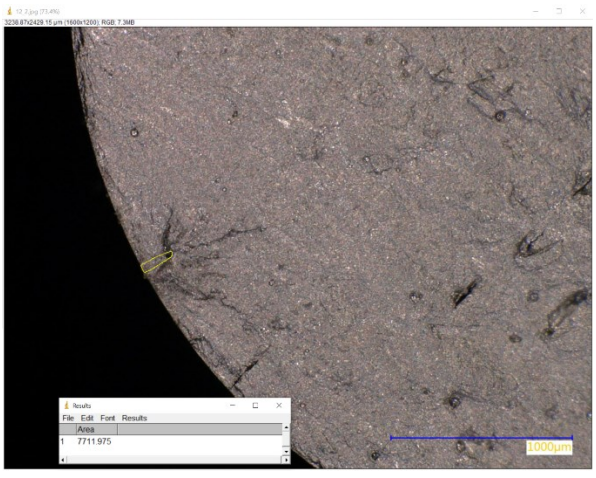

Fatigue Sample 13 : Feret Diameter

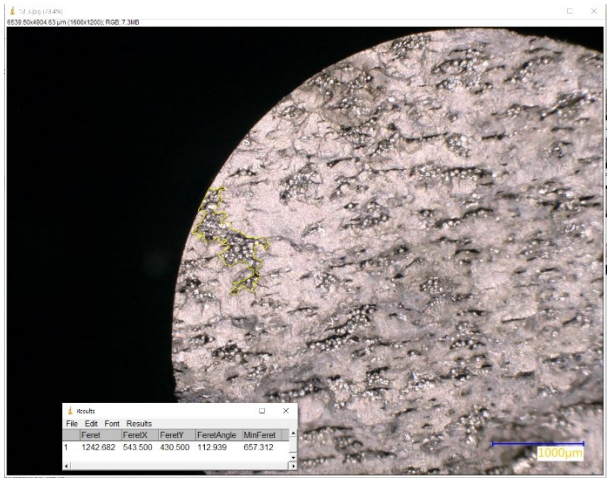

Fatigue Sample 13 : Murakami's effective root area

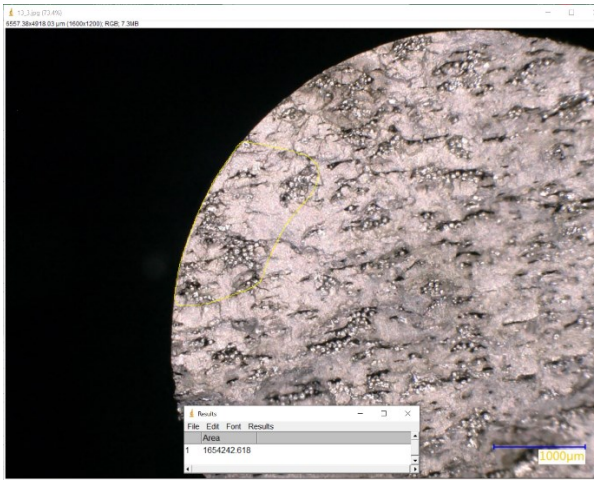

Fatigue Sample 14 : Feret Diameter

Fatigue Sample 14 : Murakami's effective root area

Fatigue Sample 15 : Feret Diameter

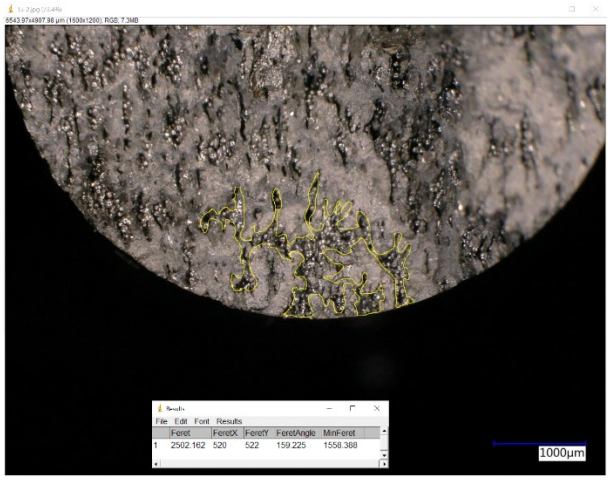

Fatigue Sample 15 : Murakami's effective root area

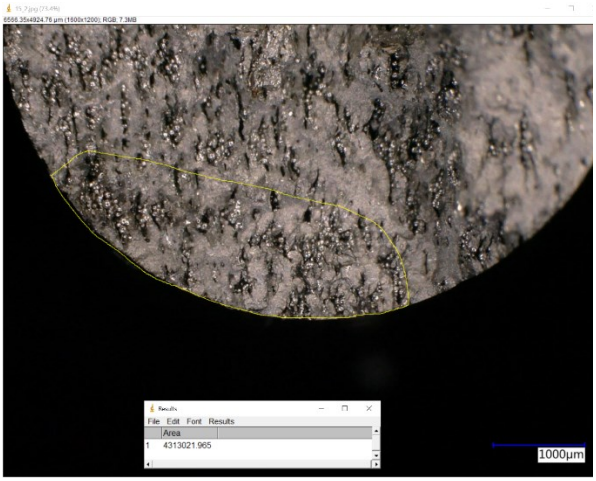

Fatigue Sample 16 : Feret Diameter

Fatigue Sample 16 : Murakami's effective root area

Fatigue Sample 18 : Feret Diameter

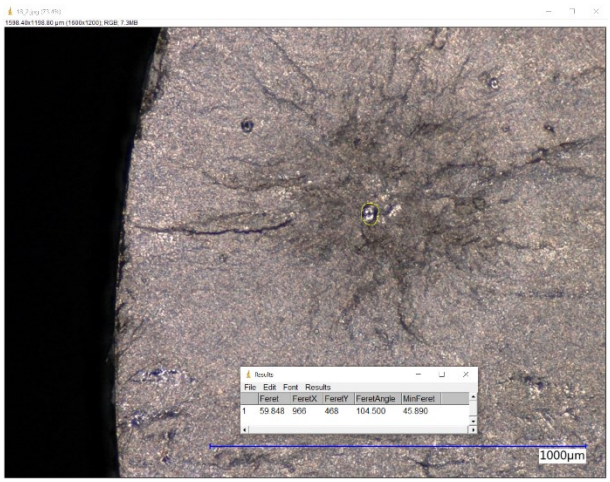

Fatigue Sample 18 : Murakami's effective root area

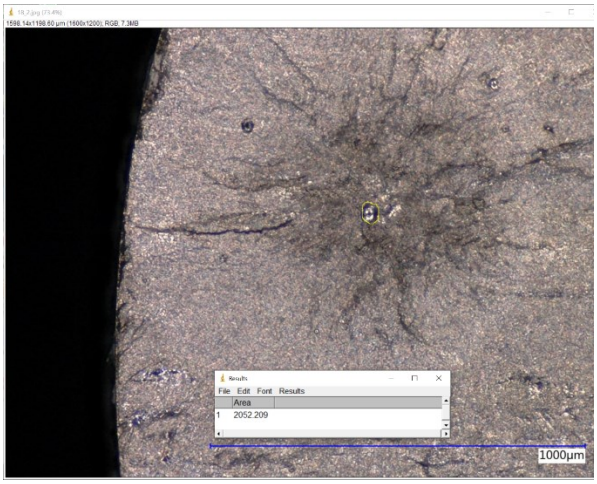

Fatigue Sample 19 : Feret Diameter

Fatigue Sample 19 : Murakami's effective root area

Fatigue Sample 20 : Feret Diameter

Fatigue Sample 20 : Murakami's effective root area

Fatigue Sample 21 : Feret Diameter

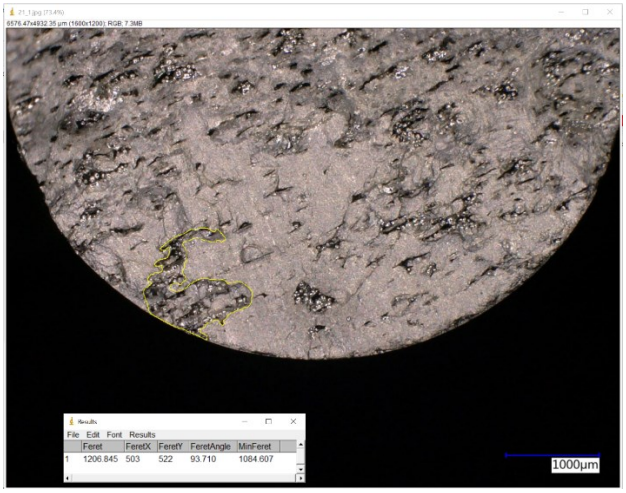

Fatigue Sample 21 : Murakami's effective root area

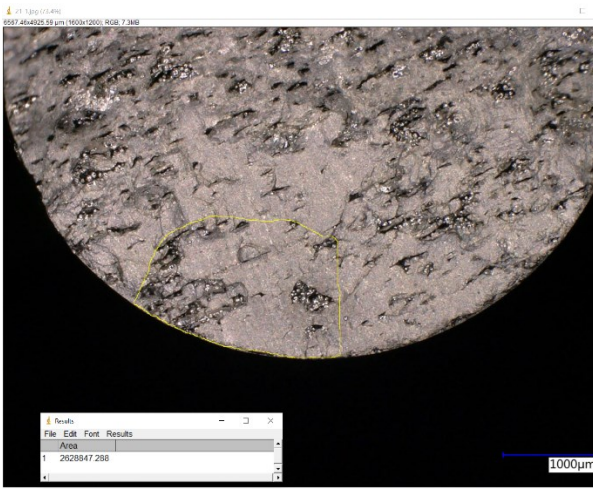

Fatigue Sample 22 : Feret Diameter

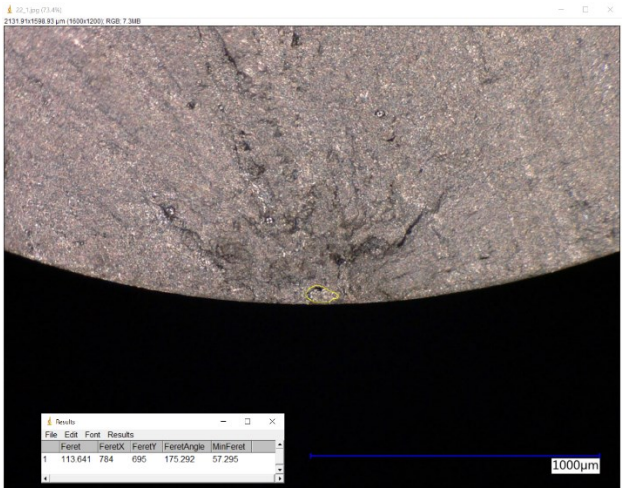

Fatigue Sample 22 : Murakami's effective root area

Fatigue Sample 23 : Feret Diameter

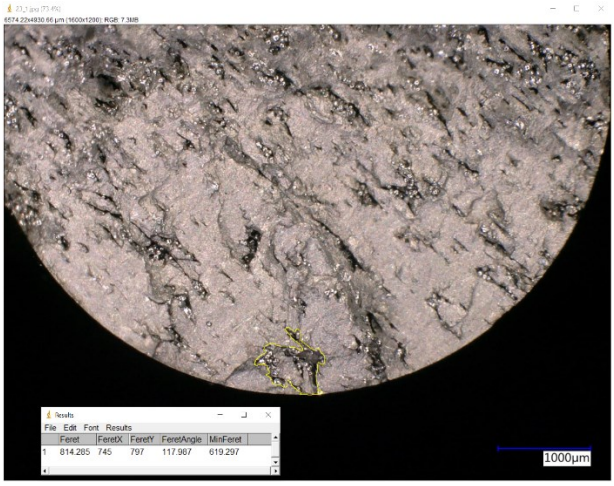

Fatigue Sample 23 : Murakami's effective root area